Many-body dynamics of laser-driven ultracold atoms in optical lattices : from strong interactions to the quantum Zeno regime in a bosonic quantum gas

Alexis Ghermaoui

Many-body dynamics of laser-driven ultracold atoms in optical lattices : from strong interactions to the quantum Zeno regime in a bosonic quantum gas

Alexis Ghermaoui

Laboratoire Kastler Brossel — Collège de France

Thèse de doctorat de Sorbonne Université

préparée par

Alexis GHERMAOUI

18 décembre 2020

Many-body dynamics of laser-driven ultracold atoms in optical lattices

From strong interactions to the quantum Zeno regime in a bosonic quantum gas

---

M. Radu CHICIREANU	Rapporteur
M. Guido PUPILLO	Rapporteur
M. Jean-Philippe BRANTUT	Examinateur
M. Nicolas DUPUIS	Examinateur
M. Jérôme BEUGNON	Membre invité
M. Fabrice GERBIER	Directeur de thèse

Travail réalisé au laboratoire Kastler Brossel, au sein du Collège de France.

Abstract

In this manuscript I present the experimental studies of the physics of ultracold bosonic ytterbium atoms trapped in an optical lattice, driven on their clock transition. The existence of this ultranarrow transition is a feature shared by the alkaline-earth like atoms, to which belongs ytterbium. The coherent driving of this transition enables an internal degree of freedom for the atoms without spontaneous emission and is of great interest in the context of metrology and quantum simulation.

Firstly I use the properties of this clock transition to characterize the coherent driving of isolated atoms. Then I use Ramsey spectroscopy to probe the dynamics taking place in unidimensional lattices in the strong interactions regime. Secondly I present experiments performed on pairs of bosons where the coupling on the ultranarrow transition is adiabatically branched, which leads to a strong suppression of the inelastic collision-induced losses. This phenomenon is a manifestation of the quantum Zeno effect that restricts the dynamics of the system to a reduced-loss subspace of the total Hilbert space. Finally I experimentally study the manifestation of the quantum Zeno effect for a many-body system, namely an unidimensional lattice in presence of strong inelastic interactions, resulting in the hindering of the atomic loss dynamics.

Résumé

Dans ce manuscrit je décris les différentes études expérimentales portant sur la physique des gaz atomiques d'ytterbium dégénérés piégés dans un réseau optique et excités sur leur transition d'horloge. L'existence de cette transition étroite, propriétée commune aux atomes alcalino-terreux et aux éléments ayant une structure électronique similaire, comme l'ytterbium, confère à ces atomes un degré de liberté interne sans voir apparaitre des phénomènes d'émission spontanée, ouvrant des perspective prometteuses dans les domaines de la simulation quantique et de le métrologie.

Dans le travail présenté ici, je commence par tirer avantage des propriétés de la transition horloge pour caractériser l'évolution de la cohérence de l'état interne d'atomes d'ytterbium excités sur cette transition. Ensuite, j'utilise la spectroscopie Ramsey pour étudier la dynamique de réseaux unidimensionels dans le régime des fortes interactions. Dans un second temps je présente les expériences conduites sur des paires de bosons, où le couplage sur la transition étroite est branchée adiabatiquement, conduisant à une forte supression des pertes liées aux collisions inélastiques. Ce phénomène relève de l'effet Zénon quantique qui restreint la dynamique du système à un sous-espace de l'espace de Hilbert. Enfin je présente l'étude expérimentale de l'effet Zéno quantique dans un système à N-corps soumis à de fortes interactions inélastiques, qui se manifeste par une inhibition de la dynamique de pertes atomiques.

Contents

Glossary

Notations used in this manuscript

1BZ First Brillouin zone,

AEL Alkaline-earth-like,

AOM Acousto-optic modulator,

BEC Bose-Einstein condensate,

BH Bose-Hubbard,

CDT Crossed dipole trap,

EP Exceptional point,

EOM Electro-optic modulator,

HCB Hard-core bosons,

LDA Local density approximation,

MI Mott insulator,

MOT Magneto-optical trap,

OD Optical density,

PDH Pound-Drever-Hall,

QZE Quantum Zeno Effect,

TOF Time-of-flight,

ULE Ultra-low expansion.

The notation C_n^p refers to the binomial coefficient "n choose p", defined as

$$C_n^p = \binom{n}{k} = \frac{n!}{k!(n-k)!}. \tag{1}$$

Introduction

In 1925 A. Einstein, following the work of S. N. Bose that had proposed a statistical description of photons as an ideal gas of identical particles to derive the Planck's law (Bose 1924), extended it to the ideal monoatomic gas and predicted the existence of a phase transition for low enough temperatures at which all the atoms would fall into the same state of minimal energy: the Bose-Einstein condensation was introduced (Einstein 1925). However the very low expected condensation temperatures led him to wonder "*It's a great theory, but does it contain a truth ?*" in his correspondence with P. Ehrenfest. Indeed, even if F. London in 1938 argued a link between the recently discovered superfluidity of liquid helium and the Bose-Einstein condensation (London 1938), the direct observation of this phenomenon appeared to be beyond reach.

The invention of the laser in 1960 (Maiman 1960) opened up new possibilities in a large panel of fields of physics. More particularly this invention, from the seminal work of Hänsch et al. 1975, is at the origin of the development of different laser cooling techniques in the 80's (Phillips 1998; Cohen-Tannoudji 1998; Chu 1998). These techniques, coupled with the evaporative cooling technique (Hess 1986; Masuhara et al. 1988) led to the achievement of Bose-Einstein condensation (Anderson et al. 1995; Bradley et al. 1995; Davis et al. 1995) and the realization of the first degenerate Fermi gas (DeMarco et al. 1999) a few years later. These pioneering experiments have paved the way for the study of a whole new scope of phenomena, leading to the emergence of the new branch of physics of ultracold atoms.

In the two decades that followed the first production of a degenerate quantum gas, the properties of these new states of matter have been extensively studied. The ondulatory nature of the Bose-Einstein condensates was demonstrated in experiments involving matter wave interference (Andrews et al. 1997) or revealing the existence of a long-range phase coherence (Bloch et al. 2000). In the meantime, experiments have brought to light their superfluid behavior (Matthews et al. 1999; Madison et al. 2000) by the observation of vortices. Experimentalists have also taken advantage of the tunability of inter-particle interactions in degenerate quantum gases provided by the existence of Feschbach resonances (Cornish et al. 2000; Bloch et al. 2008; Chin et al. 2010) to brought these dilutes gases in the strong interaction regime.

An alternative way to reach the strong interaction regime is to apply an optical lattice potential to a degenerate quantum gas. This approach has been implemented for the first time in the seminal experiment of Greiner et al. 2002 that showed the quantum phase transition from a superfluid to Mott-insulating phase, according to the proposal

of Jaksch et al. 1998. More generally ultracold atoms trapped in optical lattices offer a reliable and versatile platform to study systems described by condensed-matter models such as Hubbard models, spin models and disordered or frustrated systems (Lewenstein et al. 2012), possibly in regimes that would be difficult to reach for standard condensed-matter system, *e.g.* strong magnetic fields for the study of fractional quantum Hall effect (Tsui et al. 1982). They can also be used to simulate systems from domains beyond condensed-matter such as cosmology or nuclear physics (Georgescu et al. 2014). Thanks to their versatility and high control level (Bloch et al. 2012), much more important than most condensed-matter systems, the optical lattices appears as a promising tool in the perspective of *quantum simulation*.

This concept of quantum simulation was introduced by R. Feynman, depicting a *"computer itself* [...] *built of quantum mechanical elements which obey quantum mechanical laws."* (Feynman 1982), *i.e.* a quantum system replicating the dynamics of a system of interest in order to study is dynamics, with direct access to the relevant observables. It is particularly interesting when it comes to simulate many-body physics, often described by models that do not admit an exact analytic solution, to overcome the difficulties arisen by the exponential growth of the Hilbert space dimension with the number of particles, preventing the use of classical computers.

In the past years, in order to overcome the limitations of the first experiments on degenerate quantum gases performed with alkali atoms, such as spontaneous emission-induced heating, two new categories of atoms has begun to receive growing attention. The first category gathers atoms, such as Cr, Dy and Er, featuring an important magnetic dipole moment in the ground state (Griesmaier et al. 2005; Lu et al. 2011; Aikawa et al. 2012) that allows to probe the physics of long-range dipole-dipole interactions (Lahaye et al. 2009). The second category corresponds to two-electron atoms (Takasu et al. 2003) that includes alkaline-earth atoms such as Sr, Ca and Mg, and alkaline-earth-like atoms such as Yb (Takasu et al. 2003). These elements feature an ultranarrow optical transition coupling their ground state to a long-lived excited metastable state (Ludlow et al. 2015) that has been in a first time used in the field of metrology (Takamoto et al. 2005; Hinkley et al. 2013). More recently the advantages offered by the properties of these atomic species in the context of simulation of quantum many-body physics have been pointed out in several proposals (Cazalilla et al. 2009; Gorshkov et al. 2010; Foss-Feig et al. 2010). In the particular case of our experiments, ytterbium has been chosen for its properties (besides the clock transition, the existence of reachable magic and anti-magic wavelengths) that could be used for the simulation of artificial gauge fields in optical lattice, following the proposal of Gerbier et al. 2010.

In the work presented in this thesis, emphasis is laid on the use of Yb optical lattice clock to probe the physics described by the Bose-Hubbard model (Fisher et al. 1989; Jaksch et al. 1998; Jaksch et al. 2005). This model is a paradigm in condensed-matter physics for it can describes a panel of systems including, besides ultracold atoms, Josephson junction arrays (Langen et al. 2015), optomechanical arrays (Tomadin et al. 2012), interacting polaritons in hybrid optical systems (Hartmann et al. 2008; Leib et al. 2010). More particularly, in this thesis work we take advantage of the tunability offered by optical lattices to freeze the motion of atoms along two of the three spatial directions, leading to the realization of a quasi unidimensional system. For such systems, the constraints imposed on the motion of the atoms gives an increased role to

play to the interactions, notably compared to higher dimensions. If the interactions are sufficiently strong, the dynamics of the system can be described by the theory of the *Tonks-Girardeau gases* (Tonks 1936; Girardeau 1960), where the atoms interacting in the 1D lattice behave as impenetrable hard-core bosons. This causes the emergence of strong correlations between the bosons of the gas that reminds those induced by the Pauli's exclusion principle in the fermionic case. A Bose-Fermi mapping is thus made possible (Girardeau 1960), allowing to theoretically describe the bosons thanks to a *fermionization* approach (Efetov et al. 1976; Korepin et al. 1997). The interplay between the bosonic and the fermionic properties in a Tonks-Girardeau has been observed in its first experimental realization made by Paredes et al. 2004.

In order to probe the dynamics of ultracold ^{174}Yb atoms trapped in a quasi unidimensional optical lattice, ruled by the unidimensional Bose-Hubbard Hamiltonian, it is possible to take advantage of the existence of an ultranarrow clock transition for these atoms, that can be used to perform Ramsey spectroscopy (Ramsey 1950). Since the introduction of this technique for Nuclear Magnetic Resonance (NMR) experiments and its variants, including Ramsey with spin echo spectroscopy (Hahn 1950), their use has been extended to many field of physics, *e.g.* metrology, cavity quantum electrodynamics (Bertet et al. 2001), superconducting qubits (Wallraff et al. 2005; Leek et al. 2007)... More recently Ramsey spectroscopy and Ramsey with spin echo techniques have been used to characterize the many-body dynamics of strongly interacting ultracold atoms trapped in unidimensional optical lattices. More precisely the evolution of the Ramsey fringes contrast can be linked to the evolution of coherence of the system over time, and can be used to reveal SU (N) orbital magnetism (Zhang et al. 2014) or to study spin-orbit coupling effects (Bromley et al. 2018) in fermionic optical lattices. In this work presented in this manuscript, the Ramsey spectroscopy is used to characterize the motion in a Mott insulator.

In experiments, such as Ramsey spectroscopy, that rely on the coherent driving of the ultra-narrow transition of ^{174}Yb , atoms in the metastable excited state (with respect to this transition) interact through both elastic and inelastic collisions. The resulting two-body losses are responsible for the emergence of a dissipative dynamics alongside with the coherent driving of these atoms. Although such effect is generally considered as detrimental in ultracold atoms experiments, it is possible to take advantage of the presence of two-body losses to study non-Hermitian physics. It is indeed possible to describe an ensemble bosons interacting through inelastic collisions by a non-Hermitian Hamiltonian. These systems, whose dynamics is ruled by a non-Hermitian Hamiltonian, exhibit some interesting features, such as exceptional points (Kato 1966; Heiss 2012) or a complex spectrum (Ashida et al. 2020). The latter property offers a suitable framework to study behaviors that can be interpreted as a generalization of the *quantum Zeno effect* (Misra et al. 1977), experimentally demonstrated for the first time by Itano et al. 1990 according to the proposal of Cook 1988. This counter-intuitive effect states that repeated measurements (to which losses can be assimilated) performed on a quantum system can to a certain extent hinder or even freeze its internal dynamics. An optical lattice deep enough to treat its sites as isolated traps can be used as a platform to probe the quantum Zeno dynamics for interacting pairs of bosons.

This idea of engineering the state of a quantum system thanks to dissipation, developed in Verstraete et al. 2009, can be extended from few-body to many-body system, in par-

ticular for many bosons evolving in an unidimensional lattice in the strong interaction regime. The very low probability associated with the presence of two particles at the same position is one of properties characterizing a Tonks-Girardeau gas. More recent experimental (Syassen et al. 2008) and theoretical (García-Ripoll et al. 2009) works have shown that this property can be emulated by bosons trapped in a 1D optical lattice interaction through strong inelastic collisions. These strong inelastic collisions are responsible for losses that suppresses the probability for two bosons to be at the same position. This effect features a behavior that can be interpreted as an extension for many-body physics of the *quantum Zeno effect*.

Thesis outline

This manuscript aims at presenting the work carried out during my thesis made at laboratoire Kastler-Brossel in Paris. The experiments performed during the last three years have focused on two phenomena introduced above: the physics of strongly interacting bosons trapped in a unidimensional optical lattice and the quantum Zeno effect. In a first time, experiments implementing one of the two physics separately has been conducted, providing a better understanding of their effects. Then both have been involved in an experiment probing the quantum Zeno effect in a Tonks-Girardeau gas. Finally these experiments gave us some useful insight of our experimental platform in the long-term perspective of realizing artificial gauge fields with ytterbium atoms.

The thesis is organized as follow

Chapter 1 reminds the main theoretical notions required for the description of the physics of ultracold bosons trapped in an optical lattice. These elements are then used to discuss the adiabaticity of the preparation of an optical lattice in the ground state.

Chapter 2 presents the setup used to perform the experiments presented throughout this manuscript. Starting from the properties of bosonic ^{174}Yb atoms, the main steps leading to the production of a Bose-Einstein condensate are reminded. Finally the loading of the Bose-Einstein condenstate in the optical lattice potential is presented.

Chapter 3 presents the main features of the optical clock transition of ^{174}Yb . Then the coherent driving of the transition for individual atoms is introduced along with a theoretical description of Rabi and Ramsey experiments. Lastly we show how such experiments can be used to probe the frequency fluctuations of our narrow laser source.

Chapter 4 describes the use of Ramsey spectroscopy introduced in the previous chapter to probe the dynamics of bosons trapped in a unidimensional optical lattice in the strongly interacting regime.

Chapter 5 introduces the quantum Zeno effect in its original formulation and its extension to open quantum systems. This effect is then harnessed to prepare selectively isolated pairs of bosons driven on their clock transition in a superposition of the ground and metastable states.

Chapter 6 presents experiments performed to probe another manifestation of the quantum Zeno effect arising for an ensemble of bosons trapped in a unidimensional

optical lattice, subject to strong elastic and inelastic collisions. The results of the experiments are compared with two theoretical models, which are briefly introduced.

CHAPTER 1

Ytterbium atoms in optical lattices

In this chapter, the main theoretical notions underlying the physics of ultracold bosons trapped in an optical lattice are presented, along with some specificities related to the implementation of optical lattices with ^{174}Yb atoms.

In the first part of this chapter I start by a reminder of the building blocks of the physics of particles evolving in a periodic potential. I progressively introduce the approximations leading us to the Bose-Hubbard model, that will be at the center of the theoretical analysis of the experiments presented in this dissertation.

In the second part, I present the Bose-Hubbard model and its phase diagram. A particular emphasis will be put on the limiting cases: the weakly interacting limit, where particles are delocalized all over the lattice sites and the strongly interacting limit, where particles are localized due to strong repulsive interactions (the Mott insulator phenomenon). This will lead us to study the transition between the superfluid and the Mott insulator regimes. Finally the effects of the confining potential used to trap the atoms will be discussed with the phase diagram.

1.1 Reminder on band theory

1.1.1 Bloch waves for a 1D periodic potential

We start by considering a single particle of mass m evolving in a 1D periodic potential along the z direction, of the form :

$$V_{\text{lat}}(z) = -V_0 \cos^2(k_L z). \tag{1.1}$$

Such a potential can be produced by the interference of two counter-propagating plane waves along the z direction, with wave number k_{L}. We introduce the wavelength of the plane wave $\lambda_L = \frac{2\pi}{k_{\text{L}}}$ and the associated recoil energy $E_{\text{R}} = \frac{\hbar^2 k_{\text{L}}^2}{2m}$. The Hamiltonian describing the motion of the particle in this periodic potential :

$$\hat{H} = \frac{\hat{\text{p}}^2}{2m} + V_{\text{lat}}(\hat{z}) \tag{1.2}$$

with $\hat{p} = -\text{i}\hbar\nabla$ the momentum operator.

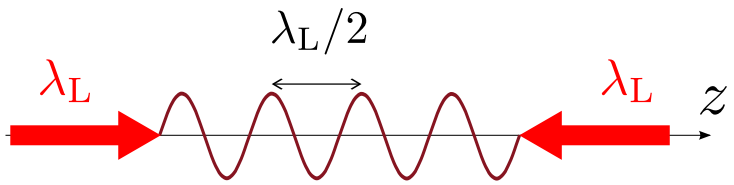

Figure 1.1 – Sketch of the interference of two counter-propagating plane waves. The resulting standing plane wave of period $d = \lambda_L/2$ forms the 1D lattice potential.

Since the system is invariant by a discrete translation of step $d = \pi/k_L = \lambda_L/2$, the Hamiltonian and the d-step discrete translation operator $\hat{T}_d = \mathrm{e}^{\mathrm{i}\hat{p}d/\hbar}$ commute : $\left[\hat{T}_d, \hat{H}\right] = 0$. According to the Bloch's theorem, the Hilbert space in which evolves the system admits a basis of wavefunctions, called *Bloch waves* (Ashcroft et al. 1976):

$$\phi_q(z) = \mathrm{e}^{\mathrm{i}qz} u_q(z)\,. \tag{1.3}$$

The Bloch waves are eigenvectors of for both $\hat{H}$ and $\hat{T}_d$. Here the $u_q(z)$ are d-periodic complex functions called *Bloch functions*.

The basis states are labeled by the quantity q, called quasi-momentum, which is analogous (up to a factor $\hbar$) to the momentum for a plane wave in free space. Replacing q by $q + m\frac{2\pi}{d}$, with $m \in \mathbb{Z}$, results in the same eigenvalue for the operator $\hat{T}_d$. Consequently it is possible to restrict the quasi-momenta q domain to the interval $\left]-\frac{\pi}{d}, \frac{\pi}{d}\right]$, called the first Brillouin zone (1BZ) and introduce the integer n to label, in the ascending order, the different energies $\epsilon_{n,q}$ (*i.e.* the eigenvalues of $\hat{H}$) for a given quasi-momentum q. This band index labels the *bands* of accessible energies for the particles and separated by energy gaps. The Bloch functions basis reads now:

$$\phi_{n,q}(z) = \mathrm{e}^{\mathrm{i}qz} u_{n,q}(z) \tag{1.4}$$

I assume, as is common, periodic boundary conditions for a lattice with N_s sites. Consequently the quasi-momenta become quantized and the first Brillouin Zone corresponds to the discrete set of quasi-momenta of the form $q_p = p\frac{\pi}{dN_s}$ with $-\frac{N_s}{2} < p \leq \frac{N_s}{2}$ (for N_s even). Although no fully analytical solution of the Bloch-Schrödinger equation is known, it is possible to diagonalize numerically the Hamiltonian. Figure 2.2 shows the few lowest Bloch energy bands for different lattice depths V_0. As can be observed from this figure the gaps widen and the bands flatten as the lattice depth increases.

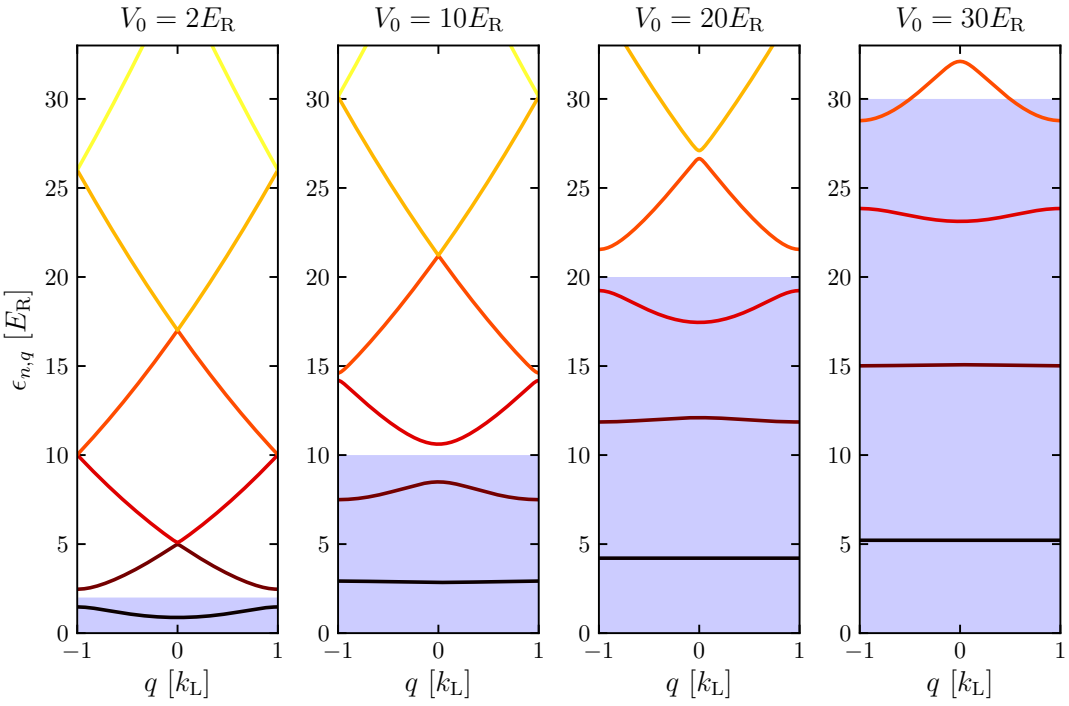

Figure 1.2 – Band structure of a 1D lattice for different lattice depths $V_0 = 2, 10, 20, 30\, E_R$. The six lower energy bands $\epsilon_{n,q}$ are displayed and the blue shaded region corresponds to the energies below the lattice depth V_0.

1.1.2 Wannier basis

The Bloch wavefunctions describe quantum states that are delocalized over the whole lattice, analogous to plane waves in the continuum. It is often then more convenient to switch to another basis of orthogonal and normalized wavefunctions, called the Wannier basis (Wannier 1937). On the contrary to the Bloch wavefunctions, the Wannier functions are maximally localized around the lattice sites. The Wannier functions are derived from the Bloch waves by a discrete Fourier transform with respect to the quasi-momentum:

$$w_n\left(z - z_i\right) = \sqrt{\frac{d}{2\pi}} \int_{-k_L}^{k_L} \phi_{n,q} \mathrm{e}^{-\mathrm{i}qz_i}\, \mathrm{d}q. \tag{1.5}$$

Here the $z_j = jd$ are the position of the lattice sites (assuming for simplicity that the origin of our coordinates correspond to a minimum for the periodic potential). In practice in order to perform numerical calculations, we take a finite size lattice of N_s sites with periodic boundary conditions. The definition of the Wannier functions (1.5) now reads:

$$w_n\left(z - z_i\right) = \frac{1}{\sqrt{N_s}} \sum_{q \in \mathrm{BZ1}} \mathrm{e}^{-\mathrm{i}qz_i} \phi_{n,q}\left(z\right). \tag{1.6}$$

The Wannier functions are *not* eigenvectors of the Hamiltonian. However they allow a more convenient description of (short range) interaction and of localized many-body states, in the limit of deep lattices $V_0 \gg E_R$.

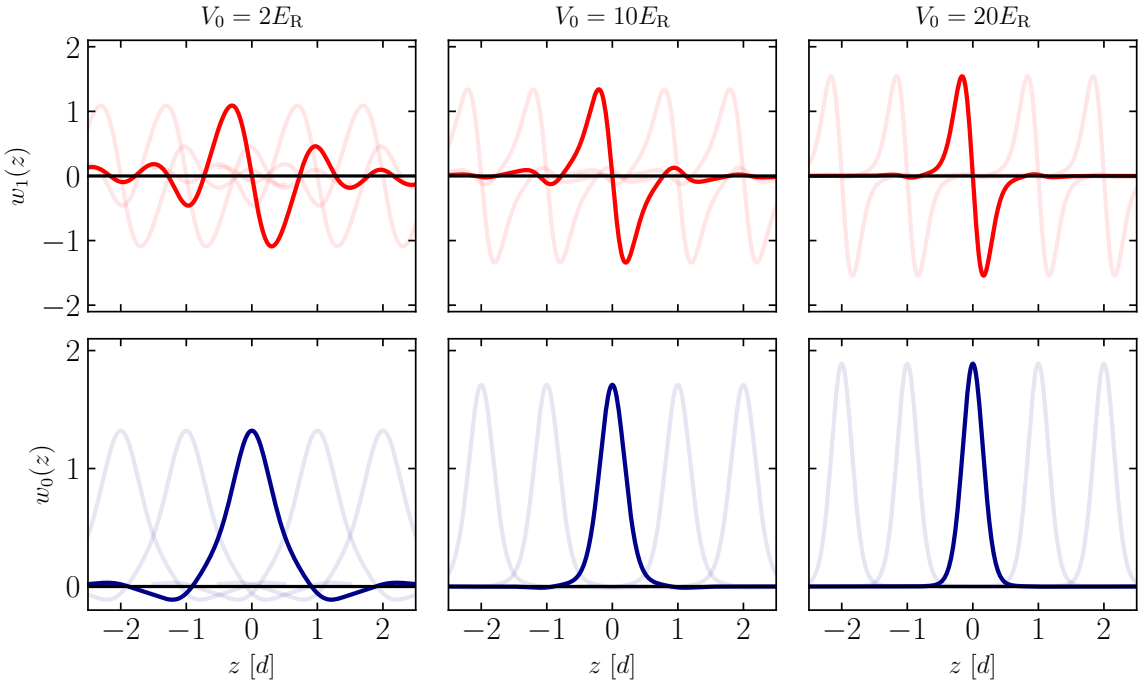

Figure 1.3 – Solid lines: Wannier functions in the lowest energy (blue) and first excited (red) bands, centered at $z = 0$ for different lattice depths $V_0 = 2,\ 10,\ 20\,E_R$. The Wannier functions of the neighboring sites are also represented as faded lines.

The Wannier functions are defined up to a phase factor. Kohn 1959 proved that for centrosymmetric lattices in one dimension, they can be defined as real-valued, symmetric or anti-symmetric functions, exponentially decaying with the distance from the origin. The last property has later been generalized to non-centrosymmetric 1D lattices (Cloizeaux 1964) and single-band 3D lattices (Nenciu 1983).

The single-particle Hamiltonian (1.2) can be rewritten using the second quantification formalism :

$$\hat{H}_0 = \int \mathrm{d}z\, \hat{\Psi}^\dagger(z) \left[-\frac{\hbar^2}{2m}\nabla^2 + V_{\mathrm{lat}}(z) \right] \hat{\Psi}(z)\,. \tag{1.7}$$

Here $\hat{\Psi}(z)$ is the field operator annihilating a particle located in z. The decomposition of this operator along the Wannier basis writes:

$$\hat{\Psi}(z) = \sum_{j,n} w_n(z - z_j)\, \hat{a}_{j,n} \tag{1.8}$$

with $\hat{a}_{j,n}$ the annihilation operator for a particle in the Wannier state $w_n(z - z_j)$. Injecting the previous expression (1.8) in (1.7) the exact representation:

$$\hat{H}_0 = -\sum_{i,j,n} J_n(i - j)\, \hat{a}^\dagger_{i,n} \hat{a}_{j,n} \tag{1.9}$$

with the tunneling matrix elements

$$J_n(i-j) = -\int \mathrm{d}z\, w_n^*(z-z_i)\left[-\frac{\hbar^2}{2m}\nabla^2 + V_{\mathrm{lat}}(z)\right] w_n(z-z_j)\,. \tag{1.10}$$

The matrix elements $J_n(i-j)/\hbar$ can be interpreted as the characteristic hopping rate from site i to site j by quantum tunneling through the potential barrier of the lattice. In 1D the energies $J_n(i-j)$ only depend on the relative distance between the two sites $|z_i - z_j|$. It is possible to express them as a discrete Fourier transform of the dispersion relation, using the inverse of the relation (1.6):

$$J_n(i-j) = -\frac{1}{N_s}\sum_{q,q'\in 1\mathrm{BZ}} \mathrm{e}^{-\mathrm{i}(qz_i - q'z_j)} \int \mathrm{d}z\, \phi_{n,q}^*(z-z_i)\left[-\frac{\hbar^2\nabla^2}{2m} + V_{\mathrm{lat}}(z)\right]\phi_{n,q'}(z-z_j) \tag{1.11}$$

$$= -\frac{1}{N_s}\sum_{q\in 1\mathrm{BZ}} \epsilon_{n,q}\,\mathrm{e}^{-\mathrm{i}q(z_i-z_j)}. \tag{1.12}$$

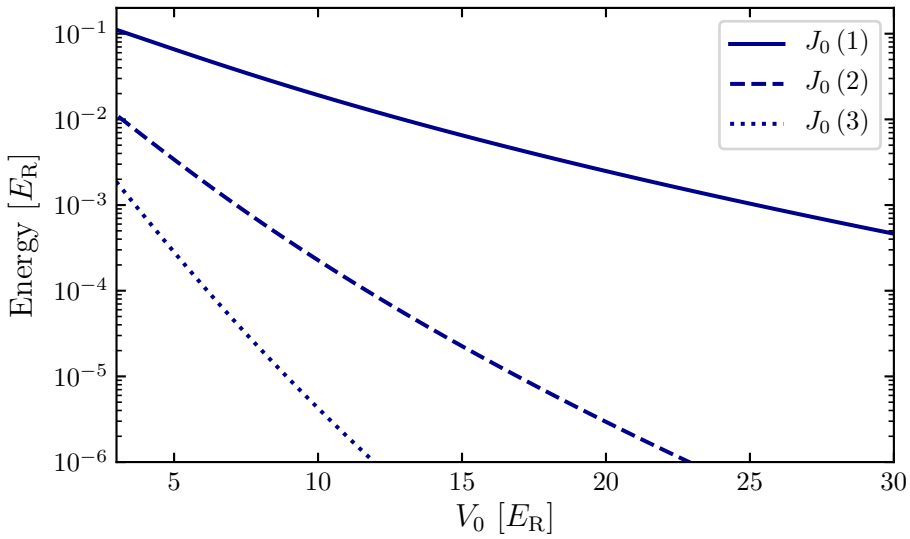

Figure 1.4 – Comparison of the tunneling energies in the fundamental band, using the notation : $J_0(|i-j|)$. For the lattice depths represented here, corresponding to the typical lattices depths considered in this thesis, higher order tunneling matrix element can be neglected compared to the nearest-neighbor tunneling term.

In order to have some insight on the behavior of the tunneling energy, it may be useful to use the approximate formula for the hopping matrix element $J_0 = J_0(1)$ found for the sinusoidal case (Bloch et al. 2008) :

$$\frac{J_0}{E_R} \approx \frac{4}{\sqrt{\pi}}\left(\frac{V_0}{E_R}\right)^{3/4} \mathrm{e}^{-2\sqrt{\frac{V_0}{E_R}}}. \tag{1.13}$$

It allows us to have a good approximation of the tunnel energy between nearest-neighbors without having to compute all the $\epsilon_{0,q}$ in the first Brillouin zone.

1.1.3 Tight binding approximation

The interpretation of the experimental results exposed in this works is considerably simplified in the *tight-binding limit*, where the lattice potential is deep enough so that hopping beyond nearest-neighbors becomes negligible. The Wannier basis is then very adequate since Wannier functions decay exponentially from the lattice site central position. Secondly the tunneling energies $J_n(i-j)$ decay very fast with the distance between sites, as seen in Fig. 1.4, and only the matrix elements coupling one site to its few closest neighbors will play a significant role. If we keep only the nearest-neighbors matrix elements , *i.e.* set $J_n(i-j) = 0$ if $|i-j| > 1$ the simplified tight-binding Hamiltonian reads:

$$\hat{H}_0 = -\sum_n J_n \sum_{\langle i,j \rangle} \hat{a}^\dagger_{n,j} \hat{a}_{n,i}, \tag{1.14}$$

with $J_n = J_n(1)$.

Moreover, in the following we will only consider systems at very low temperature so that only the fundamental band is significantly populated. From now on, unless otherwise specified, we drop the band index n and only consider the fundamental band $n = 0$.

The combination of the nearest-neighbor hopping and the single-band approximations leads us to write the *tight-binding hamiltonian*:

$$\hat{H}_{\mathrm{TB}} = -J \sum_j \left(\hat{a}^\dagger_{j+1} \hat{a}_j + \mathrm{h.c.} \right), \tag{1.15}$$

with $J = J_0(1)$ the dominant tunneling matrix element.

The tight-binding approximation allows us to simplify considerably the expression of most physical quantities. For instance the energy bands have a cosine form and the dispersion relation in the lowest band is given by

$$\epsilon_q = -2J \cos(qz) \tag{1.16}$$

Consequently the energy width of the fundamental band is given by $4J$.

1.1.4 Generalization to cubic lattices of higher dimensions

All developments above have been conducted for one-dimensional lattices. It is possible to extend to lattice potentials of higher dimensions, more particularly for the 2D and 3D cases. The relevant example for our experiment is the potential for a 3D cubic lattice,

$$V_{\mathrm{lat}}(\mathbf{r}) = V_0 \sum_{\alpha=x,y,z} \sin(k_\alpha x_\alpha)^2 . \tag{1.17}$$

Since the total potential is separable, the eigenvalue problem can be solved along each direction independently. The eigenvectors are obtained by taking the tensor product,

$$\phi_{\mathbf{n},\mathbf{q}}(\mathbf{r}) = \mathrm{e}^{\mathbf{i}\mathbf{q}.\mathbf{r}} \prod_{\alpha=x,y,z} u_{n_\alpha,q_\alpha}(r_\alpha) . \tag{1.18}$$

The Bloch's functions are now labeled by the triplet of integers $\mathbf{n}$ indexing the band and the tridimensional quasi-momentum $\mathbf{q} = (q_x, q_y, q_z)$, belonging to the first Brillouin zone $\left(\ \right]-\frac{\pi}{d}, \frac{\pi}{d}\left]^3\right)$[1]. The energy of a Bloch wave is

$$\epsilon_{\mathbf{n},\mathbf{q}} = \sum_{\alpha=x,y,z} \epsilon_{n_\alpha, q_\alpha} \tag{1.19}$$

with $\epsilon_{n_\alpha,q_\alpha}$ the energy defined in the one dimensional case.

1.2 The Bose-Hubbard model

This section aims at presenting the Bose-Hubbard model and at introducing the main results about its phase diagram. The limiting cases of weakly and strongly interactive regimes will be presented, along with the superfluid-to-Mott-insulator transition that occurs in between. Finally we will describe the spatial distribution of these phases in the optical lattice in presence of an additional trapping harmonic potential, as in the experiment.

1.2.1 Bose-Hubbard model

So far we have only discussed single particle physics. We now introduce two-body interactions and consider a system of N spinless bosons in a tridimensional cubic optical lattice, interacting only *via* s-wave contact interactions. The second-quantized Hamiltonian is

$$\hat{H} = \hat{H}_0 + \hat{H}_{\text{int}} \tag{1.20}$$

$$\hat{H}_0 = \int \mathrm{d}\mathbf{r}\, \hat{\Psi}^\dagger(\mathbf{r}) \left[-\frac{\hbar^2}{2m}\nabla^2 + V_{\text{lat}}(\mathbf{r})\right] \hat{\Psi}(\mathbf{r}) \tag{1.21}$$

$$\hat{H}_{\text{int}} = \frac{g}{2} \int \mathrm{d}\mathbf{r}\, \hat{\Psi}^\dagger(\mathbf{r})\, \hat{\Psi}^\dagger(\mathbf{r})\, \hat{\Psi}(\mathbf{r})\, \hat{\Psi}(\mathbf{r}). \tag{1.22}$$

Here g is the coupling parameter, defined by

$$g = \frac{4\pi\hbar^2 a}{m}, \tag{1.23}$$

that characterizes the s-wave contact interactions between atoms (with a the associated scattering length). $\hat{\Psi}(\mathbf{r})$ is the field operator annihilating a boson at position $\mathbf{r}$ in the fundamental band,

$$\hat{\Psi}(\mathbf{r}) = \sum_{\mathbf{j}} w(\mathbf{r} - \mathbf{r_j})\, \hat{a}_\mathbf{j}, \tag{1.24}$$

with $\mathbf{r_j}$ labeling the positions of the lattice sites. From (1.24) the tight-binding version of the non-interacting Hamiltonian $\hat{H}_0$ can be derived similarly to (1.15),

$$\hat{H}_0 = -J \sum_{\langle \mathbf{i},\mathbf{j}\rangle} \hat{a}^\dagger_\mathbf{i} \hat{a}_\mathbf{j} \tag{1.25}$$

[1] This expression is valid for cubic lattices. For more general lattice geometries, the Brillouin zone is defined as the primitive cell in reciprocal space (Ashcroft et al. 1976).

where $\langle \mathbf{i}, \mathbf{j} \rangle$ indicates that the sum runs over all pairs nearest-neighbors sites.

The interaction Hamiltonian $\hat{H}_{\text{int}}$ is

$$\hat{H}_{\text{int}} = \sum_{i,j,k,l} \frac{U_{\mathbf{i},\mathbf{j},\mathbf{k},\mathbf{l}}}{2} \hat{a}_{\mathbf{i}}^{\dagger} \hat{a}_{\mathbf{j}}^{\dagger} \hat{a}_{\mathbf{k}} \hat{a}_{\mathbf{l}} \tag{1.26}$$

with interaction matrix elements

$$U_{\mathbf{i},\mathbf{j},\mathbf{k},\mathbf{l}} = g \int \mathrm{d}\mathbf{r}\, w^{*}\left(\mathbf{r} - \mathbf{r}_{\mathbf{i}}\right) w^{*}\left(\mathbf{r} - \mathbf{r}_{\mathbf{j}}\right) w\left(\mathbf{r} - \mathbf{r}_{\mathbf{k}}\right) w\left(\mathbf{r} - \mathbf{r}_{\mathbf{l}}\right) \tag{1.27}$$

As explained in section 1.1.3, the tight-binding approximation assumes that the Wannier functions are strongly localized around lattices sites. When it holds, the overlap between the Wannier function associated with different lattice sites is very small. As a consequence the matrix elements $U_{\mathbf{i},\mathbf{j},\mathbf{k},\mathbf{l}}$ may be neglected excepted in the case where all the indices are equal : $\mathbf{i} = \mathbf{j} = \mathbf{k} = \mathbf{l}$. We call this matrix element U, the on-site interaction energy,

$$U = g \int \mathrm{d}\mathbf{r}\, |w\left(\mathbf{r}\right)|^{4}. \tag{1.28}$$

In the end, the many-body Hamiltonian (1.20) under all these assumptions reduces to the well-known the Bose-Hubbard Hamiltonian (Fisher et al. 1989; Jaksch et al. 1998):

$$\hat{H}_{\text{BH}} = -J \sum_{\langle \mathbf{i},\mathbf{j} \rangle} \hat{a}_{\mathbf{i}}^{\dagger} \hat{a}_{\mathbf{j}} + \frac{U}{2} \sum_{\mathbf{i}} \hat{n}_{\mathbf{i}} \left(\hat{n}_{\mathbf{i}} - 1\right). \tag{1.29}$$

We introduced here the one-site number operator $\hat{n}_{\mathbf{i}} = \hat{a}_{\mathbf{i}}^{\dagger} \hat{a}_{\mathbf{i}}$.

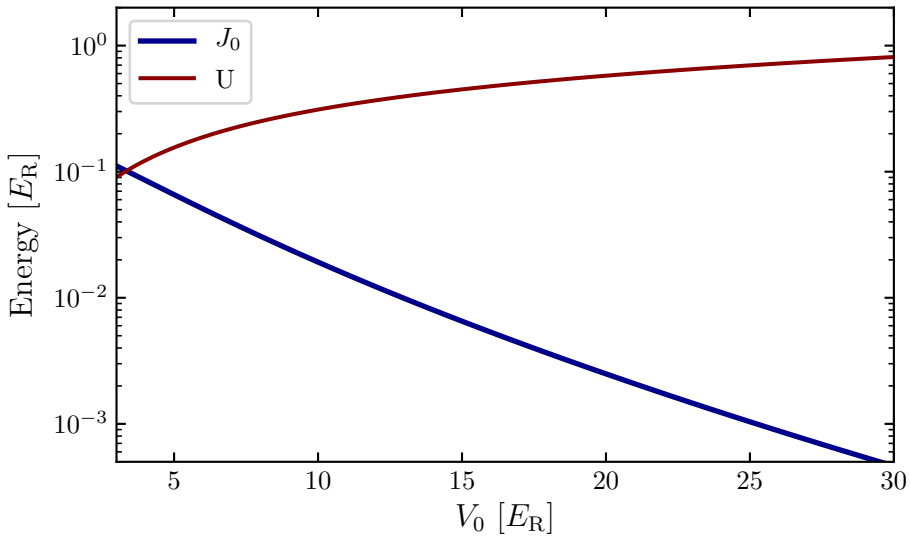

Figure 1.5 – Parameter U and J of the Bose-Hubbard model as a function of the lattice depth. The calculations are here performed for a cubic optical lattice of ^{174}Yb , using the scattering length $a \approx 105\, a_0$ for ^{174}Yb atoms in the ground state measured in Kitagawa et al. 2008. Here a_0 is the Bohr's radius.

Remark: In the limit of very deep lattices, it is possible to approximate the trapping potential of a single site by a harmonic trap, and consequently the Wannier function by a gaussian. It allows us to find an approximate expression for U in the limit of deep lattices (Bloch et al. 2008):

$$\frac{U}{E_{\mathrm{R}}} \approx \sqrt{\frac{8}{\pi}} k_{\mathrm{L}} a \left(\frac{V_0}{E_{\mathrm{R}}}\right)^{3/4}. \tag{1.30}$$

1.2.2 Ground state of the Bose-Hubbard model

The Bose-Hubbard Hamiltonian is not analytically solvable for finite values of U/J but can be studied with several numerical methods, most notably Monte-Carlo simulations (Pollet 2012). Here we will adopt an alternative approximate approach that follows the work of Gutzwiller for fermions. This *Gutzwiller ansatz* (Rokhsar et al. 1991; Krauth et al. 1992; Sheshadri et al. 1993) will allow us to understand the essential physics of the model. This variational mean field method postulates a site-factorized form for the ground state wavefunction:

$$|\Psi_G\rangle = \bigotimes_{\text{sites } \mathbf{i}} |\phi\rangle_{\mathbf{i}}, \tag{1.31}$$

with the one-site wavefunction

$$|\phi\rangle_{\mathbf{i}} = \sum_{n=0}^{\infty} c\left(n_{\mathbf{i}}\right) |n_{\mathbf{i}}\rangle_{\mathbf{i}}. \tag{1.32}$$

There $|n\rangle_{\mathbf{j}}$ denotes the Fock state with n bosons occupying the Wannier state $w_0\left(\mathbf{r}-\mathbf{r}_{\mathbf{j}}\right)$ (that we usually refer to as "occupying site $\mathbf{j}$" from now on).

Since the total atom number is not fixed for such a state, we move from the canonical ensemble to the grand canonical ensemble, by introducing a chemical potential μ to fix the value of the average particle number. The best variational ground state is determined by minimizing the average free energy, defined by

$$\langle \mathcal{G}_{\mathrm{BH}} \rangle_{\mathrm{Gutzwiller}} = \langle \Psi_G | \hat{H}_{\mathrm{BH}} - \mu \sum_{\mathbf{i}} \hat{n}_{\mathbf{i}} | \Psi_G \rangle. \tag{1.33}$$

Combining (1.33) and (1.31) leads to the expression:

$$\langle \mathcal{G}_{\mathrm{BH}} \rangle_{\mathrm{Gutzwiller}} = -J \sum_{\langle \mathbf{i},\mathbf{j} \rangle} \alpha_{\mathbf{i}}^* \alpha_{\mathbf{j}} + \sum_{\mathbf{i}} \sum_{n_{\mathbf{i}}=0}^{\infty} \left[\frac{U}{2} n_{\mathbf{i}} \left(n_{\mathbf{i}}-1\right) - \mu n_{\mathbf{i}}\right] |c\left(n_{\mathbf{i}}\right)|^2. \tag{1.34}$$

where $\alpha_{\mathbf{i}}$ is the expectation value of the matter wave field at site $\mathbf{i}$,

$$\alpha_{\mathbf{i}} = \langle \phi_{\mathbf{i}} | \hat{a}_{\mathbf{i}} | \phi_{\mathbf{i}} \rangle = \sum_{n_{\mathbf{i}}=0}^{\infty} \sqrt{n_{\mathbf{i}}+1} c^*\left(n_{\mathbf{i}}\right) c\left(n_{\mathbf{i}}+1\right) \tag{1.35}$$

Assuming that the lattice with N bosons evolving among N_s sites is uniform, the system is translation invariant, each site is equivalent and the expression of the average free energy defined in (1.34) may be simplified,

$$\langle \mathcal{G}_{\mathrm{BH}} \rangle_{\mathrm{Gutzwiller}} = N_s \left[-zJ|\alpha|^2 + \frac{U}{2}\langle n^2 \rangle - \left(\mu + \frac{U}{2}\right) \langle n \rangle\right] \tag{1.36}$$

where z is the number of nearest-neighbors for the sites of the lattice, $|\alpha|^2 = \alpha_{\mathbf{i}}^* \alpha_{\mathbf{i}}$, and

$$\langle n^p \rangle = \sum_{n=0}^{\infty} n^p |c\,(n)\,|^2. \tag{1.37}$$

The condensed fraction f_c is defined as the normalized population in the fundamental band of the Bloch state of quasi-momentum $\mathbf{q} = 0$, *i.e*

$$f_c = \frac{1}{N} \langle \hat{b}^\dagger_{\mathbf{q}=0} \hat{b}_{\mathbf{q}=0} \rangle. \tag{1.38}$$

We introduced here $\hat{b}_{\mathbf{q}}$ the annihilation operator for a particle in the Bloch state of the fundamental band ($n = 0$) associated with the quasi momentum $\mathbf{q} = 0$

The condensed fraction of the Gutzwiller ansatz is given by

$$f_c = \frac{1}{N N_s} \sum_{\mathbf{ij}} \langle \hat{a}^\dagger_{\mathbf{i}} \hat{a}_{\mathbf{j}} \rangle \underset{N, N_s \to \infty}{\longrightarrow} \frac{|\alpha|^2}{\overline{n}}. \tag{1.39}$$

In the thermodynamic limit ($N_s, N \to \infty$) the condensate fraction is determined by the modulus $|\alpha|$ which plays the role of the superfluid *order parameter*, vanishing when the system enters the Mott-Insulating phase.

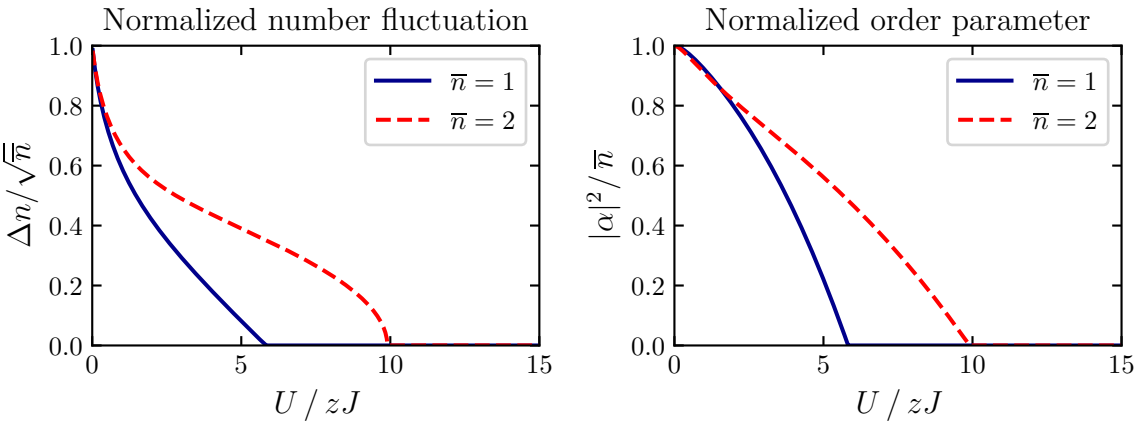

Figure 1.6 – Phase transition in the Bose-Hubbard model with the Gutzwiller ansatz. Left: normalised density fluctuations. Right: Order parameter. Both are plotted for unity filling $\overline{n} = 1$ (blue line) and $\overline{n} = 2$ (dashed red line). The transition from the superfluid phase to the Mott insulator phase occurs at $U/zJ = 5.8$ for $\overline{n} = 1$ and at $U/zJ = 9.9$ for $\overline{n} = 2$.

The Gutzwiller ansatz is exact in two limiting cases (Zwerger 2003) :

- $J/U \to 0$: the strongly interacting limit. The system may be seen as a collection of independent wells in which the atoms are fully localized. In case of commensurate fillings, *i.e.* when $\overline{n} = N/N_s \in \mathbb{N}$, the ground state a product over all sites

of identical Fock states $|\overline{n}\rangle_{\mathbf{i}}$:

$$|\Psi_{\mathrm{MI}}\rangle = \bigotimes_{\text{sites}\,\mathbf{i}} |\overline{n}\rangle_{\mathbf{i}}. \tag{1.40}$$

- $U/J \to 0$: the weakly interacting limit, all the atoms are condensed in the $|\mathbf{q}=0, \mathbf{n}=0\rangle$ Bloch state. The N particles state is given by:

$$|\Psi_{\mathrm{SF}}\rangle = \frac{1}{\sqrt{N!}} \left(\hat{b}^{\dagger}_{\mathbf{q}=0}\right)^{\otimes N} |\varnothing\rangle = \frac{1}{\sqrt{N!}} \left(\frac{1}{\sqrt{N_s}} \sum_{\mathbf{i}} \hat{a}^{\dagger}_{\mathbf{i}}\right)^{\otimes N} |\varnothing\rangle. \tag{1.41}$$

In the thermodynamic limit $N, N_s \to \infty$, the ground state $|\Psi_{\mathrm{SF}}\rangle$ can be shown to reduce to a product over the lattice sites:

$$|\Psi_{\mathrm{SF}}\rangle \underset{N,N_s\to\infty}{=} \bigotimes_{\mathbf{i}} |\alpha = \sqrt{\overline{n}}\rangle_{\mathbf{i}} \tag{1.42}$$

of coherent states

$$|\alpha\rangle_{\mathbf{i}} = \mathrm{e}^{-|\alpha|^2/2} \sum_{n=0}^{\infty} \frac{\alpha^n}{\sqrt{n!}} |n\rangle_{\mathbf{i}}. \tag{1.43}$$

Consequently the probability $p(n)$ to have n atoms in a lattice site follows a Poisson distribution with mean value $\overline{n}$ and standard deviation $\sqrt{\overline{n}}$.

The site-factorized Gutzwiller ansatz is no longer exact between these two limits but give some insights on the quantum phase transition occurring for commensurate fillings between the superfluid (SF) phase characterized by a macroscopic occupation of the Bloch state of the fundamental band with $\mathbf{q} = 0$, and the localized Mott-Insulator (MI) phase where atoms are localized on lattice sites.

1.2.3 Phase diagram

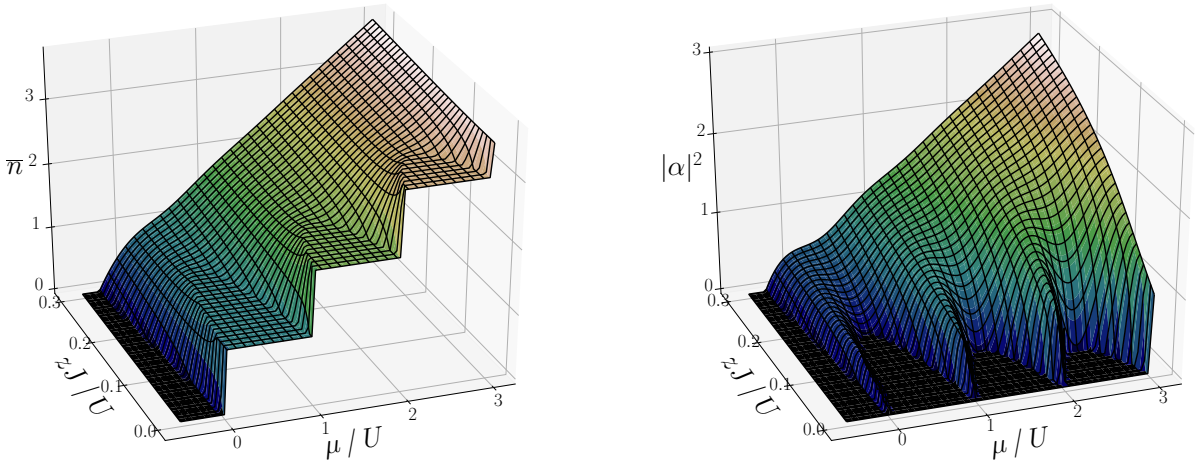

Figure 1.7 – Phase diagram of the Bose-Hubbard model at zero temperature. The left figure shows the filling factor $\overline{n}$. The right figure shows the order parameter $|\alpha|^2$.

The phase diagram of the Bose-Hubbard model (Fig. 1.7) computed from the Guntzwiller ansatz features two distinct thermodynamics phases. For small zJ/U we observe incompressible lobes, corresponding to the Mott phase, where the occupation number remains constant in a finite interval of chemical potential. In the $J \to 0$ limit these intervals are of the form $[\mu_- = pU,\, \mu_+ = (p+1)U]$. Outside is the realm of the superfluid phase where the atoms are delocalized over the whole lattice.

The transition from superfluid to Mott insulator has been observed for the first time in Greiner et al. 2002. In our experiment we follow a similar experimental protocol, described is described further in Sec 2.3.4.

1.2.4 External confinement

Experimentally the periodic potentials are realized by the interference of two counter-propagating laser beams along each spatial direction. The laser beams cannot be described by a plane wave but instead by a gaussian beam. The dipole potential they produce is then not strictly space-periodic. This introduces a serious difficulty, since the whole band theory relies on the (now broken) discrete translation symmetry. Fortunately, a perturbative approach allows one to retain the band theory picture. The amplitude of the light field for a beam propagating along the z direction has the form $E(\mathbf{r}) = E_0 \exp(-r_\perp^2/w^2(z))$ with $r_\perp^2 = x^2 + y^2$. Consequently the potential for the 1D case becomes:

$$V_{1\mathrm{D}} = -V_0 \cos^2(k_L z)\, \mathrm{e}^{-2\frac{r_\perp^2}{w^2(z)}}. \tag{1.44}$$

In cold atoms experiments, the waist of the laser beam typically varies slowly at the scale of the atomic cloud, and its spatial dependency can therefore be neglected: $w(z) \approx w$. Moreover w is almost always chosen large compared to characteristic size of the atomic cloud ($r_\perp^2 \ll w^2$), so that the factor $\mathrm{e}^{-2\frac{r_\perp^2}{w^2}}$ can be approximated by its first order expansion in $\frac{r_\perp^2}{w^2}$:

$$\mathrm{e}^{-2\frac{r_\perp^2}{w^2}} \approx 1 - 2\frac{r_\perp^2}{w^2}. \tag{1.45}$$

It shows that the effect of the Gaussian geometry of the laser beams can be accounted for by adding a non-periodic correction to the sinusoidal potential created by the interference of plane waves,

$$\delta V_z = 2V_0 \cos^2(k_L z)\, \frac{x^2 + y^2}{w^2}. \tag{1.46}$$

This expression is easily generalized for a 3D cubic lattice made of two counter-propagating plane waves along the x and y directions and a self-reflected gaussian beam along the z direction, since the contributions of each dimension are just summed up according to (1.17). The dipole potential can be rewritten in term of operators in the second quantization formalism and the expansion of field operator on the Wannier

basis reads :

$$\begin{aligned}\delta\hat{V}_z \approx \frac{2V_0}{w^2}\sum_{\mathbf{i}}\left[\int x^2 w^2\left(x-x_{\mathbf{i}}\right)\,\mathrm{d}x \times \int \cos^2\left(k_{\mathrm{L}}z\right) w^2\left(z-z_{\mathbf{i}}\right)\,\mathrm{d}z\right]\hat{a}_i^\dagger\hat{a}_i \\ +\frac{2V_0}{w^2}\sum_{\mathbf{i}}\left[\int y^2 w^2\left(y-y_{\mathbf{i}}\right)\,\mathrm{d}y \times \int \cos^2\left(k_{\mathrm{L}}z\right) w^2\left(z-z_{\mathbf{i}}\right)\,\mathrm{d}z\right]\hat{a}_i^\dagger\hat{a}_i.\end{aligned} \tag{1.47}$$

We introduce σ_x^2, σ_y^2, σ_z^2 the second order moments associated to the probability densities $|w_x(x)|^2$, $|w_y(y)|^2$, $|w_z(z)|^2$ respectively and rewrite the correction term as:

$$\delta\hat{V}_z \approx \sum_i \frac{2V_0}{w^2}\left[x_{\mathbf{i}}^2+y_{\mathbf{i}}^2+\sigma_x^2+\sigma_y^2\right]\int \cos^2\left(k_{\mathrm{L}}z\right) w_z^2\left(z\right)\,\mathrm{d}z \times \hat{a}_i^\dagger\hat{a}_i. \tag{1.48}$$

In the regime where the Bose-Hubbard model is valid, the Wannier functions are strongly-localized around their sites. It is then possible to approximate each lattice site by a harmonic trap and, consequently, the square modulus of the Wannier function by a Gaussian function. Neglecting uniform energy offsets, equation (1.48) then becomes:

$$\delta\hat{V}_z = \frac{2V_0}{w^2}\sum_{\mathbf{i}}\frac{1}{2}\left[1+\mathrm{e}^{-2k_{\mathrm{L}}^2\sigma_z^2}\right]\left(x_{\mathbf{i}}^2+y_{\mathbf{i}}^2\right)\hat{a}_i^\dagger\hat{a}_i. \tag{1.49}$$

$$\delta\hat{V}_z \approx \sum_i \frac{1}{2}m\Omega_z^2\left(x_i^2+y_i^2\right)\hat{a}_i^\dagger\hat{a}_i, \tag{1.50}$$

with

$$\Omega_z^2 = \frac{4V_0}{mw^2}\left[1-\frac{1}{2}\left(k_L\sigma_z\right)^2\right]. \tag{1.51}$$

In the harmonic oscillator approximation we have $k_{\mathrm{L}}\sigma_z = \left(E_{\mathrm{R}}/V_0\right)^{1/4}$, $\left(k_{\mathrm{L}}\sigma_z\right)^2 \ll 1$ and

$$\Omega_z^2 = \frac{4V_0}{mw^2}. \tag{1.52}$$

The same reasoning can be applied to the x and y axis. In the end the Gaussian envelope of the laser beams produces an "extra" harmonic potential term to the Bose-Hubbard Hamiltonian:

$$\begin{aligned}\hat{H}'_{\mathrm{BH}} = -J\sum_{\langle\mathbf{i},\mathbf{j}\rangle}\hat{a}_{\mathbf{i}}^\dagger\hat{a}_{\mathbf{j}} + \frac{U}{2}\sum_{\mathbf{i}}\hat{n}_{\mathbf{i}}\left(\hat{n}_{\mathbf{i}}-1\right) \\ +\frac{1}{2}m\sum_{\mathbf{i}}\left[\Omega_x^2\left(y_{\mathbf{i}}^2+z_{\mathbf{i}}^2\right)+\Omega_y^2\left(z_{\mathbf{i}}^2+x_{\mathbf{i}}^2\right)+\Omega_z^2\left(x_{\mathbf{i}}^2+y_{\mathbf{i}}^2\right)\right]\hat{a}_{\mathbf{i}}^\dagger\hat{a}_{\mathbf{i}}\end{aligned}. \tag{1.53}$$

i.e.

$$\hat{H}'_{\mathrm{BH}} = \hat{H}_{\mathrm{BH}} + \sum_{\mathbf{i}} V_{\mathrm{h}}\left(\mathbf{r}_{\mathbf{i}}\right)\hat{a}_{\mathbf{i}}^\dagger\hat{a}_{\mathbf{i}}, \tag{1.54}$$

where V_{h} is

$$V_{\mathrm{h}}\left(\mathbf{r_i}\right) = \frac{1}{2}m\left[\left(\Omega_y^2+\Omega_z^2\right)x_{\mathbf{i}}^2 + \left(\Omega_x^2+\Omega_z^2\right)y_{\mathbf{i}}^2 + \left(\Omega_x^2+\Omega_y^2\right)z_{\mathbf{i}}^2\right] \tag{1.55}$$

1.2.5 Local Density Approximation (LDA)

The superposition of an auxiliary harmonic trapping potential $V_{\mathrm{h}}\left(\mathbf{r}\right) = \frac{1}{2}m\Omega^2\mathbf{r}^2$ (isotropic here for the sake of simplicity) on the plane wave potential breaks the discrete translational invariance of the lattice, required hypothesis for the Bloch theorem. However if the variations associated to the harmonic confining potential are smooth enough, one can mentally partition the whole system as a collection of nearly-independent patches. For large enough systems the patch size (chosen large compared to the typical correlation length) is still small compared to the system size and the density within each patch is almost homogeneous. In this Local Density Approximation (LDA) a chemical potential μ_{loc} is defined for each patch around the position $\mathbf{r}$, for a fixed ratio zJ/U :

$$\mu_{\mathrm{loc}}\left(\mathbf{r}\right) = \mu - V_{\mathrm{h}}\left(\mathbf{r}\right). \tag{1.56}$$

The injection of this local chemical potential in the expression of the density for the homogeneous case $n\left[\mu\right]$, allows us to express the density profile n_{loc} for the atomic cloud in an optical lattice with a superimposed trapping harmonic potential :

$$n_{\mathrm{loc}}\left(\mathbf{r}\right) = n\left[\mu_{\mathrm{loc}}\left(\mathbf{r}\right)\right]. \tag{1.57}$$

As an illustration we consider the the atomic limit where $J \to 0$. The Mott insulator phase with $\overline{n} = p \in \mathbb{N}$ atoms per site is reached when $\mu_{\mathrm{loc}} = pU$. In the lattice in presence of the auxiliary harmonic trapping potential this occurs on the sphere of radius:

$$R_p = \sqrt{\frac{2U}{M\Omega^2}}\sqrt{\frac{\mu_0}{U}-p} = R_U\sqrt{\frac{\mu_0}{U}-p} \tag{1.58}$$

with $\mu_0 = \mu$ the chemical potential at the center of the cloud and $R_U = \sqrt{\frac{2U}{M\Omega^2}}$ the characteristic radius.

Regions between the sphere of radius R_p and R_{p-1} are filled with lattices with filling factor $\overline{n} = p$. The radius R_0 corresponds to the radius of the spatial extension of the atomic cloud, that presents a *pièce montée* structure, with concentric shells of increasing filling from the edge to the center of the cloud, as shown in Fig. 1.8. When we get away from the atomic limit, layers of superfluid appears between the Mott insulator spatial domains. The intermediate regions are characterized by finite density fluctuations.

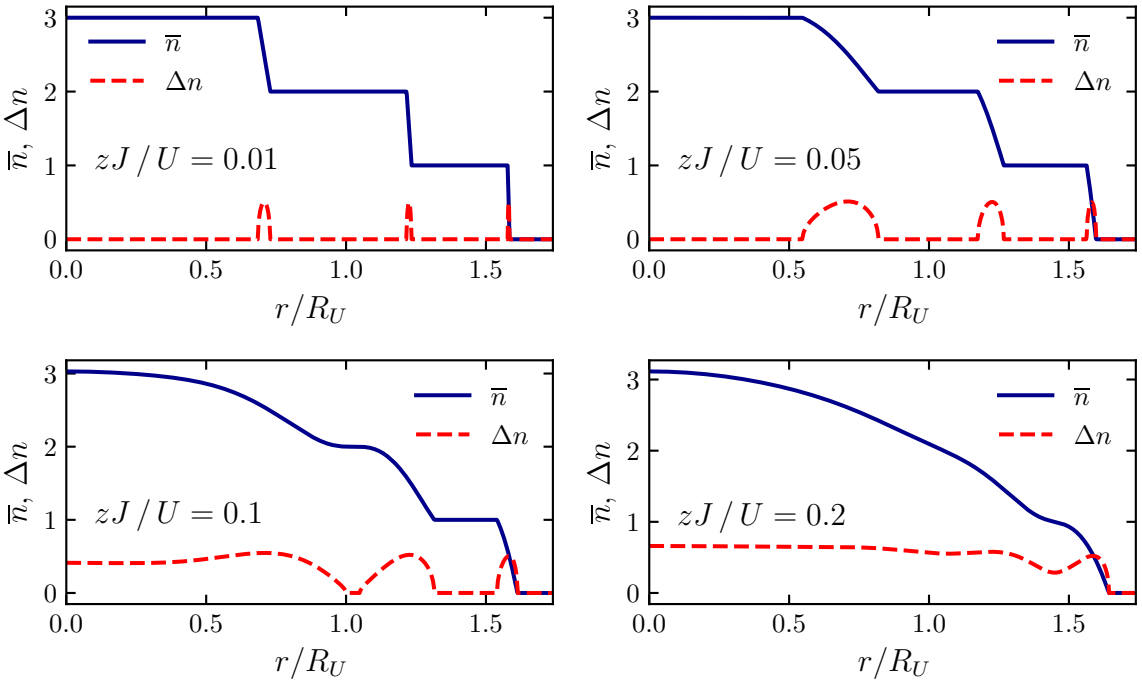

Figure 1.8 – Shell structure for a trapped Mott insulator for $zJ/U = 0.01, 0.05, 0.1, 0.2$ and $\mu_0/U = 2.5$.

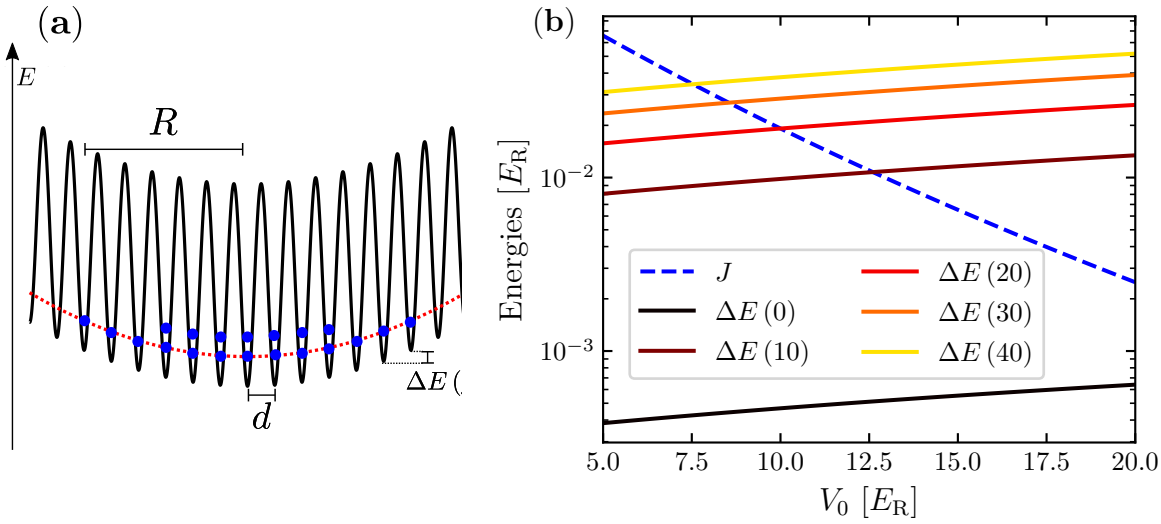

Figure 1.9 – (**a**): Scheme of the optical lattice in the Mott insulator regime in presence of an auxiliary harmonic confining potential (red dotted line). (**b**): Energy shift ΔE between neighboring sites, for sites distant of {0, 10, 20, 30 40} sites away from the center of the cloud, compared with the tunneling energy J (blue dashed line). The calculation is performed along the x axis of the optical lattice, for different $V_y = V_0$ and at fixed $V_z = 27\,E_R$, using the notations and the parameters of section 2.3.

Remark: The introduction of a site-depend energy shift by the Gaussian envelope of

the laser beams constituting the optical lattice can lead to an effective suppression of tunneling at large lattice depths. The energy shift between the site indexed by j and the site indexed by $j+1$

$$\Delta E\left(j\right) = V_{\mathrm{h}}\left(jd+d\right) - V_{\mathrm{h}}\left(jd\right) = \frac{1}{2}m\Omega^2(1+2j)d^2 \tag{1.59}$$

is bigger at the edge of the atomic cloud, of radius $R = dj_{\max}$, where it becomes approximately $\Delta E\left(j_{\max}\right) \approx m\Omega^2 Rd$ than in the center of the cloud $\Delta E\left(0\right) \approx \frac{1}{2}m\Omega^2 d^2$. When the shift ΔE becomes much larger than the tunneling energy J, the tunneling is suppressed and the local density approximation is no longer completely valid. The most restrictive condition to ensure the validity of the local density approximation is thus:

$$m\Omega^2 Rd \leq J. \tag{1.60}$$

The computations preformed in Fig. 1.9 the tunneling energy J is compared to the energy shift between neighboring lattice sites. It shows for which transverse lattice depth range the condition (1.60) is satisfied at different position in the optical lattice.

1.3 Adiabatic preparation of an optical lattice

The production of a quantum gas directly in optical lattice by evaporation cooling, the method usually used to prepare a Bose-Einstein condensate, is difficult to implement (Blakie et al. 2004; Ho et al. 2009). Consequently the common procedure to load an optical lattice in its fundamental band relies on the transfer of a Bose-Einstein condensate (BEC) in the lattice potential. The transfer procedure consist then into ramping up the lattice potential the harmonic potential in which the BEC has been prepared is ramped down (the details of our particular implementation of the transfer are detailed later in 2.3.3).

In this section we discuss the condition that the transfer procedure need to satisfy in order to end up with a system as close as possible to the ground state of the Bose-Hubbard model.

1.3.1 The adiabatic approximation

For a system evolving according to a time-dependent Hamiltonian $\hat{H}\left(t\right)$ which, for the sake of simplicity, admits the time dependent eigenvectors $|\phi_j\left(t\right)\rangle$ associated to the instantaneous eigenenergies $\epsilon_j\left(t\right)$ and initially the the state $|\phi_k\left(0\right)\rangle$, the system will be found in the state $|\phi_k\left(t\right)\rangle$ at time t with a probability 1 if the inequality

$$\hbar|\langle\phi_j|\frac{\mathrm{d}}{\mathrm{d}t}|\phi_k\rangle| \ll |\epsilon_j - \epsilon_k| \qquad \forall j \neq k \tag{1.61}$$

or equivalently

$$\hbar|\langle\phi_j|\frac{\mathrm{d}\hat{H}}{\mathrm{d}t}|\phi_k\rangle| \ll |\epsilon_j - \epsilon_k|^2 \qquad \forall j \neq k \tag{1.62}$$

is satisfied at every instant (Messiah 1999). In the rest of this section we use this criterion to determine if the system stays in the ground state at every instant of the transfer of the BEC into the optical lattice.

1.3.2 Adiabaticity for an ideal gas

The question of adiabaticity can be firstly tackled in absence of interactions ($g = 0$) (Greiner 2003): the atoms in the BEC all lies around the zero-momentum state $|\mathbf{p} = 0\rangle$ in the momentum space, *i.e.* the state $|n = 0, \mathbf{q} = 0\rangle$ in the Bloch basis, with associated energy $\epsilon_{n,\mathbf{q}}$. When the lattice is raised up, the quasi-momenta of the particles remain unchanged and the non-adiabaticity consists in populating higher energy bands ($n \neq 0$), and the adiabaticity criterion (1.61) reads

$$\left|\frac{\partial V_0}{\partial t}\right| \ll |\epsilon_{n,q} - \epsilon_{0,q}|/\hbar \qquad \forall n > 0 \tag{1.63}$$

with V_0 the time dependent lattice depth.

More particularly, if we consider ^{174}Yb atoms trapped in an optical lattice at 759 nm, the previous expression becomes, for shallow lattices with depths $V_0 < E_\mathrm{R} \approx h \times 1973\,\mathrm{Hz}$ (Ben Dahan et al. 1996),

$$\left|\frac{1}{E_\mathrm{R}}\frac{\partial V_0}{\partial t}\right| \ll 32\sqrt{2}\frac{E_\mathrm{R}}{\hbar} \approx 5.6 \times 10^5\,\mathrm{s}^{-1}. \tag{1.64}$$

In our experiment, the ramp speed is on the order of $3 \times 10^3\,\mathrm{s}^{-1}$ and this criterion is satisfied. For deeper lattices, the gap between band becomes larger and this condition for adiabaticity is more easily verified. this criterion is fulfilled.

1.3.3 Adiabaticity in presence of interactions

However this criterion is no longer enough when interactions are taken into account and becomes a necessary but not sufficient condition. In the framework of the Bose-Hubbard approximation for an optical lattice in presence of an external confinement potential (we assume the LDA to be valid), three energy scales are to be taken into account for a discussion on adiabaticity:

- the interaction energy $U \propto (V_0/E_\mathrm{R})^{3/4}$
- the tunneling energy $J \propto (V_0/E_\mathrm{R})^{3/4}\,\mathrm{e}^{-2\sqrt{V_0/E_\mathrm{R}}}$
- the auxillary trap frequency $\Omega \propto \sqrt{V_0/E_\mathrm{R}}$.

From theses quantities it is possible to define different criteria for the adiabaticity of the transfer of the BEC from the crossed-dipole trap to the optical lattice. We distinguish several regimes:

Low lattice depths regime: $V_0 \ll \mu$

In this regime the mean field description of the system prevails (interactions are *a priori* weak) and the contribution of the excited bands have to be taken into account. The system can be seen as a "spatially modulated condensate". The band structure

in this regime still exists but can be very different from the single particle situation (Morsch et al. 2006).

The Bose-Hubbard regime

When the Bose-Hubbard regime is reached, *i.e.* for $V_0 > 5\,E_\mathrm{R}$, the single band and the tight-binding approximation are valid and the adiabaticity criterion can be discussed with respect to the many-body excitations that can appear in the system. To study the adiabaticity of the transfer, we can use the work of Kajtoch et al. 2018 for infinite homogeneous optical lattice in the regime of weak interactions, that we extend to our non-homogeneous case thanks to the use of the LDA. In this reference the time dependent Bose-Hubbard Hamiltonian is treated within the Bogoliubov framework, leading to the Bogoliubov dispersion relation

$$E\left(\mathbf{q},\,\mathbf{r},\,t\right) = \sqrt{\epsilon\left(\mathbf{q},\,t\right)\left[\epsilon\left(\mathbf{q},\,t\right) + 2U\left(t\right)\overline{n}\left(\mathbf{r},\,t\right)\right]} \tag{1.65}$$

with

$$\epsilon\left(\mathbf{q},\,t\right) = 2J\left(t\right)\sum_{\alpha=x,\,y}\left[1-\cos\left(q_\alpha d\right)\right] \tag{1.66}$$

the single-particle dispersion relation in the tight-binding limit. In the limit of small $\mathbf{q}$, this expression becomes

$$\epsilon\left(\mathbf{q},\,t\right) \approx 2J\left(t\right)\mathbf{q}^2 d^2 \tag{1.67}$$

and the Bogoliubov dispersion relation becomes approximately linear

$$E\left(\mathbf{q},\,\mathbf{r},\,t\right) \approx \sqrt{4U\left(t\right)\overline{n}\left(\mathbf{r},\,t\right)\epsilon\left(\mathbf{q},\,t\right)^2} \tag{1.68}$$

$$\approx 2\sqrt{J\left(t\right)U\left(t\right)\overline{n}\left(\mathbf{r},\,t\right)}qd. \tag{1.69}$$

The adiabaticity criterion (1.61) reads

$$\hbar\left|\frac{\mathrm{d}\hat{H}}{\mathrm{d}t}\right| \ll \left|E\left(\mathbf{q}_\mathrm{min},\,\mathbf{r},\,t\right) - E\left(0,\,\mathbf{r},\,t\right)\right|^2. \tag{1.70}$$

Taking $|\mathbf{q}_\mathrm{min}| = q_\mathrm{min} \approx \frac{2\pi}{R_U}$, with R_U the characteristic radius of the atomic cloud defined in Sec. 1.2.5, the adiabaticity criterion becomes

$$\hbar\left|\frac{\mathrm{d}J}{\mathrm{d}t}\right| \ll 8\pi^2 J\left(t\right)K\overline{n}\left(\mathbf{r},\,t\right) \tag{1.71}$$

with $K = \frac{1}{2}m\Omega^2 d^2$. The adiabaticity criterion can be reformulated with respect to the lattice depth as

$$\hbar\frac{\mathrm{d}V_0}{\mathrm{d}t}\left|\frac{1}{J}\frac{\mathrm{d}J}{\mathrm{d}V_0}\right| \ll 8\pi^2 K\overline{n}\left(\mathbf{r},\,t\right). \tag{1.72}$$

In Fig. 1.10 we compare the evolution of the ratio

$$\mathcal{B} = \hbar\left|\frac{\mathrm{d}J}{\mathrm{d}t}\right|.\left(8\pi^2 J\left(t\right)K\overline{n}\left(\mathbf{r},\,t\right)\right)^{-1} \tag{1.73}$$

during the ramp we typically use to raise the horizontal optical lattice, with a fixed vertical lattice depth of $25\,\mathrm{E_R}$ (see Sec. 2.3) for a $\mathbf{r}$ where $\overline{n} = 1$. We observe that the abiabaticity condition is satisfied.

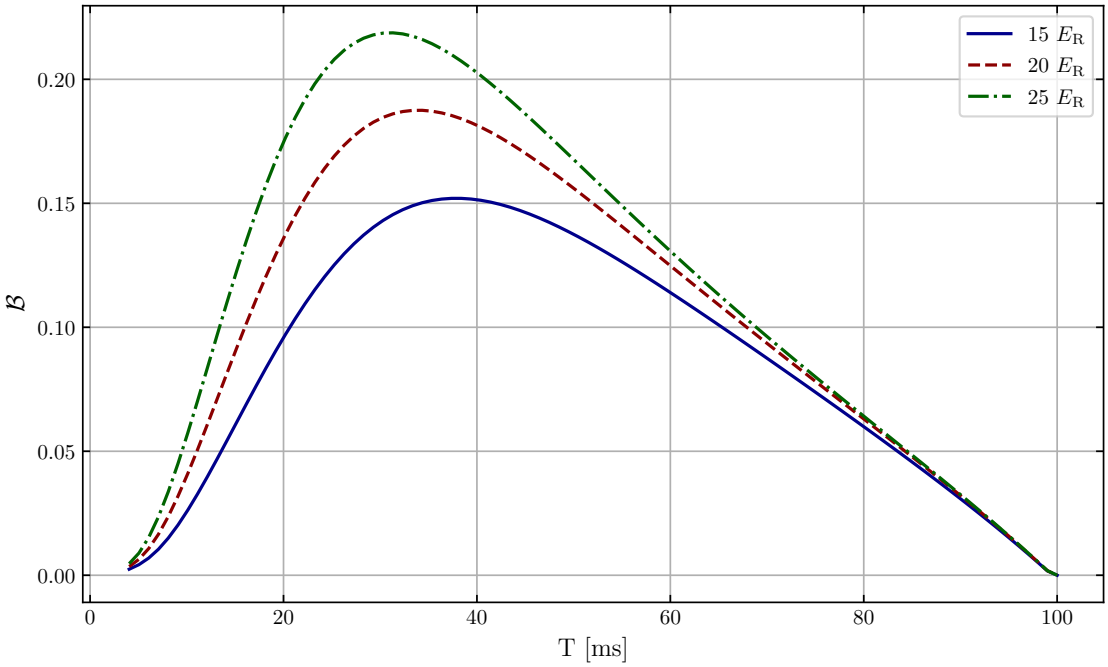

Figure 1.10 – Computation of the adiabaticity criterion $\mathcal{B}$ for the ramp of the horizontal arms of our optical lattice, for ramps of 100 ms, assuming $\overline{n}(\mathbf{r}) = 1$.

Very high lattice depths regime

When the lattice depth V_0 increases, U and Ω increase while J decreases exponentially. As a consequence a criterion for the adiabaticity of the lattice ramp, for a deep optical lattice, is the ability of the system to redistribute via tunneling the atoms across the sites according to the Thomas-Fermi distribution. This criterion can be formalised as (Gericke et al. 2007):

$$\mathcal{A} = \max \frac{\hbar}{J^2} \left| \frac{\mathrm{d}J}{\mathrm{d}t} \right| \ll 1 \tag{1.74}$$

and can be computed from the actual form of the ramp used in our experiment. As shown in Fig. 1.11, this criterion is fulfilled for lattice depths below $20\,E_R$ with ramps duration of 100 ms.

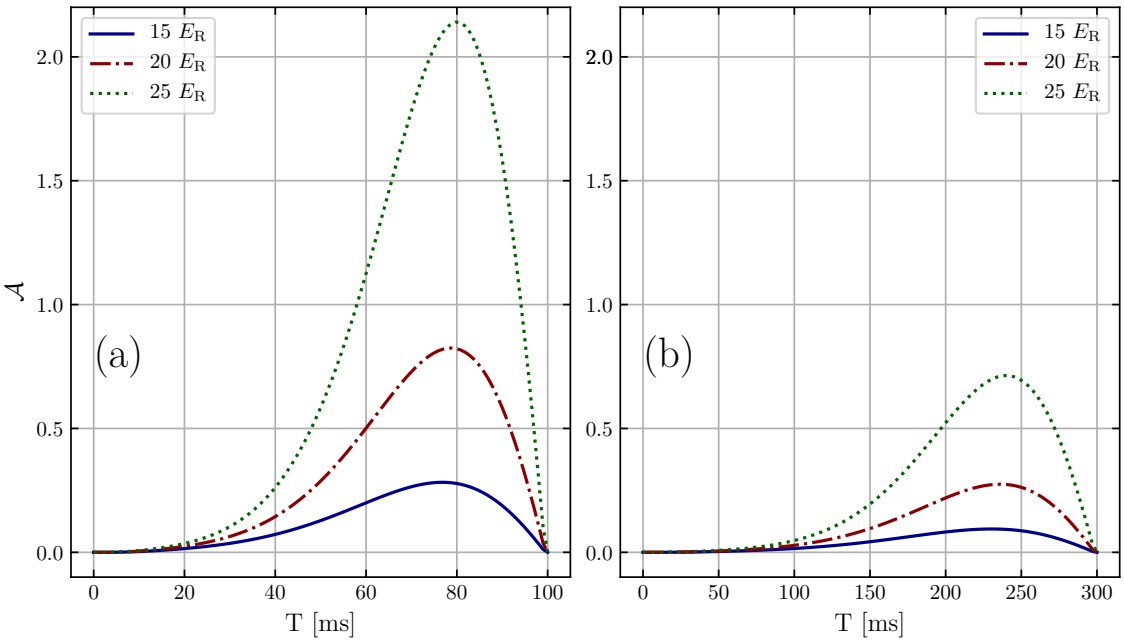

Figure 1.11 – Computation of the adiabaticity criterion $\mathcal{A}$ for the ramp of the horizontal arms of our optical lattice, for ramps of (a) 100 ms and (b) 300 ms.

CHAPTER 2

Experimental setup

This chapter aims at presenting some experimental and technical aspects specific to the atoms and the experimental setup that will be used throughout this dissertation. The key aspects of the production of a BEC and its loading in an optical lattice is described in many instances (for instance, Metcalf et al. 1999; Ketterle et al. 1999; Bloch et al. 2008). Some additional elements specific to the experimental setup used for this work. Most of the technical notions presented here were discussed in details in the work of the previous PhD students: Scholl 2014, Dareau 2015, Bouganne 2018 and Bosch Aguilera 2019.

The first part of the chapter presents the properties of the bosonic isotope of ytterbium used in our experiment and emphasizes its most interesting features in our experimental perspective. The second part of this chapter details firstly the experimental setup and the procedure used to produce a Bose-Einstein condensate and load it into an optical lattice. Then some experiments used to characterize the system created at the end of the procedure described in the first place are presented.

2.1 Properties of Ytterbium

Ytterbium (atomic number $Z = 70$) is a rare-earth element which belongs to the lanthanide series and presents seven stable isotopes : five bosonic(^{168}Yb, ^{170}Yb, ^{172}Yb, ^{174}Yb, ^{176}Yb) with nuclear spin $I = 0$ and two fermionic (^{171}Yb, ^{173}Yb) with non zero nuclear spin. Their respective natural abundances are detailed in the table 2.1.

Isotope	Abundance	Nuclear spin	Statistics
^{168}Yb	0.13 %	0	boson
^{170}Yb	3.05 %	0	boson
^{171}Yb	14.3 %	1/2	fermion
^{172}Yb	21.9 %	0	boson
^{173}Yb	16.1 %	5/2	fermion
^{174}Yb	31.8 %	0	boson
^{176}Yb	12.7 %	0	boson

Figure 2.1 – Natural abundance of the stable isotopes of ytterbium

In the work presented in this dissertation, the most abundant bosonic isotope ^{174}Yb has been used.

2.1.1 Electronic structure of Ytterbium

An interesting feature of ytterbium is its electronic structure ($[\mathrm{Xe}]4f^{14}6s^2$) with completely filled inner shells and two electrons in the outer s-shell. This is similar to the electronic structure of helium and earth-alkaline atoms like strontium. Indeed, since the two valence electrons are responsible for most of the low energy physics (Bethe et al. 1957), ytterbium exhibits electronic properties similar to earth-alkaline elements and is consequently referred as an alkaline-earth like (AEL) atom.

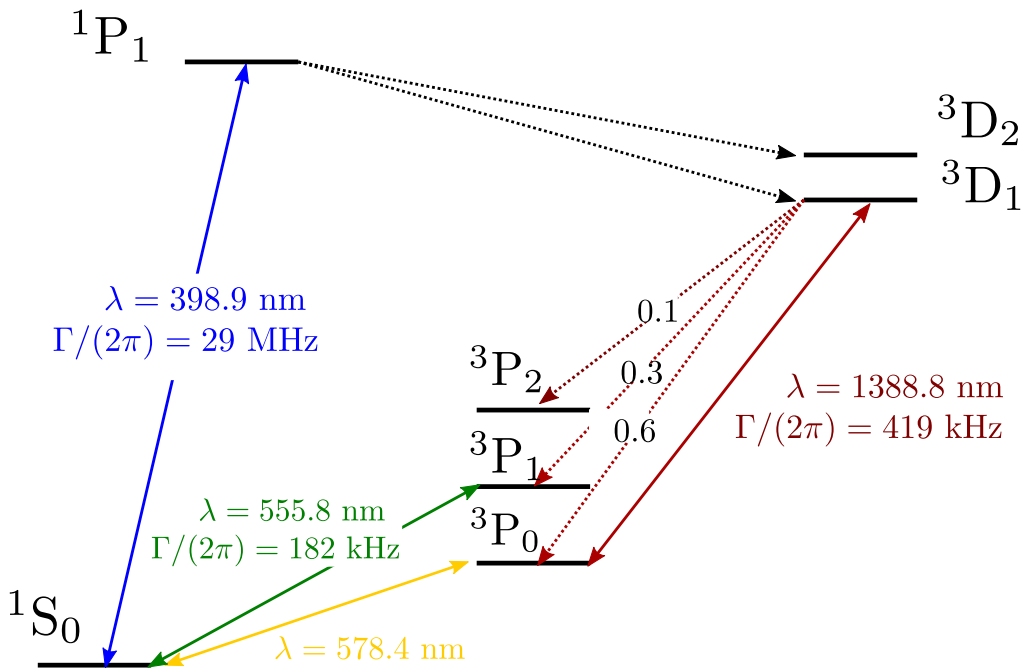

Figure 2.2 – Scheme of the lowest energy levels of ytterbium. The solid arrows represent the optical transitions that are laser-driven in our experimental setup. The dashed ones indicate possible decay channels, with the branching ratio for some of them.

The ground state of ytterbium is a singlet state $^1S_0$ with a null total electronic spin[2]. The first excited states correspond to the promotion of one electron to the $6p$ shell, leading to the electronic structure $[Xe]4f^{14}6s^16p^1$. This configuration corresponds to one singlet state $^1P_1$ and three triplet states $^3P_0$, $^3P_1$, $^3P_2$. A scheme of the energy levels is represented in 2.2.

The electronic transitions used in this work are detailed below.

Blue transition

The *blue* transition $^1S_0 \rightarrow {}^1P_1$ ($\lambda_b = 399$ nm), that leaves the total electronic spin invariant ($\Delta S = 0$) is the only electric-dipole allowed transition from the ground state to a low lying excited state. This transition presents a broad linewidth $\Gamma_b = 2\pi \times 29$ MHz and an saturation intensity $I_{\text{sat}} = 60\ \text{mW/cm}^2$. This transition is not completely closed, for the state $^3P_1$ is weakly coupled to ^3D_J manifold states (Honda et al. 1999), from which the atoms can decay to the ground state via the ^3P_J states. Although this leakage is very weak, it limits the size of the magneto-optical traps operating on this transition alone.

Green inter-combination transition

In absence of spin-orbit coupling, transitions between spin-singlet and spin-triplet states would be electric-dipole forbidden according to the Wigner-Eckart theorem, since they do not conserve the total spin quantum number ($\Delta S \neq 0$). However for heavy, many-electrons atoms like ytterbium, such transition can be enabled thanks to the effect of the spin orbit coupling. In this case J is the relevant quantum number to consider and the appropriate selection rule is $\Delta J = 1$. The $^1S_0 \rightarrow {}^3P_1$ transition ($\lambda_g = 555.8\,\text{nm}$) with a narrow linewidth $\Gamma_g = 2\pi \times 182\,\text{kHz}$ and saturation intensity $I_{\text{sat}} = 0.14\,\text{mW/cm}^2$ is thus weakly allowed. Electric-dipole transitions not conserving the spin are called *inter-combination transition*.

Yellow "clock" transition

In the **L.S** coupling regime, the transition from $^1S_0$ to the spin-triplet meta-stable state $^3P_0$ is doubly forbidden, as it violates simultaneously two selection rules: $\Delta S = 0$ and $J = 0 \longleftrightarrow J = 0$ is forbidden. As seen for the $^1S_0 \rightarrow {}^1P_1$ transition the spin-orbit coupling allows one to bypass the first rule, but the second one remains.

The fermionic isotopes of ytterbium have an non-zero nuclear angular momentum $I \neq 0$. The hyperfine interaction mixes a small fraction of the $^3P_1$ state into the $^3P_0$, and makes the transition possible (Porsev et al. 2004). This feature, used for high quality factor optical clocks (Ludlow et al. 2015), does not naturally exists for bosonic ytterbium due to their null nuclear angular momentum. However it can be artificially emulated with the method of *magnetic mixing* described in Taichenachev et al. 2006. The authors propose to use an external static magnetic field $\mathbf{B} = B\mathbf{e}_z$ to realize the high-field coupling. The introduction of the static magnetic field adds an extra Zeeman term on the Hamiltonian $\hat{H}_B = -\hat{\boldsymbol{\mu}}.\mathbf{B}$, where $\hat{\mu}$ is the magnetic dipole operator, that

[2] We are here using the spectroscopic notation $^{2S+1}L_J$, where S is the total electronic spin, L the total electronic orbital momentum and $\mathbf{J} = \mathbf{L} + \mathbf{S}$ the total electronic angular momentum.

couple the $^3P_0$ and $^3P_1$ states with the matrix element (Taichenachev et al. 2006):

$$\hbar\Omega_B = \langle {}^3P_0|\hat{\boldsymbol{\mu}}.\mathbf{B}|{}^3P_1\rangle = \sqrt{\frac{2}{3}}\mu_B B \tag{2.1}$$

with μ_B the Bohr magneton.

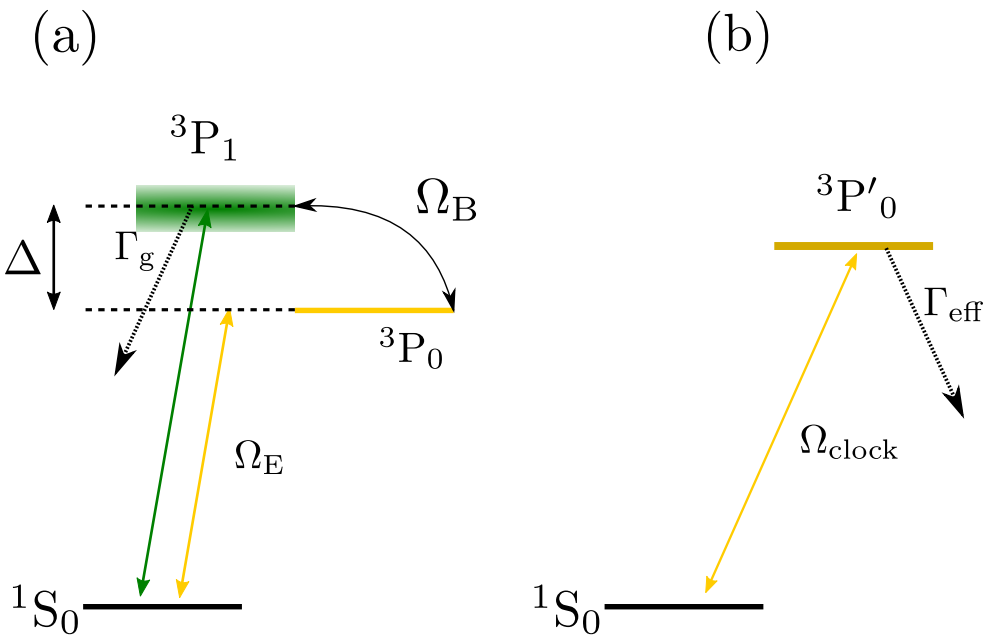

Figure 2.3 – Scheme of the magnetic mixing technique : (a) A static magnetic field couples the atomic states $^3P_0$ and $^3P_1$ with strength Ω_B. (b) Effective two level system created by magnetic mixing.

In the regime where this coupling term is small compared to the energy difference ($|\Omega_B| \gg \Delta$) the levels $^3P_0$ and $^3P_1$ ($|\frac{\Omega_B}{\Delta}| \ll 1$), the eigenstates of the modified Hamiltonian are given in first order perturbation theory by :

$$|{}^1S'_0\rangle \approx |{}^1S_0\rangle \tag{2.2}$$

$$|{}^3P'_0\rangle \approx |{}^3P_0\rangle + \frac{\Omega_B}{\Delta}|{}^3P_1\rangle \tag{2.3}$$

The small contamination of the $^3P_0$ by the $^3P_1$ state opens the $^1S_0 \longrightarrow {}^3P'_0$ transition. Indeed the states $^1S_0$ and $^3P_1$ can be coupled by an optical field of amplitude $\mathbf{E}$ with the associated Rabi frequency $\hbar\Omega_E = \langle {}^1S_0|\hat{\mathbf{d}}.\mathbf{E}|{}^3P_1\rangle$ where $\hat{\mathbf{d}}$ is the electric-dipole operator.

From these expressions the Rabi frequency for transition created by magnetic mixing writes,

$$\hbar\Omega_{clock} = \langle {}^1S'_0|\hat{\mathbf{d}}.\mathbf{E}|{}^3P'_0\rangle = \frac{\Omega_B}{\Delta}\langle {}^1S_0|\hat{\mathbf{d}}.\mathbf{E}|{}^3P_1\rangle = \hbar\frac{\Omega_B\Omega_E}{\Delta} \tag{2.4}$$

The expression of Ω_E can be made explicit :

$$\Omega_E = \sqrt{\frac{6\pi\Gamma_g c^2}{\hbar\omega_g^3}}\sqrt{I_{cl}} \tag{2.5}$$

where I_{cl} is the light intensity. The effective Rabi frequency associated with the clock transition is therefore defined by

$$\Omega_{\mathrm{clock}} = \alpha \mathrm{B} \sqrt{I_{\mathrm{cl}}}. \tag{2.6}$$

For ^{174}Yb one has

$$\alpha = \sqrt{\frac{4\pi c^2 \Gamma_{\mathrm{g}} \mu_{\mathrm{B}}^2}{\hbar \omega_{\mathrm{g}}^3 \Delta^2}} \approx 2\pi \times 18.7\,\mathrm{mHz.G^{-1}}.\left(\mathrm{mW.cm^{-2}}\right)^{-\frac{1}{2}}. \tag{2.7}$$

The small admixture of state $^3\mathrm{P}_1$, that makes the forbidden transition possible, is also responsible for a broadening of the $^3\mathrm{P}_0'$, due to the finite linewidth Γ_{g} of the $^3\mathrm{P}_1$ state. The effective spontaneous lifetime is

$$\Gamma_{\mathrm{eff}} \approx \Gamma_{\mathrm{g}} \frac{\Omega_{\mathrm{B}}^2}{\Delta^2} = 2\pi \times 535\,\mathrm{pHz} \times \left[\frac{\mathrm{B}}{1\mathrm{G}}\right]^2 \tag{2.8}$$

Power [mW]	Ω_{clock} [Hz]	δ_{E} [Hz]	δ_{B} [Hz]	Γ_{eff} [Hz]	$\Omega_{\mathrm{E}}^2/\Omega_{\mathrm{B}}^2$
12	1200	1800	-2200	1.8×10^{-5}	$\sim 10^{-1}$
0.2	150	30	-2200	1.8×10^{-5}	$\sim 10^{-3}$

Figure 2.4 – Values of the quantities related to the yellow clock transition, computed for the main power values used in the experiment presented in this thesis. The computation have been made for magnetic field B $\approx$ 182 G and beam waist $w = 80\,\mu$m actually used in our experiment.

As seen in Fig. 2.4, the values for the magnetic field B $\approx 182\,\mathrm{G}$ and the light intensity $I_{\mathrm{cl}} \approx 120\,\mathrm{W/cm^2}$ allows us to neglect the spontaneous decay rate at the timescales of our experiments. Moreover the power broadening due to the laser light is neglected, since $\Omega_{\mathrm{E}}^2 \ll \Omega_{\mathrm{B}}^2$.

The presence of the static magnetic field also causes a quadratic Zeeman shift on the resonance,

$$\delta_{\mathrm{B}} = -\beta B^2. \tag{2.9}$$

In addition the coupling laser also induces a differential light shift of the $^1\mathrm{S}_0 \rightarrow {}^3\mathrm{P}_0$ transition,

$$\delta_{\mathrm{E}} = \kappa I_{\mathrm{cl}}. \tag{2.10}$$

The magnetic mixing technique has firstly been described in Barber et al. 2006, where the value of $\beta = 2\pi \times 66\,\mathrm{mHz/G^2}$ has been measured. The value of $\kappa = 2\pi \times 15\,\mathrm{mHz}/\left(\mathrm{mW/cm^2}\right)$ has been measured in Barber et al. 2008.

2.1.2 Polarizability of the $^1S_0$ and $^3P_0$ states

The interaction of a monochromatic light field $\mathbf{E}(\mathbf{r}) = \mathcal{E}(\mathbf{r})\cos(\omega_L t)$ with an atom induces an atomic dipole moment, which interacts with the electromagnetic field. It results in the apparition of a conservative force derived from the dipole potential (Grimm et al. 2000) :

$$V_{\text{dip}}(\mathbf{r}, \omega_L) = -\frac{1}{4}\alpha(\omega_L)\,|\mathcal{E}(\mathbf{r})|^2 = -\frac{1}{2\epsilon_0 c}\alpha(\omega_L)\,I(\mathbf{r})\,. \tag{2.11}$$

Here α is the real part of the dynamic complex atomic polarizability $\underline{\alpha}$.

The atomic polarizability depends on the light angular frequency ω_L and on the internal state of the atom. Due to their different electronic structures, the polarizabilities of the $^1S_0$ and $^3P_0$ states, respectively denoted α_g and α_e present different behavior at a given wavelength. The values of α_g and α_e as functions of the wavelength λ can be computed by summing the contribution to the real part of the complex polarizability of each optical transition coupling the considered state to higher-lying energy levels. The result of the computations made from the data in Dzuba et al. 2010 is displayed in Fig. 2.5.

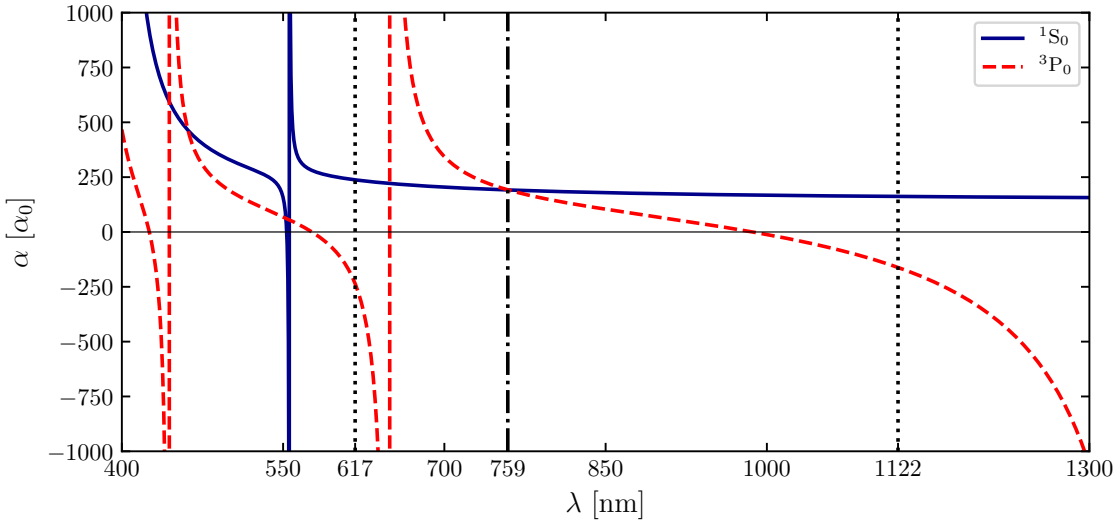

Figure 2.5 – Real parts of the dynamic complex atomic polarizability for the ground state $^1S_0$ (solid blue line) and the excited metastable state $^3P_0$. The vertical dash-dotted line points the magic wavelength λ_m while the two vertical dotted lines point the anti-magic wavelengths λ_{am} and λ'_{am} . The polarizabilites are represented here in units of α_0 the atomic unit of electric polarizability.

Another interesting feature of ytterbium atoms is the existence of reachable wavelengths where the absolute values of the real part of the dynamic polarizabilities for the $^1S_0$ and $^3P_0$ states are equal. More precisely:

- The *magic wavelength* where $\alpha_g(\lambda_m) = \alpha_e(\lambda_m)$. It occurs for ^{174}Yb around $\lambda_m \approx 759.35\,\text{nm}$ and has been precisely measured in Barber et al. 2008. The

magic wavelength are essential in the context of optical clocks, since they allow to cancel differential light shifts Ludlow et al. 2015.

- The *anti-magic wavelength* where $\alpha_g(\lambda_{\mathrm{am}}) = -\alpha_e(\lambda_{\mathrm{am}})$. Such wavelengths occur for ^{174}Yb around $\lambda_{\mathrm{am}} \approx 617\,\mathrm{nm}$ and $\lambda'_{\mathrm{am}} \approx 1122\,\mathrm{nm}$. This property plays a core role in the perspective of creating state dependent optical lattices and artificial gauge fields, pursued by the group (Gorshkov et al. 2010, Gerbier et al. 2010, Cooper 2011).

2.2 Production of a ^{174}Yb Bose-Einstein condensate

This section presents the main technical aspects involved in the process leading to the loading of a Bose-Einstein condensate in an optical lattice and the methods used to characterize the system thereby created.

2.2.1 Vacuum system

In ultracold atomic physics experiments, the collision of the atomic ensemble constitutive of the system under study with the residual background gas may strongly alter the phenomenon under study. It is necessary to operate under a ultra high vacuum (UHV) regime. For this purpose our experimental setup is composed of 3 main sections, separated by differential pumping stages in which very low pressures are maintained. In our working conditions, these pressures are:

- the oven section ($\mathrm{P_{oven}} \approx 10^{-8}$ mbar)
- the Magneto-optical trap (MOT) chamber ($\mathrm{P_{MOT}} \approx 10^{-10}$ mbar)
- the science chamber ($\mathrm{P_{science\,chamber}} < 10^{-11}$ mbar).

The atomic vapor is generated in the oven, where solid ytterbium chips are heated up to 450 °C, the melting point for ytterbium under standard pressure conditions is at 824 °C. In this section of the experiment, the pressure is maintained around 10^{-8} mbar by two 20 L/s ion pumps [3]. The oven is separated from the tube surrounded by the coils of the Zeeman slower by a differential pumping stage. Here the pumping is provided by another 20 L/s ion pump and the pressure in the Zeeman tube is of the order of 10^{-9} mbar. The pressure in the MOT chamber is lowered down to 10^{-10} thanks to the action of a 40 L/s ion pump assisted by a non-evaporative getter pump. Finally a pressure under 10^{-11} mbar is reached in the science chamber, where the experiments on the optical lattice are performed, thanks to a pump combining a 2 L/s ion pump and a non-evaporative getter pump.

2.2.2 Laser cooling of ^{174}Yb atoms

We compare here the merits of the different transitions from the perspective of atoms trapping, cooling and condensation before going in the details of the experimental realization of a Bose-Einstein condensate of ^{174}Yb . The absence of hyperfine

[3] Medium Vaclon Plus Pumps. Agilent

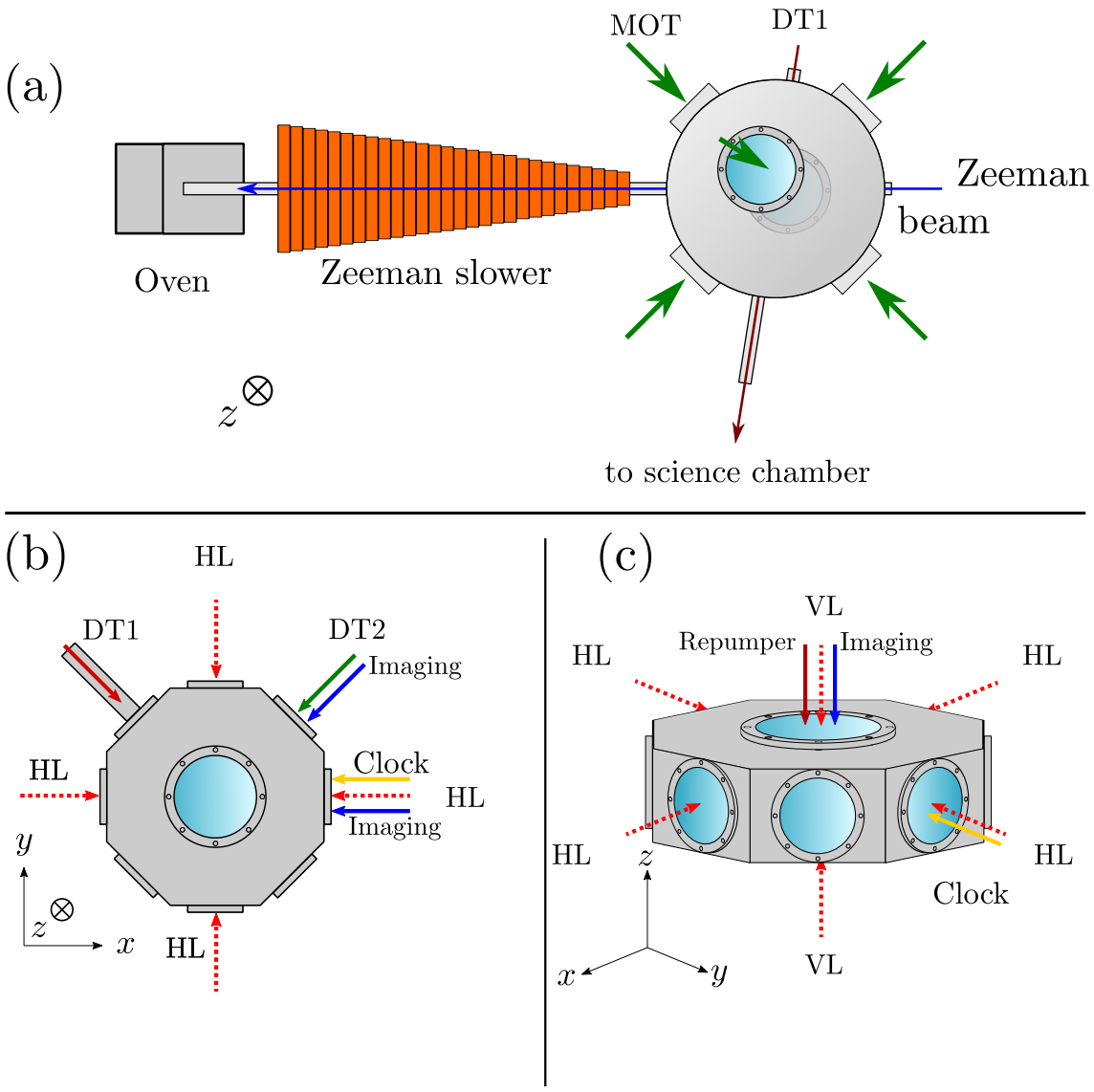

Figure 2.6 – Scheme of the experimental setup: (a) Representation of the oven, the Zeeman slower and the MOT chamber. The atomic flux generated at the output of the oven is slowed along the Zeeman slower by the blue laser beam (blue arrow). In the MOT chamber the atoms are trapped cooled and loaded in the dipole trap DT1 to be transported in the science chamber. (b) Top view of the science chamber. The atoms routed in the science chamber are loaded in a crossed dipole trap, formed by the beams DT1 and DT2 and evaporated to reach Bose-Einstein condensation. The BEC can be loaded in the optical lattice formed by the counter-propagating laser beams HL (×2) and VL. (c) Front view of the science chamber. The atoms can be probed by the yellow clock laser and imaged thanks to different imaging beam tuned operating on the blue transition.

structure ($I = 0$) for the ground state of bosonic ytterbium atoms prevents the use of sub-Doppler cooling techniques. Doppler cooling relies on radiation pressure induced friction force to cool down the atoms. The achievable minimum temperature is limited by the fluctuations introduced by the random nature of spontaneous emission to the Doppler temperature Metcalf et al. 1999 :

$$T_D = \frac{\hbar\Gamma}{2k_B} \tag{2.12}$$

with Γ the linewidth of the transition.

The capture speed v_c of a magneto-optical trap is another important experimental quantity. It corresponds to the maximal speed of an atoms that can be stopped in a magneto-optical trap (MOT) on the scale of the trap size (*i.e.* the MOT beam waist w),

$$v_c = \sqrt{\frac{w\hbar k\Gamma}{m}} \tag{2.13}$$

Armed with theses considerations we can have a look on the merits of the different available transitions.

The large linewidth of the *blue* transition enables efficient cooling of thermal atoms with high capture speed (on the order of tens of m/s) and is thus the best candidate for the Zeeman cooling step. Nevertheless it is not well suited for the cooling and trapping of atoms in the Magneto-Optical trap: with the broad linewidth comes a high Doppler temperature, and the leakage of the transition limits the number of atoms that could be trapped in a magneto-optical trap (in absence of a repumper). The narrow *green* inter-combinaison transition enables a much lower Doppler temperature but also presents a much lower capture velocity v_c. Consequently the MOT loading rate is expected to be somewhat reduced due to this low v_c . This transition is a good candidate for the magneto optical trapping, given a prior precooling step that will be realized with the *blue* transition.

2.2.3 Atomic beam and Zeeman slower

The outgoing atomic beam exiting the oven is collimated by a metallic tube of length $L = 10$ mm and diameter $d = 4$ mm, which results in a divergence angle $\theta = d/(2L) \approx 11.5°$ at the entrance of the Zeeman slower.

The average speed of atoms in the thermal vapor that exits the oven is too high ($v_0 \approx 300$ m/s) to be trapped by the Magneto Optical Trap. The atoms are thus slowed down by a counter propagating laser beam resonant with the "*blue*" $^1S_0 \rightarrow {}^1P_1$ transition. Two coils wrapped around the slower axis create a magnetic field gradient and offset to shift the Zeeman sublevels. This shift compensates the change of the Doppler shift experienced by the atoms when they are slowed down, in order to keep the transition frequency close to the laser frequency. At the end of the *Zeeman slower*, the average axial speed of the atoms has been lowered down to about 10 m/s. The blue laser beam is made slightly convergent in order to approximately match the transverse spatial divergence of the atomic beam.

The blue laser light at 399 nm is obtained by doubling frequency: 1.5 W of infrared light at 798 nm provided by a commercial laser source [4] are sent in a bow tie cavity with a non-linear crystal [5] inside (Scholl 2014;Dareau 2015). We obtain in typical working condition 240 mW of blue light. A feedback loop driving a piezoelectric actuator mounted on one of the cavity mirror maintains the resonance condition for the cavity. The frequency of the blue light is controlled thanks to a modulation transfer spectroscopy scheme, more extensively described in Dareau 2015, performed in a ytterbium hollow cathode lamp with Yb inside and stabilized by correcting the laser current Bouganne 2018.

2.2.4 Magneto-Optical Trap (MOT)

The atoms emerging from the Zeeman slower are slow enough to be trapped using the "*green*" $^1S_0 \rightarrow {}^3P_1$ inter-combination transition. An optical molasses, applying a friction force $F(\mathbf{r}) = -\alpha\dot{\mathbf{r}}$ on the atoms, is created by three counter propagating laser beams with circular polarization, slightly red detuned compared with the $^1S_0 \rightarrow {}^3P_1$ transition frequency. In order to actually trap the atoms, a quadrupole magnetic field is added that introduce a spatial dependency of the light force. The combination of the light beams and the quadrupole magnetic field forms a *Magneto-Optical Trap* (MOT).

As mentioned earlier, the inter-combination transition is very narrow and consequently the capture velocity is small. In order to widen the extent of velocity classes that are trapped, the transition is artificially broadened by optical saturation and by adding frequency sidebands.

In practice, we load the magneto-optical trap for 6 ms and end up with about 2×10^8 atoms trapped at a temperature on the order of 10 μK (Dareau 2015; Scholl 2014). The loading of the MOT can be modelled as a competition between the loading process at a rate R and one-body losses at a rate κ, which can be formalized by the equation

$$\frac{\mathrm{d}N}{\mathrm{d}t} = R - \kappa N. \tag{2.14}$$

The solution is :

$$N(t) = \left(1 - \mathrm{e}^{-\kappa t}\right) \frac{R}{\kappa}. \tag{2.15}$$

In our current experimental configuration, the loading rate is of the order of $R \sim 10^7\,\mathrm{s}^{-1}$ and the lifetime of the atoms is of the order of $\kappa^{-1} \approx 50\,\mathrm{s}$. The working conditions are thus far from the regime of saturation, $N_\infty = R/\kappa \approx 2 \times 10^9$. However they allow to saturate the optical dipole trap in a dozen of seconds, which is sufficient in the perspective of the production of a Bose-Einstein condensate.

The green light at 556 nm is also obtained using frequency doubling. A narrow-line distributed feedback fiber laser [6] at 1122 nm delivers 1.7 W of infrared light at 1112 nm after its passage trough a fiber amplifier [7]. This laser is sent to another bow-tie

[4] TA pro, Toptica.
[5] ppKTP (periodically poled potassium titanyl phosphate) crystal from Raicol crystals.
[6] Koheras Adjustik. NKT photonics
[7] Elysa. Quantel laser.

doubling cavity with a non-linear crystal [8] inside, analogous to the one used for the blue laser light. The resonance of the cavity is ensured by a similar feedback loop and the frequency is stabilized thanks to another feedback loop that uses the signal of a saturated absorption spectroscopy in a glass cell containing iodine (Dareau 2015) to retro-act on the laser current.

2.2.5 Dipole trap loading and transport

At the end of the MOT loading step, the trapped atomic cloud is compressed by an increase of the magnetic gradient and its position is shifted to coincide with the focal point of a high-intensity ($P \approx 45\,\mathrm{W}$) infrared ($\lambda = 1070\,\mathrm{nm}$) fibered laser [9] beam. The laser beam intensity distribution can be approximated by the one of a focused Gaussian beam:

$$I\left(\mathrm{r}\right) = \frac{2P}{\pi w^2\left(z\right)} \mathrm{e}^{-2r^2/w^2(z)}. \tag{2.16}$$

Here z is the propagation axis coordinate, r is the radial distance from the propagation axis, P the beam power and $w\left(z\right)$ the $1/e^2$ radius defined by

$$w\left(z\right) = w_0 \sqrt{1 + \frac{z^2}{z_R^2}}, \tag{2.17}$$

with w_0 the beam waist and $z_R = \pi w_0^2/\lambda$ the Rayleigh length. The induced dipole potential, described earlier in 2.1.2, forms a *dipole trap*, denoted DT1, whose expression is

$$V_{\mathrm{DT1}}\left(\mathbf{r}\right) \approx -V_0 + \frac{1}{2} M \left(\omega_{\mathrm{rad}}^2 r^2 + \omega_{\mathrm{ax}}^2 z^2\right). \tag{2.18}$$

Here $V_0 = P\alpha\left(\lambda_{\mathrm{DT1}}\right) / \left(\pi \epsilon_0 c w_0^2\right)$ is the trap depth and ω_{ax} and ω_{rad} are the axial and radial frequencies, given by:

$$\omega_{\mathrm{ax}} = \frac{\lambda_{\mathrm{DT}}}{2\pi w_0^2}\sqrt{\frac{8V_0}{M}}, \qquad \omega_{\mathrm{rad}} = \sqrt{\frac{4V_0}{M w_0^2}} \tag{2.19}$$

The polarizability of the ground state of ^{174}Yb at the wavelength λ_{DT} is $\alpha_g\left(\lambda_{\mathrm{DT}}\right) \approx 164\,\alpha_0$, with $\alpha_0 \approx 1.65 \times 10^{-41}\,\mathrm{C^2m^2/J}$ the atomic unit of electric polarizability. From this value we can estimate that the trap created by the laser beam has a depth $V_0 \approx k_{\mathrm{B}} \times 600\mu\mathrm{K}$, much higher than the measured temperature of the MOT. The trapping frequencies ω_{ax} and ω_{rad} have been measured (Bouganne 2018; Bosch Aguilera 2019) thanks to, respectively, center-of-mass oscillations and parametric heating (Savard et al. 1997) techniques. For the max power of 45 W the measurements give:

$$\omega_{\mathrm{ax}} \approx 2\pi \times 8\,\mathrm{Hz} \qquad \omega_{\mathrm{rad}} \approx 2\pi \times 1.4\,\mathrm{kHz} \tag{2.20}$$

These values are consistent with the ones calculated with a beam waist $w = 40\mu\mathrm{m}$, which is independently measured by imaging of the laser beam on CCD camera. The temperature of the cloud can be measured to be $T_{\mathrm{DT}} = 40\,\mu\mathrm{K}$, using time of flight

[8] ppSLT (periodically poled stoichiometric lithium tanalate) crystal from Covesion
[9] YLR-50-LP-AC-Y12.IPG Photonics

expansion (Ketterle et al. 1999). In our operating regime we succeed to saturate the loading of the dipole trap for loading time for the MOT on the order of ten milliseconds (see Fig. **??**)

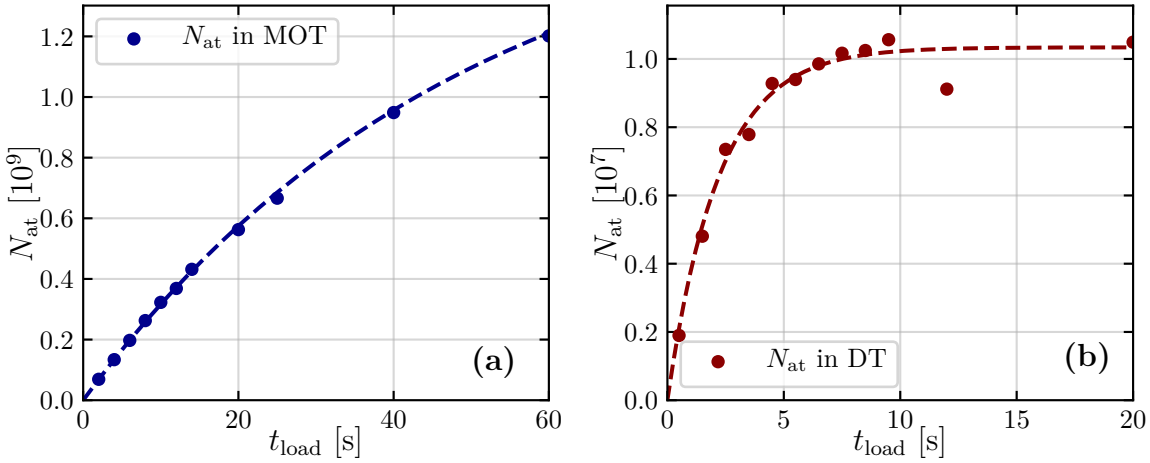

Figure 2.7 – Loading curves for the magneto-optical trap and the dipole trap. The points are the experimentally measured number of atoms in the traps and the solid lines are the results of the fits performed according to the model described in 2.14. The extracted loading rates are $R_{MOT} = 3.7 \times 10^7\,s^{-1}$ for the MOT and $R_{DT} = 4.7 \times 10^6\,s^{-1}$.

After loading, the trapped atomic cloud is then transported to the science chamber, where the vacuum is better and where more optical access is available. The transport is realized by moving a corner cube mirror on which the dipole trap beam is reflected before entering in the experiment using a precision translation stage [10]. The focus of the beam is translated over 18 cm in 1.5 s as the stage moves. Almost 80 % of the atoms are successfully transported to the science chamber, where further evaporative cooling will takes place (Scholl 2014).

2.2.6 Transfer in a crossed dipole trap and evaporative cooling

In order to achieve quantum degeneracy in the science chamber, we rely on the evaporative cooling technique. This technique consists in reducing progressively the depth of the trap to remove the most energetic atoms while letting the remaining ones thermalize thanks to the inter-atomic collisions. A more comprehensive description of the experimental procedures used for the evaporative cooling described below can be found in Dareau 2015 and Scholl 2014.

The use of optical trap to condensate the ^{174}Yb is imposed by the absence of nuclear spin for this isotope. One of the main drawback of this kind of trap is the impossibility to reduce its depth without reducing its trapping frequency during the whole evaporative cooling ramp. The slackness of the single-beam dipole trap in the axial direction prevents the collision rate in the trapped atomic cloud to be high enough for a proper thermalization during the evaporative cooling. In order to increase the

[10] 27XMS160. Newport

trapping frequency along the loose direction, a second laser beam [11] at wavelength $\lambda_{DT2} = 532\,\text{nm}$ of power $P = 1\,\text{W}$ and waist $w \approx 16\,\mu\text{m}$, is applied perpendicularly to the first one in the horizontal plane, the ensemble forming a *crossed dipole trap* (CDT). The real part of the polarizability at λ_{DT2} is equal to $\alpha(\lambda_{DT2}) = 262.5\,\alpha_0$, that gives calculated value for the depth of the second trap $V_0 = k_B \times 100\mu\text{K}$. The focus the two beams are matched so that the resulting trap total depth is equal to the sum of each individual trap depth and the trapping frequencies along each axis j are given by : $\omega_j^2 = \omega_{j,DT}^2 + \omega_{j,DT2}^2$.

Forced evaporative cooling is performed by ramping down the power of the dipole traps. The power of the second dipole trap at $\lambda_{DT2} = 556\,\text{nm}$ is ramped down to approximatively 40 mW by controlling the radio-frequency amplitude of an AOM with a feedback loop on the power measured on a photodiode. The evaporation on the first infra-red dipole trap requires to control the power on a important dynamic range, from $P_{init} \approx 45\,\text{W}$ to $P_{fin} \approx 200\,\text{mW}$, that is complicated to achieved with a single feedback loop on an intensity signal. Instead a dual control is used : the power is firstly reduced down to 10 % of its initial value, slightly above its lasing threshold, by directly lowering the current send on the laser. Then, in order to reach the desired final value for the power, a feedforward ramp is sent to a motorized rotation stage [12] to rotate a half-wave waveplate associated with a Glan-Taylor polarizer [13]. At the very end of the evaporation ramp, when the power goes below 1 % of the initial power, its evolution is monitored on a photodiode whose signal is send to a feedback loop (Scholl 2014).

The geometry of a crossed dipole trap also makes it critical to minimize the fluctuations of the pointing of its constitutive laser beams. In our experiment the position of the foci are imaged on position detectors that are coupled in a feedback loop to motorized mirror mounts on the optical path of the laser beams in order to keep their crossing position stable[14]. In practice, this correction is not done constantly but only performed several times per day, to counter long timescale (presumably thermal) drifts.

2.2.7 Characterization of the Bose-Einstein condensate

During the forced evaporative cooling step, the depth of the dipole trap is lowered. The temperature of the atomic cloud decreases and end up reaching the critical phase space density where Bose-Einstein condensation occurs. This phase transition is experimentally characterized by the appearance of a bimodal distribution on the observed atomic density profiles. This distribution can be used to extract the condensed fraction and the temperature of the thermal part (Ketterle et al. 1999). In practice, at the end of the 4 s evaporation ramp, a Bose-Einstein condensate of 9×10^4 atoms, without a detectable thermal fraction is obtained. The relative fluctuations on the atom number in the BEC stay below 5 % when monitored over a period of several minutes.

The final trapping frequencies for the CDT are $(\omega_x, \omega_y, \omega_z) = 2\pi \times (80, 240, 250)$ Hz and we introduce their geometric average $\overline{\omega} = (\omega_x \omega_y \omega_z)^{1/3} = 2\pi \times 153\,\text{Hz}$. At and below the condensation point, the dynamics of the BEC is dominated by the interaction

[11] Verdi V-6. Coherent
[12] DRTM-40. OWIS
[13] GL15-C26. Thorlabs
[14] Aligna 4D. TEM Messtechnik

between the atoms and the *Thomas Fermi approximation* becomes relevant (Dalfovo et al. 1999). In this regime the spatial density profile then mirror the shape of the trap according to

$$n\left(\mathbf{r}\right) = \max\left[\frac{\mu - V_{\text{trap}}\left(\mathbf{r}\right)}{g},\, 0\right] \tag{2.21}$$

Here g is the coupling constant seen earlier 1.2.1 and μ the chemical potential. For an harmoni trapping potential V_{trap}, the density profile can be rewritten as an *inverted parabola*,

$$n\left(\mathrm{r}\right) = n_0 \times \max\left[1 - \frac{x^2}{R_x^2} - \frac{y^2}{R_y^2} - \frac{z^2}{R_z^2},\, 0\right]. \tag{2.22}$$

Here n_0 is the maximum density and the

$$R_j = \sqrt{\frac{2\mu}{m\omega_j^2}} \tag{2.23}$$

are the Thomas-Fermi radii in each direction $j \in \{x, y, z\}$. The chemical potential can be determined as

$$\mu = \frac{\hbar\overline{\omega}}{2}\left(\frac{15aN_{\text{at}}}{a_{\text{ho}}}\right)^{\frac{2}{5}} \tag{2.24}$$

with N_{at} is the total number of atoms in the BEC, a is the scattering length, and $a_{\text{ho}} = \sqrt{\frac{\hbar}{m\overline{\omega}}}$ is the average harmonic oscillator length. For ^{174}Yb atoms in the ground state the scattering length has been measured in Kitagawa et al. 2008 and Borkowski et al. 2017: $a = 105a_0$. We typically find a chemical potential $\mu \approx h \times 3700\,\text{Hz}$, a peak density $n_0 \approx 9 \times 10^{14}\,\text{atoms/cm}^3$ and Thomas-Fermi radii $(R_x, R_y, R_z) \approx (8.2, 2.7, 2.6)\,\mu\text{m}$.

2.2.8 Imaging system

This section presents the method of absorption imaging used to study the atomic cloud. To image the atoms, a pulse of light resonant with the transition $^1\text{S}_0 \rightarrow {}^1\text{P}_1$ with wavelength $\lambda_{\text{b}} = 399$ nm and linewidth $\Gamma = 2\pi \times 29$ MHz is sent on the atoms. The atoms experience several absorption spontaneous emission cycles that scatter light randomly and reduce the number of photons measured on the photo-detector. The spatial density distribution of atoms n along the light propagation direction is related to the light intensity by the Beer-Lambert law :

$$\frac{\mathrm{d}I}{\mathrm{d}z} = -n\sigma_0\frac{I}{1 + I/I_{\text{sat}}} \tag{2.25}$$

where $\sigma_0 = 3\lambda_{\text{b}}^2/2\pi$ is the resonant cross section, I the light intensity, and $I_{\text{sat}} = \hbar\Gamma_{\text{b}}\omega_{\text{b}}^3/\left(12\pi c^2\right)$ the saturation intensity for the transition, with $\omega_{\text{b}} = \frac{2\pi c}{\lambda_{\text{b}}}$. The integration of this relation along the propagation direction of the imaging light pulse, gives the optical depth of the atomic cloud OD:

$$\text{OD}\left(\mathbf{r}_\perp\right) = \sigma_0\int n\left(\mathbf{r}_\perp, z\right)\mathrm{d}z = -\ln\left(\frac{I_f\left(\mathbf{r}_\perp\right)}{I_0\left(\mathbf{r}_\perp\right)}\right) + \frac{I_f\left(\mathbf{r}_\perp\right) - I_0\left(\mathbf{r}_\perp\right)}{I_{\text{sat}}} \tag{2.26}$$

where I_0 is the initial intensity profile and I_f the intensity profile after the atomic cloud. One may notice that for intensities small compared to I_{sat}, the second term of

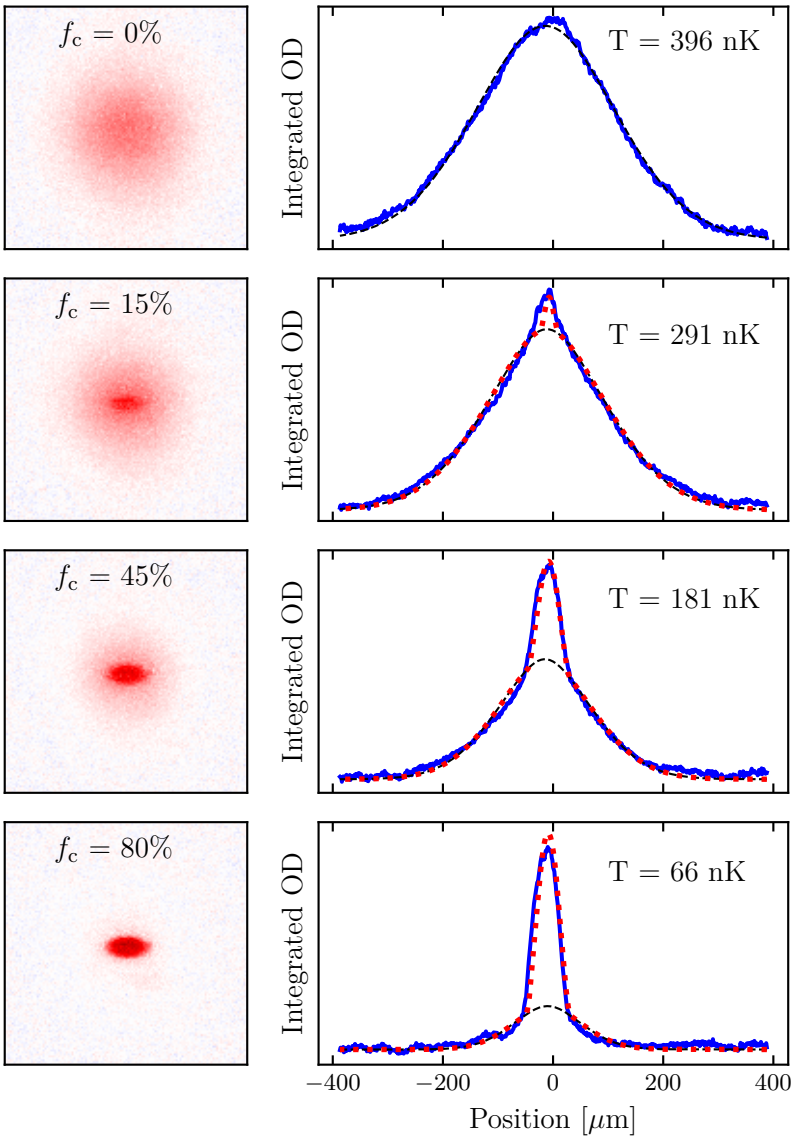

Figure 2.8 – Absorption pictures (left) and horizontal OD integrated along the vert direction (right) taken at different times along the evaporation ramp. The red dashed line fits the remaining thermal fraction while the red dotted line represent the result of the fit of the integrated density (shown as a solid blue line) by a weighted sum of the thermal bosonic and of the Thomas-Fermi distribution. The condensed fraction and the temperature of the thermal fraction are then extracted from the weight and width of the distribution. Adapted from Bosch Aguilera 2019

the right-hand side of the equation is negligible and the expression of the optical depth becomes $\mathrm{OD} = -\ln(I_f/I_0)$.

In practice, the intensities are measured by taking two successive pictures at the same position: a first picture in presence of the atoms is taken, that gives I_f and destruct the system. Then the camera waits a few milliseconds, the time needed for the atoms to leave the camera field of view under the action of the gravity, and a second picture is taken as reference, that gives I_0.

Limitations on the exposition time

During the imaging pulse, the atoms probed experience several absorption-spontaneous cycles that can modify the atomic density distribution of atoms and alter the absorption signal. Two effects more particularly have to be considered: the Doppler shift and the heating of the atoms. Indeed the N_{ph} photons absorbed by an atom during the imaging pulse confer it a momentum $N_{\mathrm{ph}}\hbar k_{\mathrm{b}}$ that is responsible for a Doppler shift of $\Delta\omega = N_{\mathrm{ph}}\hbar k_{\mathrm{b}}^2/m$. In order to be able to image the atoms, this shift must remains smaller that the blue transition linewidth Γ_{b}, which gives the following upper limit on the number of absorbed photons:

$$N_{\mathrm{ph}} \leq \frac{m\Gamma_{\mathrm{b}}}{\hbar k_{\mathrm{b}}^2}. \tag{2.27}$$

Moreover the spontaneous emission of N_{ph} photons by an atom induces a heating in the two transverse directions of $E_\perp = E_{\mathrm{R}}/3N_{\mathrm{ph}} = \hbar^2 k_{\mathrm{b}}^2 N_{\mathrm{ph}}/(6m)$ Grimm et al. 2000 which corresponds to a broadening $\Delta p_\perp = \hbar k_{\mathrm{b}}\sqrt{N_{\mathrm{ph}}/3}$ of the momentum distribution. Assuming that the associated spatial broadening during the pulse of duration τ reads $\Delta r_\perp = \Delta p_\perp \tau/m$, we set the limit for the pulse duration so that $\Delta r_\perp \leq p_s$, with p_s the size of a pixel of the imaging device (for the numerical application here we take $p_s = 2\,\mu$m). We end up with the following condition for the imaging pulse:

$$\frac{\hbar k_{\mathrm{b}}\tau}{m}\sqrt{\frac{N_{\mathrm{ph}}}{3}} \leq p_s \tag{2.28}$$

For $I \approx I_{\mathrm{sat}}$, the number of absorbed-spontaneously emitted photons for a pulse of duration τ reads $N_{\mathrm{ph}} = \Gamma_{\mathrm{b}}\tau/4$ and the previous conditions on the number of absorbed photons can be translated in terms of pulse duration as:

- $\tau \leq 44\,\mu$s for the Doppler shift
- $\tau \leq 20\,\mu$s for the heating.

The experiments presented in this thesis have been performed with imaging pulse durations between 10 μs and 20 μs with beam intensities on the order or smaller than I_{sat}.

Computation of the reference image

As explained above, the computation of the optical density (OD), relies on the hypothesis that the intensity profile I_0 taken a few milliseconds after the first one I_f

gives a good approximation of the intensity profile of the first beam imaging the atoms before the atomic cloud: in absence of atoms we would expect to find $I_0 = I_f$. In practice the imaging pulse is subject to some fluctuations and the bare computation of the OD according to the relation (2.26) results in the appearance of spurious fringes, as observed in Fig. 2.9.

Hopefully, an experiment usually requires to take an important number N_{runs} of these pairs $\{I_{f,\text{i}}, I_{0,\text{i}}\}$ with $1 \leq \text{i} \leq N_{\text{runs}}$. In the following we will treat these 2D images as 1D vectors of size n_{pixels} and assume, in order to lighten the notations, that all the pictures $I_{f,\text{i}}$ do not present any atoms. Our aim is to compute a reference image $\tilde{I}_{0,\text{i}}$ for $I_{f,\text{i}}$ as a linear combination of all reference images:

$$\tilde{I}_{0,\text{i}} = \beta_0 + \sum_{\text{i}=1}^{N_{\text{runs}}} \beta_{\text{i}} I_{0,\text{i}} = \mathbf{X}\beta, \tag{2.29}$$

with $\beta = [\beta_0,\, \beta_1,\, \ldots,\, \beta_{N_{\text{runs}}}]^\top$ the $N_{\text{runs}} \times 1$ vector and $\mathbf{X} = [\mathbf{1},\, I_{0,1}, I_{0,2},\, \ldots, I_{0,N_{\text{runs}}}]$ the $n_{\text{pixels}} \times (N_{\text{runs}} + 1)$ matrix of reference images. Here $\mathbf{1}$ is the vector of dimension n_{pixels} with all its coefficients equal to 1.

We choose β to be the solution of the minimization problem:

$$\beta^* = \underset{\beta}{\text{argmin}} \left\| I_{f,\text{i}} - \mathbf{X}\beta \right\|^2, \tag{2.30}$$

which is

$$\beta^* = \left(\mathbf{X}^\top \mathbf{X}\right)^{-1} \mathbf{X}^\top I_{f,\text{i}}. \tag{2.31}$$

Consequently, $\forall\, \text{i}$, the best reference image $\tilde{I}_{0,\text{i}}$ can be computed from $I_{f,\text{i}}$ by the linear relation:

$$\tilde{I}_{0,\text{i}} = \mathbf{X} \left(\mathbf{X}^\top \mathbf{X}\right)^{-1} \mathbf{X}^\top I_{f,\text{i}} \tag{2.32}$$

Finally in presence of atoms we apply the same procedure to $I_{f,\text{i}}$ deprived from its pixels in the region of interest to compute the vector $\left(\mathbf{X}^\top \mathbf{X}\right)^{-1} \mathbf{X}^\top I_{f,\text{i}}$ and then we apply it to the matrix $\mathbf{X}$.

2.3 Experimental realization of the optical lattice

2.3.1 Loading of the optical lattice

Experimental aspects of the optical lattice

The Bose-Einstein Condensate produced in the crossed-dipole trap at the end of the evaporative cooling step is finally transferred in a cubic optical lattice (OL). The three retro-reflected laser beams used to form the cubic optical lattice are derived from the same source, a 5 W TiSaph laser [15] at $\lambda_L = 759\,\text{nm}$. This laser is split between three optical paths, each associated with an axis of the lattice $\{x, y, z\}$ (z the vertical axis). In each path, an AOM shifts the frequency of the laser beam by

[15] Titanium-sapphire laser: SolsTiS. M Squared Lasers.

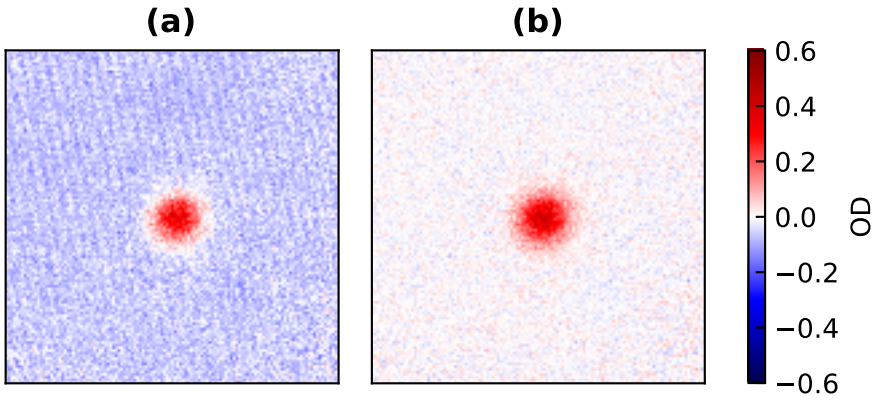

Figure 2.9 – Comparison between the OD computed with the bare reference image I_0 (a) and the OD computed using the best reference algorithm (b). We observe the disappearance of the fringes and of the offset on the OD.

$(\delta_x, \delta_y, \delta_z) = 2\pi \times (80, -80, 110)$ MHz so that any interference between two beams from different arms of the lattice oscillates at very high frequency (tens of MHz) compared to the motion of atoms (at most tens of kHz), and consequently average out to a negligible perturbation. In order to further prevent the apparition of such cross-axis terms, the polarization of the arms of the optical lattice has also been chosen mutually orthogonal. The intensity of the lasers are controlled by a feedback loop.

Moreover, the laser beam are coupled to polarization maintaining optical fibers with polarizing beam splitter at the output in order to select the proper polarization prior to the science chamber. Polarization fluctuations are converted into power fluctuations and compensated by the intensity feedback loop active on each axis. These feedback loops monitor the power on each axis thanks to photodiodes and change accordingly the diffraction efficiency of the AOMs.

We end up with the working parameters for the optical lattice liste in Table 2.10.

Axis	Power (mW)	Waist (μm)	Depth (E_R)	Trap frequency ($2\pi \times$ Hz)
x	400	115	24.0	42
y	400	125	25.6	38
z	600	150	27.0	33

Figure 2.10 – Typical lattice parameters used in our experiment. Here $E_\mathrm{R} = \frac{\hbar^2 k_\mathrm{L}^2}{2m}$ is the recoil energy at λ_L the lattice wavelength. The quoted trap frequencies correspond to the auxiliary potential associated with the gaussian envelope of the laser beams.

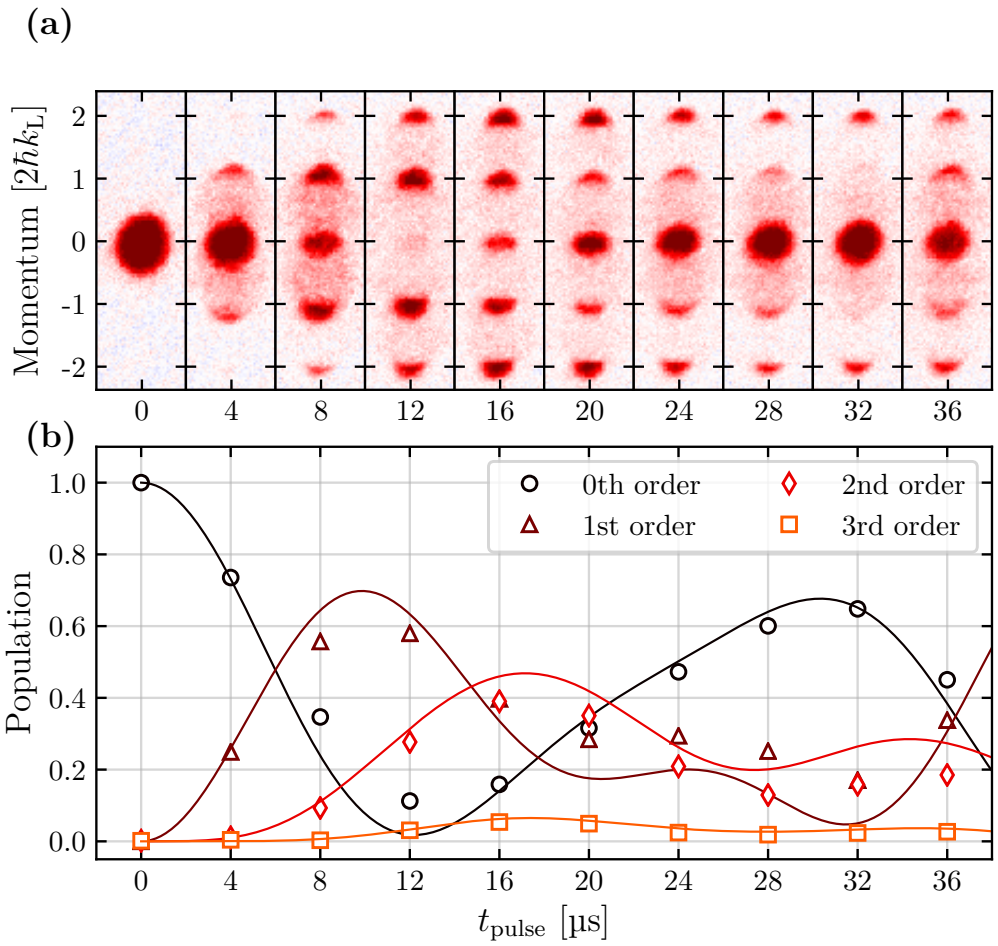

Figure 2.11 – Kapitza Dirac diffraction to calibrate the lattice depth : (a) Absorption images after TOF of the atomic cloud submitted to a lattice pulse of increasing duration. Diffraction peaks appears on the positions associated with integer multiples of the lattice reciprocal vector. (b) The population in each peak is measured and its evolution with respect to the lattice pulse duration is fitted according to the model presented in (2.36).

2.3.2 Optical lattice calibration

To calibrate the lattice depths along each axis, of each lattice axis we use a method known as *Kapitza-Dirac diffraction* (Kapitza et al. 1933; Ovchinnikov et al. 1999). This method consists in pulsing the optical lattice on the BEC for a duration τ and measuring the resulting momentum distribution. In practice we let the atoms fall after the pulse under the action of gravity and observe the resulting pattern. The principle is to diffract the matter wave of the condensate on the standing wave. The initial condensate can be modeled for simplicity as a plane wave with zero momentum $p = 0$. When the lattice is switched on abruptly, this plane wave is projected on the Bloch basis (Denschlag et al. 2002) :

$$|\Psi\,(t=0)\rangle = \sum_{n=0}^{\infty} |\phi_{n,q=0}\rangle\langle\phi_{n,q=0}|p=0\rangle \tag{2.33}$$

During the lattice pulse, the wavepacket evolves as

$$|\Psi(\tau)\rangle = \sum_{n=0}^{\infty} \tilde{u}^*_{n,q=0}(0) \exp\left(-\frac{\mathrm{i}\epsilon_{n,0}\tau}{\hbar}\right) |\phi_{n,q=0}\rangle. \tag{2.34}$$

Here the $\tilde{u}_{n,q}$ are the (Fourier) coefficients of the Bloch function in the plane wave basis

$$u_{n,q} = \sum_{m\in\mathbb{Z}} \tilde{u}_{n,q}(m)\, \mathrm{e}^{2\mathrm{i}mk_L}. \tag{2.35}$$

After the lattice is suddenly switched off, the momentum distribution

$$n(p = 2m\hbar k_{\mathrm{L}}) = \left| \sum_{n=0}^{\infty} \tilde{u}^*_{n,0}(0)\, \tilde{u}_{n,0}(m) \exp\left(-\frac{\mathrm{i}\epsilon_{n,0}\tau}{\hbar}\right) \right|, \quad m \in \mathbb{Z} \tag{2.36}$$

remains constant (if one neglect the role of interactions between the atoms, which is the main limitation of this method). The measured fractions of atoms in each diffraction $n(2m\hbar k_L)$ order oscillate at a rate, function of the lattice depth V_0. We use the this feature of the diffraction pattern to extract the lattice depth. Such measurement is presented in Fig. 2.11.

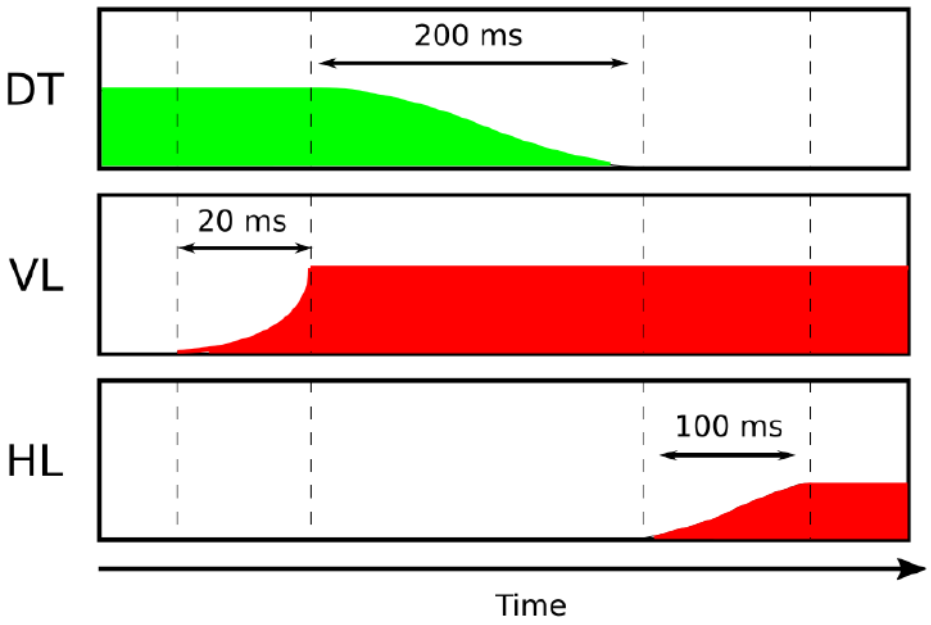

Figure 2.12 – Scheme of the evolution in time of the intensity of the trapping laser, *i.e.* the crossed dipole-trap (DT), the vertical (VL) and the horizontal (HL) axes of the lattice, during the loading sequence.

2.3.3 Optical lattice loading

Loading sequence

The experimental parameters of our optical lattice having been measured or calibrated, we describe the protocol used for the loading of a Bose-Einstein condensate of

^{174}Yb into it. Firstly we raise quickly (20 ms) the vertical axis z of the optical lattice to its maximum depth ($27\,E_R$), slicing the Bose-Einstein condensate in quasi 2D planes. The goal is to compensate the effects of the gravity on the atoms using the lattice alone. The crossed dipole trap is then progressively extinguished in 200 ms. The horizontal arms of the optical lattice are ramped up in 100 ms and the system is finally kept in this configuration for 50 ms before performing any experiment.

Model for the optical lattice loading

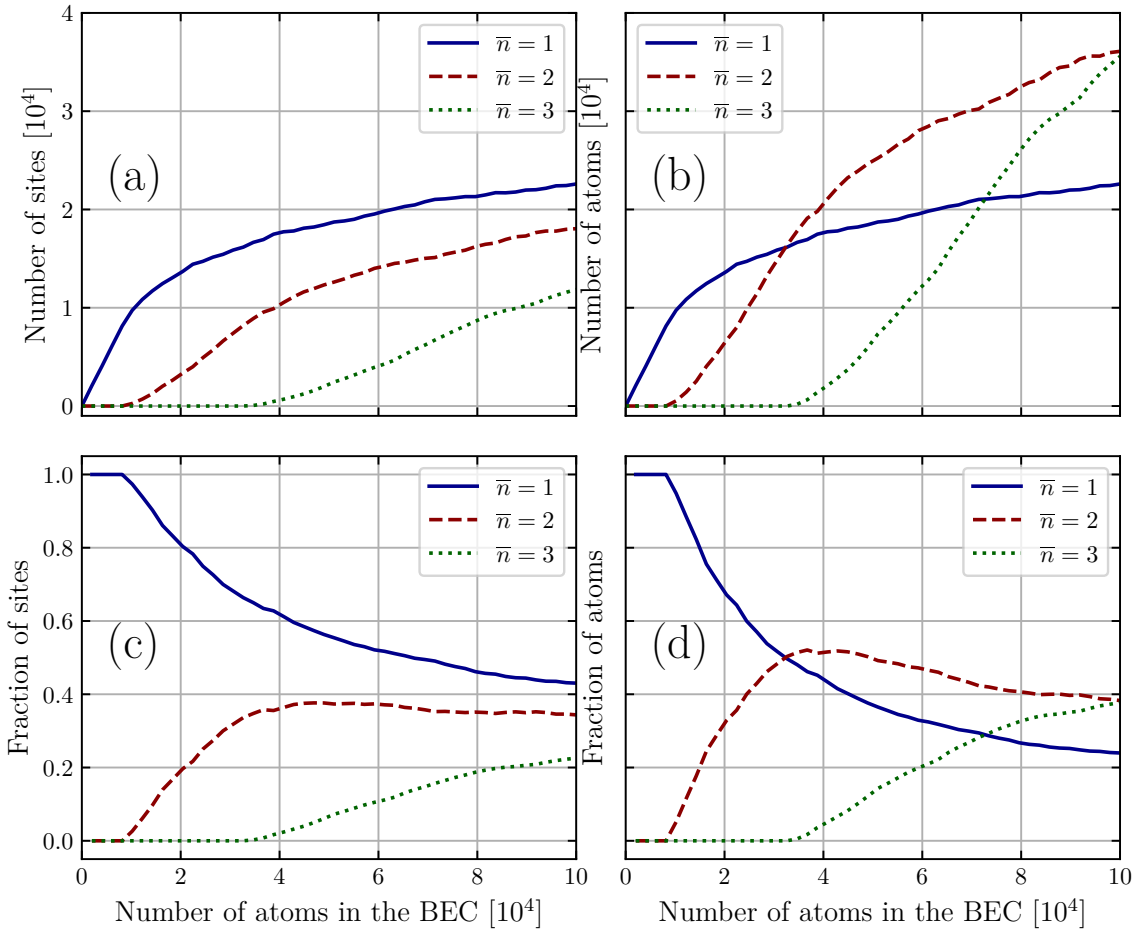

Figure 2.13 – Distribution of atoms among the singly $\overline{n} = 1$, doubly $\overline{n} = 2$ and triply $\overline{n} = 3$ occupied sites for different atoms numbers in the BEC. (a) Number of sites with filling $\overline{n}$. (b) Number of atoms in sites with filling $\overline{n}$. (c) Fraction of sites with filling $\overline{n}$. (d) Fraction of atoms in sites with filling $\overline{n}$. The computations have been performed for the typical depths $V_0 = \{25, 25, 27\}\,E_R$ used in our experimental setup for an optical lattice in the Mott-insulator regime, with the trapping frequencies listed in Table 2.10. The "wiggles" on the curve are a consequence of the fact that the number of lattice sites is a discrete in the calculation.

From the protocol used to load the optical lattice a model to compute numerically the spatial distribution of the atoms over the lattices sites can be inferred. In the model we assume that the spatial density of the Bose-Einstein condensate evaporated in the crossed dipole trap can be described according to the *Thomas-Fermi approximation* (2.24). The BEC occupies a spatial domain that correspond to an ellipsoid whose principal axes have lengths $2R_x$, $2R_y$ and $2R_z$, with R_j the Thomas-Fermi radius defined in (2.22). We also assumes that the fast ramp-up of the vertical lattice "slices" the Bose-Einstein condensate into vertically stacked layers of width $d = \lambda_L/2$, centered on the position $z_j = jd$ corresponding to the minima of the potential. The number of atoms in the layer centered around z_j is given by the relation:

$$N_j = \int_{z_j-d/2}^{z_j+d/2} \int\int n_{\mathrm{TF}}(\mathbf{r})\, \mathrm{d}x\, \mathrm{d}y\, \mathrm{d}z \approx \frac{15 N_{\mathrm{at}} d}{16 R_z} \left[1 - \left(\frac{jd}{R_z}\right)^2\right] \quad \text{for} \quad R_z \gg d. \tag{2.37}$$

In the model we assume the absence of redistribution of atomic populations between the different planes. This assumption is relevant since gravity helps suppress tunneling which otherwise would not be necessarily negligible at all times. As a result redistribution is negligible at all times.

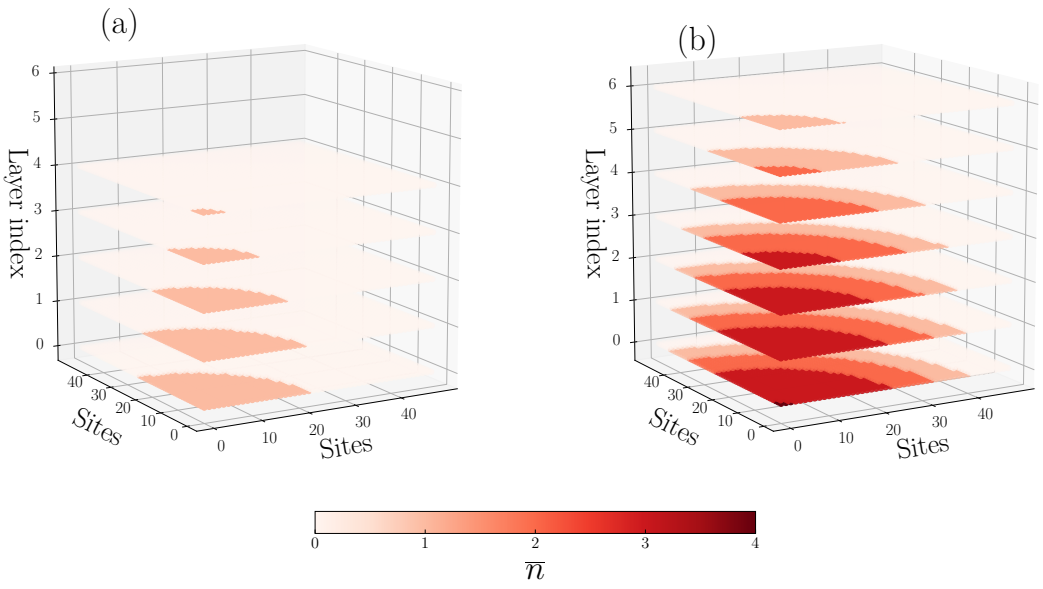

Figure 2.14 – Spatial distribution of the atomic density for deep optical lattices loaded with BEC of (a) 8×10^3 and (b) 8×10^4 atoms, using the parameters in 2.10. Only one quarter of the upper "hemisphere" of the domain populated with atoms is represented.

After the extinction of the crossed-dipole trap, the horizontal axes of the optical lattice are ramped up adiabatically and the atoms in each layer are distributed over the raising 2D horizontal lattice following its ground state. We end up with a vertical stack of

independent 2D quantum gases that can each be described by a 2D Bose-Hubbard model with an additional harmonic confining potential, as discussed in 1.2.4. We consequently combine the local density approximation (see **??**) and the Gutzwiller ansatz to compute the atomic density in each layer, with the population in each layer determined by 2.37.

The model allows us in particular to determine the total amount (Fig. 2.13) as well as the spatial distribution (Fig. 2.14) of singly, doubly and triply occupied sites. For the sake of simplicity we discuss these distribution in the strongly interacting limit $J/U \to 0$ where the atoms are localized around the lattice sites. We present below the spatial distribution computed for systems with $N_{\text{at}} = 8 \times 10^3$ and $N_{\text{at}} = 8 \times 10^4$ atoms.

2.3.4 Superfluid to Mott insulator transition

After the different calibrations of the experimental parameters mentioned above, one can use time of flight imaging to study the superfluid to Mott insulator transition. This phase transition has been observed for the first time in Greiner et al. 2002 after a proposal of Jaksch et al. 1998. The experiment consists in observing the disappearance of interference peaks of the atoms after a time of flight as the lattice depth V_0 is increased.

For long time of flight, the inter atomic interaction do not play a significant role during the expansion (Gerbier et al. 2008). The field operator describing the atoms released from an optical lattice of depth V_0 after a free fall of duration t can be expressed on the Wannier basis (restricted to the fundamental band) as :

$$\hat{\Psi} = \sum_{\mathbf{i}} w\left(\mathbf{r} - \mathbf{r_i}, t\right) \hat{a}_{\mathbf{i}} \approx \left(\frac{m}{\hbar t}\right)^{3/2} \tilde{w}\left(\frac{m\mathbf{r}}{\hbar t}\right) \sum_{\mathbf{i}} \mathrm{e}^{\mathrm{i}\frac{m\mathbf{r}.\mathbf{r_i}}{\hbar t}} \hat{a}_{\mathbf{i}}. \tag{2.38}$$

This asymptotic expression (formally valid in the limit $t \to \infty$) establishes a mapping between the position of atoms in the real space after the time of flight and their initial momentum in the lattice $\mathbf{K}$:

$$\mathbf{K} = \frac{m\mathbf{r}}{\hbar t}. \tag{2.39}$$

This mapping allows us to express the observed atomic density after the time of flight

$$\langle n_{\text{TOF}}\left(\mathbf{K}\right)\rangle \approx \mathcal{G}\left(\mathbf{K}\right)\mathcal{S}\left(\mathbf{K}\right) \tag{2.40}$$

with the Wannier envelope function

$$\mathcal{G}\left(\mathbf{K}\right) = \left(\frac{m}{\hbar t}\right)^3 |\tilde{w}\left(\mathbf{K}\right)|^2 \tag{2.41}$$

and the *structure factor*

$$\mathcal{S}\left(\mathbf{K}\right) = \sum_{\mathbf{i},\mathbf{j}} \mathrm{e}^{\mathrm{i}\mathbf{K}.\left(\mathbf{r_j}-\mathbf{r_i}\right)} \langle \hat{a}_{\mathbf{i}}^{\dagger} \hat{a}_{\mathbf{j}} \rangle \tag{2.42}$$

that determines the fine structure of the interference pattern. Note that $\mathcal{S}\left(\mathbf{K}\right)$ is also the Fourier transform of the first order correlation function $g_1\left(\mathbf{i},\mathbf{j}\right) = \langle \hat{a}_{\mathbf{i}}^{\dagger} \hat{a}_{\mathbf{j}} \rangle$. This expression, analogous to the one for the structure factor found for Bragg diffraction experiments on solids, points out privileged vectors in the reciprocal lattice $\mathbf{K}$. $\left(\mathbf{r_j} - \mathbf{r_i}\right)/2\pi \in$

$\mathbb{Z}$ where the terms of the structure factor add up coherently to form sharp peaks, while the sum vanishes in the others regions of the reciprocal space.

In order to study the transition, it is useful to consider the expression of the structure factor $\mathcal{S}(\mathbf{K})$ for the two limiting case for the Bose-Hubbard model introduced in 1.2.2:

- In the deep superfluid regime ($U/J \to 0$), we have $g_1(\mathbf{i},\mathbf{j}) \approx \overline{n}$ *i.e.* the phase coherence extends over the whole lattice and the structure factor reads:

$$\mathcal{S}_{\mathrm{SF}}(\mathbf{K}) \approx \overline{n} \sum_{\mathbf{i},\mathbf{j}} \mathrm{e}^{\mathrm{i}\mathbf{K}.(\mathbf{r_j}-\mathbf{r_i})}. \tag{2.43}$$

  The distribution pattern is then made of sharp peaks corresponding to the sites of the reciprocal lattice, modulated by the Wannier envelope function $\mathcal{G}$. The Wannier envelope function imposes a cutoff on the sum over the lattice sites in (2.43) too, responsible for the finite width of the peaks.

- In the deep Mott insulator phase ($J/U \to 0$), there is no phase coherence over the lattice and the first order correlation function becomes $g_1(\mathbf{i},\mathbf{j}) \approx n_0 \delta_{\mathbf{ij}}$. The the structure factor reads:

$$\mathcal{S}_{\mathrm{MI}}(\mathbf{K}) \approx N_s n_0 = N. \tag{2.44}$$

  We expect a uniform distribution of atoms, only modulated by the Wannier envelope $\mathcal{G}$.

In the end the disappearance of the Bragg peaks, whose intensity is a signature of the transition from the superfluid to the Mott insulator phase, as it reflects the behavior of the first order correlation function g_1. The results of such experiment are presented in Fig.2.15 . In practice we study the evolution of the visibility defined as (Gerbier et al. 2005)

$$\mathcal{V} = \frac{n_{\mathrm{TOF}}(\mathbf{K}_1) - n_{\mathrm{TOF}}(\mathbf{K}_2)}{n_{\mathrm{TOF}}(\mathbf{K}_1) + n_{\mathrm{TOF}}(\mathbf{K}_2)} \tag{2.45}$$

where $\mathbf{K}_1 = 2k_{\mathrm{L}}\mathbf{e}_x$ is the center of the first order diffraction peak (the center of the second Brillouin zone) and $\mathbf{K}_1 = \sqrt{2}k_{\mathrm{L}}\mathbf{e}_x + \sqrt{2}k_{\mathrm{L}}\mathbf{e}_y$ on the angle bisector between the axes, on the same circle of radius $2k_{\mathrm{L}}$. This non-standard definition of the visibility normalizes away the contribution of Wannier envelope. Finally we have verified that the disappearance of the peaks has been proven to be *reversible*, *i.e.* it is possible to restore the superfluid interference pattern by ramping down the lattice depth from the Mott insulator regime.

Remark: The vanishing of q_1 is a necessary but not sufficient condition for the transition to a Mott-insulator. Indeed the emergence of a uniform structure factor similar to (2.44) could be a consequence of a heating of the atomic gas. To discard this possible cause for the vanishing of the interference pattern, we perform experiments consisting is ramping up the lattice into the Mott-insulator regime. Then we ramp the lattice down to the superfluid regime and observe the reappearance of the diffraction peaks. This points out the reversibility of the disappearance of the coherence.

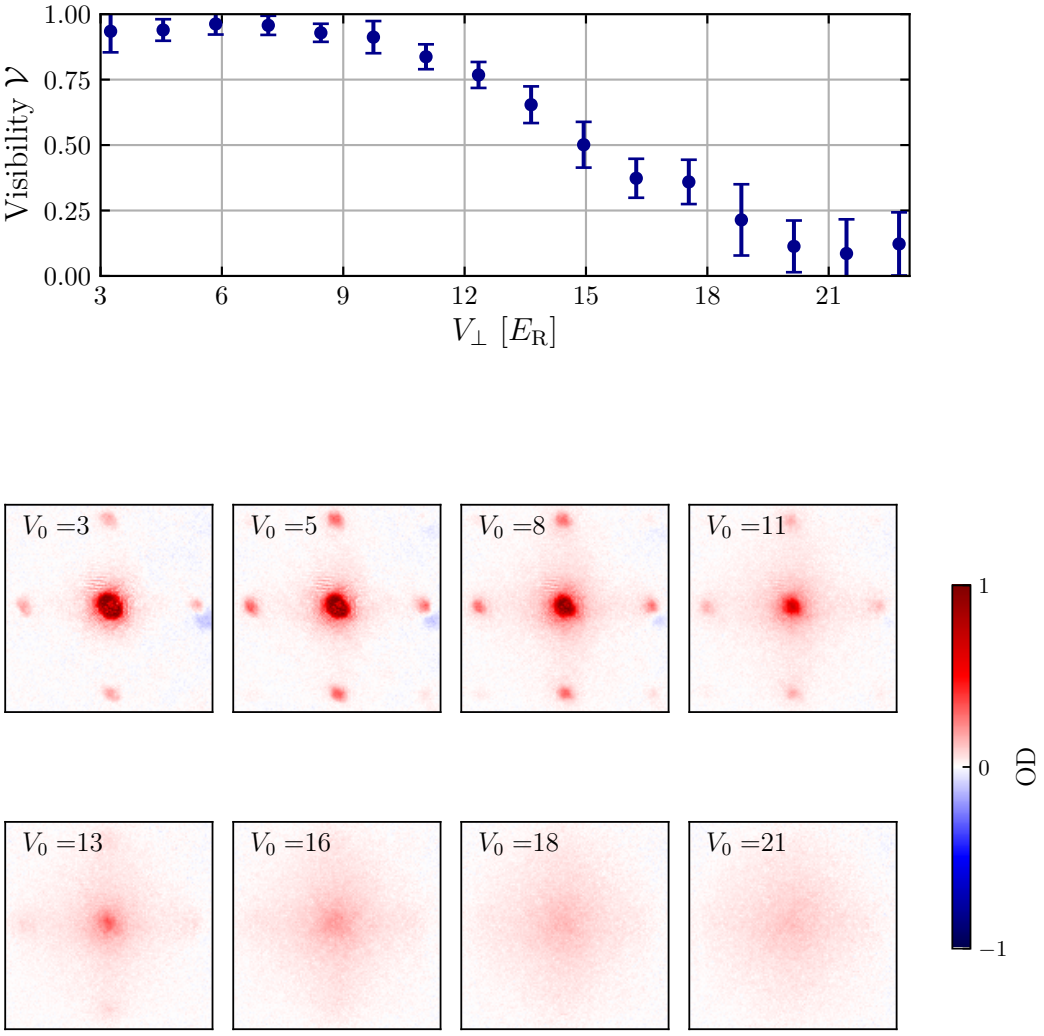

Figure 2.15 – Top: Decay of the visibility of the atomic interference peaks when the lattice depth is increased, as signature of the superfluid to Mott insulator transition. Bottom : Recorded interference peaks for some of the lattice depths.

CHAPTER 3

Coherent driving of the clock transition

This chapter focuses on some technical and experimental aspects involved in the coherent driving of ^{174}Yb atoms on the $^1S_0 \longleftrightarrow {}^3P_0$ transition: after a brief description of the experimental setup used to generate the clock laser that probes the atoms on the clock transition, we introduce a first description for the dynamics of single two-level atoms evolving in a near resonant monochromatic light field. Then we propose to study the driving of individual atoms trapped in isolated sites of our optical lattice using Rabi and Ramsey experiments. The results of the experiments perfomed are presented along with the formalism used to describe them. From these experimental results we finally perform the characterization of effects that could alter the coherent driving of individual atoms trapped on the sites of the optical lattice and, if possible, propose a protocol to reduce their impact.

3.1 The clock laser experimental setup and techniques

We present here the optical setup we use to produce a narrow enough laser source to drive the clock transition. More detail about the setup may be found in the thesis of previous PhD students on the Yb experiment, in particular in Dareau 2015.

3.1.1 Experimental setup

The light at $\lambda_{\text{clock}} \simeq 578\,\text{nm}$ is generated using sum frequency generation (SFG). 5 W of light at 1030 nm, generated by an amplified fiber laser[16], and 200 mW of light at 1319 nm, generated by a Nd:Yag laser[17], are both focused (to about $40\,\mu\text{m}$) inside a non linear crystal[18]. The SFG produces about 65 mW of light at $\lambda_{\text{clock}} \simeq 578\,\text{nm}$ at the output. This light is sent trough a first AOM, used as fast actuator in the frequency locking loop. A part of the beam is sent in an iodine spectroscopy setup, used to calibrate the absolute frequency of the cavity (Dareau 2015). The rest is coupled into an optical fiber to be sent on the experiment table. The outgoing light from this fiber

[16] Koheras BoostiK Y10, NKT Photonics
[17] Mephisto, Coherent
[18] ppLN (periodically poled lithium niobate) crystal from Coherent

is split between a path going to the science chamber *via* another AOM that controls the frequency seen by the atoms, and another path going to the high finesse cavity[19] (Dareau 2015) used for frequency locking. A scheme of the laser optical chain used to produce the light at $\lambda_{\text{clock}} \simeq 578\,\text{nm}$ is displayed in Fig. 3.1.

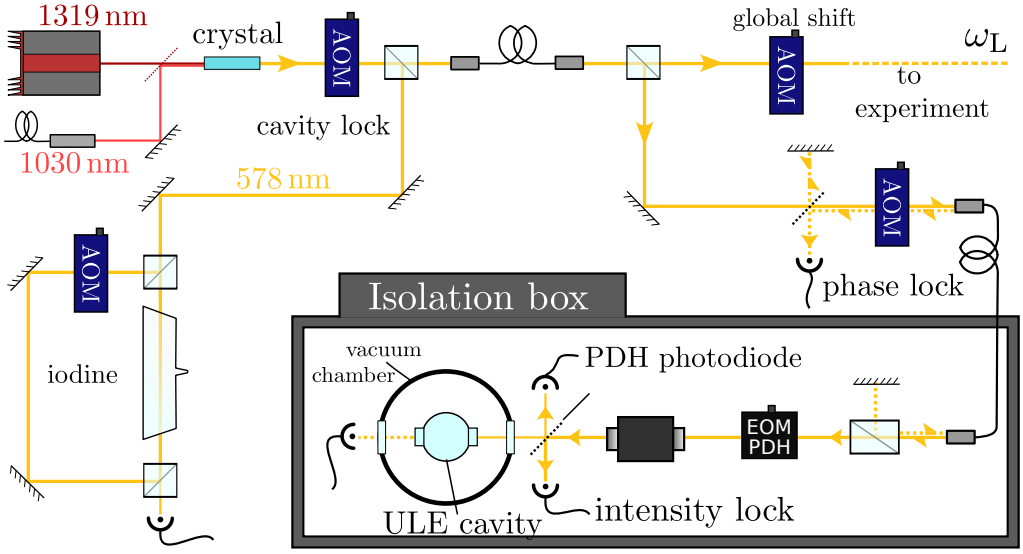

Figure 3.1 – Optical laser chain for the clock laser. The laser light at $\lambda_{\text{clock}} \simeq 578\,\text{nm}$ is generated by frequency sum in the crystal. The outgoing light is split between the iodine spectroscopy setup and a fiber going to the experiment table. The power at the output of the fiber is then again split between two paths: one used to probe the atoms in the science chamber and another sent to the ULE cavity for the frequency lock of the laser. A part of this light is sent back to the experiment table to correct the phase shift that the propagation in the optical fiber may create. Adapted from Dareau 2015.

In addition, a small part of the light sent to the cavity platform is retro-reflected to the experiment table where it is used as the second arm of a Michelson interferometer in order to perform a phase lock. The aim here is to correct the phase changes occurring in the fiber between the experiment table and the cavity box because of thermal or mechanical perturbations.

The *ultra-low expansion* (ULE) cavity consists in a plano-concave Fabry-Perot cavity made of two high-reflectivity mirrors separated of 47.6 cm by a spherical ULE glass body. The finesse of the cavity $\mathcal{F} \simeq 257000$ and the free spectral range $\Delta_{\text{FSR}} \simeq 2\pi \times 3144366(2)\,\text{kHz}$ have been measured in Dareau 2015. Both are in good agreement with the specifications. The full width at half-maximum for the cavity resonances is then $\delta\omega_{\text{cav}} = \Delta_{\text{FSR}}/\mathcal{F} \simeq 2\pi \times 12\,\text{kHz}$.

ULE cavity temperature control

The ULE cavity is mounted inside a thermal shield whose temperature is regulated thanks to a Peltier cooler associated with a feedback loop. This device allows us to set the temperature of the ULE cavity around the zero crossing temperature $T_{\text{ZC}} = 4.13(2)\,°\text{C}$, experimentally measured in Bouganne 2018 and Bosch Aguilera 2019, where

[19] ATF-6301, Advanced Thin Films

the thermal expansion coefficient of the cavity vanishes (see Fig. 3.2). At this *zero-crossing point*, the cavity length, and consequently its frequency, is the least sensitive to the temperature fluctuations. In our experimental setup, if the set point of the regulated temperature of the cavity falls withing one standard deviation away from the estimate of the zero-crossing temperature (shaded region in Fig. 3.2), the thermal fluctuation translates into frequency fluctuations whose r.m.s. is smaller than 15 Hz (Bosch Aguilera 2019).

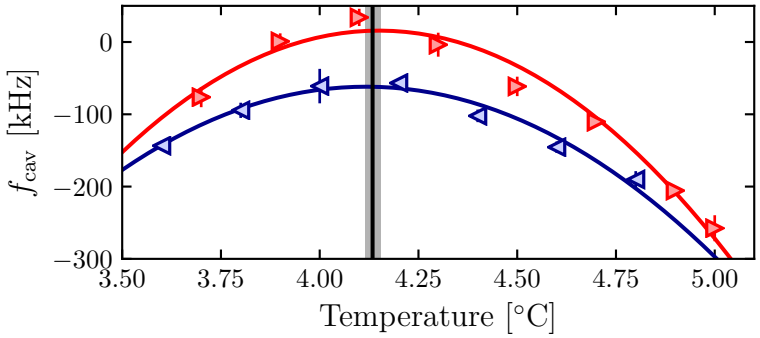

Figure 3.2 – Determination of the zero-crossing point of the cavity. The red curve has been taken by increasing the temperature while the blue curve has been taken by decreasing it. The vertical line corresponds to the zero-crossing temperature, $T_0 = 4.13(2)\,°C$. The shaded region around it indicates one standard deviation. (Taken from Bosch Aguilera 2019)

In order to decouple the ULE cavity from the laboratory environment and reduce the acoustic and thermal noise, it is placed inside a ultra-high vacuum chamber[20] where a pressure on the order of 1×10^{-8} mbar is established. The chamber is mounted on a vibration isolation platform[21]. The platform sits inside a wooden box, itself placed inside a soundproof box[22]. The temperature inside the wooden box is stabilized thanks to a chill plate cooled by circulating water from a thermo-regulated chiller[23]. However, in spite of all these precautions, the atmospheric conditions (temperature and pressure) in the laboratory still have a small but measurable influence on the cavity frequency, on the order of a dozen of Hz. Furthermore a slow linear drift (about −2.3 kHz/day) of the resonance frequency has been observed over the past 4 years and is imputed to the aging of the ULE cavity (see Fig. 3.3). The combination of this slow drift and the environment-related fluctuations, sometimes at the scale of the day, require us to perform several spectroscopy measurements of the clock transition of ^{174}Yb atoms per day in order to keep the probe laser resonant with the $^1S_0 \rightarrow {}^3P_0$ transition.

Cavity frequency lock

The frequency of the cavity is locked thanks to the Pound-Drever-Hall (PHD) technique (Drever et al. 1983). This technique consists in measuring the light intensity reflected from the cavity: the reflected field is the result of the coherent superposition of the

[20] Stable Laser Systems.
[21] Nano-K 50 BM-10, Minus K Technology.
[22] Custom-made, Keoda.
[23] ThermoCube, SSCS.

field directly reflected by the entrance mirror and the intra-cavity field leaking trough this mirror, that vanishes on resonance. Using the reflected field for frequency locks on a high finesse cavity allows a fast response to frequency variations. By contrast the intra-cavity field response is limited by the time taken by the constructive interference to build up in the cavity (*i.e.* the inverse of the cavity linewidth). The incoming beam is modulated by an Electro-Optic Modulator (EOM) prior to its entrance in the cavity. The EOM generates sidebands at $\Omega_{\mathrm{sb}} = 2\pi \times 4\,\mathrm{MHz}$, which is much larger than the cavity bandwidth $\Omega_{\mathrm{sb}} \ll \delta_{\mathrm{cav}}$, so that the sidebands are completely reflected. A fast photodiode[24] measures the reflection from the cavity and the beatnote between the sidebands and the reflected carrier is demodulated with a commercial laser servo controller [25] to generate the error signal used to lock the cavity, with a slope of 1 mV/Hz. The output of the servo controller is sent on a frequency synthesizer that drives the first AOM after the non linear crystal in order to correct the fast fluctuations. The slow fluctuations and the long-term drifts of the laser frequency are corrected by using a doubly-integrated output of the servo controller to drive the 1319 nm laser piezoelectric actuator.

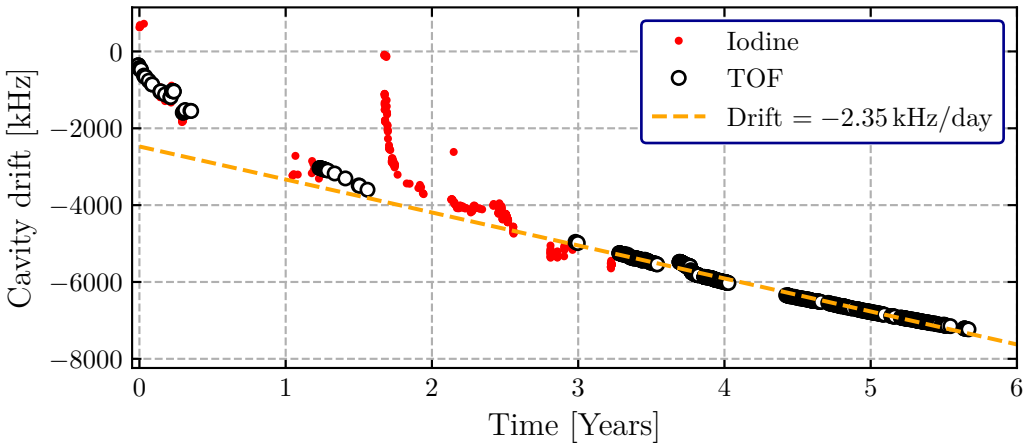

Figure 3.3 – Drift of the ULE cavity with respect to the $^1\mathrm{S}_0 \rightarrow {}^3\mathrm{P}_0$ of ^{174}Yb over the years. The black hollow dots correspond to measurement of the resonance for atoms in free space. The red dots correspond to measurements realized with the iodine spectroscopy setup. The dashed orange line is a linear fit to the data over the last 3 years. It gives a slow drift rate of the resonance frequency of −2.35 kHz/day. (Taken from Bosch Aguilera 2019)

3.1.2 Imaging the metastable state

As explained in Chap. 2 the experimental system is mainly studied by performing time of flight absorption imaging on the broad and closed $^1\mathrm{S}_0 \rightarrow {}^1\mathrm{P}_1$ blue transition. Consequently in experiments involving a coherent driving of the clock $^1\mathrm{S}_0 \rightarrow {}^3\mathrm{P}_0$ transition, only the atoms in the ground state $|{}^1\mathrm{S}_0\rangle \equiv |g\rangle$ can be directly imaged. Atoms in the metastable state $|{}^3\mathrm{P}_0\rangle \equiv |e\rangle$ are repumped to the ground state $|{}^1\mathrm{S}_0\rangle$ to be imaged on the blue transition. The repumping step is realized by the use of the $^3\mathrm{P}_0 \rightarrow 4f^{14}5d6s\ {}^3\mathrm{D}_1$ transition at $\lambda_{\mathrm{rep.}} \simeq 1388.8\,\mathrm{nm}$ with width $\Gamma_{\mathrm{rep.}} \simeq 2\pi \times 419\,\mathrm{kHz}$

[24] PDA8A, Thorlabs
[25] D2-125, Vescent Photonics

(Bowers et al. 1996). Due to the finite lifetime, $\tau_{\text{rep.}} \simeq 380\,\text{ns}$, of the $^3\text{D}_1$ state, the atoms in this state decay to the $^3\text{P}_{J=0,1,2}$ manifold with the branching ratios $\{b_J = \gamma_J/\Gamma_{\text{rep.}}\}_{J=0,1,2} = \{0.6, 0.3, 0.1\}$. The $^3\text{P}_0$ and $^3\text{P}_2$ states are metastable and thus the decay channel toward $^3\text{P}_2$ is a dead end for the repumping cycle. On the contrary, the atoms decaying in $^3\text{P}_1$ decay through spontaneous emission to the ground state $^1\text{S}_0$ with a rate Γ_g. Since the branching ratio to $^3\text{P}_2$ is small, it is possible to repump atoms in $^3\text{P}_0$ to $^1\text{S}_0$ with an efficiency Υ close to 1 by performing several cycles on the $^3\text{P}_0 \rightarrow {}^3\text{D}_1$ transition (see Fig. 3.4).

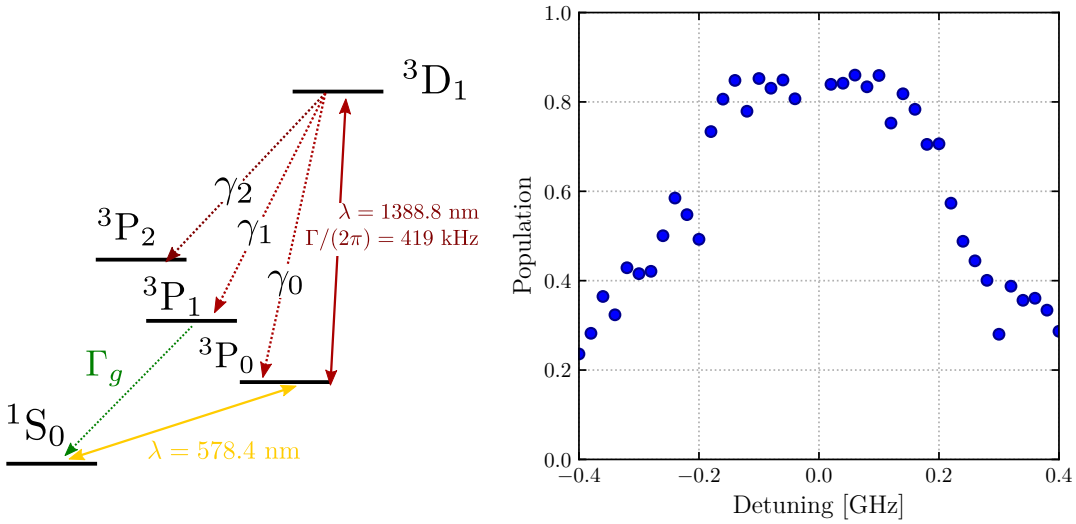

Figure 3.4 – **(Left):** Scheme of the energy levels involved in the repumping of the metastable state. **(Right):** Spectrum of the repumper transition performed with $P = 5\,\text{mW}$, $w_0 = 500\,\mu\text{m}$, and $t_{\text{rep}} = 500\,\mu\text{s}$.

In practice, the repumping $^3\text{P}_0 \rightarrow {}^3\text{D}_1$ is driven by a commercial laser diode[26] generating 20 mW of light at $\lambda_{\text{rep.}} = 1389\,\text{nm}$. The repumping procedure consists in illuminating the atoms with a 5 mW collimated beam of about $500\,\mu\text{m}$ waist for $500\,\mu\text{s}$. It has been shown, theoretically (Bosch Aguilera 2019), by solving the optical Bloch equation associated with this system, that this configuration allows an efficient repumping of the atoms in the $^3\text{P}_0$ state over a frequency span of about 1 GHz, with an efficiency of about $\Upsilon = 0.86$. This value is consistent with the one experimentally measured when performing a spectrum of the repumping transition, as in Fig. 3.4. More details on the pratical implementation of the repumper optical setup can be found in the thesis of Bosch Aguilera 2019, in particular concerning the temperature control of the laser diode.

Remark: If one wants to image the atoms in $|e\rangle$ only, the atoms in $|g\rangle$ have to be removed prior to the reumping pulse. This can be made by sending a pulse of blue light focused at $40\,\mu\text{m}$ for a few μs that expels the atoms from the trap.

[26] NEL Laser Diode, NTT Electronics.

3.2 Coherent driving of a single atom in optical lattices

In this section, some theoretical aspects of the coherent driving of a single atom trapped in an optical lattice on a narrow transition are reminded.

3.2.1 Description of the resonant atom-light interaction

In the rest of this section we will consider the coherent driving of a single ^{174}Yb atom trapped in an optical lattice by a monochromatic electric field, nearly resonant with the $^1\mathrm{S}_0 \rightarrow {}^3\mathrm{P}_0$ transition, that we will assimilate to a plane wave:

$$\mathbf{E}_{\text{clock}}\left(\hat{\mathbf{r}}\right) = \mathbf{E}_0 \cos\left(\mathbf{k}_{\text{clock}}.\hat{\mathbf{r}} - \omega_{\text{L}} t - \phi\right). \tag{3.1}$$

Here ω_{L} is the angular frequency of the coupling laser field, $\mathbf{k}_{\text{clock}}$ its wave number and $\mathbf{E}_0$ its amplitude. ϕ is a phase determined by the choice of time origin.

The Hamiltonian describing the coupling between an atom trapped in the optical lattice and the electric field (3.1) writes:

$$\hat{V}_{\text{AL}} = \langle e| -\mathbf{d}.\mathbf{E}_0 |g\rangle \int \mathrm{d}\mathbf{r} \left(\hat{\Psi}_e^\dagger\left(\mathbf{r}\right)\hat{\Psi}_g\left(\mathbf{r}\right) + \hat{\Psi}_g^\dagger\left(\mathbf{r}\right)\hat{\Psi}_e\left(\mathbf{r}\right)\right)\cos\left(\mathbf{k}_{\text{clock}}.\hat{\mathbf{r}} - \omega_{\text{L}} t - \phi\right). \tag{3.2}$$

Here $\mathbf{d}$ is the atomic dipole matrix element coupling the $|g\rangle$ state with the $|e\rangle$ state, that we assume to be real, since in practice we will only deal with linear polarization for the coupling light. The matrix element $\langle e| - \mathbf{d}.\mathbf{E}_0 |g\rangle$ is the Rabi frequency Ω_{clock}. $\hat{\Psi}_g\left(\hat{\mathbf{r}}\right)$ (resp. $\hat{\Psi}_e\left(\hat{\mathbf{r}}\right)$) is the field operator annihilating a boson in state $|g\rangle$ (resp. $|e\rangle$) at position $\hat{\mathbf{r}}$, in the optical lattice.

In order to ease the description of the system we perform a change of representation by applying the unitary transformation $\hat{T}$ on the system defined by:

$$\hat{T} = \mathrm{e}^{-\mathrm{i}\frac{\omega_{\text{L}} t}{2}\hat{\sigma}_z}, \tag{3.3}$$

with $\hat{\sigma}_z$ the Pauli matrix, acting on the internal state of the atom. In the new representation, the Hamiltonian associated with the atom-light coupling writes:

$$\hat{\tilde{V}}_{\text{AL}} = \hat{T}^\dagger \hat{V}_{\text{AL}} \hat{T} + \mathrm{i}\hbar \frac{\mathrm{d}\hat{T}^\dagger}{\mathrm{d}t}\hat{T}. \tag{3.4}$$

Then using the Rotating Wave Approximation, the first term of the expression (3.4) can be simplified in:

$$\hat{V}_{\text{AL}} = \frac{\hbar\Omega_{\text{clock}}}{2} \int \mathrm{d}\mathbf{r} \left(\hat{\Psi}_e^\dagger\left(\mathbf{r}\right)\hat{\Psi}_g\left(\mathbf{r}\right)\mathrm{e}^{\mathrm{i}(\mathbf{k}_{\text{clock}}.\hat{\mathbf{r}} - \phi)} + \hat{\Psi}_g^\dagger\left(\mathbf{r}\right)\hat{\Psi}_e\left(\mathbf{r}\right)\mathrm{e}^{-\mathrm{i}(\mathbf{k}_{\text{clock}}.\hat{\mathbf{r}} - \phi)}\right). \tag{3.5}$$

Here we dropped the $\tilde{.}$ for the operators in the rotating representation in order to lighten the notations. The second term of the expression (3.4) is diagonal and therefore leave the internal state of the atom unchanged. It is usually associated with the internal energy term of the Hamiltonian to form the term:

$$\hat{H}_0 = \frac{\hbar\delta_{\text{L}}}{2} \int \mathrm{d}\mathbf{r} \left(\hat{\Psi}_g^\dagger\left(\mathbf{r}\right)\hat{\Psi}_g\left(\mathbf{r}\right) - \hat{\Psi}_e^\dagger\left(\mathbf{r}\right)\hat{\Psi}_e\left(\mathbf{r}\right)\right). \tag{3.6}$$

3.2.2 "Conservation" of the quasi-momentum

The difference between the description of our system made in the previous section and the textbook case of a two-level atom interacting with a near resonant light field comes from the fact that for atoms trapped in an optical lattice, the band structure described in 1.1.1 quantizes the external degree of freedom of the driven atom. The interplay between the coherent driving of the internal state of the atom in the optical lattice and its external degree of freedom has to be taken into account.

As seen in 1.1.1, the Bloch functions are the eigenstates of the Hamiltonian describing the evolution of a particle in an homogeneous optical lattice. It is then possible to decompose the field operators $\hat{\Psi}_\sigma$ (with $\sigma \in \{g, e\}$) according to this basis:

$$\hat{\Psi}_\sigma(\mathbf{r}) = \frac{1}{L^{3/2}} \sum_{\mathbf{n},\mathbf{q}} u_{\mathbf{n},\mathbf{q}}(\mathbf{r})\, \mathrm{e}^{\mathrm{i}\mathbf{q}\mathbf{r}} \hat{c}_{\mathbf{n}\,\mathbf{q}\,\sigma}. \tag{3.7}$$

Here L is the number of lattice sites in each direction, $u_{\mathbf{n},\mathbf{q}}(\mathbf{r})$ the Bloch functions and $\hat{c}_{\mathbf{n}\,\mathbf{q}\,\sigma}$ the operator annihilating a boson in band $\mathbf{n}$ with quasi-momentum $\mathbf{q}$ and internal state σ.

Using this decomposition, the atom-light coupling Hamiltonian written in (3.5) becomes:

$$\hat{V}_{\mathrm{AL}} = \frac{\hbar\Omega_{\mathrm{clock}}}{2L^3} \sum_{\mathbf{n},\mathbf{m},\mathbf{q},\mathbf{q}'} \int \mathrm{d}\mathbf{r} \left[u^*_{\mathbf{n}\,\mathbf{q}} u_{\mathbf{m}\,\mathbf{q}'} \mathrm{e}^{-\mathrm{i}\mathbf{q}\mathbf{r}} \mathrm{e}^{\mathrm{i}\mathbf{k}_{\mathrm{clock}}\mathbf{r}} \mathrm{e}^{\mathrm{i}\mathbf{q}'\mathbf{r}} \hat{c}^\dagger_{\mathbf{n}\,\mathbf{q}\,e} \hat{c}_{\mathbf{m}\,\mathbf{q}'\,g} + \mathrm{h.c.} \right], \tag{3.8}$$

setting $\phi = 0$.

The spatial integral $\int \mathrm{d}\mathbf{r}$ over the whole lattice can be decomposed as a (discrete) sum of the contribution of each cell around each lattice site, *i.e.*:

$$\int ...\mathrm{d}\mathbf{r} = \sum_{\mathbf{r}_i} \int_{\mathrm{LC}_i} ...\mathrm{d}\mathbf{r} = \sum_{\mathbf{r}_i} \int_{\mathrm{LC}} ...\mathrm{d}\mathbf{r}, \tag{3.9}$$

with $\mathbf{r}_i$ the position of the lattice site, indexed by i and LC_i the lattice cell centered on $\mathbf{r}_i$, defined for a lattice of spacing d by:

$$\mathrm{LC}_i = \prod_{\alpha=x,y,z} \left[r_{i,\alpha} - \frac{d}{2},\, r_{i,\alpha} + \frac{d}{2} \right], \tag{3.10}$$

denoting $r_{i,\alpha}$ the coordinates of $\mathbf{r}_i$. The dependence with i can actually be dropped thanks to the periodic nature of the lattice.

With this decomposition, we rewrite $\hat{V}_{\mathrm{AL}}$ as:

$$\hat{V}_{\mathrm{AL}} = \frac{\hbar\Omega_{\mathrm{clock}}}{2L^3} \sum_{\mathbf{r}_i} \mathrm{e}^{\mathrm{i}(\mathbf{q}'+\mathbf{k}_{\mathrm{clock}}-\mathbf{q}).\mathbf{r}_i} \int_{\mathrm{LC}} \mathrm{d}\mathbf{r}\, u^*_{\mathbf{n},\mathbf{q}}(\mathbf{r})\, \mathrm{e}^{\mathrm{i}(\mathbf{q}'+\mathbf{k}_{\mathrm{clock}}-\mathbf{q}).\mathbf{r}} u_{\mathbf{m},\mathbf{q}'}(\mathbf{r})\, \hat{c}^\dagger_{\mathbf{n}\,\mathbf{q}\,e} \hat{c}_{\mathbf{m}\,\mathbf{q}'\,g} + \mathrm{h.c.} \tag{3.11}$$

The sum on the lattice sites can be reformulated as a sum on the vectors $\mathbf{G}$ of the reciprocal lattice RL (Ashcroft et al. 1976), *i.e.* the vectors of the from $\mathbf{G} = \frac{2\pi}{d}\mathbf{p}$ with

$\mathbf{p} \in \mathbb{Z}^3$.

$$\hat{V}_{\mathrm{AL}} = \frac{\hbar\Omega_{\mathrm{clock}}}{2} \sum_{\mathbf{G}\in\mathrm{RL}} \delta_{\mathbf{q},\,\mathbf{q}'+\mathbf{k}_{\mathrm{clock}}+\mathbf{G}} \int_{\mathrm{LC}} \mathrm{d}\mathbf{r}\, u^*_{\mathbf{n},\,\mathbf{q}}(\mathbf{r})\, \mathrm{e}^{\mathrm{i}\mathbf{G}.\mathbf{r}} u_{\mathbf{m},\,\mathbf{q}'}(\mathbf{r})\, \hat{c}^\dagger_{\mathbf{n}\,\mathbf{q}\,e} \hat{c}_{\mathbf{m}\,\mathbf{q}'\,g} + \mathrm{h.c.} \quad (3.12)$$

The expression (3.12) translates the fact that the absorption of a photon from the clock laser by an atom evolving in the optical lattice, besides changing its internal state, changes its quasi-momentum and can induce transition to other Bloch bands. The strength of these transitions, mediated by the lattice, are given by the integral term of (3.12), under the constraint given by the Kronecker term:

$$\mathbf{q} = \mathbf{q}' + \mathbf{k}_{\mathrm{clock}} + \mathbf{G}. \quad (3.13)$$

The equation (3.13) stresses the conservation of the quasi-momentum up to a vector of the reciprocal lattice. This kind of transition is known in the field of condensed matter as *Umklapp* processes and are of importance for the description of the conductivity of crystal at low temperatures (Ashcroft et al. 1976).

3.2.3 Wannier basis formulation

It has been shown experimentally in Bosch Aguilera 2019 that for lattice depths above a few recoils, the transitions inducing a change in the quasi-momentum of the atom are strongly suppressed. In this section we propose some quantitative theoretical results to discuss the single band approximation made in the rest of this chapter.

The coupling Hamiltonian introduced in (3.2) can be computed alternatively: when the lattice depth increases the Wannier basis, introduced in 1.1.2, can be more convenient to span the Hilbert space. In this basis the field operators $\hat{\Psi}_\sigma$ rewrites:

$$\hat{\Psi}_\sigma = \frac{1}{L^{3/2}} \sum_{\mathbf{n},\mathbf{i}} w_{\mathbf{n}}(\mathbf{r} - \mathbf{r}_{\mathbf{i}})\, \hat{a}_{\mathbf{n}\,\mathbf{i}\,\sigma}, \quad (3.14)$$

with $\hat{a}_{\mathbf{n}\,\mathbf{i}\,\sigma}$ the operator annihilating a boson in the Wannier state located around $\mathbf{r}_{\mathbf{i}}$, indexed by $\mathbf{i} \in \mathbb{Z}^3$, in band $\mathbf{n}$ and with internal state σ. Here $w_{\mathbf{n}}(\mathbf{r})$ is the Wannier function in band $\mathbf{n}$ centered around the origin.

Using this decomposition the atom-light coupling Hamiltonian written in (3.5) becomes:

$$\hat{V}_{\mathrm{AL}} = \frac{\hbar\Omega_{\mathrm{clock}}}{2L^3} \sum_{\mathbf{n},\,\mathbf{m},\,\mathbf{i},\,\mathbf{j}} \int \mathrm{d}\mathbf{r} \left[w^*_{\mathbf{n}}(\mathbf{r} - \mathbf{r}_{\mathbf{i}})\, \mathrm{e}^{\mathrm{i}\mathbf{k}_{\mathrm{clock}}.\mathbf{r}} w_{\mathbf{m}}(\mathbf{r} - \mathbf{r}_{\mathbf{j}})\, \hat{a}^\dagger_{\mathbf{n}\,\mathbf{i}\,e} \hat{a}_{\mathbf{m}\,\mathbf{j}\,g} + \mathrm{h.c.} \right]. \quad (3.15)$$

By substituting the variable $\mathbf{r}$ by $\mathbf{r}' = \mathbf{r} - \mathbf{r}_{\mathbf{j}}$ and introducing the vector $\boldsymbol{\delta} = \mathbf{i} - \mathbf{j}$, the expression above becomes:

$$\hat{V}_{\mathrm{AL}} = \frac{\hbar\Omega_{\mathrm{clock}}}{2L^3} \sum_{\mathbf{n},\,\mathbf{m},\,\mathbf{j},\,\delta} \int \mathrm{d}\mathbf{r} \left[w^*_{\mathbf{n}}(\mathbf{r} - d\delta)\, \mathrm{e}^{\mathrm{i}\mathbf{k}_{\mathrm{clock}}.\mathbf{r}} w_{\mathbf{m}}(\mathbf{r})\, \mathrm{e}^{\mathrm{i}\mathbf{k}_{\mathrm{clock}}.\mathbf{r}_{\mathbf{j}}} \hat{a}^\dagger_{\mathbf{n}\,\mathbf{j}+\delta\,e} \hat{a}_{\mathbf{m}\,\mathbf{j}\,g} + \mathrm{h.c.} \right] \quad (3.16)$$

Similarly to what has been done in 1.1.3, it is possible to rewrite the Hamiltonian using the tight-binding approximation: since the Wannier functions decay exponentially from lattice site around their center, it is possible to neglect in $\hat{V}_{\mathrm{AL}}$ the integrals involving the overlap between the Wannier functions associated with different lattice sites, *i.e.* the terms in the sum (3.16) involving $|\delta| \neq 0$. Under this approximation, $\hat{V}_{\mathrm{AL}}$ becomes:

$$\hat{V}_{\mathrm{AL}} \approx \frac{\hbar\Omega_{\mathrm{clock}}}{2} \sum_{\mathbf{n},\mathbf{m},\mathbf{j}} \left[\eta_{\mathbf{n}\,\mathbf{m}} \mathrm{e}^{\mathrm{i}\mathbf{k}_{\mathrm{clock}}\cdot\mathbf{r}_{\mathbf{j}}} \hat{a}^{\dagger}_{\mathbf{n}\,\mathbf{j}\,e} \hat{a}_{\mathbf{m}\,\mathbf{j}\,g} + \mathrm{h.c.} \right], \tag{3.17}$$

introducing the *Lamb-Dicke factor*:

$$\eta_{\mathbf{n},\mathbf{m}} = \int w^{*}_{\mathbf{n}}(\mathbf{r})\, \mathrm{e}^{\mathrm{i}\mathbf{k}_{\mathrm{clock}}\cdot\mathbf{r}} w_{\mathbf{m}}(\mathbf{r})\, \mathrm{d}\mathbf{r}. \tag{3.18}$$

Under the approximations made to express (3.17), the coupling strength between the bands $\mathbf{n}$ and $\mathbf{m}$ is given by:

$$\Omega_{\mathrm{L}}(\mathbf{n},\mathbf{m}) = \eta_{\mathbf{nm}}\Omega_{\mathrm{clock}} \tag{3.19}$$

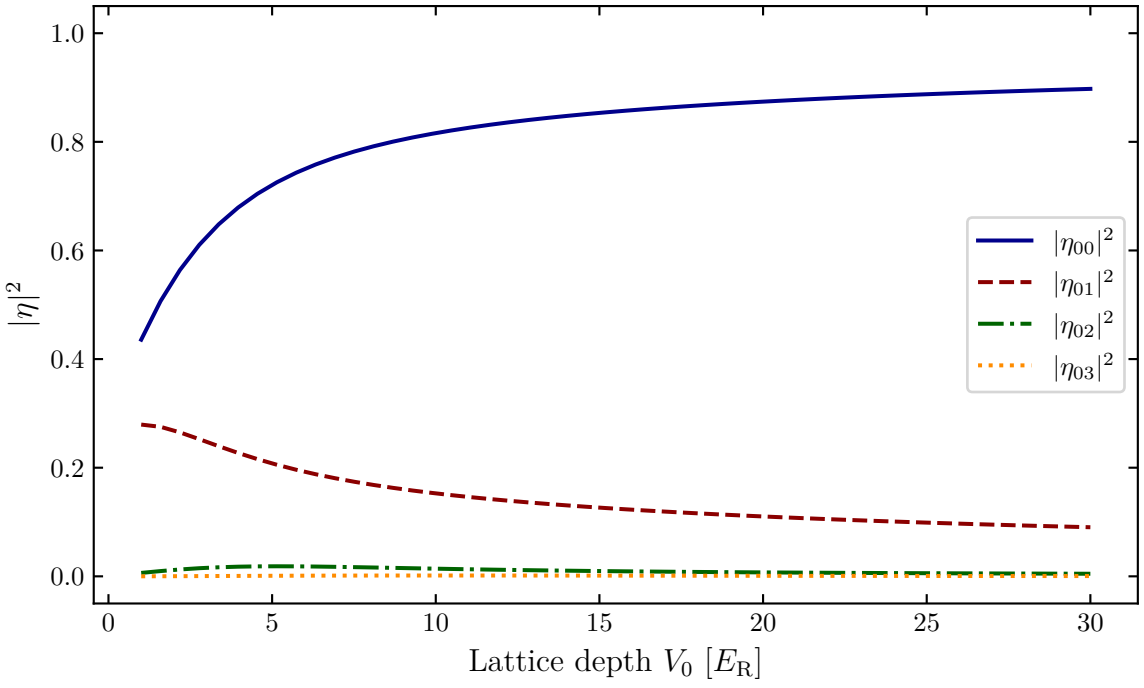

Figure 3.5 – Computation of the modulus square of the Lamb-Dicke factor η_{0n} for $n \in \{0, 1, 2, 3\}$ in a 1D optical lattice. At high lattice depth, the transition probability from the ground band to excited bands is strongly suppressed.

Assuming that the ^{174}Yb are initially loaded in the ground band of the optical lattice, their probability to be send to a higher band of index n due to the absorption of a photon of the clock laser is given by $|\eta_{0n}|^2$. The values of this coefficient for $n \in \{0, 1, 2, 3\}$ and for several lattice depths of a 1D optical lattice are represented in Fig. 3.5. For deep

optical lattices, the transition to higher bands is suppressed. This can be understood by the fact that for deep optical lattice depths, the Wannier functions are strongly localized around the lattice sites. Therefore their decomposition on the plane wave basis is very wide and the translation in the momentum space induced by the term $e^{i\mathbf{k}_{clock}.\mathbf{r}}$ leave the Wannier functions almost unchanged. Since the Wannier functions belongings to different bands are orthogonal, the term $\eta_{\mathbf{nm}} = \langle w_{\mathbf{m}}|e^{i\mathbf{k}_{clock}.\mathbf{r}}|w_{\mathbf{n}}\rangle \approx \langle w_{\mathbf{m}}|w_{\mathbf{n}}\rangle$ becomes small except for the case $\mathbf{n} = \mathbf{m}$. This regime where the lattice is deep enough to suppress the recoil shift of the absorbed photon is called the *Lamb-Dicke regime* (Dicke 1953).

For the lattice depths $V_{x,y,z} = \{25, 25, 27\}E_R$ considered in the rest of this chapter, we will assume that the transition to higher bands due to the clock laser photon absorption is small enough to be neglected and all the dynamics under study is in the scope of the single band approximation. It allows us to reduce the expression of $\hat{V}_{AL}$ to:

$$\hat{V}_{AL} \approx \frac{\hbar\Omega_L}{2} \sum_{\mathbf{r_j}} \left[e^{i\mathbf{k}_{clock}.\mathbf{r_j}} \hat{a}^\dagger_{0\mathbf{j}e} \hat{a}_{0\mathbf{j}g} + \text{h.c.} \right] \quad \text{with} \quad \Omega_L = \eta_{00}\Omega_{clock}. \tag{3.20}$$

In the context of an optical lattice at magic wavelength, the factor $e^{i\mathbf{k}_{clock}.\mathbf{r_j}}$ enables spin-orbit coupling in the dynamics of the atoms. It also at the core of the realization of artificial gauge fields (Dalibard et al. 2011; Goldman et al. 2014) in 2D optical lattice at magic wavelength along one direction and at anti-magic wavelengh along the second one, following the protocol presented in Gerbier et al. 2010.

3.3 Coherent driving of an ensemble of isolated individual atoms trapped in a deep optical lattice.

In this chapter we will focus on the simple case of the coherent driving of individual atoms trapped in an optical lattice deep enough to treat its sites as independent potential wells. Under this assumption, the relative phase between the lattice sites does not play a role anymore and the full Hamiltonian describing the dynamics of these atoms writes:

$$\hat{H} = \sum_{\mathbf{j}} \left[\frac{\hbar\Omega_L}{2} \left(\hat{a}^\dagger_{\mathbf{j}e} \hat{a}_{\mathbf{j}g} e^{-i\phi} + \text{h.c.} \right) - \frac{\hbar\delta_L}{2} \left(\hat{a}^\dagger_{\mathbf{j}e} \hat{a}_{\mathbf{j}e} - \hat{a}^\dagger_{\mathbf{j}g} \hat{a}_{\mathbf{j}g} \right) \right], \tag{3.21}$$

The Hamiltonian (3.21) actually consists in a sum of local Hamiltonians without site coupling. Consequently it is possible to restrict the description of the system to a single lattice site filled with one atom. To sum up, after getting rid of the sum on the lattice sites, in the Lamb-Dicke regime, where the couplings between the fundamental and the excited bands of the optical lattice are negligible, the Hamiltonian describing each single trapped atom coupled to the laser field, assumed to be monochromatic, can be written as:

$$\hat{H} = -\frac{\hbar\delta_L}{2} \left(\hat{\mathbb{1}} - \hat{\sigma}_z \right) + \frac{\hbar\Omega_L}{2} \left(\hat{\sigma}_x \cos\phi + \hat{\sigma}_y \sin\phi \right), \tag{3.22}$$

in the $\{|g\rangle, |e\rangle\}$ basis. Here the $\hat{\sigma}_{x,y,z}$ are the Pauli matrices, $\delta_L = \omega_L - \omega_0$ is the detuning between the laser angular frequency ω_L and the $|g\rangle \longleftrightarrow |e\rangle$ transition angular

frequency ω_0 and Ω_L the Rabi frequency coupling the two internal states of the atom. The phase ϕ is fixed by a choice of the origin of time. The dynamics of such system is described by the Liouville-Von Neumann equation:

$$\mathrm{i}\hbar\frac{\mathrm{d}\hat{\rho}}{\mathrm{d}t} = \left[\hat{H},\, \hat{\rho}\right]. \tag{3.23}$$

Remark: The density operator describing one atom can be decomposed on the $\{\hat{\mathbb{1}},\, \hat{\sigma}_x,\, \hat{\sigma}_y,\, \hat{\sigma}_z\}$ basis as (Haroche et al. 2013) :

$$\hat{\rho} = \frac{1}{2}\left(\hat{\mathbb{1}} + \mathbf{u}.\hat{\sigma}\right) \quad \text{with} \quad \mathbf{u} = (u_x,\, u_y,\, u_z) \quad \text{and} \quad \hat{\sigma} = (\hat{\sigma}_x,\, \hat{\sigma}_y,\, \hat{\sigma}_z)\,. \tag{3.24}$$

The vector $\mathbf{u}$ can thus be used to represent the state of the two-level atom and its modulus is bounded $\|\mathbf{u}\| \leq 1$, with equality only reached for pure states. Consequently in this framework, any pure state can be represented as a point on a sphere of radius 1, the Bloch sphere, whose "north" $(0, 0, 1)$ and "south" $(0, 0, -1)$ poles correspond respectively to the states $|g\rangle$ and $|e\rangle$. The mixed states lies inside the sphere and the evolution of the system is given by the differential equation:

$$\frac{\mathrm{d}\mathbf{u}}{\mathrm{d}t} = \Omega_\mathrm{R}\mathbf{u}_\omega \times \mathbf{u} \tag{3.25}$$

where Ω_R is the generalized Rabi frequency, defined by:

$$\Omega_\mathrm{R}^2 = \Omega_\mathrm{L}^2 + \delta_\mathrm{L}^2, \tag{3.26}$$

and $\mathbf{u}_\omega$ an unitary vector, defined by:

$$\Omega_\mathrm{R}\mathbf{u}_\omega = (\Omega_\mathrm{L}\cos\phi,\, \Omega_\mathrm{L}\sin\phi,\, \delta_\mathrm{L})\,. \tag{3.27}$$

Since the differential equation on $\mathbf{u}$ describing the dynamics of the system is analogous to the Larmor precession equation, the evolution of the system in the Bloch sphere picture can be seen as a rotation of the vector $\mathbf{u}$ around the vector $\mathbf{u}_\omega$ at angular frequency Ω_R. Consequently the propagator associated with the Schrödinger equation describing the evolution of the system can be written as a rotation operator:

$$\hat{U}(t) = \hat{R}_{\mathbf{u}_\omega}(\Omega_\mathrm{R}t) = \mathrm{e}^{-\mathrm{i}(\Omega_\mathrm{R}t/2)\mathbf{u}_\omega.\hat{\sigma}} = \cos\left(\frac{\Omega_\mathrm{R}t}{2}\right)\hat{\mathbb{1}} - \mathrm{i}\sin\left(\frac{\Omega_\mathrm{R}t}{2}\right)\mathbf{u}_\omega.\hat{\sigma}. \tag{3.28}$$

In the rest of this chapter we will consider a deep optical lattice ($V_{x,y,z} = \{25,\, 25,\, 27\}E_\mathrm{R}$), in which a BEC with atom number $N_\mathrm{atoms} < 8 \times 10^3$ atoms is loaded, according to the protocol detailed in 2.3.3, so that the filling of the occupied sites in each of the superposed 2D lattices are all equal to $\overline{n} = 1$. We consequently create a collection of independent (for experiments shorter than the tunneling time) dipole traps, formed by the sites of the optical lattice, each filled with a single atoms in $|g\rangle$ and lying in the fundamental band of the lattice. We use this system to study the evolution of the coherence for a atom driven by our probe laser. For this purpose we perform different type of experiments on our atoms.

3.3.1 Rabi flopping

The Rabi flopping experiment is one of the simplest experiment involving the coherent driving of two-level atoms. It consists in coherently driving the transition $|g\rangle \longleftrightarrow |e\rangle$ for different durations T. Assuming that all the atoms are initially in the state $|g\rangle$, one can derive from (3.28) that the probability $P_g(\delta_{\mathrm{L}}, T)$ to measure an atom in the ground state $|g\rangle$ after a coherent driving of the transition by a monochromatic field detuned from the transition by δ_{L} for a duration T, is given by the relation:

$$P_g(\delta_{\mathrm{L}}, T) = \langle g|\hat{U}(T)|g\rangle = \frac{\Omega_{\mathrm{L}}^2}{\Omega_{\mathrm{L}}^2 + \delta_{\mathrm{L}}^2} \cos^2\left(\frac{\sqrt{\Omega_{\mathrm{L}}^2 + \delta_{\mathrm{L}}^2}}{2} T\right) \tag{3.29}$$

In the Rabi experiments presented in this section, the clock laser driving the atoms propagates in the plane formed by the two horizontal arms of the optical lattice, with an angle $\frac{\pi}{4}$ with respect to them and is centered on the atomic cloud. The measured fractions of atoms in $|g\rangle$ for a Rabi flopping experiment at $\Omega_{\mathrm{L}} = 2\pi \times 1329\,\mathrm{Hz}$ are plotted in Fig.3.11. On may notice that the amplitude of the Rabi oscillations is damped over time. In the rest of this chapter we will investigate the possible causes for such decay.

3.3.2 Time domain Ramsey spectroscopy

An alternative possibility to study the evolution of the coherence during the driving of the atom by our laser is to realize time domain Ramsey spectroscopy Ramsey 1986. This experiment consists in performing a time-domain interference experiment on the atoms: a first pulse of light send the state of the atoms in the equatorial plane of the Bloch sphere with a controlled phase. After a time during which the atoms evolve freely, a second probe pulse is sent on the atoms in order measure the rotation of the Bloch vector in the equatorial plane. This technique originally used in the field of Nuclear Magnetic Resonance (NMR) has since been transposed in different fields involving the coherent driving of a two-level system.

The system is assumed to be initially in the configuration described in 3.3.1 and the experiments are performed at $\Omega_{\mathrm{L}}(0) \simeq 2\pi \times 1300\,\mathrm{Hz}$.

The protocol of a time domain Ramsey spectroscopy can be decomposed as follow:

- A first resonant probe pulse ($\delta = \delta_{\mathrm{L}} - \delta_{\mathrm{E}} = 0$), of area $\Omega_{\mathrm{L}} T_{\frac{\pi}{2}} = \frac{\pi}{2}$, is sent on the atoms. The propagator associated to this step is:

$$\hat{U}_{\frac{\pi}{2}}(0) = \mathrm{e}^{-\mathrm{i}\frac{\pi}{4}\hat{\sigma}_x}. \tag{3.30}$$

- The light is switched off for a duration T_{hold}. The evolution operator for the system is:

$$\hat{U}_{\mathrm{hold}}(T_{\mathrm{hold}}) = \exp\left(-\frac{\mathrm{i}}{2}\int_{T_{\frac{\pi}{2}}}^{T_{\frac{\pi}{2}}+T_{\mathrm{hold}}} \delta(t)\,\mathrm{d}t\,\hat{\sigma}_z\right). \tag{3.31}$$

- A second resonant pulse of duration $T_{\frac{\pi}{2}}$ is sent on the atoms, dephased by ϕ with respect to the first pulse. The propagator for this step is:

$$\hat{U}_{\frac{\pi}{2}}(\phi) = \mathrm{e}^{-\mathrm{i}\frac{\pi}{4}(\hat{\sigma}_x \cos\phi + \hat{\sigma}_y \sin\phi)} \tag{3.32}$$

- Then the lattice and the coupling light are switched off and, after a time of flight of 2 ms, the populations of atoms in the different atomic states are imaged.

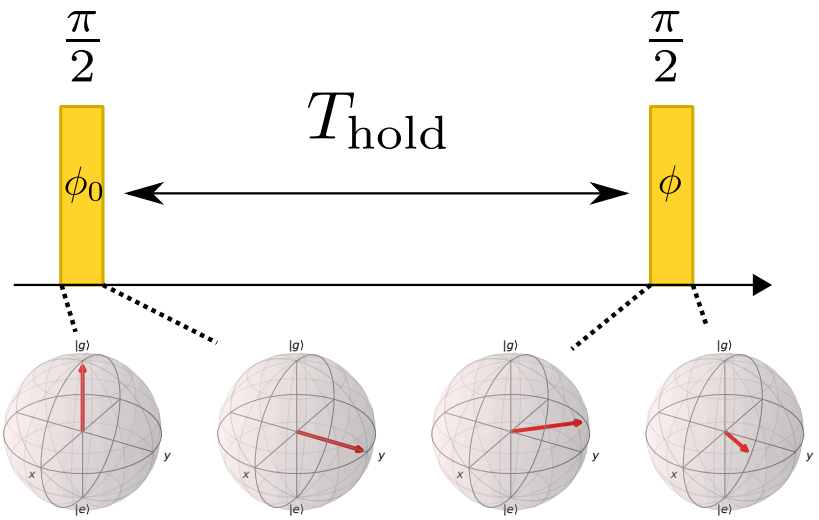

Figure 3.6 – Scheme of a Ramsey sequence. The internal state of the probed two levels is represented in the Bloch sphere picture (red arrow) before and after each laser pulse, here for $\delta_{\mathrm{E}} T_{\mathrm{hold}} = \frac{\pi}{4}$ and $\phi = 0$.

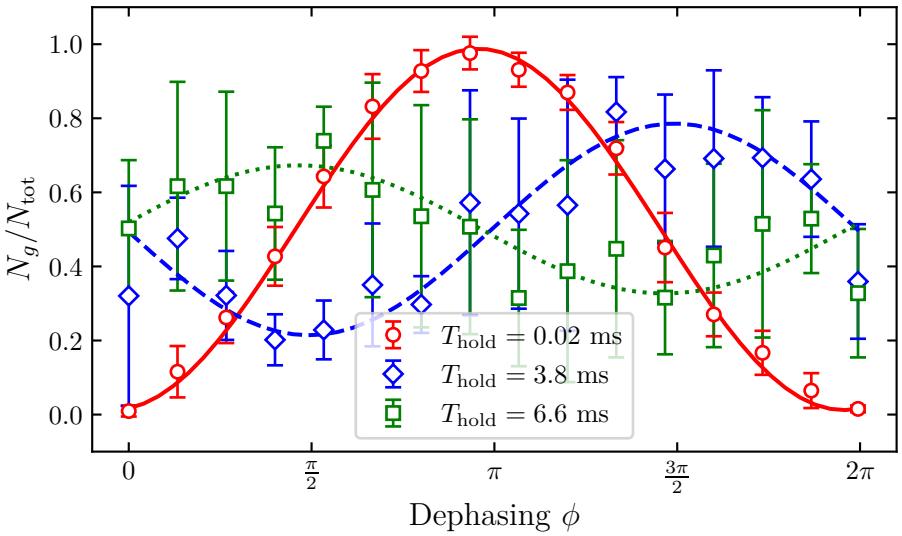

Figure 3.7 – Experimental Ramsey fringes. The fraction of atoms in the $|g\rangle$ state at the end of the Ramsey sequence is measured for different dephasings $\phi \in [0, 2\pi]$. Here the fringes for $T_{\mathrm{hold}} = \{0.02, 3.8, 6.6\}$ ms are represented. The dephasing between these fringes is a consequence of the non zero detuning $\delta_{\mathrm{L}} = \delta_{\mathrm{E}}$ during the hold time, that induces a dephasing of $\delta_{\mathrm{L}} T_{\mathrm{hold}}$.

The evolution operator associated to the whole Ramsey sequence is:

$$\hat{U}_{\mathrm{R}}\left(T_{\mathrm{hold}},\,\phi\right)=\hat{U}_{\frac{\pi}{2}}\left(\phi\right)\hat{U}_{\mathrm{hold}}\left(T_{\mathrm{hold}}\right)\hat{U}_{\frac{\pi}{2}}\left(0\right), \tag{3.33}$$

and the probability to find an atom in $|g\rangle$ at the end of the sequence described above is equal to:

$$P_g\left(T_{\mathrm{hold}},\,\phi\right)=\left|\langle g|\hat{U}_{\mathrm{R}}\left(T_{\mathrm{hold}},\,\phi\right)|g\rangle\right|^2=\sin^2\left(\frac{\phi}{2}-\frac{1}{2}\int_{T_{\frac{\pi}{2}}}^{T_{\frac{\pi}{2}}+T_{\mathrm{hold}}}\delta\left(t\right)\,\mathrm{d}t\right). \tag{3.34}$$

In particular, when the detuning is constant so that $\delta_{\mathrm{L}}=\delta_{\mathrm{E}}$, the previous expression becomes:

$$P_g\left(T_{\mathrm{hold}},\,\phi\right)=\left|\langle g|\hat{U}_{\mathrm{R}}\left(T_{\mathrm{hold}},\,\phi\right)|g\rangle\right|^2=\sin^2\left(\frac{\phi-\delta_{\mathrm{E}}T_{\mathrm{hold}}}{2}\right). \tag{3.35}$$

3.3.3 Time domain Ramsey spectroscopy with spin echo

Another way to probe the evolution of the coherence during the driving of the atoms by our laser source is to use the *spin echo* technique (Hahn 1950) initially applied to the nuclear magnetic resonance (NMR) field. Since this initial demonstration, this technique and its different variations have been widely transposed to other fields. They have been more particularly used in order to enhance the dephasing time for superconducting qubits (Cywiński et al. 2008; Bylander et al. 2011).

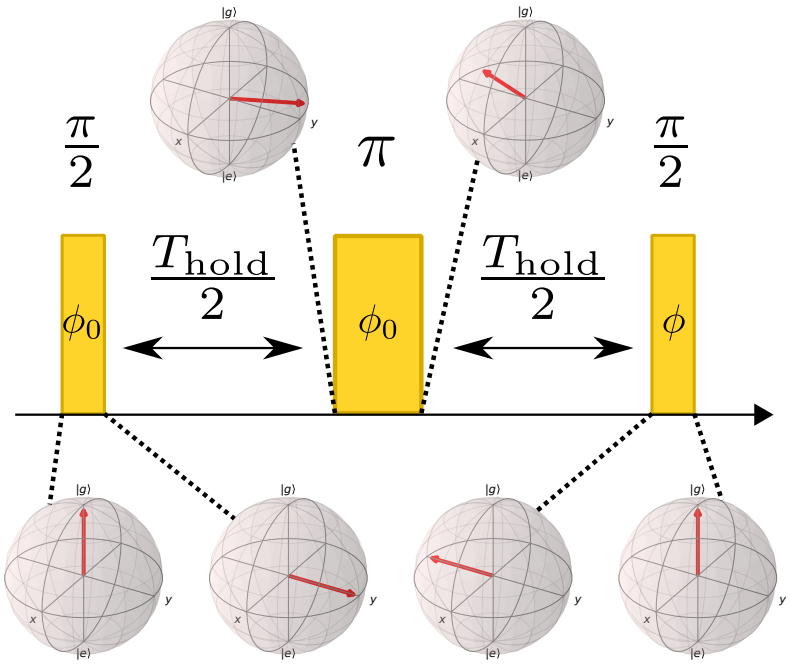

Figure 3.8 – Scheme of a Ramsey with spin echo sequence. The internal state of the probed two levels is represented in the Bloch sphere picture (red arrow) before and after each laser pulse, here for $\delta_{\mathrm{E}}T_{\mathrm{hold}}=\frac{\pi}{4}$ and $\phi=0$. Here the effect of the static dephasing has been canceled by the intermediate π pulse.

The Ramsey with spin echo sequence consists in:

- A first resonant probe pulse of duration $\Omega_{\mathrm{L}} T_{\frac{\pi}{2}} = \frac{\pi}{2}$, is sent on the atoms. The propagator associated to this step is:

$$\hat{U}_{\frac{\pi}{2}}(0) = \mathrm{e}^{-\mathrm{i}\frac{\pi}{4}\hat{\sigma}_x} \tag{3.36}$$

- The light is switched off for a duration $T_{\mathrm{hold}}/2$. The evolution operator for the system is:

$$\hat{U}_{\mathrm{hold}}\left(\frac{T_{\mathrm{hold}}}{2}\right) = \exp\left(-\frac{\mathrm{i}}{2}\int_{T_{\frac{\pi}{2}}}^{T_{\frac{\pi}{2}}+T_{\mathrm{hold}}/2} \delta(t)\ \mathrm{d}t\,\hat{\sigma}_z\right) \tag{3.37}$$

- A resonant probe pulse of duration $\Omega_{\mathrm{L}} T_{\pi} = \pi$, is sent on the atoms. The propagator associated to this step is:

$$\hat{U}_{\pi}(0) = \mathrm{e}^{-\mathrm{i}\frac{\pi}{2}\hat{\sigma}_x} = -\mathrm{i}\hat{\sigma}_x \tag{3.38}$$

- The light is switched off for a duration $T_{\mathrm{hold}}/2$. The evolution operator for the system is:

$$\hat{U}_{\mathrm{hold}}\left(\frac{T_{\mathrm{hold}}}{2}\right) = \exp\left(-\frac{\mathrm{i}}{2}\int_{T_{\frac{\pi}{2}}+T_{\pi}+T_{\mathrm{hold}}/2}^{T_{\frac{\pi}{2}}+T_{\pi}+T_{\mathrm{hold}}} \delta(t)\,\mathrm{d}t\,\hat{\sigma}_z\right) \tag{3.39}$$

- A second resonant pulse of duration $T_{\frac{\pi}{2}}$ is sent on the atoms, dephased of ϕ with respect to the first pulse. The propagator for this step is:

$$\hat{U}_{\frac{\pi}{2}}(\phi) = \mathrm{e}^{-\mathrm{i}\frac{\pi}{4}(\hat{\sigma}_x\cos\phi+\hat{\sigma}_y\sin\phi)} \tag{3.40}$$

- Then the lattice and the coupling light are switched off and, after a time of flight of 2 ms, the populations of atoms in the different atomic states are imaged.

The evolution operator associated to the whole Ramsey with spin echo sequence is:

$$\hat{U}_{\mathrm{SE}}(T_{\mathrm{hold}}) = \hat{U}_{\frac{\pi}{2}}(\phi)\,\hat{U}_{\mathrm{hold}}\left(\frac{T_{\mathrm{hold}}}{2}\right)\hat{U}_{\pi}(0)\,\hat{U}_{\mathrm{hold}}\left(\frac{T_{\mathrm{hold}}}{2}\right)\hat{U}_{\frac{\pi}{2}}(0)\,, \tag{3.41}$$

and the probability to find an atom in $|g\rangle$ at the end of the sequence described above is equal to:

$$\begin{aligned} P_g(T_{\mathrm{hold}},\,\phi) &= |\langle g|\hat{U}_{\mathrm{SE}}(T_{\mathrm{hold}},\,\phi)\,|g\rangle|^2 \\ &= \frac{1}{2}\left[1+\cos\left(\phi-\frac{1}{2}\left(\int_{T_{\frac{\pi}{2}}+T_{\pi}+T_{\mathrm{hold}}/2}^{T_{\frac{\pi}{2}}+T_{\pi}+T_{\mathrm{hold}}}\delta(t)\,\mathrm{d}t\ -\int_{T_{\frac{\pi}{2}}}^{T_{\frac{\pi}{2}}+T_{\mathrm{hold}}/2}\delta(t)\,\mathrm{d}t\right)\right)\right]. \end{aligned} \tag{3.42}$$

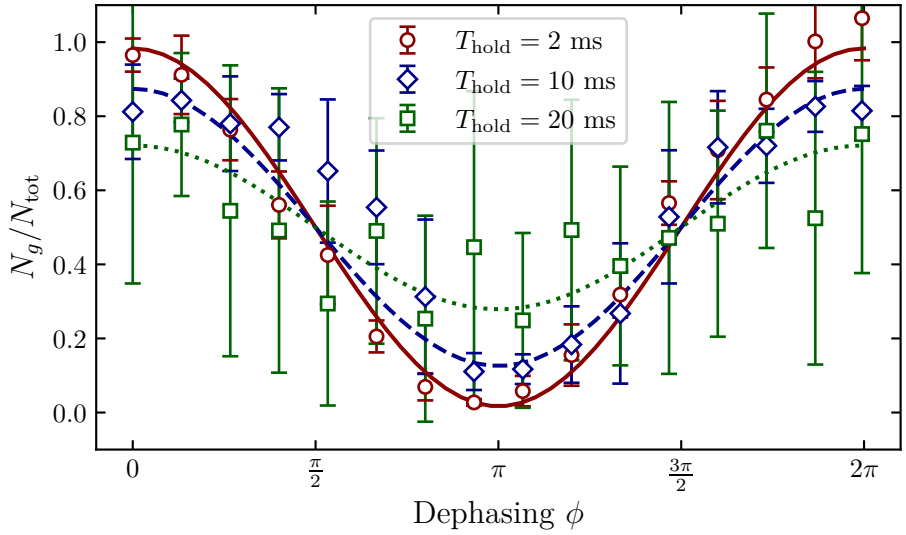

Figure 3.9 – Experimental Ramsey with spin echo fringes. The fraction of atoms in the $|g\rangle$ state at the end of the Ramsey sequence is measured for different dephasings $\phi \in [0, 2\pi]$. Here the fringes for $T_{\text{hold}} = \{2, 10, 10\}$ ms are represented. Here, unlike the Ramsey case, there no shift of the phase of the Ramsey fringes due to a static dephasing.

3.4 Sources of decoherence

In order to discuss the results of the study of the dynamics in the deep optical lattice and later in the 1D optical lattice, the different phenomena that could be responsible for a dephasing of the system should be considered. In this section we will focus our attention on the effects of the inhomogeneity induced by the probe and the effects related to the frequency fluctuations of our probe.

3.4.1 Inhomogeneous dephasing

The probe-induced inhomogeneity over the lattice sites is a first candidate to explain the decay of the amplitude of the Rabi oscillations. Indeed the laser intensity sent on the atoms to probe the clock transition is not homogeneous but displays a Gaussian profile in the directions $\mathbf{r}_\perp$ transverse to its propagation axis:

$$I_{\text{clock}}(\mathbf{r}_\perp) = I_0 \mathrm{e}^{-2\mathbf{r}_\perp^2/w_{\text{clock}}^2} \tag{3.43}$$

where $I_{\text{clock}} = 2P_{\text{clock}}/(\pi w_{\text{clock}}^2)$ and P_{clock} is the power of laser light sent on the atoms and $w_{\text{clock}} = 80\,\mu$m the waist of the laser beam. The inhomogeneity of the probe has two consequences for the Rabi oscillations:

- The coupling between the two internal states of the atoms, given by the Rabi frequency $\Omega_{\text{L}} = \eta_{00}\Omega_{\text{clock}}$ is now lattice site-dependent since

$$\Omega_{\text{clock}}(\mathbf{r_i}) = \alpha \mathrm{B}\sqrt{I_{\text{clock}}(\mathbf{r_i})}. \tag{3.44}$$

Here $\mathbf{i}$ is the lattice index, η_{00} the Lamb-Dicke factor introduced in (3.18), B the amplitude of the magnetic field used for the magnetic mixing (see 2.1.1) and α the coefficient expressed in (2.7).

- The presence of the probe induces a differential light shift $\delta_{\mathrm{E}}(\mathbf{r_i}) = \kappa I_{\mathrm{clock}}(\mathbf{r_i})$ (see 2.1.1) which creates an inhomogeneity for the detunings over the different occupied lattice sites $\delta(\mathbf{r_i}) = \delta_{\mathrm{L}} - \delta_{\mathrm{E}}(\mathbf{r_i})$.

Consequently, for N individual atoms trapped in a deep optical lattice, the fraction of atoms in the ground state evolves as:

$$\overline{P}_g(T) = \frac{1}{N}\sum_{\mathbf{i}} \frac{\Omega_{\mathrm{L}}^2(\mathbf{r_i})}{\Omega_{\mathrm{L}}^2(\mathbf{r_i}) + \delta^2(\mathbf{r_i})} \cos^2\left(\frac{\sqrt{\Omega_{\mathrm{L}}^2(\mathbf{r_i}) + \delta^2(\mathbf{r_i})}}{2} T\right), \tag{3.45}$$

where the sum runs over the N populated lattice sites, indexed by $\mathbf{i}$. The expression (3.45) shows that the inhomogeneity induced by the probe will result in averaging the Rabi oscillations with different amplitudes and frequencies. While the coexistence of different amplitudes for the oscillations merely limit the amplitude of the oscillations of $\overline{P}_e(T)$ below 1, averaging oscillations at different frequencies results in the dephasing of the oscillations associated with different lattice sites. The oscillatory part of the signal $\overline{P}_e$ thus progressively disappears and $\overline{P}_e$ converges toward $\frac{1}{2}$ in the limit $T \to \infty$.

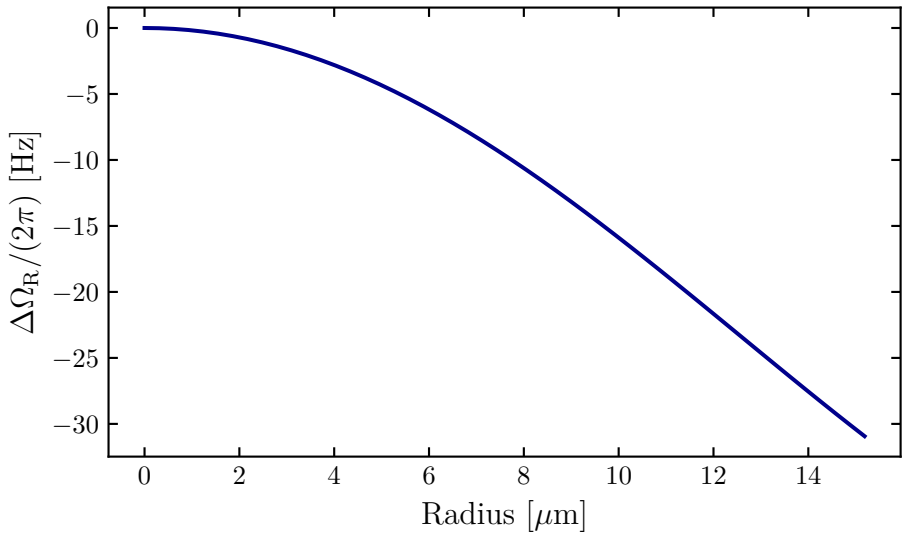

Figure 3.10 – Evolution of the effective Rabi $\Delta\Omega_{\mathrm{R}} = \Omega_{\mathrm{R}}(\mathbf{r}) - \Omega_{\mathrm{R}}(0)$ frequency shift from the center. For the maximal radius $r_{\perp,\max} \simeq 8\,\mu$m of the optical lattices used for the experiments presented in this chapter, the shift at the edge is around -10 Hz.

According to the model for the loading of the optical lattice developed earlier in 2.3.3 an optical lattice loaded with 8×10^3 atoms, the typical atom number used in our experiments, has a maximal radius $R_{\max} \simeq 8\,\mu$m. In the following we will denote $\Omega_0 = \Omega_{\mathrm{L}}(0)$ and $\delta_0 = \delta_{\mathrm{L}} - \delta_{\mathrm{E}}(0)$ respectively the Rabi frequency and the detuning at the center of the optical lattice (on which the probe is supposed to be pointing) and

assume that at resonance $\delta_0 = 0$. Since the ratio $r_{\perp,\max}/w_{\text{clock}}$ is small compared to 1, it is possible to expand the expression for the generalized Rabi frequency $\Omega_R = \sqrt{\Omega_L^2 + \delta^2}$ as:

$$\Omega_R^2 = \Omega_L^2(r) + \delta^2(r) = \Omega_0^2 - 2\Omega_0^2 \frac{r_\perp^2}{w_{\text{clock}}^2} + \mathcal{O}\left(\frac{r_\perp^4}{w_{\text{clock}}^4}\right). \tag{3.46}$$

This expression shows that the maximum difference of angular frequency for the Rabi oscillations, between an atom at the center of the optical lattice $r_\perp = 0$ and an atom at the edge $r_\perp = r_{\perp,\max}$, is equal to:

$$|\Delta\Omega_R| = \Omega_0 \frac{r_{\perp,\max}^2}{w_{\text{clock}}^2}. \tag{3.47}$$

The numerical computation of $\Delta\Omega_R$ presented in Fig. 3.10 gives a shift of about -10 Hz at the edge of optical lattices loaded with 8×10^3 atoms, used in our experiments.

The expression (3.47) points out the fact that the effect of inhomogeneous dephasing increases with the Rabi frequency applied on the atoms. We use the model for the loading of the optical lattice presented earlier (see 2.3.3) to compute the spatial distribution of the atoms with respect to the probe beam and simulate numerically the function $\overline{P}_e$. The result of the simulation is presented in Fig. 3.11 along with the experimental data for a Rabi flopping experiment at $\Omega_0 = 2\pi \times 1329$ Hz. Although a very small decay of the oscillations amplitude can be seen over 10 ms for the simulated curve, the damping of the experimental oscillations is faster than expected for inhomogeneous dephasing alone.

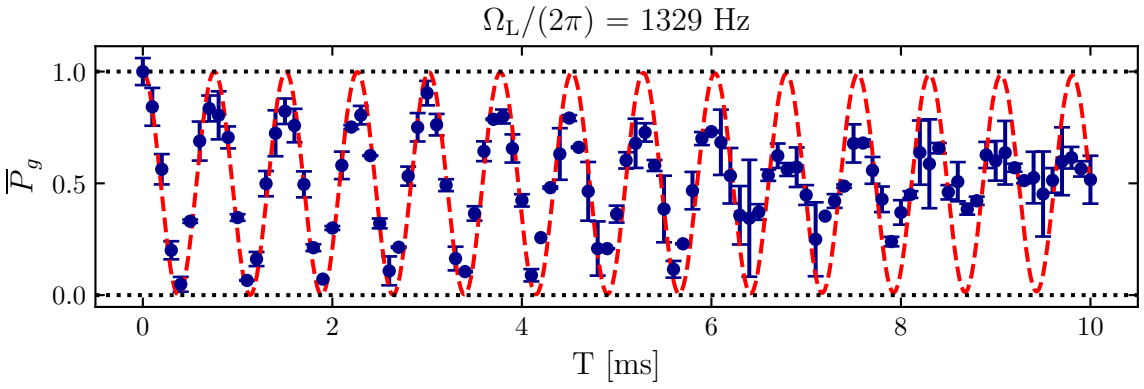

Figure 3.11 – Rabi oscillations. The normalized measured population of atoms in the $|g\rangle$ state (blue dots) for different Rabi pulse duration T are compared to the simulated fraction of atoms in the ground state computed using the loading model for the optical lattice presented in 2.3.3 (dashed red line).

3.4.2 Frequency fluctuation of the probe

Frequency fluctuations of the clock laser probing the atoms constitute another source of damping. They are in general difficult to extract from Rabi oscillations where inhomogeneity and frequency fluctuations of the probe both lead to damping. In a first attempt to model this effect, it is possible to consider the case of a Gaussian white

noise of parameter γ. In the case where the laser frequency is resonant with the driven transition (taking into account the light shift), the dynamics of the system can be described by the Optical Bloch Equation equation:

$$\frac{\mathrm{d}\hat{\rho}}{\mathrm{d}t} = -\mathrm{i}\left[\frac{\Omega_\mathrm{L}}{2}\hat{\sigma}_x, \hat{\rho}\right] + \frac{\gamma}{2}\left(2\hat{\sigma}_z\hat{\rho}\hat{\sigma}_z - \hat{\rho}\hat{\sigma}_z^2 - \hat{\sigma}_z^2\hat{\rho}\right), \tag{3.48}$$

which can be translated in the Bloch sphere picture similarly to (3.25) as:

$$\frac{\mathrm{d}u_x}{\mathrm{d}t} = -2\gamma u_x \tag{3.49}$$

$$\frac{\mathrm{d}u_y}{\mathrm{d}t} = -\Omega_\mathrm{L} u_z - 2\gamma u_y \tag{3.50}$$

$$\frac{\mathrm{d}u_z}{\mathrm{d}t} = \Omega_\mathrm{L} u_y. \tag{3.51}$$

The solution of this system of ordinary differential equation gives us an expression for the fraction of atoms in the $|g\rangle$ state at the end of a Rabi pulse of duration T:

$$\overline{P}_g(T) = \frac{1}{2} + \frac{\mathrm{e}^{-\gamma T}}{2}\cos\left(\sqrt{\Omega_\mathrm{L}^2 - \gamma^2}.T\right) + \frac{\gamma \mathrm{e}^{-\gamma T}}{2\sqrt{\Omega_\mathrm{L}^2 - \gamma^2}T}\sin\left(\sqrt{\Omega_\mathrm{L}^2 - \gamma^2}.T\right), \tag{3.52}$$

assuming $\gamma < \Omega_\mathrm{L}$.

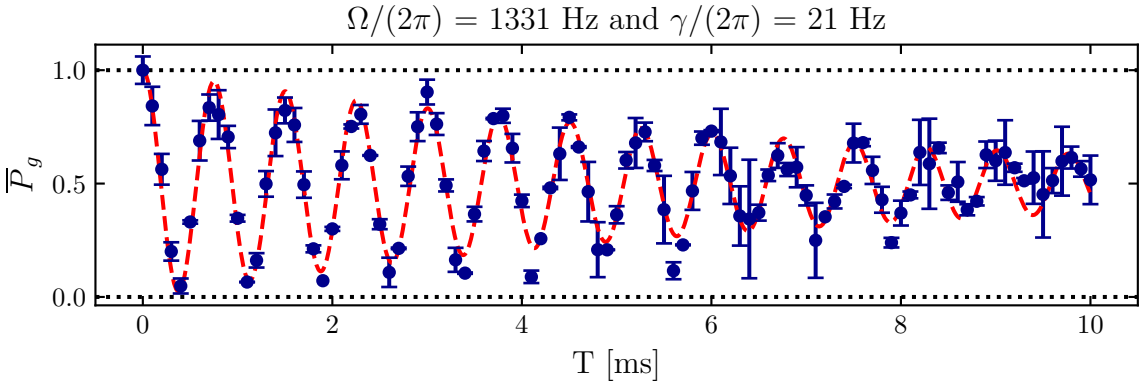

Figure 3.12 – Rabi oscillations in presence of a Gaussian white noise. The fraction of atoms in the $|g\rangle$ state (blue dots) are fitted by the expression found in (3.52) (dashed red line). The extracted values for Ω_L and γ are indicated above the graph.

The measured populations in the $|g\rangle$ state for different Rabi pulse durations are fitted with this model in Fig. 3.12 , giving the estimate $\gamma = 2\pi \times 21 \pm 1\,\mathrm{Hz}$ for the white noise parameter γ. The good agreement between the experiment and the model leads us to consider the frequency fluctuations of a laser as a good "culprit" for the loss of coherence that translates into a damping of the Rabi oscillations. However using the Rabi experiment to characterize the probe noise may not be the best option, since the different effects that play a role during the coherent driving (such as the inhomogeneous effects) of the clock transition cannot be decoupled. Moreover the long duration of the pulse makes it very sensitive at long time to any error on the pointed frequency for the resonance.

3.5 Noise characterization from time-domain Ramsey spectroscopy

In order to estimate the spectral width of the probe without dealing with the effect of the inhomogeneous dephasing: the time-domain Ramsey spectroscopy experiments involves illumination time of the atoms, inferior or equal to one Rabi period. Consequently the effect of the inhomogeneous dephasing is negligible and the inhomogeneity of the probe can be neglected for these experiments and all the spatially dependent quantities can be set to their values at the center of the optical lattice. The Ramsey spectroscopy experiments can be used to decouple the effects of the probe frequency fluctuations from the inhomogeneous dephasing and estimate the spectral width of probe.

For this purpose we can use the formal description of the Ramsey and Ramsey with spin echo sequences developped earlier in 3.3.2 and 3.3.3, with the detuning δ_{L} of the laser with respect to the probed atomic transition no longer assumed to be constant: it can be decomposed between its average value $\overline{\delta_{\mathrm{L}}}$, set to verify $\delta_0 = \overline{\delta_{\mathrm{L}}} - \delta_{\mathrm{E}} = 0$ and a stochastic part ξ as:

$$\delta_{\mathrm{L}}(t) = \overline{\delta_{\mathrm{L}}} + \xi(t) \quad \text{with} \quad \overline{\xi} = 0. \tag{3.53}$$

Here the overline $\overline{\xi}$ stands for the average over the realizations of the stochastic process ξ. Taking this representation of the frequency fluctuations of the probe, we can re-express the functions $P_g(T_{\mathrm{hold},\phi})$ derived earlier.

3.5.1 Time domain Ramsey spectroscopy

In the case of the Ramsey spectroscopy without spin echo, taking into account the frequency fluctuations of the probe changes the integral involved in the expression of the propagator $\hat{U}_{\mathrm{hold}}$ introduced in 3.3.2 which becomes:

$$\exp\left(-\frac{\mathrm{i}}{2}\int_{T_{\frac{\pi}{2}}}^{T_{\frac{\pi}{2}}+T_{\mathrm{hold}}} \delta(t)\,\mathrm{d}t\,\hat{\sigma}_z\right) = \delta_{\mathrm{E}} T_{\mathrm{hold}} + W_{\mathrm{R}}, \tag{3.54}$$

with W_{R} the stochastic integral:

$$W_{\mathrm{R}} = \int_{T_{\frac{\pi}{2}}}^{T_{\frac{\pi}{2}}+T_{\mathrm{hold}}} \xi(t)\,\mathrm{d}t \underset{T_{\mathrm{hold}} \gg T_{\frac{\pi}{2}}}{\approx} \int_0^{T_{\mathrm{hold}}} \xi(t)\,\mathrm{d}t. \tag{3.55}$$

The probability to find an atom in $|g\rangle$ at the end of the sequence described above is then equal to:

$$P_g(T_{\mathrm{hold}},\,\phi) = |\langle g|\hat{U}_{\mathrm{R}}(T_{\mathrm{hold}},\,\phi)\,|g\rangle|^2 = \sin^2\left(\frac{\phi - \delta_{\mathrm{E}} T_{\mathrm{hold}} - W_{\mathrm{R}}}{2}\right). \tag{3.56}$$

After averaging over different realizations of the random variable W_{R}, this gives:

$$\overline{P}_g(T_{\mathrm{hold}},\,\phi) = \frac{1}{1}\left[1 - \cos(\phi - \delta_{\mathrm{E}} T_{\mathrm{hold}})\,\mathrm{e}^{-\chi_{\mathrm{R}}(T_{\mathrm{hold}})}\right] \tag{3.57}$$

with

$$\mathrm{e}^{-\chi_\mathrm{R}(T_\mathrm{hold})} = \overline{\mathrm{e}^{-\mathrm{i}W_\mathrm{R}}} \tag{3.58}$$

$$= \mathrm{e}^{-\frac{1}{2}W_\mathrm{R}^2} \quad \text{for } W_\mathrm{R} \text{ gaussian random variable.} \tag{3.59}$$

The damping function χ_R can be expressed as a correlation function, by assuming that the random variable W_R obeys gaussian statistics:

$$\chi_\mathrm{R}(T) = \frac{1}{2}\int_0^T \int_0^T \overline{\xi(t)\,\xi(t')}\,\mathrm{d}t\,\mathrm{d}t'. \tag{3.60}$$

The autocorrelation function for the noise can be related to the spectral density of the fluctuations $S_\xi(\omega)$ thanks to the Wiener–Khinchine theorem, and χ_R can be rewritten as:

$$\chi_\mathrm{R}(T) = \int_0^\infty \frac{\mathrm{d}\omega}{2\pi}\frac{S_\xi(\omega)}{\omega^2} 4\sin^2\left(\frac{\omega T}{2}\right) = T^2\int_0^\infty \frac{\mathrm{d}\omega}{2\pi} S_\xi(\omega)\,\mathcal{F}_\mathrm{R}(\omega T)\,. \tag{3.61}$$

The damping function is proportional to the sum of the components of the frequency noise spectral density, filtered by a T_hold dependent function $\mathcal{F}_\mathrm{R}(\omega T)$, represented in Fig. 3.13, playing the role of a low-pass filter. For the particular case where the noise is white, *i.e.* $S_\xi(\omega) = \gamma$, the damping function becomes: $\chi_\mathrm{R}(T_\mathrm{hold}) = \frac{1}{2}\gamma T_\mathrm{hold}$.

To sum up, the Ramsey fringes obtained by scanning the dephasing ϕ in the interval $[0,\, 2\pi]$ of the second pulse, at different fixed T_hold, ends up being a period of a sine curve, whose phase at $\phi = 0$ is equal to $-\delta_\mathrm{E} T_\mathrm{hold}$ and whose contrast decays with T_hold as $\mathrm{e}^{-\chi_\mathrm{R}(T_\mathrm{hold})}$. These fringes are fitted by the function:

$$\mathcal{P}_g(\phi) = p_0 + p_1\cos(\phi) + p_2\sin(\phi) \tag{3.62}$$

from which the contrast $\mathcal{C} = \frac{\sqrt{p_1^2+p_2^2}}{p_0}$ is extracted. The evolution of the contrast with T_hold is represented in Fig. 3.14.

3.5.2 Time domain Ramsey spectroscopy with spin echo

Similarly for the Ramsey spectroscopy with spin echo, taking into account the frequency fluctuations of the probe changes the integral involved in the expression of the propagators $\hat{U}_\mathrm{hold}$ introduced in 3.3.3 which become:

$$\int_{T_{\frac{\pi}{2}}}^{T_{\frac{\pi}{2}}+T_\mathrm{hold}/2} \delta(t)\;\mathrm{d}t = \delta_\mathrm{E} T_\mathrm{hold} + W_{\mathrm{SE}_1} \tag{3.63}$$

$$\int_{T_{\frac{\pi}{2}}+T_\pi+T_\mathrm{hold}/2}^{T_{\frac{\pi}{2}}+T_\pi+T_\mathrm{hold}} \delta(t)\,\mathrm{d}t = \delta_\mathrm{E} T_\mathrm{hold} + W_{\mathrm{SE}_2} \tag{3.64}$$

with W_{SE_1} and W_{SE_2} the stochastic integrals:

$$W_{\mathrm{SE}_1} = \int_{T_{\frac{\pi}{2}}}^{T_{\frac{\pi}{2}}+T_\mathrm{hold}/2} \xi(t)\;\mathrm{d}t \underset{T_\mathrm{hold}\gg T_{\frac{\pi}{2}}}{\approx} \int_0^{T_\mathrm{hold}/2} \xi(t)\;\mathrm{d}t \tag{3.65}$$

$$W_{\mathrm{SE}_2} = \int_{T_{\frac{\pi}{2}}+T_\pi+T_\mathrm{hold}/2}^{T_{\frac{\pi}{2}}+T_\pi+T_\mathrm{hold}} \xi(t)\;\mathrm{d}t \underset{T_\mathrm{hold}\gg T_{\frac{\pi}{2}}}{\approx} \int_{T_\mathrm{hold}/2}^{T_\mathrm{hold}} \xi(t)\;\mathrm{d}t \tag{3.66}$$

The probability to find an atom in $|g\rangle$ at the end of the sequence described above is equal to:

$$P_g\left(T_{\text{hold}},\,\phi\right) = |\langle g|\hat{U}_{\text{SE}}\left(T_{\text{hold}},\,\phi\right)|g\rangle|^2 = \frac{1}{2}\left[1+\cos\left(\phi - \frac{W_{\text{SE}_2}-W_{\text{SE}_1}}{2}\right)\right]. \tag{3.67}$$

After averaging over different realizations of the random variable W_{R}, this gives:

$$\overline{P}_g\left(T_{\text{hold}},\,\phi\right) = \frac{1}{1}\left[1+\cos\left(\phi\right)\mathrm{e}^{-\chi_{\text{SE}}(T_{\text{hold}})}\right] \tag{3.68}$$

with

$$\mathrm{e}^{-\chi_{\text{SE}}(T_{\text{hold}})} = \overline{\mathrm{e}^{-\mathrm{i}W_{\text{SE}}}} \tag{3.69}$$

$$= \mathrm{e}^{-\frac{1}{2}W_{\text{SE}}^2} \quad \text{for } W_{\text{SE}} \text{ gaussian random variable.} \tag{3.70}$$

The stochastic integral W_{SE} is defined by:

$$W_{\text{SE}} = W_{\text{SE}_2} - W_{\text{SE}_1} \tag{3.71}$$

The damping function χ_{SE} can be expressed a correlation function, modulated by a function equal to 1 in the first half hold time, and equal to -1 in the second. The autocorrelation function for the noise can be related to the spectral density of the fluctuations $S_\xi\left(\omega\right)$ thanks to the Wiener–Khinchine theorem, and χ_{R} can be rewritten as:

$$\chi_{\text{SE}} = \int_0^\infty \frac{\mathrm{d}\omega}{2\pi}\frac{S_\xi\left(\omega\right)}{\omega^2}16\sin^4\left(\frac{\omega T}{2}\right) = T^2\int_0^\infty \frac{\mathrm{d}\omega}{2\pi}S_\xi\left(\omega\right)\mathcal{F}_{\text{SE}}\left(\omega T\right) \tag{3.72}$$

Similarly to the Ramsey case, the damping function is proportional to the sum of the components of the frequency noise spectral density, filtered by a T_{hold} dependent function $\mathcal{F}_{\text{SE}}\left(\omega T\right)$, represented in Fig. 3.13. However, for the spin echo case, the filter function is a pass band, cutting off the low frequency components of the laser noise. For the particular case where the noise is white, *i.e.* $S_\xi\left(\omega\right) = \gamma$, the damping function becomes: $\chi_{\text{SE}}\left(T_{\text{hold}}\right) = \frac{1}{2}\gamma T_{\text{hold}}$.

The Ramsey fringes obtained with the Ramsey with spin echo sequence, scanning the dephasing of the last pulse ϕ in the interval $[0,\,2\pi]$ ends up being a period of a sine curve, without a phase at the origin and whose contrast decays with T_{hold} as $\mathrm{e}^{-\chi_{\text{SE}}(T_{\text{hold}})}$. Similarly to the Ramsey case, these fringes are fittes by the function in (3.62) and the evolution of the contrast with T_{hold} is represented in Fig. 3.14. Here we notice that the decay of the contrast is slower in presence of a spin echo pulse.

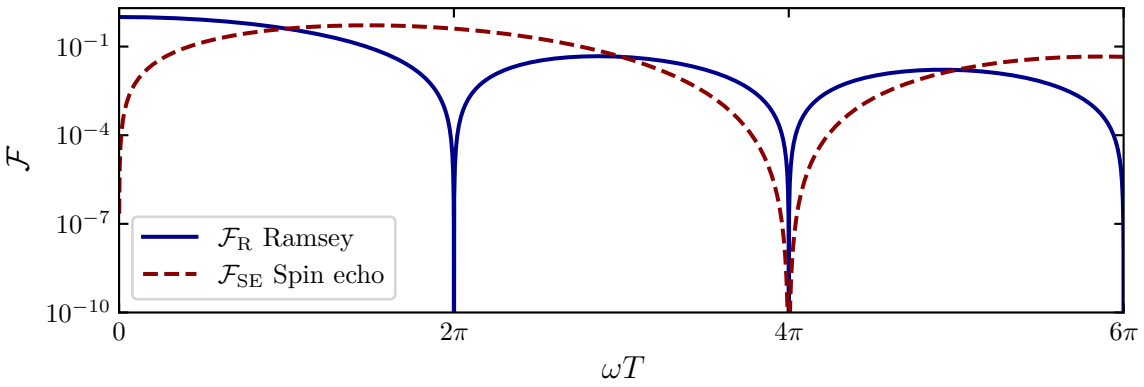

Figure 3.13 – Functions filtering the noise spectral density involved in the computation of the decay of the contrast of the observed fringes for Ramsey and Ramsey with spin echo experiments. In the spin echo case, $\mathcal{F}_{\mathrm{SE}}$ filters out the low frequency component and cancel the noise of frequency 0, *i.e.* any static effect.

3.5.3 A simple model for the laser noise

The results on the evolution of the contrast of the fringes at the end of Ramsey with and without spin echo experiments, represented in Fig. 3.14, can be used to propose a model for the statistics of the laser frequency noise, and from there, infer the spectral width of our laser.

The strong difference observed between the timescale for the decays of the Ramsey and Ramsey with spin-echo fringes discard the Gaussian white noise as a candidate to model the probe noise: indeed for a Gaussian white noise (*i.e.* $S_\omega(\omega) = \gamma = \text{constant}$) the decay function of the contrast for both protocol would be identical,

$$\chi_{\mathrm{R}}(T) = \chi_{\mathrm{SE}}(T) = \frac{1}{2}\gamma T \tag{3.73}$$

since the correlation function for this noise is a Dirac distribution. Moreover the white noise presents the additional drawback to be a non-stationary process, which means that standard deviation of the laser frequency from its mean value would keeps on increasing over time, while we expect its fluctuations to stay close to the expected value.

In order to take into account the previous remarks, we propose to model the noise with a pink noise generated by a Ornstein-Uhlenbeck process: this stationary Gauss-Markov process is therefore defined by its mean and covariance,

$$\overline{\xi(t)} = 0 \tag{3.74}$$

$$\overline{\xi(t)\,\xi(t')} = \frac{\sigma^2}{2\beta} \mathrm{e}^{-\beta(t+t')} \left(\mathrm{e}^{2\beta.\min(t,t')} - 1\right), \tag{3.75}$$

from which we extract the expression for the spectral density of noise:

$$S_\omega(\omega) = \frac{\sigma^2}{\beta^2 + \omega^2}. \tag{3.76}$$

This Lorentzian form for the spectral density of noise is consistent with the observation on some other clock laser locked on a ULE cavity setup (e.g. Westergaard 2010). This expression for $S_\omega(\omega)$ can be used to compute the damping functions for the fringes contrast for Ramsey and Ramsey with spin echo experiments.

$$\chi_{\mathrm{R}}(T) = \frac{\sigma^2}{2\beta^3}\left(\beta T + \mathrm{e}^{-\beta T} - 1\right) \underset{\beta T \ll 1}{\approx} \frac{\sigma^2 T^2}{4\beta} \tag{3.77}$$

$$\chi_{\mathrm{SE}}(T) = \frac{\sigma^2}{2\beta^3}\left(\beta T + 4\mathrm{e}^{-\frac{\beta T}{2}} - \mathrm{e}^{-\beta T} - 3\right) \underset{\beta T \ll 1}{\approx} \frac{\sigma^2 T^3}{24} \tag{3.78}$$

The decays of the contrast for the fringes for Ramsey with and without spin echo are fitted with these functions are fitted with the functions in order to extract the parameter of the noise:

$$\beta = 3 \pm 0.6\,\mathrm{s}^{-1} \tag{3.79}$$

$$\sigma = 1400 \pm 100\,\mathrm{s}^{-3/2}. \tag{3.80}$$

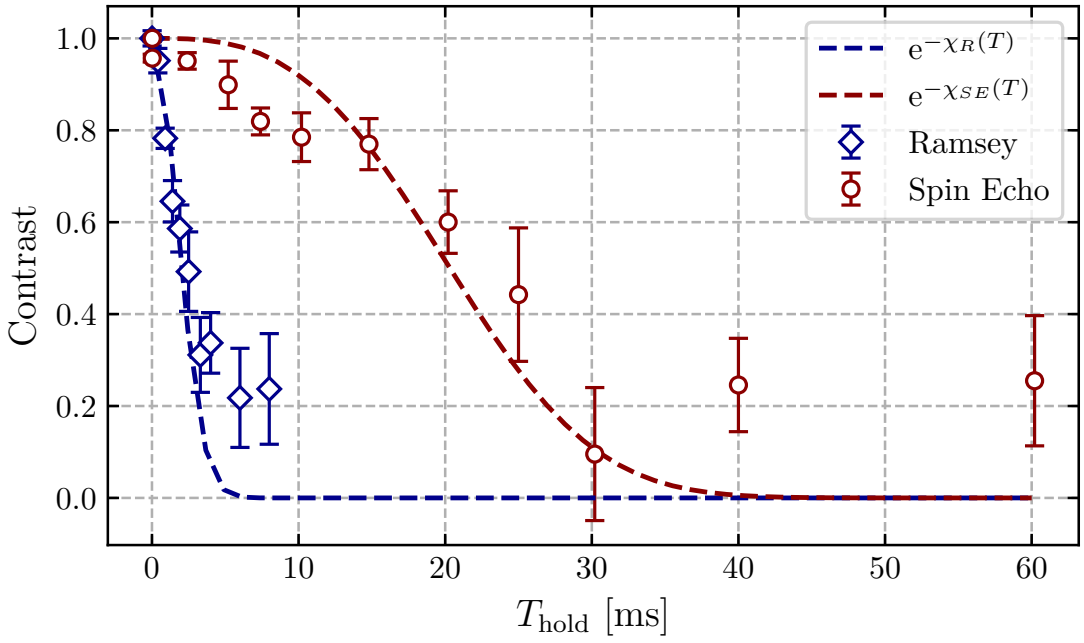

Figure 3.14 – Experimentally measured contrast of the fringes for Ramsey (blue diamonds) and Ramsey with spin echo (red dots) experiments. These dashed lines of the same color are the decay function, introduced in (3.77), whose parameter have been found by fitting the experimental points. The observed disagreement at long times for both protocol may be caused by the difficulty to fit Ramsey fringes when their contrast become very small. The last two points of each data set has not been taken into account to fit the parameters of the colored noise model used: it comes from the fact that contrast for long T_{hold} times, when the contrast of the Ramsey fringes start to vanish, is hard to fit and is very sensitive to the presence of any outlier point.

From these values it is possible to extract the characteristic decay times for both protocol:

$$\tau_{\mathrm{SE}} = \sqrt[3]{\frac{24}{\sigma^2}} \approx 23\,\mathrm{ms} \tag{3.81}$$

$$\tau_{\mathrm{R}} = \sqrt{\frac{4\beta}{\sigma^2}} \approx 2.4\,\mathrm{ms} \tag{3.82}$$

3.6 Conclusion

At the end of this section, we have characterized the different systemic effect that could alter the result of any further experiment involving the coherent driving of the clock transition of individual atoms trapped on the sites of the optical lattice. We have seen that the dephasing due to the inhomogeneity induced by the probe is negligible at for small atoms number and that pointed out the laser frequency fluctuations as the main effect responsible for the lose of coherence during the driving of the transition, which translates into a damping of the Rabi and Ramsey fringes. In order to enhance the lifetime of the coherence, we performed Ramsey with spin echo experiments, that allows us to filter out the contribution of the low frequency component of the frequency noise as well as all the static detuning effects. Consequently, in our further study of interacting atoms in a 1D optical lattice, we will use this protocol in order to get rid of all these undesired effects.

CHAPTER 4

Ramsey spectroscopy in 1D optical lattices

Optical lattice clocks (Ludlow et al. 2015) are a very interesting and promising platform to study topological states and spin-orbit coupling (SOC) physics and more generally to simulate condensed matter systems (Dalibard et al. 2011). Experiments performed on neutral alkali atoms, using optical Raman transitions to couple their internal states have allowed to investigate these effects in the regime where inter-particle interactions do not play a significant role. This kind of experiments has been realized for the first time with ultracold ^{87}Rb atoms by Lin et al. 2011, and later with ^{40}K (Wang et al. 2012) and ^{6}Li (Cheuk et al. 2012) atoms. However the spontaneous emission and the resulting heating have been limiting factors for the study of many-body physics (Wang et al. 2012; Cheuk et al. 2012). The use of shaken optical lattice is an alternative way to implement spin-orbit coupling effects with alkali atoms (Struck et al. 2012; Aidelsburger et al. 2013; Miyake et al. 2013; Jotzu et al. 2014), but these experiments (except the one presented in Jotzu et al. 2014) also suffer from heating issues, related to the external periodic driving of the lattice, that prevent to consider interacting systems. The introduction of alkaline-earth and alkaline-earth like (AEL) atoms (such as ytterbium) in the past years, whose internal structure presents long-lived excited metastable states which can be directly coupled with the ground state by a single laser light, has allowed to overcome these detrimental effects. The transition between these two states, forming an effective spin 1/2 manifold (Wall et al. 2016), can be coherently driven by a clock laser to enable spin-orbit coupling without dealing with spontaneous emission related heating, putting the study of many-body interacting systems within reach. Examples of experiments taking advantage of the existence of a clock transition in lanthanide atoms can be found in Livi et al. 2016 and Kolkowitz et al. 2017. One must also mention that pure magnetic methods to implement the spin-orbit coupling without Raman coupling (and thus without their inherent heating) have been proposed (Anderson et al. 2013; Xu et al. 2013).

In the work presented here the emphasis has been laid on the study of 1D optical lattices filled with strongly interacting bosonic ^{174}Yb atoms, with an initial average filling close to $\overline{n} = 1$, driven on the $^{1}S_0 \longleftrightarrow {}^{3}P_0$ clock transition. In this chapter we firstly see how such system, described by the two component Bose-Hubbard model with coupling light field can be mapped, in the strongly interacting regime, to a doped Heisenberg model.

Then we show how it is possible to take advantage to the site dependent phase imprinted by the clock laser during the driving of the transition to probe the dynamics of the bosons in presence of a non unitary filling, that can be interpreted using the classical picture by the presence of "holes" in the lattice: this is implemented by time-domain Ramsey spectroscopy with spin echo. Finally we propose an approximate model involving hard-core bosons (HCB) to perform numerical simulations and have some quantitative insight on the average filling in the system.

4.1 Ramsey spectroscopy in 1D optical lattices

4.1.1 Coupled two-components bosons in a 1D optical lattice

We introduce briefly some theoretical elements that may be useful for further discussions on the experiments.

Two-component bosons in a unidimentional optical lattice

In the rest of this chapter the system under study is an orthogonal optical lattice at magic wavelength initially loaded with a BEC made of a small enough number of ^{174}Yb atoms ($N_{\text{atoms}} < 8 \times 10^3$) to prevent the formation of any doubly occupied site, according to the loading model introduced in 2.3.3. The lattice depths in the vertical and in the y horizontal directions are chosen deep enough ($V_{y,z} = \{25,\, 27\}\, E_{\text{R}}$) to prevent any tunneling on a timescale of a few seconds, while the lattice depth V_x on the x horizontal direction is shallower, but still in the range of validity for the Bose-Hubbard model, and taken as a parameter for the experiments. Consequently this system can be pictured as a collection of 1D independent optical lattices, with depth $V_x \in [8,\, 25]\ E_{\text{R}}$ and filled with bosons with two relevant internal states, that are mapped on pseudo-spins by denoting $\{|\downarrow\rangle,\, |\uparrow\rangle\}$ the states that correspond respectively to $\{|g\rangle,\, |e\rangle\}$.

Under the *single band approximation*, i.e. if only the lowest Bloch band of the optical lattice is populated, the dynamics of the system can be described by the two component Bose-Hubbard Hamiltonian (Jaksch et al. 1998) in 1D:

$$\hat{H}_{\text{BH}} = -J \sum_{\substack{i \\ s\in\{\uparrow,\downarrow\}}} \left(\hat{a}^\dagger_{i,s}\hat{a}_{i+1,s} + \hat{a}^\dagger_{i+1,s}\hat{a}_{i,s}\right) + \sum_{i,s} \frac{U_{ss}}{2}\hat{n}_{i,s}\left(\hat{n}_{i,s} - 1\right) + U_{\uparrow\downarrow}\sum_i \hat{n}_{i,\uparrow}\hat{n}_{i,\downarrow}. \quad (4.1)$$

Here $\hat{a}_{i,s}$ is the annihilation operator for a boson with internal state s in the lattice site labeled by i and $\hat{n}_{i,s} = \hat{a}^\dagger_{i,s}\hat{a}_{i,s}$ the associated number operator. The $U_{s\,s'}$ are the on-site interaction energies, resulting of the s wave two-body collisions between one atom in state s and another in state s'. The tunneling constant J along the x direction does not depend on the internal state of the atoms, since the optical lattice is set at a magic wavelength.

In the strongly interacting regime, *i.e.* $J \ll U_{s\,s'}\ \forall s,\ s' \in \{|\downarrow\rangle,\, |\uparrow\rangle\}$, a 1D Mott insulator at unit filling can be mapped to the ferromagnetic Heisenberg model (Duan et al. 2003;

Kuklov et al. 2003; Altman et al. 2003),

$$\hat{H}_{\text{Heis.}} = -J_z \sum_{\langle i,\, j\rangle} \hat{S}_i^z \hat{S}_j^z - J_\perp \sum_{\langle i,\, j\rangle} \left(\hat{S}_i^x \hat{S}_j^x + \hat{S}_i^y \hat{S}_j^y \right), \tag{4.2}$$

introducing the pseudo-spin operators $\hat{\mathbf{S}}_i$ whose components are defined by,

$$\hat{S}_i^x = \frac{1}{2}\left(\hat{S}_i^+ + \hat{S}_i^-\right), \quad \hat{S}_i^y = \frac{1}{2\mathrm{i}}\left(\hat{S}_i^+ - \hat{S}_i^-\right), \quad \hat{S}_i^z = \frac{1}{2}\left(\hat{a}_{i,\uparrow}^\dagger \hat{a}_{i,\uparrow} - \hat{a}_{i,\downarrow}^\dagger \hat{a}_{i,\downarrow}\right), \tag{4.3}$$

with

$$\hat{S}_i^+ = \hat{a}_{i,\uparrow}^\dagger \hat{a}_{i,\downarrow}, \quad \hat{S}_i^- = \hat{a}_{i,\downarrow}^\dagger \hat{a}_{i,\uparrow}. \tag{4.4}$$

The operators defined above obey the angular momentum commutation rules and commute if they are associated with different lattice sites. In addition, here $\langle i,\, j\rangle$ stands for the sum on nearest neighbors. Finally the following constants has been introduced,

$$J_z = 4J^2\left(\frac{1}{U_{gg}} + \frac{1}{U_{ee}} - \frac{1}{U_{eg}}\right) \quad \text{and} \quad J_\perp = \frac{4J^2}{U_{eg}}. \tag{4.5}$$

In practice, for ^{174}Yb atoms, the values for the on-site interaction energies are very close one to another $U_{gg} \approx U_{eg} \approx U_{ee}$ (see Chap. 5) and therefore to their average $\overline{U}$. From this observation it is possible to reduce the two constants previously introduced to one,

$$J_z \approx J_\perp \approx J_{\text{ex}} = \frac{4J^2}{\overline{U}}. \tag{4.6}$$

J_{ex} is called the *superexchange* coupling constant. Its associated Hamiltonian (4.2) renders the mechanism involving spin exchange between neighboring bosons mediated *via* a virtual state outside of the low energy subspace considered after the perturbation expansion.

If the unit filling assumption allows to map the Bose-Hubbard model on the ferromagnetic Heisenberg model, the experimental implementation of the 1D optical lattice in the strongly interacting regime often comes with the formation of mobile hole-defects, corresponding to empty sites in the localized picture. Their dynamics is thus taken into account by adding a doping Hamiltonian to the ferromagnetic Heisenberg one, leading to the effective Hamiltonian (Essler et al. 2005; Hild et al. 2014),

$$\hat{H}_{\text{eff}} = \hat{H}_{\text{Heis.}} + \hat{H}_{\text{d}} \tag{4.7}$$

$$\hat{H}_{\text{d}} = -J \sum_{\substack{\langle i,\, j\rangle \\ s\in\{\uparrow,\downarrow\}}} \hat{a}_i^\dagger \hat{a}_j - \frac{J^2}{\overline{U}} \sum_{\substack{\langle i,\, j,\, k\rangle \\ s\in\{\uparrow,\downarrow\}}} \left[\hat{a}_{s,\,i}^\dagger \hat{n}_{\bar{s},\,j} \hat{a}_{s,\,k} + \hat{a}_{\bar{s},\,i}^\dagger \hat{S}_j^s \hat{a}_{s,\,k} + 2\hat{a}_{s,\,i}^\dagger \hat{n}_{s,\,j} \hat{a}_{s,\,k}\right] \tag{4.8}$$

where $\langle i,\, j,\, k\rangle$ stands for the sum over nearest neighbor pairs $i,\, j$ and $j,\, k$ with $i \neq k$ and $\overline{s}$ flips the internal state s. In $\hat{H}_{\text{d}}$ two kinds of dynamics are involved: the first term $\propto J$ corresponds to the usual *tunneling* of the bosons to neighboring "empty" sites, without any spin flipping, while the second term $\propto J_{\text{ex}}$ renders interaction-mediated tunneling mechanisms involving spin exchange between neighboring bosons.

Field coupling for two-component bosons in an optical lattice

The two-component Bose-Hubbard developed in the previous section describes the dynamics in absence of coupling light. However the preparation and the analysis of the system is made by driving the atoms on their clock transition. The coupling laser send on the atoms to drive their clock transition transfers them momentum too. The component of the momentum transferred along the deep direction is suppressed by the lattice potential. Consequently, in order to complete the description of the system under study, we remind from Sec. 3.2 the expression of the Hamiltonian for the electric-dipole coupling induced by the near resonant monochromatic electric field of the probe on the atoms in the optical lattice. This Hamiltonian, in the Rotating Wave approximation (RWA), can be re-expressed in terms of pseudo-spin operators (4.3) as,

$$\hat{H}_{\mathrm{AL}} = \hat{V}_{\mathrm{L}} + \hat{H}_{\delta} \tag{4.9}$$

$$\hat{V}_{\mathrm{L}}(\phi) = \frac{\hbar\Omega_{\mathrm{L}}}{2} \sum_{\text{sites } i} \left[\hat{S}_i^{+} \mathrm{e}^{\mathrm{i}(\eta_i - \phi)} + \hat{S}_i^{-} \mathrm{e}^{-\mathrm{i}(\eta_i - \phi)} \right] \tag{4.10}$$

$$\hat{H}_{\delta} = -\hbar(\delta_{\mathrm{L}} - \delta_{\mathrm{E}}) \sum_{\text{sites } i} \hat{S}_i^{z} \tag{4.11}$$

Here $\eta_j = \mathbf{k}_{\text{clock}}.\mathbf{r}_j = j\eta$ is the local phase imprinted by the recoil induced by the absorption of a laser photon at site j, introducing the constant $\eta = k_{\mathrm{L}} d \cos\theta$, where θ is the angle formed by the laser beam propagation direction with the x axis of the lattice, in the horizontal plane and $d = \lambda_{\mathrm{L}}/2$ the lattice spacing. $\hat{H}_{\delta}$ is the detuning term introduced in 3.2.1, with δ_{E} the differential light shift introduced in 2.1.1 and δ_{L} the detuning between the laser angular frequency ω_{L} and the angular frequency of the driven transition.

By analogy to the individual lattice case studied in Chap. 3.2, it is possible to show that the expression for the propagator associated with the light coupling term $\hat{V}_{\mathrm{L}}$ at resonance $\delta_0 = \delta_{\mathrm{L}} - \delta_{\mathrm{E}} = 0$ writes:

$$\begin{aligned} \hat{U}(t, \phi) &= \mathrm{e}^{-\mathrm{i}\frac{\hat{V}_{\mathrm{L}}(\phi)}{\hbar}t} \\ &= \bigotimes_{\text{sites } i} \left[\cos\left(\frac{\Omega_{\mathrm{L}} t}{2}\right) \hat{\mathbb{1}} - \mathrm{i}\sin\left(\frac{\Omega_{\mathrm{L}} t}{2}\right) \left(\mathrm{e}^{\mathrm{i}(\eta_i - \phi)} \hat{S}_i^{+} + \mathrm{e}^{-\mathrm{i}(\eta_i - \phi)} \hat{S}_i^{-} \right) \right]. \end{aligned} \tag{4.12}$$

In an extended Bloch sphere picture applied on each lattice site, this operator rotates the vector representing the state of the "atom on site i" around a vector $\mathbf{v}_i$ in the $x-y$ plane. From one site to another the vector is rotated by an angle $\eta_j = j.\eta$ (see Fig. 4.2). Consequently this propagator will imprint a phase gradient in the 1D optical lattice, that will result in the formation of a "spin helix" over the lattice sites, in the Bloch sphere picture.

In the following, we will focus on two particular cases:

- $\hat{U}_{\frac{\pi}{2}}$ for pulses of area $\Omega_{\mathrm{L}} T_{\frac{\pi}{2}} = \frac{\pi}{2}$,

$$\hat{U}_{\frac{\pi}{2}}(\phi) = \bigotimes_{i} \frac{1}{\sqrt{2}} \left[\hat{\mathbb{1}} - \mathrm{i} \left(\mathrm{e}^{\mathrm{i}(\eta_i - \phi)} \hat{S}_i^{+} + \mathrm{e}^{-\mathrm{i}(\eta_i - \phi)} \hat{S}_i^{-} \right) \right]. \tag{4.13}$$

- $\hat{U}_\pi$ for pulses of area $\Omega_\mathrm{L} T_\pi = \pi$,

$$\hat{U}_\pi(\phi) = \bigotimes_i \left[-\mathrm{i} \left(\mathrm{e}^{\mathrm{i}(\eta_i - \phi)} \hat{S}_i^+ + \mathrm{e}^{-\mathrm{i}(\eta_i - \phi)} \hat{S}_i^- \right) \right]. \tag{4.14}$$

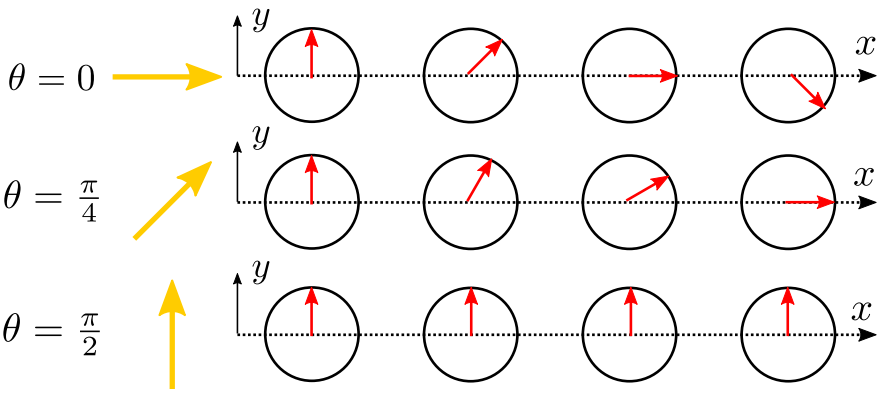

Figure 4.1 – Scheme of "the helix" imprinted on the internal state of the atoms by the coupling laser, for different angle. Here the internal state of the atoms is represented by a Bloch vector (red arrows) in the equatorial plane of the Bloch sphere of each atoms. The spin helix is represented for different values of the angle θ formed by the laser with the direction of the lattice, oriented along the x axis here.

4.1.2 Time domain Ramsey spectroscopy of 1D optical lattice

The framework introduced or reminded in the previous section allows to describe the dynamics of strongly interacting two-levels bosons evolving in an unidimensional lattice, whose internal states are coupled by a resonant monochromatic light field. More particularly we have seen that the coherent driving of such system in a regime where the average filling $\overline{n} \leq 1$ imprint a site depend phase on the internal state of the atoms, that translates into a spin helix in the Bloch sphere picture generalized to an unidimensional ensemble of atoms. In the rest of this chapter we will see how we can take use this imprinted phase as a way to labels atoms and monitor their dynamics, in order to probe the dynamics taking place in our quasi-unidimensional optical lattice filled with ^{174}Yb atoms.

In order to probe the dynamics of the strongly interacting bosons in the 1D optical lattice at short timescales (on the order of h/J), the Ramsey with spin echo sequence described earlier (see 3.3.3) and schematized in Fig. 4.2 is performed on the system for different lattice depths.

- Initially all the atoms in the 1D optical lattice are assumed to be in the ground state:

$$|\Psi_0\rangle = \bigotimes_{\substack{\text{occupied} \\ \text{sites } j}} |\downarrow\rangle_j. \tag{4.15}$$

- The first $\frac{\pi}{2}$ of the clock laser transfers the atoms in a coherent superposition of the $|\uparrow\rangle$ and $|\downarrow\rangle$ states with a local phase $\eta_j = j\eta$:

$$|\Psi_1\rangle = \hat{U}_{\frac{\pi}{2}} = \bigotimes_{\substack{\text{occupied} \\ \text{sites } j}} \frac{1}{\sqrt{2}} \left(|\downarrow\rangle_j - \mathrm{i}\mathrm{e}^{\mathrm{i}\eta_j} |\uparrow\rangle_j \right). \tag{4.16}$$

- The atoms evolve "freely", *i.e.* in absence of coupling light, for a duration $T_{\text{hold}}/2$.
- A π pulse is applied on the system, that reverse the spins of the atoms according to a site dependent axis.
- The atoms evolve "freely" again for a duration $T_{\text{hold}}/2$.
- Finally the second $\frac{\pi}{2}$ pulse with variable phase ϕ close the internal-state interferometer that constitutes the whole Ramsey sequence. In particular for $\phi = 0$, this final pulse remaps the spin helix to the $|\downarrow\rangle$ state all over the lattice.

In absence of tunneling the imprinted site-dependent phase η_j on the internal state of the atoms would be irrelevant and the behaviour of the atoms would be the one described in Chap. 3 for individual ones. In the experiments presented in this chapter we study the evolution of contrast of the Ramsey fringes in order to probe the evolution of the spin helix built over the 1D optical lattice by the first $\frac{\pi}{2}$ pulse during the free evolution time. The π echo pulse is used similarly to Bromley et al. 2018 to filter out the detrimental dephasing effect pointed out in the previous Chap. 3 (as well as the static dephasing caused by the light-induced shift of the transition frequency).

In the following we assume that the evolution of the system during the light pulses is fully determined by $\hat{V}_{\text{L}}$ alone irrespective of $\hat{H}_{\text{eff}}$. For our system of strongly-interacting bosons evolving in a 1D lattice, this assumption requires that $\Omega_{\text{L}} \gg J$, to neglect the motion of atoms at the timescale of the pulses. During the free evolution times, the dynamics of the bosons is driven by $\hat{H}_{\text{eff}}$, that involves the two mechanisms discussed in 4.1.1.

- The superexchange: From the results of similar experiments presented in Hild et al. 2014, Bardon et al. 2014 and Jepsen et al. 2020, we expect that the superexchange mechanism, responsible for spin transport in the Heisenberg model picture, will progressively destroy the spiral pattern imprinted on the optical lattice, with a characteristic time that scales with $\hbar/J_{\text{ex}}$.
- The tunneling: In the presence of holes, the bosons in the optical lattice will be able to tunnel to new location where their initial imprinted phase will *a priori* no longer match the phase of the local rotation operator. Consequently we expect that the tunneling will prevent the Ramsey interferometer to close properly, because of the displacement of the atoms between the pulses, resulting in a decay of the contrast of the Ramsey fringes, on a characteristic time scaling with $\hbar/J$. The tunnel-induced decay of the Ramsey fringes contrast will also presumably depends on the number of holes in the lattice, *i.e.* its initial average filling $\overline{n} = \langle \hat{n} \rangle$.

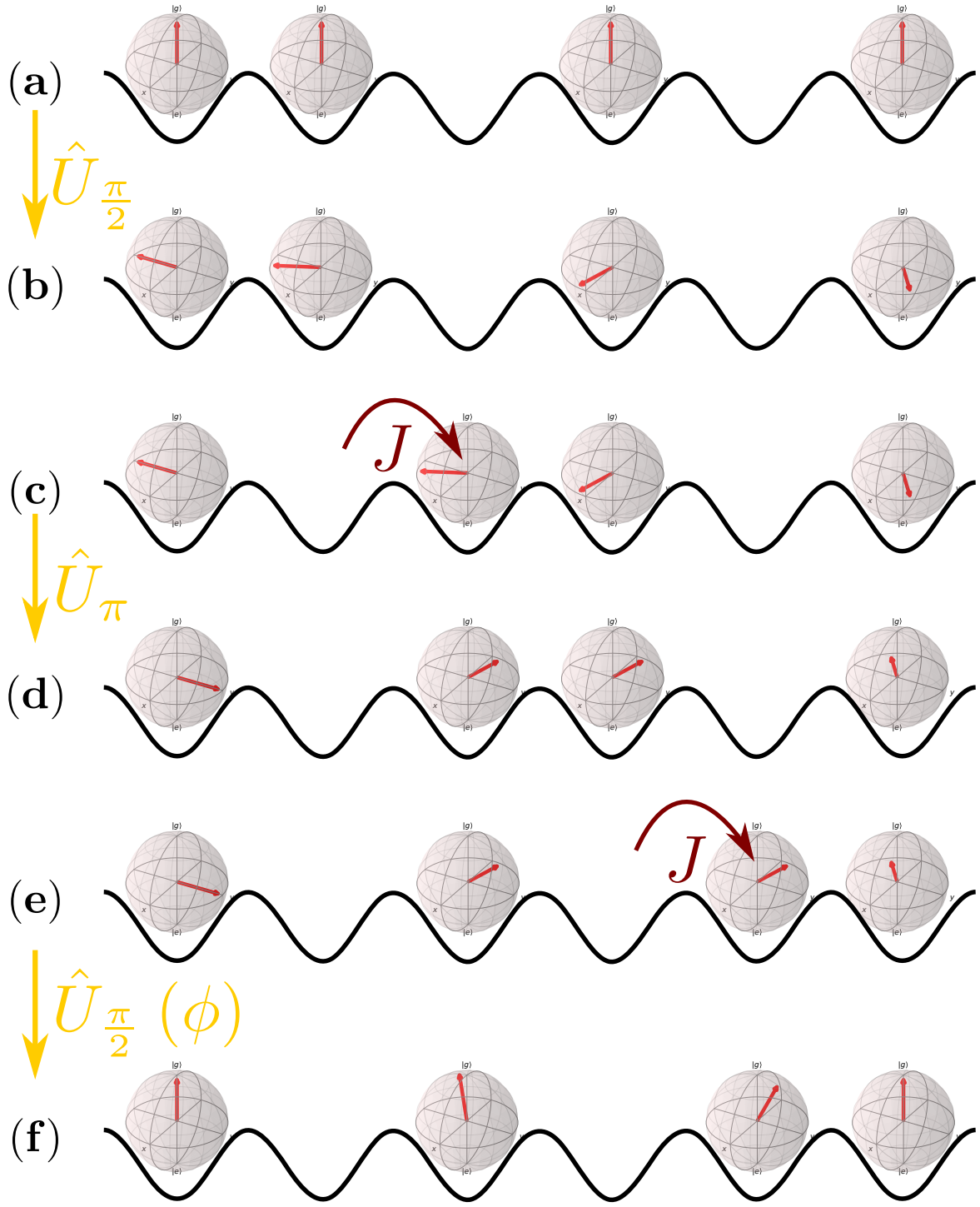

Figure 4.2 – Scheme of the Ramsey with spin echo sequence used to probe the dynamics in the 1D optical lattice: (**a**) The atoms in the optical lattice are initially in the ground state. In the classical picture some lattice sites are empty. (**b**) the first $\frac{\pi}{2}$ build the spin helix: it transfers the atoms in a superposition of the two internal states, of the form $\bigotimes_j \left(|\downarrow\rangle_j + \mathrm{e}^{\mathrm{i}j\eta}|\uparrow\rangle\right)$, up to a global phase factor. Here the product is made on the occupied lattice sites. (**c**) the system evolves in absence of coupling light. (**d**) The π pulse reverse the vector representing the internal state of the atom on each site according to the local rotation axis. (**e**) The system evolves again in absence of coupling light. (**f**) The second $\frac{\pi}{2}$ pulse remaps the spin helix on the $|\downarrow\rangle$ state, up to eventual dephasing due to the displacement of atoms during the free-evolution times.

In the experiments detailed in this section we consider an observable, the contrast of the Ramsey fringes, that results from the contribution of all the sites of the optical lattice, whereas the experiments presented in Hild et al. 2014 use correlations over a short range in the lattice to monitor its evolution and are consequently more suitable to observe the superexchange dynamics.

To sum up the state of the system at the end of the sequence can be expressed in terms of evolution operators as:

$$|\Psi_f\rangle = \hat{U}_{\frac{\pi}{2}}(\phi)\,\hat{U}_{\text{hold}}\hat{U}_{\pi}(0)\,\hat{U}_{\text{hold}}\hat{U}_{\frac{\pi}{2}}(0)\,|\Psi_0\rangle. \tag{4.17}$$

Here $\hat{U}_{\text{hold}}$ is the evolution operator obtained by the integration of the Schrödinger equation for the Hamiltonian $\hat{H}_0$ on a duration $T_{\text{hold}}/2$, corresponding to the evolution of the hard-core bosons on the optical lattice between the light pulses.

The Ramsey fringes are experimentally measured for different T_{hold} and for different lattice depths and a contrast $\mathcal{C}$ is extracted from these data with the same methods introduced in Sec. 3.3.2. The evolution of this quantity with T_{hold} for different lattice depth is represented in Figs. 4.3 and 4.4 for an angle of the coupling laser with respect to the shallow lattice axis of $\theta = 0$ and $\frac{\pi}{4}$ respectively. In these figures, the evolution of the contrast is also represented with T_{hold} rescaled with the characteristic time scales $\hbar/J$ and $\hbar/J_{\text{ex}}$ involved in the Hamiltonian (4.7), associated with the tunneling and the superexchange dynamics, respectively. In both cases the rescaling by $\hbar/J_{\text{ex}}$ shows that the dynamics measured here is faster than the characteristic time associated with the superexchange dynamics. Moreover for lower lattice depths, between $8\,E_{\text{R}}$ and $13\,E_{\text{R}}$, all the points seem to collapse on the same decaying curve, when the time is rescaled by the tunneling time $\hbar/J$. This observation is consistent with a description of the evolution of the system dominated by the dynamics of the holes in the optical lattice, given by the tunneling terms $\propto J$ in the Hamiltonian $\hat{H}_{\text{eff}}$. We can also remark from the experimentally measured contrast evolutions for the deep lattices $V_x = V_y = 26\,E_{\text{R}}$, represented in Fig. 4.5, that for these lattice depths the decay rate does not seems to depend on the angle that from the coupling laser with the lattice arms. It strengthen the hypothesis that the momentum transferred by the laser in the deep direction of the lattice does not play a role in the Ramsey fringes contrast decay.

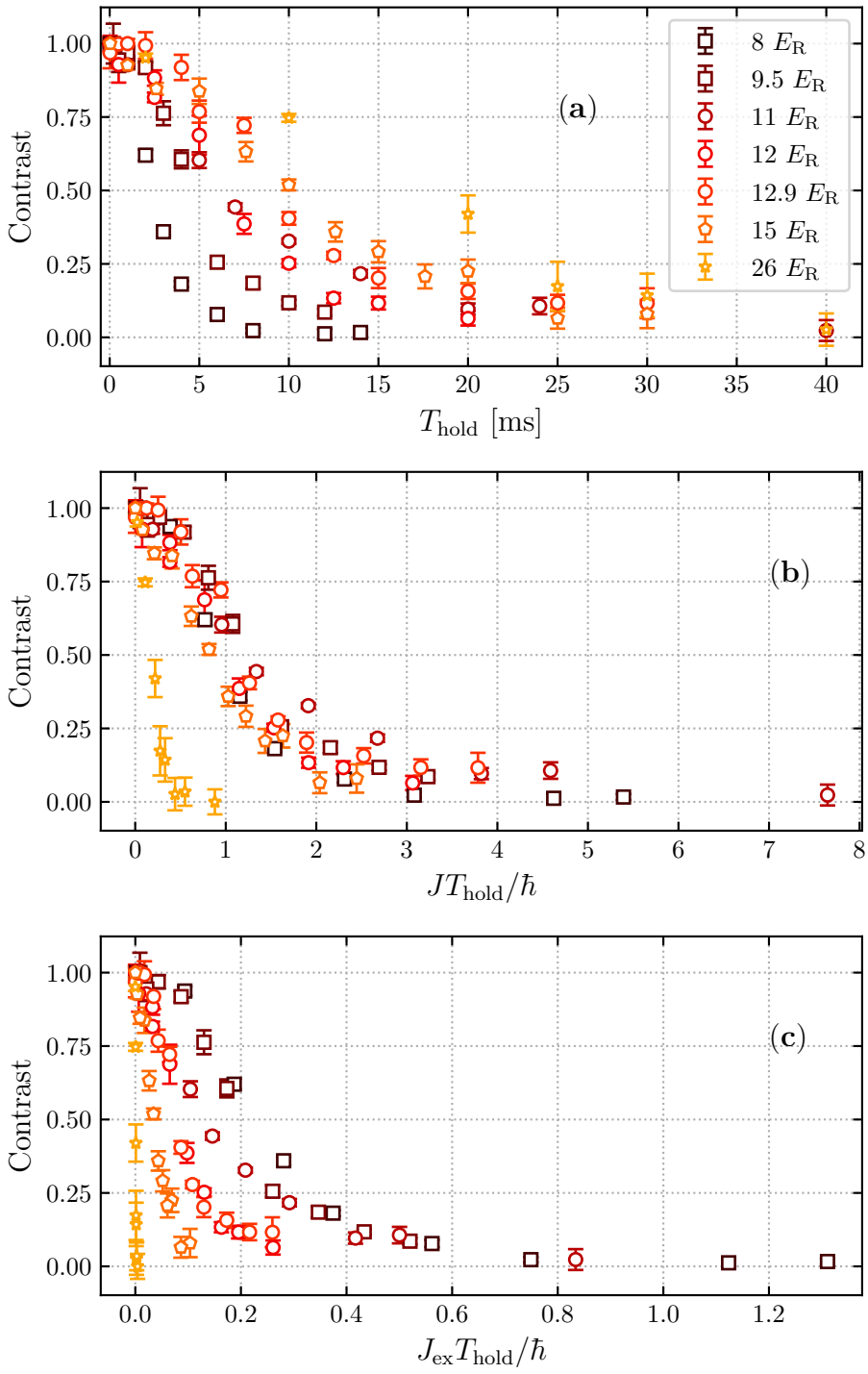

Figure 4.3 – Evolution of the contrast for different lattice depths ranging from $8\,E_{\mathrm{R}}$ to $26\,E_{\mathrm{R}}$ for an angle $\theta = 0$ (**a**) between the coupling laser beam and the horizontal axes of the optical lattice. The same data are represented as functions of $JT_{\mathrm{hold}}/\hbar$ in (**b**) and of $J^2T_{\mathrm{hold}}/(\hbar U) = J_{\mathrm{ex}}T_{\mathrm{hold}}/\hbar$ in (**c**). This points out that the evolution of the systems is faster that the dynamics involving superexchange mechanism. The rescaling of time by the tunneling time made data for low lattice depths ($V_0 \in [8, 13]\ E_{\mathrm{R}}$) to collapse on a single curve, which is consistent with the tunneling as the main effect responsible for the damping of the Ramsey fringes contrast.

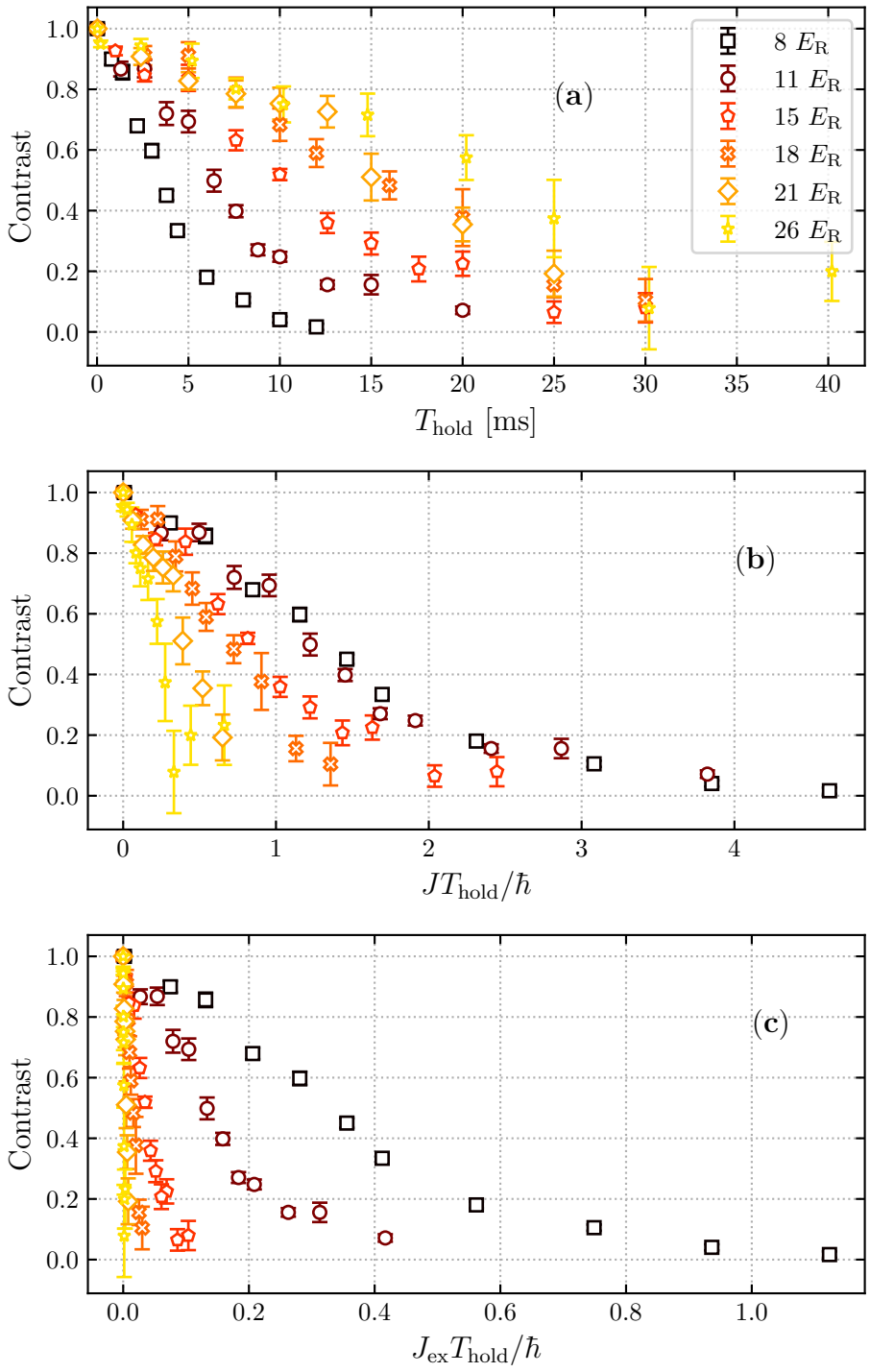

Figure 4.4 – Evolution of the contrast for different lattice depth ranging from $8\,E_R$ to $26\,E_R$ for an angle $\theta = \frac{\pi}{4}$ (**a**) between the coupling laser beam and the horizontal axes of the optical lattice. The same data are represented as functions of $JT_{hold}/\hbar$ in (**b**) and of $J^2T_{hold}/(\hbar U) = J_{ex}T_{hold}/\hbar$ in (**c**). This points out that the evolution of the systems is faster that the dynamics involving superexchange mechanism. The rescaling of time by the tunneling time made data for low lattice depths ($V_0 \in [8, 11]\ E_R$) to collapse on a single curve, which is consistent with the tunneling as the main effect responsible for the damping of the Ramsey fringes contrast.

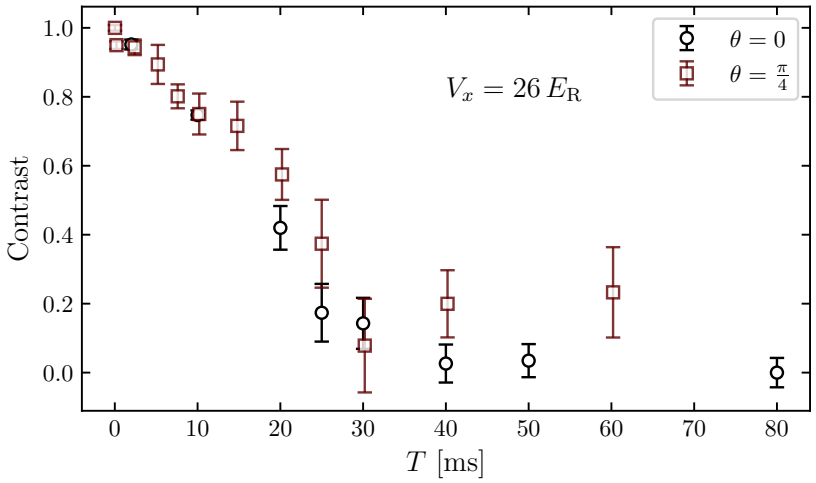

Figure 4.5 – Evolution of the Ramsey fringes contrast measured in a deep lattice $V_x = V_y = 26\,E_\mathrm{R}$, for an angle of the coupling laser with respect to the axes of the lattice $\theta = 0$ (black circles) and $\theta = \frac{\pi}{4}$ (red squares).

In absence of an exact analytically solvable model for the dynamics of the systems, we choose empirically to fit the evolution of the contrast for these lattice depths $V_0 \in [8,\, 26]\ E_\mathrm{R}$ with the empirical function

$$\mathcal{C}\left(T_\mathrm{hold}\right) = \mathrm{e}^{-\chi_\mathrm{SE}(T_\mathrm{hold})}\mathrm{e}^{-(\gamma T_\mathrm{hold})^\alpha} \tag{4.18}$$

with α and a characteristic decay time γ left as fit parameters. The prefactor $\mathrm{e}^{-\chi_\mathrm{SE}(T_\mathrm{hold})}$ in front of the stretched exponential fit function aims to decouple the part of the decay of the Ramsey fringes due to the frequency fluctuations of the coupling laser, studied earlier in Chap. 3, from the part related to the tunneling dynamics in the 1D optical lattice. Here χ_SE is the function introduced in 3.5.3, with its two parameters $\{\sigma,\, \beta\}$ fixed at the values measured in 3.5.3. An example of such fit is represented in Fig. 4.6.

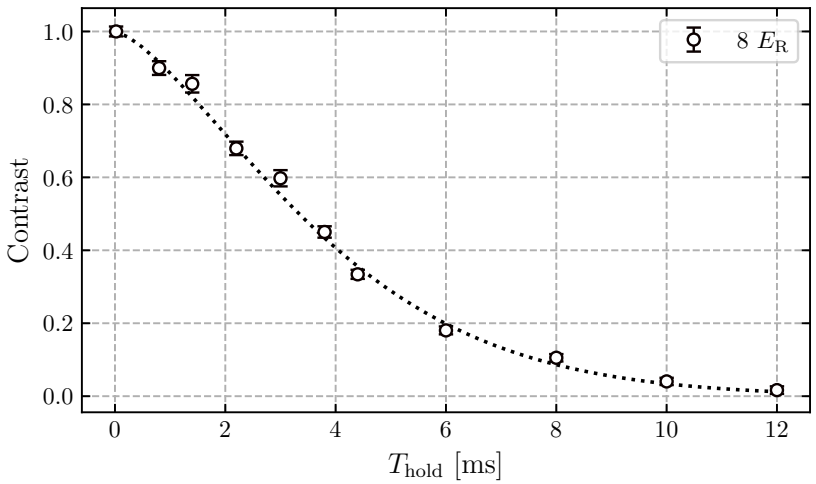

Figure 4.6 – Evolution of the contrast of the Ramsey fringes over time for 1D optical lattice with lattice depth $8\,E_\mathrm{R}$ and angle $\theta = \frac{\pi}{4}$ (hollow black dots). The evolution of the contrast is fitted with the function (4.18) (dotted line).

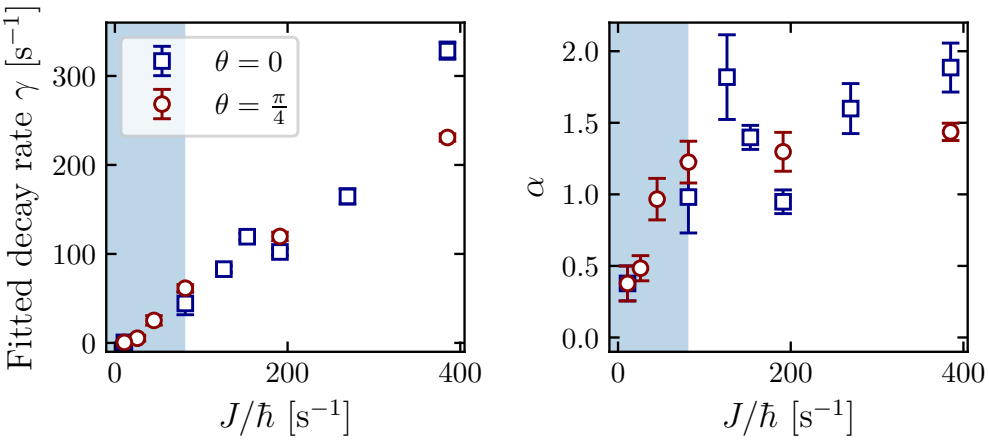

Figure 4.7 – Extracted fit parameters from the Ramsey contrast decay, using (4.18) as fit function for different lattice depths. The experiments are performed with the coupling laser in the horizontal plane forming an angle $\theta = 0$ (blue squares) and $\theta = \frac{\pi}{4}$ (red dots) with the shallow axis of the optical lattice. Left: Fitted decay rates γ. Right: fitted exponent α. We observe that for lattice depths below $15\,E_\mathrm{R}$, the decay rate of the contrast seems to scale linearly with $J/\hbar$. The blue shaded area corresponds to the lattice depths superior to $15\,E_\mathrm{R}$.

The extracted decay rates γ and exponents α are represented in Fig. 4.7. For the lower lattice depths, *i.e.* for $V_0 \in [8,\, 13]\ E_\mathrm{R}$, we observe an apparent linear dependence of the decay rate γ with the tunneling rate $J/\hbar$, which is consistent with our hypothesis of considering the tunneling as the main cause for decay of the Ramsey fringes for these lattice depths.

To sum up, the results of our Ramsey experiments performed on an ensemble of bosons trapped in an unidimensional optical lattice, gathered in Figs. 4.3 and 4.4, point toward the tunneling as the relevant mechanism to explain the decay of the contrast of the Ramsey fringes with respect to T_hold. However the qualitative approach used in this section, based on a rescaling of T_hold by the tunneling time $\hbar/J$, fails to give us quantitative information on the system. The integration of the Schrodinger equation for the system under study do not lead to any simple analytic solution. In order to access more quantitative results for the experimentally measured Ramsey fringes contrasts, we will have to use numerical simulations, whose details are precised in the next section.

4.2 Simulation of the Ramsey sequence for the hard-core bosons.

In this section we present the method and the assumptions made to perform numerical simulations of the dynamics of the system during the Ramsey with spin-echo sequence in order to compare it to the experimental data.

4.2.1 Description of the system

The results presented in Sec. 4.1.2 points out the tunneling, made possible by the presence of holes in the optical lattice, as the main mechanism responsible for the decay of the Ramsey fringes. Since the decay of the Ramsey fringes takes place on a timescale much shorter than $\hbar/J_{\text{ex}}$ (see Figs. 4.4 and 4.3.), we will in the following do an extra approximation to describe the dynamics of our system between the laser pulses by taking $\{U_{gg}/J,\, U_{eg}/J,\, U_{ee}/J\} \to \infty$, that will led us to consider the dynamics of *hard-core bosons*. Under these assumptions, the effective Hamiltonian, in absence of coupling light, reduces to

$$\hat{H}_{\text{eff}} \approx \hat{H}_{\text{HCB}} = -J \sum_{\substack{\langle i,j \rangle \\ s\in\{\uparrow,\downarrow\}}} \hat{\beta}^{\dagger}_{i,s}\hat{\beta}_{j,s} + \hat{H}_{\delta}, \tag{4.19}$$

with $\hat{\beta}_j$ the hard-core bosons annihilation operators on site j. This approximation is relevant since $J \ll U_{gg}, U_{eg}, U_{ee}$ (see. Sec. 1.2.1 Fig. 1.5).

This assumption is coupled with the one made in Sec. 4.1.2 that states that the dynamics is successively driven by the Hamiltonians $\hat{V}_{\text{L}}$ and $\hat{H}_{\text{HCB}}$, depending on the presence or the absence of the coupling light. While $\hat{V}_{\text{L}}$ only changes the internal states of the atoms with a spatial dependence, the Hamiltonian $\hat{H}_{\text{HCB}}$ only acts on their external degree of freedom, up to a global lattice-site-independent phase acquired on their internal degree of freedom, due to the light shift. Consequently, in order to simulate the dynamics of p hard-core bosons evolving in a lattice with n sites by exact diagonalization of the Hamiltonian, it is convenient to span its Hilbert space by a basis that allows to decouple easily the internal and the motional states of the p bosons. We introduce the basis defined by

$$|m, \sigma\rangle = \bigotimes_{\{l_1,\ldots,l_p\},\,\sigma} \hat{a}^{\dagger}_{l_p,\sigma_p}|\emptyset\rangle. \tag{4.20}$$

of $D = 2^p \times C_n^p$ basis states for the Hilbert space. Here:

- The $m \sim \{i_1, ..., i_p\}$ are the C_n^p possible set of p sites, among the n possible, occupied by the bosons, *i.e.* the spatial distribution of the bosons among the sites of the lattice.
- The σ are the set of the 2^p internal states configuration of the p bosons. Given a spin configuration σ, $\overline{\sigma}$ is the configuration with each respective internal state in the opposite state. We denote $[\sigma]_p$ the state of the p^{th} component of the spin configuration σ, taken as a p-tuple.

In oder to conduct more easily the simulations, the following additional reasonable assumptions are made:

- At the timescale of the experiment, there are no losses.
- All the inhomogeneous effects, probe or lattice related, are neglected.

- The frequency fluctuations of the laser are neglected.

Moreover in order to ease the simulation, we use the approximation $\eta = \pi\lambda_L/\lambda_{\text{clock}} \approx 4\pi/3$ in the configuration where $\theta = 0$ and use periodic boundary conditions for the lattice.

The system shall be described by a $D = 2^p \times C_n^p$ dimensional Hilbert space, but one may notice that it is impossible for the hard core bosons to reorder the internal state sequence $|\sigma\rangle$. The kinetic Hamiltonian H_K (corresponding to the terms $\propto J$ in $\hat{H}_{\text{eff}}$) can be represented by a d-dimensional hermitian matrix, diagonal by block, with 2^p identical blocks of dimension C_n^p, denoted $\hat{h}_K$. Indeed the tunneling does not depend on the internal state of the atoms. Consequently to compute the evolution of the system during the interval of time where the coupling laser is switched off, it is sufficient to diagonalize the C_n^p-dimensional Hamiltonian $\hat{h}_K$.

4.2.2 Evolution operators in the new basis

Before going into the details of the Ramsey with spin echo sequence for the system, the evolution operators introduced in (4.13) and (4.14) are expressed on the $|m,\, \sigma\rangle$ basis.

$\frac{\pi}{2}$ pulse:

$$\hat{U}_{\frac{\pi}{2}}|m_0,\, \sigma_0\rangle = \frac{1}{\sqrt{2^p}} \sum_{\sigma} \alpha^{m_0}_{\sigma_0,\,\sigma} |m_0,\, \sigma\rangle \quad \text{with} \quad \alpha^{m_0}_{\sigma_0,\,\sigma} = \prod_{\substack{l \in \left\{l_1^0,\ldots,l_p^0\right\} \\ [\sigma_0]_p = [\overline{\sigma}]_p}} \left(-\mathrm{i}\mathrm{e}^{-i[\sigma]_p(\eta_l - \phi)}\right). \tag{4.21}$$

Here $(\sigma)_p$ is equal to $+1$ (resp. -1) when the spin state of the p^{th} atom in the spin configuration $|\sigma\rangle$ is $|\uparrow\rangle_p$ (resp. $|\downarrow\rangle_p$). The condition $[\sigma_0]_p = [\overline{\sigma}]_p$ means that the product runs over components of the spin configuration σ that has been "flipped" with respect to the initial spin configuration σ_0.

π pulse:

$$\hat{U}_{\pi}|m_0,\, \sigma_0\rangle = \gamma_{m_0,\sigma_0}|m_0,\, \overline{\sigma_0}\rangle \quad \text{with} \quad \gamma_{m_0,\,\sigma_0} = (-\mathrm{i})^p \prod_{l \in \{l_1^0,\ldots,l_p^0\}} \mathrm{e}^{-\mathrm{i}[\sigma_0]_p \eta_l} \tag{4.22}$$

Evolution between the pulses: The evolution in the time interval between pulses of coupling light is driven by the Hamitonian $\hat{H}_0$ whose expression in the new basis is :

$$\hat{H}_0 = -J \sum_{\sigma} \sum_{\langle m,m' \rangle} |m,\, \sigma\rangle\langle m',\, \sigma| - \hbar\delta_{\text{E}} \sum_l \hat{S}_l^z. \tag{4.23}$$

The two terms of the Hamitonian commute and we can write the associated propagator as:

$$\hat{U}_{\text{hold}}\left(T_{\text{hold}}\right)|m_0,\,\sigma_0\rangle = f\left(T_{\text{hold}},\,\sigma_0\right)\sum_m \beta_{m_0,\,m}\left(T_{\text{hold}}\right)|m,\,\sigma\rangle \tag{4.24}$$

Here the $\beta_{m_0,\,m}$ are the coefficients found by integrating the Schödinger equation for the Hamiltonian $\hat{H}_0$ in absence of static dephasing. The latter effect is rendered by the factor

$$f\left(T_{\text{hold}},\,\sigma_0\right) = \prod_p \mathrm{e}^{\mathrm{i}(\sigma_0)_p \delta_{\mathrm{E}} T_{\text{hold}}/4} \tag{4.25}$$

From the expression of $f\left(T_{\text{hold}},\,\sigma_0\right)$ in (4.25), it comes

$$\forall\sigma,\,T,\quad f\left(T,\,\sigma\right).f\left(T,\,\overline{\sigma}\right) = 1 \tag{4.26}$$

Remark: If laser frequency fluctuations would have been taken into account in our model, the product $f\left(T,\,\sigma\right).f\left(T,\,\overline{\sigma}\right)$ would have been the damping factor of the Ramsey with spin echo fringes $\mathrm{e}^{-\chi_{\mathrm{SE}}}$ studied in the previous chapter in Sec. 3.3.3. Since the experiments are performed in a regime where the effect of the laser noise does not dominate, the corrections made by the factor $\mathrm{e}^{-\chi_{\mathrm{SE}}}$ at the considered timescales are small and for the sake of simplicity, this coefficient is kept equal to 1 in our simulations.

We consider $\hat{U}_K = \hat{U}_{\text{hold}}\hat{U}_\pi\left(0\right)\hat{U}_{\text{hold}}$ the evolution operator rendering the evolution of the system between the two $\frac{\pi}{2}$ pulses. This operator acts on the basis states as:

$$\hat{U}_K|m_0,\,\sigma_0\rangle = \sum_{m_1,\,m_2} \beta_{m_0,\,m_1}\gamma_{m_1\,,\sigma_0}\beta_{m_1,\,m_2} f\left(T_{\text{hold}},\,\sigma_0\right) f\left(T_{\text{hold}},\,\overline{\sigma_0}\right)|m_2,\,\overline{\sigma_0}\rangle \tag{4.27}$$

$$= \sum_{m_1,\,m_2} \beta_{m_0,\,m_1}\gamma_{m_1\,,\sigma_0}\beta_{m_1,\,m_2}|m_2,\,\overline{\sigma_0}\rangle \tag{4.28}$$

$$= \sum_{m_2} \tilde{\beta}^{\sigma_0}_{m_0,\,m_2}|m_2,\,\overline{\sigma_0}\rangle \quad \text{with} \quad \tilde{\beta}^{\sigma_0}_{m_0,\,m_2} = \sum_{m_1} \beta_{m_0,\,m_1}\gamma_{m_1\,,\sigma_0}\beta_{m_1,\,m_2} \tag{4.29}$$

4.2.3 Ramsey with spin echo sequence

Initial state

We assume that the initial state of the system corresponds to a situation where the hard-core bosons all the $|\downarrow\rangle$ state and localized in p sites among the n of the lattice. In the new basis, it corresponds to one of the C_n^p states of the form,

$$|\psi_0\rangle = \bigotimes_{l\in\left\{l_1^0,\ldots,l_p^0\right\}\sim m_0} \hat{a}_{l,\downarrow}|\emptyset\rangle = |m_0,\downarrow_1,\ldots,\downarrow_p\rangle. \tag{4.30}$$

Here the l_j are p ordered positive integers taken strictly smaller than n, which are the indexes of the sites where the p bosons can be found.

First $\frac{\pi}{2}$ pulse

A first $\frac{\pi}{2}$ pulse is applied to the system, leading to the state:

$$|\psi_1\rangle = \hat{U}_{\frac{\pi}{2}}(0)\,|\psi_0\rangle = \frac{1}{\sqrt{2^p}}\sum_{\sigma}\alpha^{m_0}_{\sigma_0,\sigma}|m_0,\sigma\rangle. \tag{4.31}$$

Here $|\sigma_0\rangle$ is the spin configuration where the internal state of each atom is in the $|\downarrow\rangle$ state.

Free evolution with the echo rephasing

The coupling light field is switched off and the atoms are let evolve during a hold time interspersed with a π pulse, performing the echo.

$$|\psi_2(T_{\text{hold}})\rangle = \hat{U}_K|\psi_1\rangle = \frac{1}{\sqrt{2^p}}\sum_{\sigma}\alpha^{m_0}_{\sigma_0,\sigma}\sum_{m_2}\tilde{\beta}^{\sigma}_{m_0,m_2}(T_{\text{hold}})\,|m,\,\overline{\sigma}\rangle \tag{4.32}$$

Final $\frac{\pi}{2}$ pulse and populations measurements

At the end of the Ramsey with spin echo sequence, the populations of atoms in the ground state $|\downarrow\rangle$ are measured. In absence of atomic losses, measuring the fractions of atoms in $|\uparrow\rangle$ or $|\downarrow\rangle$ is equivalent to compute the average for the observable :

$$\hat{S}_z = \frac{1}{p}\sum_{l=1}^{n}\hat{S}^z_l. \tag{4.33}$$

for the state

$$\hat{U}_{\frac{\pi}{2}}(\phi)\,|\psi_2(T_{\text{hold}})\rangle. \tag{4.34}$$

This average can be rewritten as an average for the state $|\psi_2(T_{\text{hold}})\rangle$ at the end of the hold time by introducing the effective ϕ-dependent observable:

$$\hat{\mathcal{S}}_z(\phi) = \hat{U}^{\dagger}_{\frac{\pi}{2}}(\phi)\,\hat{S}_z\hat{U}_{\frac{\pi}{2}}(\phi) \tag{4.35}$$

$$= \frac{1}{2p}\sum_{l=1}^{n}\left[-\mathrm{i}\left(\hat{S}^+_l\mathrm{e}^{\mathrm{i}(\eta_l-\phi)} - \hat{S}^-_l\mathrm{e}^{-\mathrm{i}(\eta_l-\phi)}\right)\right] \tag{4.36}$$

and the fraction of atoms in the ground state is given by,

$$\mathcal{P}(T_{\text{hold}},\,\phi) = \frac{1}{2} - \langle\psi_2(T_{\text{hold}})|\hat{\mathcal{S}}_z(\phi)\,|\psi_2(T_{\text{hold}})\rangle \tag{4.37}$$

$$= \frac{1}{2} - \frac{1}{2\mathrm{i}p}\sum_{l=1}^{n}\left[\langle\psi_2(T_{\text{hold}})|\hat{S}^+_l\mathrm{e}^{\mathrm{i}\eta_l}|\psi_2(T_{\text{hold}})\rangle\mathrm{e}^{-\mathrm{i}\phi} - \text{h.c.}\right] \tag{4.38}$$

$$= \frac{1}{2} - \left[\langle\hat{\mathcal{S}}_z(0)\rangle\cos(\phi) + \langle\hat{\mathcal{S}}_z(\pi/2)\rangle\sin(\phi)\right]. \tag{4.39}$$

We conclude that $\mathcal{P}(T_{\text{hold}},\,\phi)$ is a sine function of the phase ϕ of period 2π, from which it is thus possible to extract a contrast $\mathcal{C}(T_{\text{hold}})$.

Simulations with $N_{\text{sites}} = 12$

The results of the simulations conducted for $N_{\text{sites}} = 12$ (N_{sites} has to be a multiple of 3) and $\eta = \frac{4\pi}{3}$ for different average fillings are represented in Fig. 4.8. The total rephasing by the spin echo expected for the single particle case is observed and the fringe contrast damping seems to be maximal around half filling. In order to have some insight on the presence of finite size effect in our simulations, we compare in the lower pane of Fig. 4.8 the evolution of the contrast half decay time $T_{1/2}$ with respect to the number of sites $N_{\text{sites}} \in \{6, 9, 12\}$ considered in our simulations, for different initial fillings.

The results of the numerical simulations are compared to the experimental data in Fig. 4.9. A relative good agreement between the measured contrast and the model for filling around $\overline{n} = 0.5$ is observed. In order to get more quantitative information on the average filling, we represent in Fig. 4.10 the time $T_{1/2}$ at which the contrast reach 0.5 for simulations performed with $N_{\text{sites}} = 12$ lattice sites. From the results of the fitting procedures realized in Fig. 4.7, we also extract the quantities $T_{1/2}$ for the experimental data as a function of the tunneling rate $J/\hbar$. The time at half decay are computed from the fit function, deprived from the prefactor taking into account the decay of the contrast related to the laser noise. We then perform a linear regression on these quantities to extract a global $T_{1/2}$ in units of $\hbar/J$ and we compare it to the simulated values in order to determine an estimate of the average filling of the probed lattices. (see Fig. 4.10). If we assume that the laser frequency fluctuations and the tunneling are the only mechanisms responsible for the decay of the Ramsey fringes, we conclude that the average initial filling is equal to $\overline{n} = 0.5 \pm 0.2$. However we have to remark that contribution of any effect, not taken into account in our model, will be reported to the ones taken into account, and results in a overestimation of the decay rate. Consequently the value found for the filling may be underestimated.

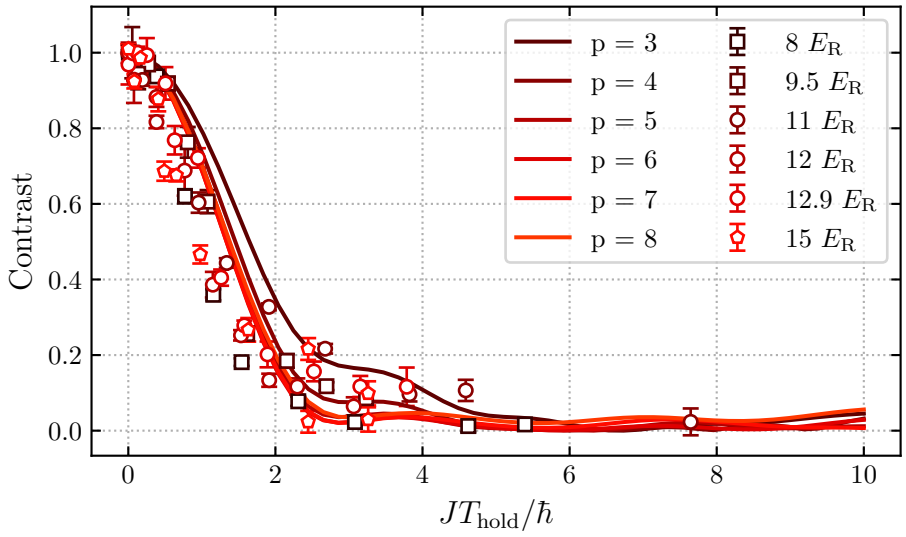

Figure 4.9 – Comparison between the measured contrasts at low lattice depths and the simulated evolution of the contrast for different number of particles in the lattice, corresponding to different initial average fillings.

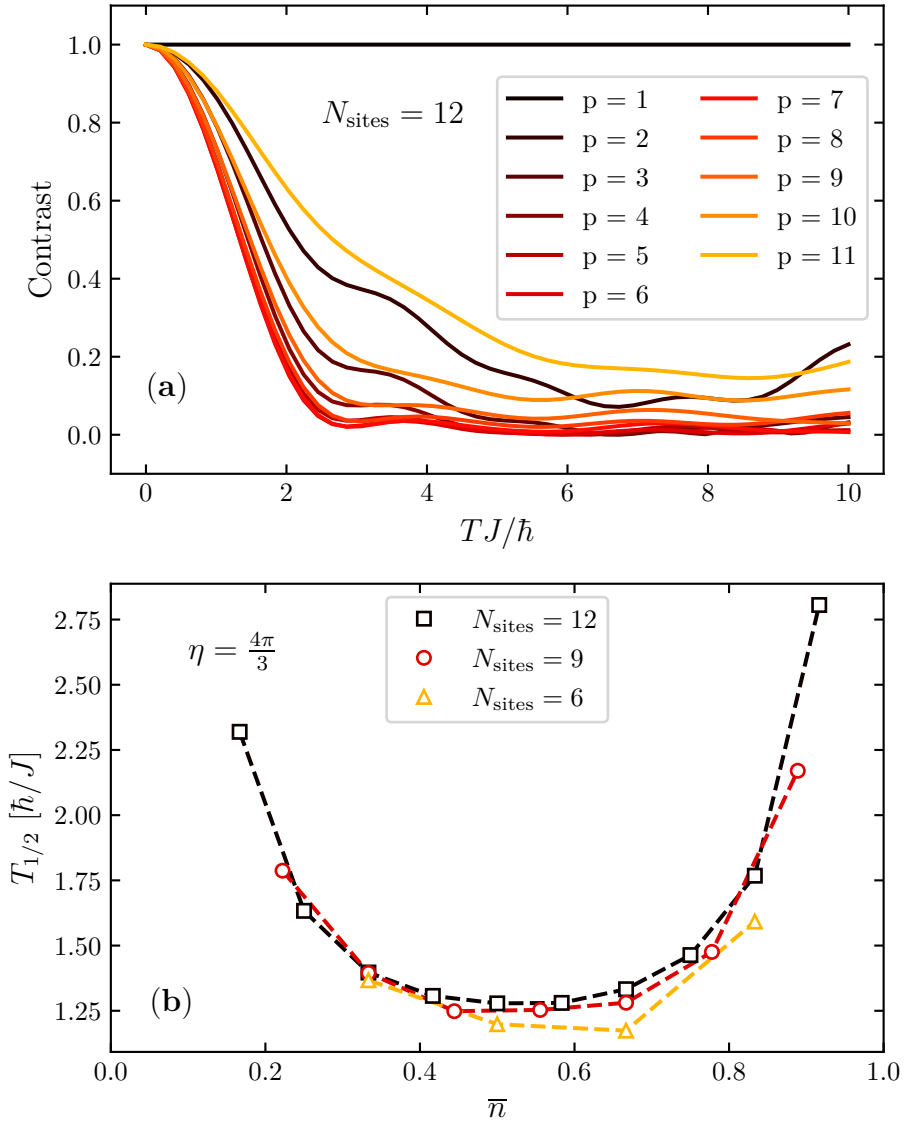

Figure 4.8 – Simulations of the evolution of the contrast $\mathcal{C}$. **(a)** The results of simulations performed for $N_{\text{sites}} = 12$ for different numbers of particles p in the lattice, corresponding to different initial average fillings $\overline{n}$. **(b)** From the simulations realized for different $N_{\text{sites}} \in \{6, 9, 12\}$, we extract the time of half-decay $T_{1/2}$ for the contrast for different filling $\overline{n}$ of the lattice. Here the we have taken $\eta = \frac{4\pi}{3}$, which is a good approximation of the experimental configuration with $\theta = 0$

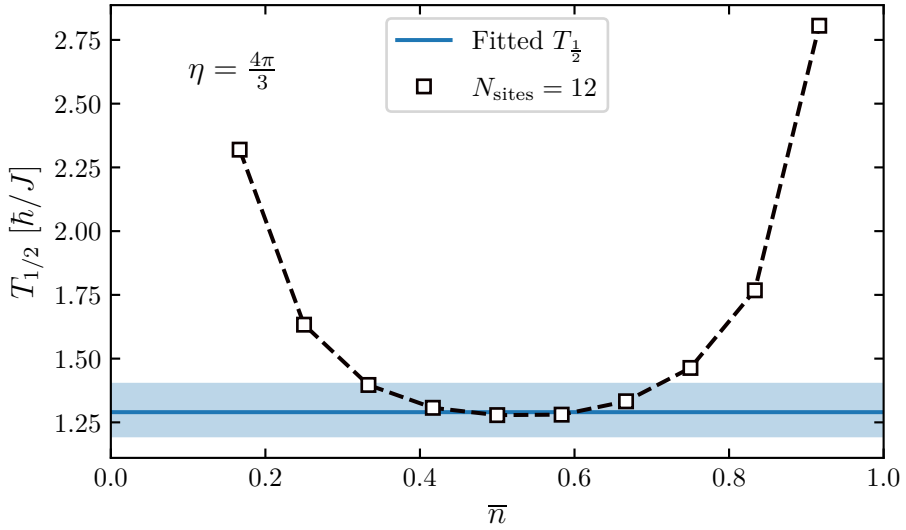

Figure 4.10 – Evolution of the time $T_{1/2}$ at which the simulated contrast of the Ramsey fringes reach 0.5 for the first time, for different number of particles p computed in simulations with a number of lattice sites equal to $N_{\text{sites}} = 12$ (black square). These simulated quantities are compared to an experimental global $T_{1/2}$ (blue line) computed by performing a linear regression on the experimental $T_{1/2}$ obtained for different lattice depths, with $\theta = 0$, as a function of the tunneling rate $J/\hbar$. The blue shaded area correspond the uncertainty on the experimental $T_{1/2}$, taken at one statistical standard deviation and estimated by the linear regression procedure.

The analysis developed in this section of the evolution of the contrast of the Ramsey fringes gives us an initial average filling further from unity than expected. However we have to remark that physical quantities measured in our experiments are actually averaged values over the many isolated unidimensional optical lattices created by our loading procedure, whose initial average filling can be very different. Moreover, the local density approximation, introduced in Sec. 1.2.5, assert the presence of shells in the superfluid phase in the optical lattices, on the margin of the regions in the Mott-insulator phase. The effect resulting from the presence of such regions are not taken into account in our model. Lastly the effect of the harmonic auxiliary trapping potential is not taken into account in our modelization.

4.3 Conclusion

In this chapter we have proposed a first theoretical description of our experimental unidimensional optical lattice, in the general case with the Bose-Hubbard model, and in the strongly interacting regime, which leads us to introduce the formalism of *hard-core bosons*, that will be detailed later in this dissertation. This modeling coupled with the work made in the previous chapter allowed us to propose the use of Ramsey spectroscopy to probe the dynamics of the defects in our 1D optical lattice, by taking advantage of the phase imprinted by the clock laser on the atoms during the pulse of the Ramsey sequence. Finally, these results are compared to numerical simulations in order to have some quantitative information on the average filling of the optical lattice.

This information will be considered in our latter study of the 1D systems.

CHAPTER 5

Zeno effect and adiabatic passages in presence of atom losses

The long term perspective for our experiment is to use the clock transition of ^{174}Yb atoms to produce artificial gauge field, according to the protocol proposed in Gerbier et al. 2010. However the losses induced by the inelastic-collision between ^{174}Yb atoms in the $^1P_0$ state raise a supplementary difficulty. Moreover, as we will see in this chapter, it is experimentally difficult to selectively excite one atoms only in doubly occupied sites. In this chapter we will see how it is possible to overcome this issue by taking advantage of the *quantum Zeno effect* (QZE) arising from the existence of two-body losses between two atoms in the $^1P_0$ state.

After a presentation of the original quantum Zeno effect, due to repeated measurements, we will see how it arises an a generalized from in dissipative open quantum systems. We will reformulate the dynamics in the framework of non-hermitian Hamiltonian. We will finally show that adiabatic passage experiment can be used to avoid populating lossy states involving lattice sites populated with a pair of interacting ^{174}Yb atoms both in the $^1P_0$ state. Indeed the losses will restrict the dynamics to the loss-restriced subspace of the Hilbert space.

5.1 The quantum Zeno effect and its avatars

In its *Physics* Aristotle, recount the paradox enunciated by Zeno of Elea:

"If everything when it occupies an equal space is at rest at that instant of time, and if that which is in locomotion is always occupying such a space at any moment, the flying arrow is therefore motionless at that instant of time and at the next instant of time but if both instant of time are taken as the same instant or continuous instant of time then it is in motion."

— Aristotle, *Physics* VI:9, 239b5

The paradox that states that an arrow, while being in motion, is motionless at each considered instant of the motion, since the duration of a instant is null? Since its for-

mulation, this paradox had been discussed and refuted by many authors after Aristotle, until progress in the mathematics of infinitesimal calculus of the late 19$^{\text{th}}$ century formally solve it, by introducing the notion of instantaneous speed, coming for differential calculus.

5.1.1 A toy model for "pulsed" repeated measurements

Zeno's paradox found a resonance in the realm of quantum physics with the so-called *quantum Zeno effect*, highlighted for the first time in the seminal publication of Misra et al. 1977. The core idea behind the quantum Zeno effect is that it is possible to hinder or even freeze the dynamic evolution of a quantum system *via* repeated measurements of the system. This phenomenon can be illustrated by a simple model inspired by the proposal of Cook 1988. As previously seen in 3.3.1, the evolution of a two-level atom driven by a resonant monochromatic field with Rabi frequency Ω_{L} is given by the Liouville-Von Neumann equation:

$$\mathrm{i}\hbar\frac{\mathrm{d}\hat{\rho}}{\mathrm{d}t} = \left[\hat{H},\,\hat{\rho}\right] \quad \text{with} \quad \hat{H} = \frac{\hbar\Omega_{\text{L}}}{2}\hat{\sigma}_x, \quad \hat{\rho}\,(0) = \frac{1}{2}\left(\mathbb{1} - \hat{\sigma}_z\right) = |e\rangle\langle e|. \tag{5.1}$$

We note $|g\rangle$ and $|e\rangle$ the ground and the excited states respectively of the atom and assume that it is initially in $|e\rangle$. The resolution of the differential equations (5.1) gives

$$\hat{\rho}\,(t) = \begin{pmatrix} \sin^2\left(\Omega_{\text{L}}t/2\right) & -\frac{\mathrm{i}}{2}\sin\left(\Omega_{\text{L}}t\right) \\ \frac{\mathrm{i}}{2}\sin\left(\Omega_{\text{L}}t\right) & \cos^2\left(\Omega_{\text{L}}t/2\right) \end{pmatrix}. \tag{5.2}$$

When the internal state of the atom is measured over time, by considering observables such as $\hat{\mathcal{A}} = \hat{\sigma}_z$, the probability for the atom to be projected back on the $|e\rangle$ state is:

$$P_e\,(0,\tau,1) = \mathrm{Tr}\Big[|e\rangle\langle e|\hat{\rho}\,(\tau)\Big] = \rho_{ee}\,(\tau) = \frac{1}{2}\left[1 + \cos\left(\Omega_{\text{L}}\tau\right)\right], \tag{5.3}$$

with τ the time after the measurement. From this expression it is possible to see that for duration τ short enough after the measurement, *i.e.* if $\Omega_{\text{L}}\tau \ll 1$, the probability to measure again the atom in state $|e\rangle$ can be expanded as $P_e\,(0,\tau,1) \approx 1 - \frac{1}{4}\Omega_{\text{L}}^2\tau^2 + \mathcal{O}\left(\Omega_{\text{L}}^4\tau^4\right)$ and remains close to one. As a consequence if n measurements $\hat{\mathcal{A}}$ are performed during a time lapse T at regular intervals separated by $\tau = T/n$, so that $\Omega_{\text{L}}\tau \ll 1$, the atom is likely to be projected every time on the $|e\rangle$ state. More precisely, the probability for the atom to stay in $|e\rangle$ over the whole time T is equal to

$$P_e\,(0,\,T,\,n) = \left[\cos^2\left(\frac{\Omega_{\text{L}}T}{2n}\right)\right]^n = 1 - \frac{\Omega_{\text{L}}^2T^2}{4n} + \mathcal{O}\left(\frac{1}{n^2}\right), \tag{5.4}$$

which can be approximated for $n \to \infty$ as:

$$P_e\,(0;\,T;\,n) \approx \frac{1}{2}\left[1 + \mathrm{e}^{-\frac{1}{2}\Omega_{\text{L}}^2\tau T}\right] \quad \text{with} \quad \tau = T/n. \tag{5.5}$$

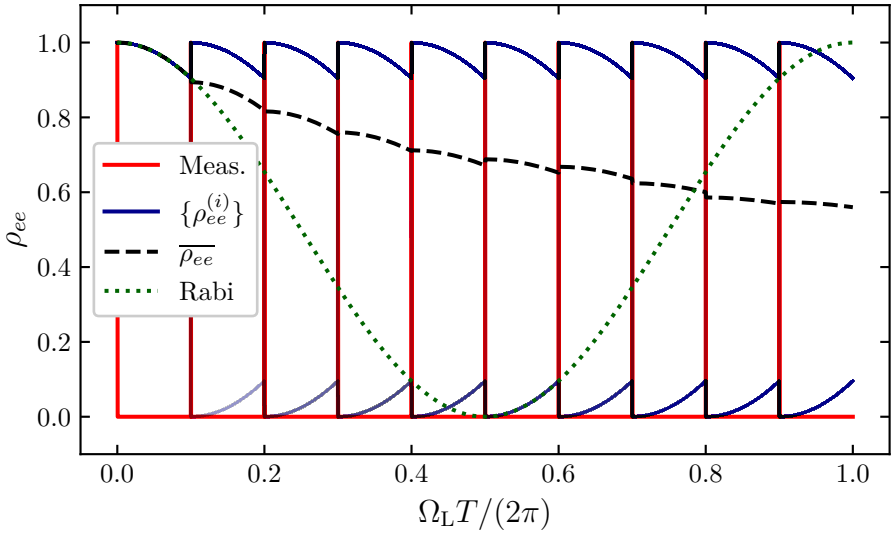

Figure 5.1 – Pulsed quantum Zeno effect. The probability to find a two-level atoms driven by a resonant monochromatic electric field with Rabi frequency Ω_L whose internal state is measured every $\Omega_L \tau = 2\pi \times 0.1$. The superposed light blue curves represent 200 quantum trajectories for such system. For each curve, between each pulse, the system evolves driven by the Hamiltonian $\hat{H}$ written in (5.1) until the next measurement (represented as read peaks), where the system is projected in state $|e\rangle$ or $|g\rangle$ with probabilities ρ_{ee} and $1 - \rho_{ee}$ respectively. The dashed black line is their average. The green dotted line corresponds to the the Rabi flopping observed in absence of measurement. In average, the dynamics of the internal state of the atom towards $|g\rangle$ has been hindered.

The probability for the atom to stay in the state $|e\rangle$ now only decay at rate $\frac{1}{2}\Omega_L^2 \tau$: the evolution of the internal state of the atom has been slowed down. A simulation of this example over 200 quantum trajectories is proposed in Fig. 5.1 for $\Omega_L \tau = 2\pi \times 0.1$.

The quantum Zeno effect has been observed for the first time in Itano et al. 1990 in an experiment involving beryllium ions, with a protocol following the ideas developed in Cook 1988: the states $|g\rangle$ and $|e\rangle$ are two hyperfine sublevels of the ground state of $^9Be^+$, with negligible spontaneous emission from $|e\rangle$ to $|g\rangle$, coupled by a RF field. Here the measurement consists in coupling the ground state to a third level $|f\rangle$ which has a strong decay channel to the ground state $|g\rangle$ only: the number of photons spontaneously emitted after each measurement pulse is proportional to the number of ions in the $|g\rangle$ state. The experiment showed that it was possible to arbitrarily hinder the transfer to state $|e\rangle$ by increasing the frequency at which the system is probed, highlighting the Zeno effect.

5.1.2 Zeno effect in the case of continuous measurement

According to the description given by Von Neumann 1932 each pulsed measurement considered so far projects the system in one of the eigenstates (or eigenspace in case of degeneracy) of the measured observable $\hat{\mathcal{A}}$. However in most cases, a measurement

actually consists in coupling the system with an external measurement device for a given period of time. Typically the measurement device has many degrees of freedom and functionally behaves as an "environment", as in the theory of decoherence. Keeping this idea in mind, it is possible to reconsider the quantum Zeno effect as a consequence of the coupling between the state of the system under study and a this large external environment. In particular, if the measurements are not read, the state of the system after each measurement can only be described as statistical mixture of the possible outcomes. Moreover, if the time between two unread measurements is much shorter than the characteristic timescales at which the system under study evolves, it is possible to write its evolution in the continuous measurement limit, using the same Born-Markov approach leading to the quantum master equation (Haroche et al. 2013, Breuer et al. 2007). Consequently the dynamics of the system can be described by a Lindblad master equation (Lindblad 1976; Gorini et al. 1976):

$$\frac{\mathrm{d}\hat{\rho}}{\mathrm{d}t} = -\frac{\mathrm{i}}{\hbar}\left[\hat{H},\hat{\rho}\right] + \frac{\gamma}{2}\left[2\hat{\mathcal{A}}\hat{\rho}\hat{\mathcal{A}}^\dagger - \hat{\mathcal{A}}^\dagger\hat{\mathcal{A}}\hat{\rho} - \hat{\rho}\hat{\mathcal{A}}^\dagger\hat{\mathcal{A}}\right], \tag{5.6}$$

with γ characterizing the frequency and the strength of the measurements.

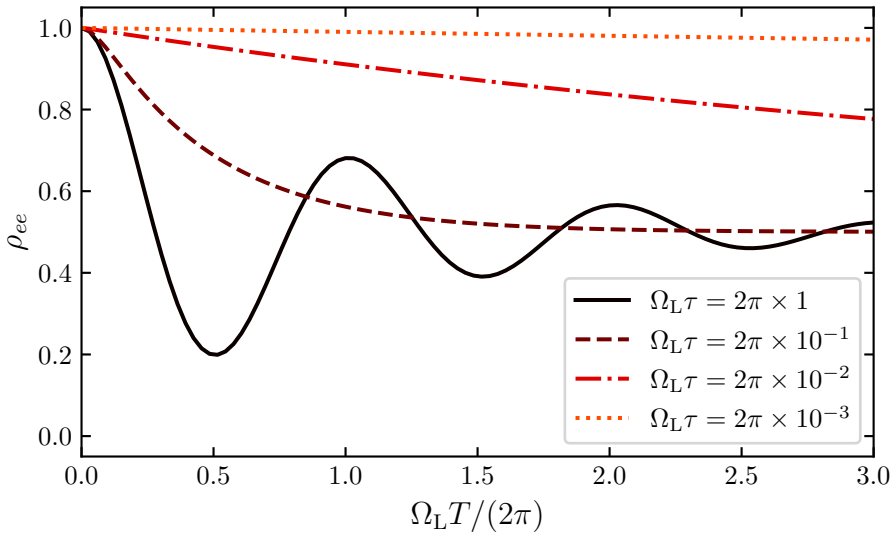

Figure 5.2 – Quantum Zeno effect. Evolution of the population in the excited state $|e\rangle$ in the model presented in (5.7) for different measurement frequencies. When the frequency of the measurement becomes much higher than the Rabi frequency, the internal dynamics of the atoms is hindered.

The continuous unread measurement limit for the model described in 5.1.1, with $\hat{\mathcal{A}} = \hat{\sigma}_z$ and $\gamma = 1/\tau$, gives the following master equation to describe its evolution:

$$\frac{\mathrm{d}\hat{\rho}}{\mathrm{d}t} = -\mathrm{i}\frac{\Omega_\mathrm{L}}{2}\left[\hat{\sigma}_x,\hat{\rho}\right] + \frac{1}{2\tau}\left[2\hat{\sigma}_z\hat{\rho}\hat{\sigma}_z^\dagger - \hat{\sigma}_z^\dagger\hat{\sigma}_z\hat{\rho} - \hat{\rho}\hat{\sigma}_z^\dagger\hat{\sigma}_z\right]. \tag{5.7}$$

The probability to find the atom in its initial state $|e\rangle$ at time t in presence of repeated

measurements $\hat{\mathcal{A}} = \hat{\sigma}_z$ at frequency τ^{-1} is given by:

$$\langle e|\hat{\rho}\,(t)\,|e\rangle = \rho_{ee}\,(t) = \frac{1}{2} + \frac{K_+ \mathrm{e}^{-K_- t} - K_- \mathrm{e}^{-K_+ t}}{2\,(K_+ - K_-)} \tag{5.8}$$

$$K_\pm = \frac{1 \pm \sqrt{1 - \Omega_\mathrm{L}^2 \tau^2}}{\tau}. \tag{5.9}$$

From the expression (5.9), we notice that the transition from under- to over- damping of ρ_{ee} as τ decays, occurring for $\Omega_\mathrm{L}\tau = 1$.

In the limit where $\Omega_\mathrm{L}\tau \ll 1$, this expression can be approximated as $\rho_{ee}\,(t) \approx \frac{1}{2}\left[1 + \mathrm{e}^{-\gamma_\mathrm{eff} t}\right]$ with $\gamma_\mathrm{eff} = \frac{1}{2}\Omega_\mathrm{L}^2 \tau$. This decay rate is the same as the one found in (5.5). The probability to find the atom in $|e\rangle$ decays exponentially, with a characteristic time that can be tuned by the choice of τ. For infinitely fast measurements ($\tau \to 0$), it is possible to "freeze" the atom in its initial state.

5.1.3 Losses induced quantum Zeno effect

The reasoning developed above can be extended (Haroche et al. 2013, Breuer et al. 2007), in the framework of generalized measurements and using the Kraus sum representation Kraus et al. 1983, to any linear quantum process which does not involve a read-out measurement. It is especially the case for open quantum system facing two-body inelastic collisions-induced losses, which corresponds to the situation studied in our experiments. More precisely the experimental apparatus under study in this chapter consists in a collection of independent dipole traps (the sites of the optical lattice), initially filled with two interacting bosons, each with two internal states $\{|g\rangle, |e\rangle\}$, whose unitary evolution, enclosed in the Hamiltonian $\hat{H}^{(2)}$ (that will be explicited later) is interrupted by stochastic inelastic two-body losses. The full Lindblad master equation describing such system is:

$$\begin{aligned}
\frac{d\hat{\rho}_2}{dt} = &-\frac{\mathrm{i}}{\hbar}\left[\hat{H}^{(2)}, \hat{\rho}_2\right] \\
&+ \frac{\Gamma_{gg}}{4}\left(2\hat{a}_g\hat{a}_g\hat{\rho}_2\hat{a}_g^\dagger\hat{a}_g^\dagger - \hat{\rho}_2\hat{a}_g^\dagger\hat{a}_g^\dagger\hat{a}_g\hat{a}_g - \hat{a}_g^\dagger\hat{a}_g^\dagger\hat{a}_g\hat{a}_g\hat{\rho}_2\right), \\
&+ \frac{\Gamma_{eg}}{2}\left(2\hat{a}_e\hat{a}_g\hat{\rho}_2\hat{a}_g^\dagger\hat{a}_e^\dagger - \hat{\rho}_2\hat{a}_g^\dagger\hat{a}_e^\dagger\hat{a}_e\hat{a}_g - \hat{a}_g^\dagger\hat{a}_e^\dagger\hat{a}_e\hat{a}_g\hat{\rho}_2\right) \\
&+ \frac{\Gamma_{ee}}{4}\left(2\hat{a}_e\hat{a}_e\hat{\rho}_2\hat{a}_e^\dagger\hat{a}_e^\dagger - \hat{\rho}_2\hat{a}_e^\dagger\hat{a}_e^\dagger\hat{a}_e\hat{a}_e - \hat{a}_e^\dagger\hat{a}_e^\dagger\hat{a}_e\hat{a}_e\hat{\rho}_2\right).
\end{aligned} \tag{5.10}$$

Here $\hat{a}_g$ (resp. $\hat{a}_e$) is the annihilation operator for a boson in state $|g\rangle$ (resp. $|e\rangle$) and $\Gamma_{i,j}$ are the two-body losses rates for a boson in state i and the other in state j.

In our particular case, there is no inelastic collision between two atoms in the ground state $|g\rangle$ ($\Gamma_{gg} = 0$) and that at the timescales of our experiments, the loss rate for the inelastic collisions between two atoms in different states is negligible ($\Gamma_{eg} \ll \Gamma_{ee}$). We thus rewrite the master equation (5.10) as:

$$\frac{d\hat{\rho}_2}{dt} = -\frac{\mathrm{i}}{\hbar}\left[\hat{H}^{(2)}, \hat{\rho}_2\right] + \frac{\Gamma_{ee}}{4}\left(2\hat{a}_e\hat{a}_e\hat{\rho}_2\hat{a}_e^\dagger\hat{a}_e^\dagger - \hat{\rho}_2\hat{a}_e^\dagger\hat{a}_e^\dagger\hat{a}_e\hat{a}_e - \hat{a}_e^\dagger\hat{a}_e^\dagger\hat{a}_e\hat{a}_e\hat{\rho}_2\right), \tag{5.11}$$

which is analogous to the Lindblad master equation (5.6) taking $\gamma = \Gamma_{ee}$ and $\hat{\mathcal{A}} = \frac{1}{\sqrt{2}}\hat{a}_e\hat{a}_e$ as the generalized non-Hermitian measurement operator.

5.2 Effective Non Hermitian Hamiltonian

5.2.1 Effective dynamics and quantum jumps

The master equation (5.11) can be unraveled as a way to compute the average of the quantum trajectories of each individual system which follow an unitary evolution interspersed with stochastic quantum jumps (here the inelastic two-body collisions). This point of view can be emphasized by rearranging the different terms of the master equation (5.11) as:

$$\frac{d\hat{\rho}_2}{dt} = -\frac{\mathrm{i}}{\hbar}\left(\hat{H}_{\text{eff}}\hat{\rho}_2 - \hat{\rho}_2\hat{H}_{\text{eff}}^\dagger\right) + \hat{L}_{ee}\hat{\rho}_2\hat{L}_{ee}^\dagger \tag{5.12}$$

with

$$\hat{H}_{\text{eff}} = \hat{H}^{(2)} - \frac{\mathrm{i}\hbar}{2}\hat{L}_{ee}^\dagger\hat{L}_{ee} \quad \text{and} \quad \hat{L}_{ee} = \sqrt{\frac{\Gamma_{ee}}{2}}\hat{a}_e\hat{a}_e = \sqrt{\Gamma_{ee}}\hat{\mathcal{A}}. \tag{5.13}$$

The first term of the r.h.s. of the master equation (5.12) expresses an evolution of the system driven by the effective non-Hermititan Hamiltonian $\hat{H}_{\text{eff}}$, according to the Schrödinger equation,

$$\mathrm{i}\hbar\frac{\mathrm{d}|\psi\rangle}{\mathrm{d}t} = \hat{H}_{\text{eff}}|\psi\rangle, \tag{5.14}$$

interrupted at random times by sudden quantum jumps corresponding to a two-body inelastic collision,

$$|\psi\rangle \to \hat{L}_{ee}|\psi\rangle, \tag{5.15}$$

These jumps occur with a probability density $\mathcal{P}(t)$, such that:

$$\mathrm{d}\mathcal{P} = \langle\psi|\hat{L}_{ee}^\dagger\hat{L}_{ee}|\psi\rangle\mathrm{d}t = \mathrm{Tr}\left[\hat{L}_{ee}\hat{\rho}_2\hat{L}_{ee}^\dagger\right]\mathrm{d}t. \tag{5.16}$$

The occurrence of these random events are enclosed in the second term of the r.h.s of (5.12). This picture of the dynamics of the system is at the core of the *Monte-Carlo wave-function* (MCWF) approach has been originally developed in Dalibard et al. 1992; Dum et al. 1992; Plenio et al. 1998 to deal with dissipative process in quantum optics, in particular when only averaged predictions matters, as it is the case for the quantum master equation point of view.

In the case of inelastic two-body collisions induced losses, the effect of the dissipative term $\hat{L}_{ee}$ results in sending a lattice site initially lying in the sub-Hilbert space defined by $\langle\hat{a}_g^\dagger\hat{a}_g + \hat{a}_e^\dagger\hat{a}_e\rangle = 2$, and spanned by the Fock states $\{|2\rangle_g\otimes|0\rangle_e,\ |1\rangle_g\otimes|1\rangle_e,\ |0\rangle_g\otimes|2\rangle_e\}$, to the vacuum state $|0\rangle_g \otimes |0\rangle_e$ where its dynamics stops. In a context where the experiment is performed on a large number of independent and identical lattice sites initially filled with two bosons, only the average dynamics of the "surviving" ones, described by $\hat{H}_{\text{eff}}$ will be recorded. Consequently, we can restrict the description of our system to the hyperplane of the Hilbert space generated by $\{|2\rangle_g \otimes |0\rangle_e,\ |1\rangle_g \otimes$

$|1\rangle_e$, $|0\rangle_g \otimes |2\rangle_e\}$ and not worry about the two-body losses are then rendered by the non-unitarity of the evolution, due to the anti-Hermitian part of $\hat{H}_{\text{eff}}$ that will damp the norm of the wave-function during its evolution.

In the rest of this chapter we adopt this picture and describe the system as a doubly-occupied lattice site evolving according to a non-Hermitian Hamiltonian $\hat{H}_{\text{eff}}$.

5.2.2 Interacting bosonic pairs in a deep optical lattice

Before going further in our study of the quantum Zeno effect for bosons pairs trapped in the sites of an optical lattice, we have to do a little detour to precise some aspects of our experimental setup and complete the model established above.

As seen in section 1.2.4 the gaussian nature of the beam constitutive of the optical lattice creates a spatial modulation of the lattice depth that can be rendered by adding an auxiliary harmonic confining potential to the one of the homogeneous optical lattice. It results in a inhomogeneous distribution of atoms over the lattice. In this chapter we will pay a special attention to the case of a deep optical lattice at magic wavelength $\lambda_{\text{m}} = 759.35\,\text{nm}$, in the strongly interacting regime ($J/U \to 0$), with only singly ($\overline{n} = 1$) and doubly ($\overline{n} = 2$) occupied sites. This situation is experimentally realized by loading an optical lattice with depths $V_{x,y,z} = \{25,\, 25,\, 27\}\, E_{\text{R}}$ with a BEC of $N_{\text{at}} \leq 6 \times 10^4$ atoms so that the fraction of triply occupied sites is small (below 10 %) if not negligible, according to the loading model presented in section 2.3.3. Moreover we may consider, similarly to Bouganne et al. 2017 that the triply occupied sites are emptied quickly by three-body collisions mechanisms and do not play any significant role.

For the considered lattice depths, the tunneling between sites can be neglected ($h/J \approx 500\,\text{ms}$ at $25\,E_{\text{R}}$) and the lattice sites can be treated as a collection of independent traps with one or two bosons. These atoms are probed on the ${}^1\text{S}_0 \to {}^3\text{P}_0$ clock transition by a laser beam that propagates in the horizontal plane, along the x axis of the optical lattice. The high lattice depth of the trap ensures to work in the Lamb-Dicke regime.

In the rest of this chapter we adopt the notations for the internal states of the atoms: $|g \equiv {}^1\text{S}_0\rangle$ and $|e \equiv {}^3\text{P}_0\rangle$.

Model for singly occupied sites

As explained in Chap. 2, according to the loading model for the optical lattice detailed in 2.3.3, a Mott-insulator with a core of doubly-occupied sites is necessary surrounded by a ring of singly-occupied sites, because of the presence of an auxiliary trapping potential. Using the same language as for the doubly-occupied sites, the dynamics in the singly-occupied sites is described by the Liouville-Von Neumann equation:

$$\frac{\mathrm{d}\hat{\rho}_1}{\mathrm{d}t} = -\frac{\mathrm{i}}{\hbar}\left[\hat{H}^{(1)}, \hat{\rho}_1\right], \tag{5.17}$$

with $\hat{\rho}_1$ the density matrix for singly-occupied sites and $\hat{H}^{(1)}$ the Hamiltonian:

$$\hat{H}^{(1)} = -\frac{\hbar\Omega_{\text{L}}}{2}\left(\hat{a}_e^\dagger \hat{a}_g + \hat{a}_g^\dagger \hat{a}_e\right) - \hbar\delta_{\text{L}}\hat{a}_e^\dagger \hat{a}_e \tag{5.18}$$

where Ω_{L} is the Rabi frequency and $\delta_{\mathrm{L}} = \omega_{\mathrm{L}} - \omega_0$ the detuning of the coupling laser, already introduced in Chap. 3.

This Hamiltonian can put into matrix from, in the $\{ |g\rangle, |e\rangle \}$ basis that span the sub-Hilbert space in which evolves the singly occupied sites as:

$$\hat{H}^{(1)} = \begin{pmatrix} 0 & \frac{\hbar\Omega_{\mathrm{L}}}{2} \\ \frac{\hbar\Omega_{\mathrm{L}}}{2} & -\hbar\delta_{\mathrm{L}} \end{pmatrix}. \tag{5.19}$$

In the following, at a given Rabi frequency Ω_{L}, we will denote $|-\rangle$ the eigenstate of $\hat{H}^{(1)}$ which converges toward $|g\rangle$ in the limit $\delta_{\mathrm{L}} \to -\infty$. The other eigenstate will be denoted $|+\rangle$ and converges toward $|g\rangle$ in the limit $\delta_{\mathrm{L}} \to +\infty$.

Model for doubly occupied sites

The non-dissipative dynamics of the doubly-occupied sites enclosed in the Hamiltonian $\hat{H}^{(2)}$ is the results of the elastic collisions on the one hand and of the electromagnetic coupling on the other hand. The Hamiltonian can be express in the Rotating Wave approximation (RWA) (see Chap. 3) as:

$$\hat{H}^{(2)} = \frac{U_{gg}}{2}\hat{a}_g^\dagger\hat{a}_g^\dagger\hat{a}_g\hat{a}_g + \frac{U_{ee}}{2}\hat{a}_e^\dagger\hat{a}_e^\dagger\hat{a}_e\hat{a}_e + U_{eg}\hat{a}_e^\dagger\hat{a}_g^\dagger\hat{a}_g\hat{a}_e - \frac{\hbar\Omega_{\mathrm{L}}}{2}\left(\hat{a}_e^\dagger\hat{a}_g + \hat{a}_g^\dagger\hat{a}_e\right) - \hbar\delta_{\mathrm{L}}\hat{a}_e^\dagger\hat{a}_e. \tag{5.20}$$

The energy levels associated to the different possible internal configurations are shifted by the inter-atomic on-site interactions energies $U_{i,j}$. These energies can be expressed from the Wannier function $w(\mathbf{r})$ (which at magic wavelength is independent of the internal state for a lattice) as:

$$U_{ij} = \frac{4\pi\hbar^2}{m}a_{ij}\int |w(\mathbf{r})|^4 \,\mathrm{d}\mathbf{r}. \tag{5.21}$$

Here $i, j \in \{e, g\}$ and the a_{ij} are the scattering lengths characterizing the elastic collisions between an atom in state i and an atom in state j.

Two ^{174}Yb atoms in the $|g\rangle$ state only interact trough elastic collisions. However if one or both atoms are in the state $|e\rangle$, inelastic two-body collisions are also possible for pairs of atoms with one or two of them in $|e\rangle$, at rates Γ_{eg} and Γ_{ee} respectively. The coefficients $\Gamma_{i,j}$ are related to the Wannier functions by the relation:

$$\Gamma_{ij} = \beta_{ij}\int |w(\mathbf{r})|^4 \,\mathrm{d}\mathbf{r} \tag{5.22}$$

involving the coefficient β_{ij}, analogous, up to a factor $\hbar/2$, to the coupling parameter $g_{ij} = 4\pi\hbar^2 a_{ij}/m$ introduced in 1.2.1 that characterizes the s-wave contact interactions between atoms[27] .

[27]The quantity $-\frac{\hbar}{2}\beta_{ij}$ may be considered as the imaginary part of a complex coupling coefficient

In the end, using the derivation made in 5.2, we can express the effective non-Hermtitian Hamiltonian describing the dynamics of the doubly occupied sites as:

$$\hat{H}_{\text{eff}} = \hat{H}^{(2)} - \mathrm{i}\frac{\hbar\Gamma_{eg}}{2}\hat{n}_e\hat{n}_g - \mathrm{i}\frac{\hbar\Gamma_{ee}}{4}\hat{n}_e\left(\hat{n}_e - 1\right). \tag{5.24}$$

Here $\hat{n}_\alpha = \hat{a}_\alpha^\dagger \hat{a}_\alpha$ with $\alpha \in \{g, e\}$.

In the Fock basis $\{\ |gg\rangle = |2\rangle_g|0\rangle_e,\ |eg\rangle = |1\rangle_g|1\rangle_e,\ |ee\rangle = |0\rangle_g|2\rangle_e\ \}$ corresponding to the different possible configurations for the internal degrees of freedom of the trapped bosons, the Hamiltonian reduces to the matrix:

$$\hat{H}_{\text{eff}} = \begin{pmatrix} U_{gg} & \frac{\hbar\Omega_{\text{L}}}{\sqrt{2}} & 0 \\ \frac{\hbar\Omega_{\text{L}}}{\sqrt{2}} & U_{eg} - \hbar\delta_{\text{L}} - \mathrm{i}\frac{\hbar\Gamma_{eg}}{2} & \frac{\hbar\Omega_{\text{L}}}{\sqrt{2}} \\ 0 & \frac{\hbar\Omega_{\text{L}}}{\sqrt{2}} & U_{ee} - 2\hbar\delta_{\text{L}} - \mathrm{i}\frac{\hbar\Gamma_{ee}}{2} \end{pmatrix}. \tag{5.25}$$

This effective model for the dynamics of the doubly occupied sites has been used in Bouganne et al. 2017 and Franchi et al. 2017 to determine experimentally the values of the quantities associated with the two-body elastic and inelastic collisions of ^{174}Yb atoms.

Elastic scattering length measurements

As mentioned earlier the $a_{gg} = 105\,a_0$ scattering length has been measured in Kitagawa et al. 2008 with a_0 the Bohr's radius. The scattering lengths associated with the other eg and ee elastic interaction have been experimentally measured in Bouganne et al. 2017 and Franchi et al. 2017 by performing clock spectroscopy in a deep optical lattice showing different filling over the sites:

- the resonance for the $|g\rangle \to |e\rangle$ transition is observed for $\delta_{\text{L}} = 0$
- the resonance for the $|gg\rangle \to |eg\rangle$ transition is observed for $\delta_{\text{L}} = \left(U_{eg} - U_{gg}\right)/\hbar$
- the resonance for the $|gg\rangle \to |ee\rangle$ transition is observed for $\delta_{\text{L}} = \left(U_{ee} - U_{gg}\right)/(2\hbar)$.

A scheme of these transition is proposed in Fig. 5.3.

$\underline{g}_{ij} = \frac{4\pi\hbar^2}{m}\underline{a}_{i,j}$, with $\underline{a}_{i,j}$ the complex scattering length. From this it is possible to define a extended complex on-site interaction energy:

$$\underline{U}_{ij} = U_{ij} - \mathrm{i}\frac{\hbar\Gamma_{ij}}{2} = \left[\frac{4\pi\hbar^2}{m}a_{i,j} - \mathrm{i}\frac{\hbar}{2}\beta_{ij}\right]\int |w\left(\mathbf{r}\right)|^4\,\mathrm{d}\mathbf{r}. \tag{5.23}$$

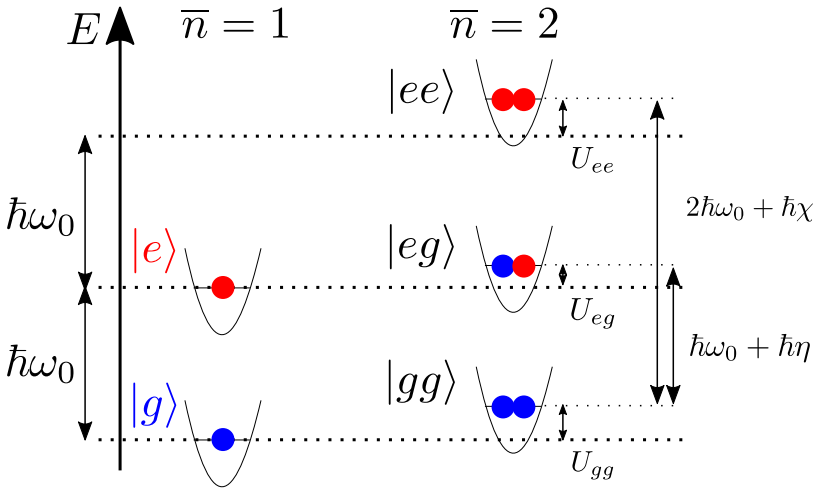

Figure 5.3 – Scheme of the energy levels for the different states of singly $\overline{n} = 1$ and doubly $\overline{n} = 2$ occupied sites. The on-site two-body elastic collisions in the $\overline{n} = 2$ case shift the energy between the different possible states separated by multiple of $\hbar\omega_0$, the energy gap between the two accessible internal states.

Consequently, the spacings between the peaks of the spectrum give access to the quantities: $a_{eg} - a_{gg}$ and $a_{ee} - a_{gg}$ and, from the known value of a_{gg}, the values of a_{eg} and a_{gg}.

Inelastic collision rates

The two-body losses rates are measured by performing lifetimes experiments in optical lattice populates with a significant fraction of doubly occupied sites in the state associated to the two-body loss mechanism under study ($|ee\rangle$ for Γ_{ee} and $|eg\rangle$ for Γ_{eg}).

The experiments performed in Bouganne et al. 2017 and Franchi et al. 2017 do not allow to give a value for Γ_{eg}, only a upper bound, which is specified for both references in Table 5.5. In the following, we will neglect this effect at the timescales of our experiments and take $\Gamma_{eg} \approx 0$.

To measure Γ_{ee}, a π pulse resonant with the $|gg\rangle \rightarrow |ee\rangle$ transition is send in an optical lattice with sites of filling $\overline{n} \in \{1, 2\}$, in order have a majority of doubly osccupied sites in the state $|ee\rangle$. Then the coupling light is switched off and the decay of atomic population is monitored. According to the model used in (5.25), the evolution the population of atoms in $|e\rangle$, given by the operator $\hat{n}_e = \hat{a}_e^\dagger \hat{a}_e$, in an individual doubly occupied lattice site, follow the equation:

$$\frac{\mathrm{d}\langle \hat{n}_e \rangle}{\mathrm{d}t} = -\Gamma_{ee} \langle \hat{n}_e \left(\hat{n}_e - 1 \right) \rangle, \tag{5.26}$$

and the probability P_{ee} to find atoms in a lattice site initially in state $|ee\rangle$ follow the equation:

$$\frac{\mathrm{d}P_{ee}}{\mathrm{d}t} = -\Gamma_{ee} P_{ee}. \tag{5.27}$$

Consequently the total population of atoms in $|e\rangle$, N_e evolves according to:

$$N_e\left(t\right) = 2\mathcal{N}^{(\overline{n}=2)} P_{ee}\left(0\right) \mathrm{e}^{-\Gamma_{ee} t} + \mathcal{N}^{(\overline{n}=1)} P_e\left(0\right) \tag{5.28}$$

with $\mathcal{N}^{(\overline{n}=2)}$ and $\mathcal{N}^{(\overline{n}=1)}$ the number of doubly and singly occupied sites in the lattice respectively, $P_{ee}(0)$ the initial probability to find a site with filling $\overline{n}=2$ in the $|ee\rangle$ state and $P_e(0)$ the initial probability to find a site with filling $\overline{n}=1$ in the $|e\rangle$ state. In Fig. 5.4 is displayed the experimental results of a lifetime experiment. The decay of atomic population is fitted according to fit techniques, more detailed in B. The first one, referred as χ^2 consists in evaluating the fit parameters by minimizing the weighted quadratic error between the fit function and the experimental points. The uncertainty on the fitted parameters is then determined by a $F-$test (Venables et al. 2002). The second one use bootstrap to compute from the experimental data estimates for the fit parameters and their distribution. In Fig. 5.4 we found $\Gamma_{ee} = 6 \pm 1 \times 10^3\,\mathrm{s}^{-1}$ with the statistic approach and $\Gamma_{ee} = 8 \pm 5 \times 10^3\,\mathrm{s}^{-1}$ with the bootstrap. These values consistent with the one found in Bouganne et al. 2017 and measured on a larger experimental dataset, but less accurate .

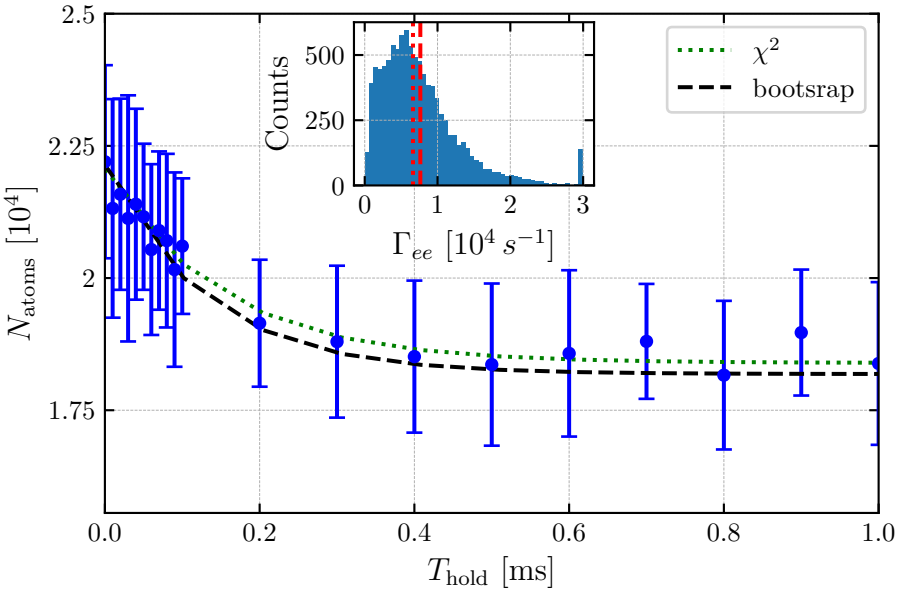

Figure 5.4 – Lifetime measurement in an optical lattice filled with ^{174}Yb atoms all in the $|e\rangle$ state. The population decay is the manifestation of the two-body inelastic collisions in the doubly occupied sites. The asymptote corresponds to the population of atoms in singly occupied sites. The fitted $N_e(t)$ functions obtained by two different fit procedures (see B) are represented: one relying on statistical tests, called χ^2 (green dotted line), and another one relying on bootstrap method (black dashed line). The decay rates estimated with both methods are respectively: $\Gamma_{ee} = 8 \pm 5 \times 10^3\,\mathrm{s}^{-1}$ with the bootstrap.

Summary

The experimental values found for the different parameters mentioned above by the groups of the Laboratoire Kastler Brossel (LKB) and the European Laboratory for Non-Linear Spectroscopy (LENS) are summarized in Fig. 5.5. In the rest of this dissertation we will use the more accurate values from LENS for the elastic-collision parameters and the LKB result for the loss coefficient β_{ee}.

Quantity	LKB (Bouganne et al. 2017)	LENS (Franchi et al. 2017)
a_{eg} $[a_0]$	86(11)	94.7(1.6)
a_{ee} $[a_0]$	102(25)	126.7(2.3)
β_{eg} $[\mathrm{cm}^3.\mathrm{s}^{-1}]$	$\leq 1 \times 10^{-15}$	$\leq 1 \times 10^{-14}$
β_{ee} $[\mathrm{cm}^3.\mathrm{s}^{-1}]$	$2.5(1) \times 10^{-11}$	$1.3(7) \times 10^{-11}$

Figure 5.5 – Values found experimentally for the elastic and inelastic collision parameters in Bouganne et al. 2017 and Franchi et al. 2017.

5.2.3 Properties of non-Hermitian Hamiltonian

The non-Hermitian effective Hamiltonian

Now that we have all the element to describe the evolution of single atoms and pairs of ^{174}Yb atoms trapped at the sites of our optical lattice, we focus on the study of a system driven by a non-Hermitian Hamiltonian.

In the rest of this chapter, in order to simplify the notations we will refer to $\hat{H}_{\mathrm{eff}}$ as $\hat{H}^{(2)}$. We rewrite it in a more compact form:

$$\hat{H}^{(2)}\left[\Omega_{\mathrm{L}},\, \delta_{\mathrm{L}}\right] = \hbar \begin{pmatrix} 0 & \frac{\Omega_{\mathrm{L}}}{\sqrt{2}} & 0 \\ \frac{\Omega_{\mathrm{L}}}{\sqrt{2}} & \eta - \delta_{\mathrm{L}} & \frac{\Omega_{\mathrm{L}}}{\sqrt{2}} \\ 0 & \frac{\Omega_{\mathrm{L}}}{\sqrt{2}} & \chi - 2\delta_{\mathrm{L}} - \mathrm{i}\frac{\Gamma}{2} \end{pmatrix}, \tag{5.29}$$

with the typical parameters:

- $\eta = \left(U_{eg} - U_{gg}\right)/\hbar \approx -2\pi \times 140\,\mathrm{Hz}$,
- $\chi = \left(U_{ee} - U_{gg}\right)/\hbar \approx 2\pi \times 290\,\mathrm{Hz}$,
- $\Gamma = \Gamma_{ee} \approx 2\pi \times 1400\,\mathrm{Hz}$,

for an optical lattice with depths $V_{x,y,z} = \{25,\, 25,\, 27\} E_{\mathrm{R}}$. Furthermore we can tune the light coupling strength Ω_{L} in the range $2\pi \times [0,\, 1500]$ Hz. We explore a range of detuning of a few kHz around the atomic resonance $\delta_{\mathrm{L}} = 0$ with a accuracy limited to about 50 Hz (see Chap. 3).

General properties of non-Hermitian Hamiltonian

Hermitian matrices can always be diagonalized on an orthogonal basis of eigenvectors $|\phi_j\rangle$ as

$$\hat{H}_{\mathrm{h}} = \sum_j \lambda_j |\phi_j\rangle\langle\phi_j| \quad \text{with} \quad \langle\phi_j|\phi_k\rangle = \delta_{jk} \quad \text{and} \quad \forall j,\ \lambda_j \in \mathbb{R}. \tag{5.30}$$

In the general case non-Hermitian matrices are not guaranteed to be diagonalizable. Their eigenvalues λ_j are complex and the eigenvectors associated with different eigen-

values are not necessary orthogonal. Assuming that a non-Hermitian matrix is diagonalizable, its eigendecomposition becomes (Ashida et al. 2020):

$$\hat{H}_{\mathrm{nh}} = \sum_j \lambda_j |\phi_j^{(r)}\rangle\langle\phi_j^{(l)}| \quad \text{with} \quad \langle\phi_j^{(l)}|\phi_k^{(r)}\rangle = \delta_{jk}, \quad \langle\phi_j^{(r)}|\phi_j^{(r)}\rangle = 1, \quad \lambda_j \in \mathbb{C}. \tag{5.31}$$

Here $\langle\phi_j^{(l)}|$ and $|\phi_j^{(r)}\rangle$ denote respectively the left and right eigenvectors (*a priori* non equal) of $\hat{H}_{\mathrm{nh}}$ associated to the complex eigenvalue λ_j, forming biorthogonal bases.

Properties of the symmetric non-Hermitian Hamiltonian

In our experiments, we are dealing with a continuous family of 3×3 symmetric non-Hermitian matrices parameterized by $\{\Omega_{\mathrm{L}}, \delta_{\mathrm{L}}\}$. They happen to be diagonalizable almost everywhere on the $(\Omega_{\mathrm{L}}, \delta_{\mathrm{L}})$ plane. Moreover, since the non-Hermitian Hamitonians under study are symmetric, the left and the right eigenvectors (when they exists) are related by the equation

$$\forall\, j \quad |\phi_j^{(r)}\rangle = \left(|\phi_j^{(l)}\rangle\right)^*. \tag{5.32}$$

In the following, in order to ease the notations, we will denote $\{|\lambda_j\rangle\}_{j=1,2,3}$ (resp. $\{\langle\tilde{\lambda}_j|\}_{j=1,2,3}$) the right (resp. left) eigenvectors associated to the eigenvalues $\{\lambda_j\}_{j=1,2,3}$, which form a *a priori* non-orthogonal basis of the Hilbert space. In this basis the Schrödinger equation becomes:

$$\mathrm{i}\hbar\frac{\mathrm{d}}{\mathrm{d}t}|\psi\,(t)\rangle = \sum_{j=1}^{3} \lambda_j |\lambda_j\rangle\langle\tilde{\lambda}_j|\psi\,(t)\rangle = \sum_{j=1}^{3} \lambda_j \hat{\Lambda}_j |\psi\rangle, \tag{5.33}$$

where $\hat{\Lambda}_j = |\lambda_j\rangle\langle\tilde{\lambda}_j|$ is the non-Hermitian projector related to the eigenvalue λ_j. Since the eigenvalues are complex we can decompose them as:

$$\lambda_j = \hbar\omega_j - \mathrm{i}\frac{\hbar\gamma_j}{2}. \tag{5.34}$$

From the theory of generalized measurements (Haroche et al. 2013), it is possible to express the probability π_j for a lattice site, described by the wavefunction $|\psi\rangle$ to lie in the eigenspace $\mathcal{E}_j$ associated to the eigenvalue λ_j:

$$\pi_j = \mathrm{Tr}\left[\hat{\Lambda}_j \hat{\rho} \hat{\Lambda}_j^\dagger\right] = \langle\tilde{\lambda}_j|\psi\rangle\langle\psi|\tilde{\lambda}_j\rangle \tag{5.35}$$

where $\hat{\rho}$ is the density matrix associated to the pure state $|\psi\rangle$. From the Schrödinger equation (5.33), it is possible to express the evolution of the quantity π_j as:

$$\frac{\mathrm{d}\pi_j}{\mathrm{d}t} = -\frac{\mathrm{i}}{\hbar}\left(\lambda_j - \lambda_j^*\right)\pi_j = -\gamma_j \pi_j, \tag{5.36}$$

which gives:

$$\pi_j\,(t) = \mathrm{e}^{-\gamma_j t}\pi_j\,(0)\,. \tag{5.37}$$

We recover here the idea that the imaginary part of the eigenvalues renders the lifetime of their corresponding eigenstate due to the two-body losses occurring in state $|ee\rangle$ at a rate:

$$\gamma_j = \Gamma_{ee}\langle ee|\lambda_j\rangle\langle\tilde{\lambda}_j|ee\rangle = \Gamma_{ee}|\langle ee|\lambda_j\rangle|^2. \tag{5.38}$$

The strength of the coupling between an eigenstate and the dissipative state $|ee\rangle$ determine the lifetime of the dressed state.

Since we are considering a continuous family of Hamiltonian $\hat{H}^{(2)}$ depending on the parameters $\{\Omega_\mathrm{L},\, \delta_\mathrm{L}\}$, the associated eigenvalues λ_j and eigenvectors $|\lambda_j\rangle$ ($j = 1,\, 2,\, 3$) are continuous and regular functions of the parameters almost everywhere on the $(\Omega_\mathrm{L},\, \delta_\mathrm{L})$ plane. We will by convention call $|\lambda_1\rangle$ the eigenstate that corresponds to the state $|gg\rangle$ in the limit of very large *negative* detunings ($\delta_\mathrm{L} \to -\infty$) and call $|\lambda_3\rangle$ the eigenstate that corresponds to the state $|gg\rangle$ in the limit of very large *positive* detunings ($\delta_\mathrm{L} \to +\infty$). We introduce the notation that will be used in the rest of this chapter to characterize the projection of the eigen-wavefunction for the doubly occupied sites on the Fock basis:

$$\begin{aligned}
\Pi^{(j)}_{gg}\left(\Omega_\mathrm{L},\, \delta_\mathrm{L}\right) &= |\langle gg|\lambda_j\left(\Omega_\mathrm{L},\, \delta_\mathrm{L}\right)\rangle|^2 \quad \text{and} \quad \theta^{(j)}_{gg}\left(\Omega_\mathrm{L},\, \delta_\mathrm{L}\right) = \arg\left[\langle gg|\lambda_j\left(\Omega_\mathrm{L},\, \delta_\mathrm{L}\right)\rangle\right]. \\
\Pi^{(j)}_{eg}\left(\Omega_\mathrm{L},\, \delta_\mathrm{L}\right) &= |\langle eg|\lambda_j\left(\Omega_\mathrm{L},\, \delta_\mathrm{L}\right)\rangle|^2 \quad \text{and} \quad \theta^{(j)}_{eg}\left(\Omega_\mathrm{L},\, \delta_\mathrm{L}\right) = \arg\left[\langle eg|\lambda_j\left(\Omega_\mathrm{L},\, \delta_\mathrm{L}\right)\rangle\right]. \\
\Pi^{(j)}_{ee}\left(\Omega_\mathrm{L},\, \delta_\mathrm{L}\right) &= |\langle ee|\lambda_j\left(\Omega_\mathrm{L},\, \delta_\mathrm{L}\right)\rangle|^2 \quad \text{and} \quad \theta^{(j)}_{ee}\left(\Omega_\mathrm{L},\, \delta_\mathrm{L}\right) = \arg\left[\langle ee|\lambda_j\left(\Omega_\mathrm{L},\, \delta_\mathrm{L}\right)\rangle\right].
\end{aligned} \tag{5.39}$$

And similarly we introduce for the singly occupied sites:

$$\begin{aligned}
\Pi^{(j)}_{g}\left(\Omega_\mathrm{L},\, \delta_\mathrm{L}\right) &= |\langle g|\epsilon_j\left(\Omega_\mathrm{L},\, \delta_\mathrm{L}\right)\rangle|^2. \\
\Pi^{(j)}_{e}\left(\Omega_\mathrm{L},\, \delta_\mathrm{L}\right) &= |\langle eg|\epsilon_j\left(\Omega_\mathrm{L},\, \delta_\mathrm{L}\right)\rangle|^2.
\end{aligned} \tag{5.40}$$

Exceptional points

As seen earlier, the continuous family of non-Hermitian Hamiltonian $\hat{H}^{(2)}$ parameterized by $\{\Omega_\mathrm{L},\, \delta_\mathrm{L}\}$ is diagonalizable almost everywhere. However at some points of the parameter plane the Hamitonian is nondiagonalizable. At these singularities called exceptional points (EP) (Kato 1966; Heiss 2012), two or more eigenvalues and their corresponding eigenvectors *coalesce*: they become identical and the dimension of the resulting eigenspace inferior to the sum of the dimension of the merged eigenspace around this point.

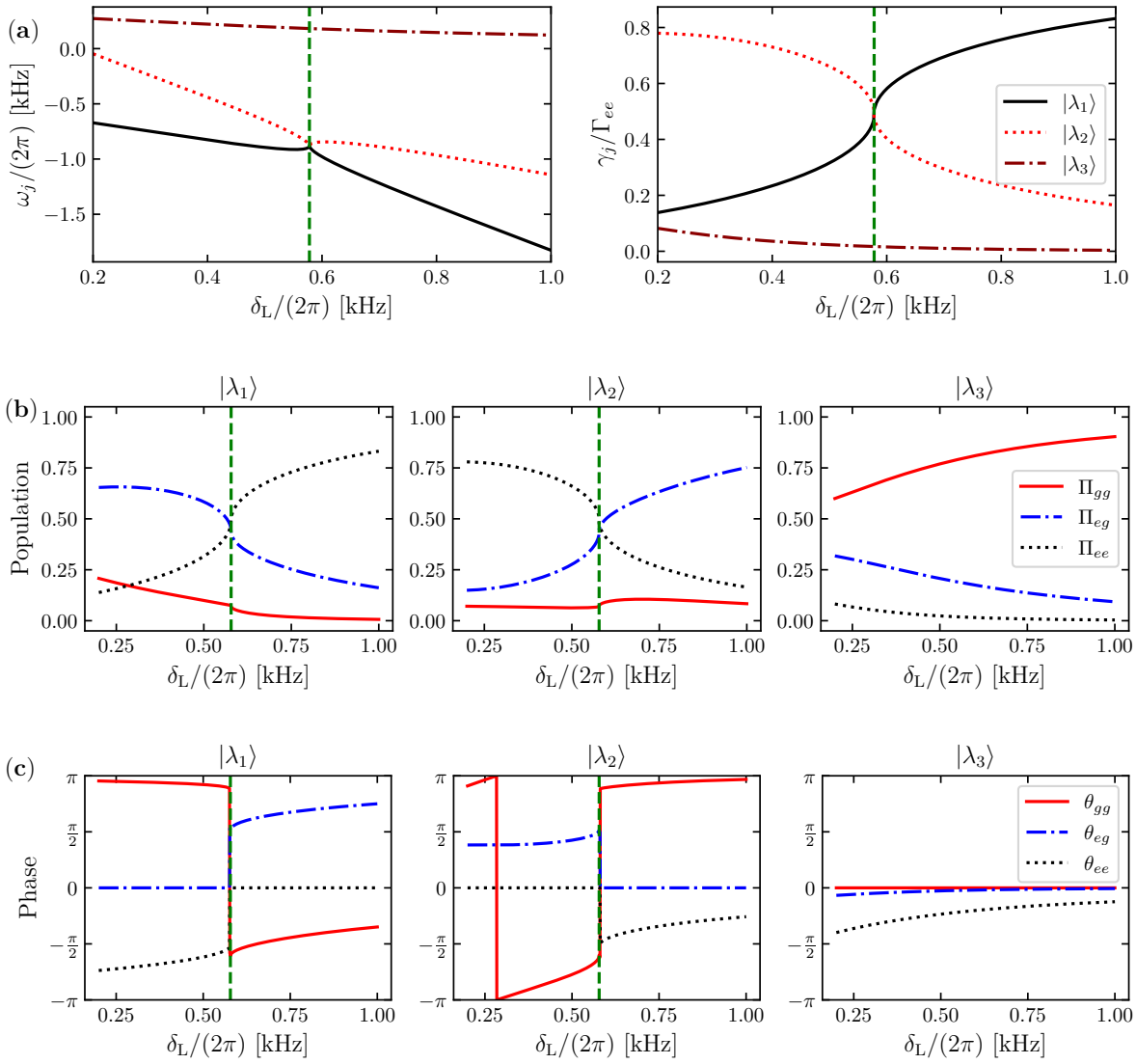

Figure 5.6 – Spectrum of $\hat{H}^{(2)}$ for $\Omega_{\mathrm{L},1,2}$. **(a)** Real (**left**) and imaginary (**right**) parts of of the eigenvalues. **(b)** Bare state composition of each dressed state. **(c)** Complex arguments of the projections of the dressed states on the bare states Fock basis. The vertical dashed line is located at $\delta_\mathrm{L} = \delta_{\mathrm{L},1,2}$. At this detuning, corresponding to an exceptional point, the eigenvalues λ_1 and λ_2 becomes identical, along with their associated eigenvectors $|\lambda_1\rangle$ and $|\lambda_2\rangle$

With our particular values of U_{gg}, U_{eg}, U_{ee} and Γ_{ee}, the eigenvalues of $\hat{H}^{(2)}$ only coalesce pairwise, in two points of the $(\Omega_\mathrm{L},\, \delta_\mathrm{L})$ plane:

- $\mathrm{EP}_{1,2}$ between $|\lambda_1\rangle$ and $|\lambda_2\rangle$ at $(\Omega_\mathrm{L},\, \delta_\mathrm{L})_{1,2} \approx 2\pi \times (541,\, 578)$ Hz
- $\mathrm{EP}_{2,3}$ between $|\lambda_2\rangle$ and $|\lambda_3\rangle$ at $(\Omega_\mathrm{L},\, \delta_\mathrm{L})_{2,3} \approx 2\pi \times (713,\, -12)$ Hz

The spectrum and some features of the eigenvectors for different detunings δ_L, at fixed Rabi frequency $\Omega_\mathrm{L} = 2\pi \times 541\,\mathrm{Hz}$ are represented in Fig. 5.6. The coalescence of the eigenvalues λ_1 and λ_2 and of their corresponding eigenvectors can be observed.

The exceptional points are an interesting feature arising from non-Hermitian dynamics. Even if these points are of null measure on the parameter space in which the Hamiltonian is considered, the non-Hermitian dynamics in their vicinities exhibits some interesting topological properties. In the Hermitian case, when circling adiabatically on closed loop of the parameter space, a system initially in the eigenstate $|\lambda_{i_0}\rangle$ returns to its initial position, up to a geometric phase acquired during the circling, called Berry phase (Berry 1984). In the non-Hermitian case, if the closed loop circles around an exceptional point, a system initially in the eigenstate $|\lambda_{i_0}\rangle$ may be sent at the end of the circling to another eigenstate $|\lambda_{i\neq i_0}\rangle$ of the Hamiltonian at the starting point of the loop, and some extra circling will be necessary to reach the initial eigenvector (Dembowski et al. 2001; Dembowski et al. 2004). The adiabaticity of such circling has been studied in (Milburn et al. 2015), and its chirality in Doppler et al. 2016.

The interest for exceptional points and their properties has arisen in a wide range of fields of physics and lead to the observation of several related effect such as: loss induced transmission and unidirectional invisibility (Peng et al. 2014;Lin et al. 2011), mode selection in lasers (Peng et al. 2014;Feng et al. 2014), enhanced sensing (Wiersig 2014; Chen et al. 2017) and topological energy transfert (Xu et al. 2016).

Unfortunately, we have not been able to study any of the properties related to the presence of exceptional points so far: going in the vicinity of the these points in the parameter plane require to go trough regions where the atomic losses are too important to have a significant population of doubly occupied sites at the end of the experiments.

Strong versus weak coupling regime

Away from the region of the parameter plane where lie the exceptional points, we will considers two regimes of coupling:

- The strong coupling regime: $\Omega_{\mathrm{L}} \gg \Omega_{\mathrm{L}}^{(EP)}$,
- The weak coupling regime: $\Omega_{\mathrm{L}} \ll \Omega_{\mathrm{L}}^{(EP)}$.

Here $\Omega_{\mathrm{L}}^{(EP)}$ stands for any Rabi frequency at which the exceptional points occur. The spectrum of the Hamiltonian and the composition of its eigenvectors in terms of bare states is represented for particular cases of strong coupling $\Omega_{\mathrm{L}} = 2\pi \times 1500\,\mathrm{Hz}$ in Fig. 5.7 and weak coupling in Fig. 5.8. The bare states composition for the same Hamiltonian in absence of dissipation are also plotted for the sake of comparison.

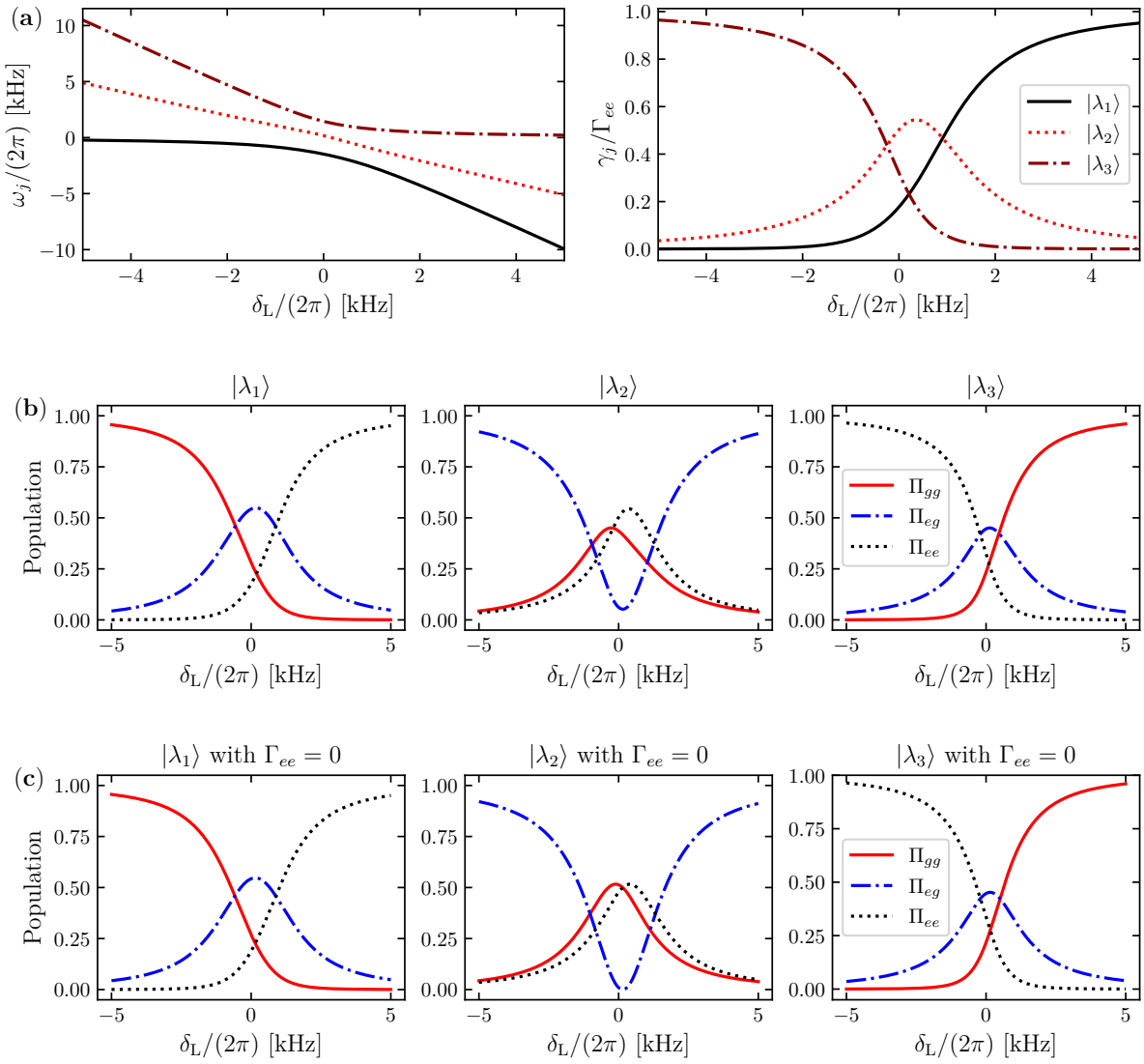

Figure 5.7 – Diagonalization of $\hat{H}^{(2}$ in the strong coupling limit. **(a)** Real (**left**) and imaginary (**right**) parts of the eigenvalues. **(b)** Bare state composition of each dressed state. **(c)** Bare state composition of each dressed state in absence of dissipation.

In the strong coupling case, the real parts of the eigenvalues are separated and behave qualitatively as they would in absence of the dissipative term, $\Gamma_{ee} = 0$. When scanning δ_L, the eigenvectors successively populate significantly the dissipative bare state $|ee\rangle$, and accordingly all three states acquire a finite lifetime $\sim \Gamma_{ee}$ when the detuning becomes $\sim \Omega_L$.

In the weak coupling regime, crossings, that would be forbidden for an Hermitian Hamiltonian, between the real parts of the eigenvalues appears (but not between the eigenvalues themselves) and for all detunings, the dissipative state $|ee\rangle$ is almost entirely taken in charge by the eigenvector, $|\lambda_2\rangle$, which consequently inherits of most of the dissipative dynamics. On the contrary the two other eigenvectors $|\lambda_1\rangle$ and $|\lambda_3\rangle$ span an subspace of the Hilbert space where the losses are strongly suppressed. The crossing in the spectrum of the $\hat{H}^{(2)}$ Hamiltonian, made possible by the loss responsible for its

non-Hermitian nature, allows the states $|\lambda_1\rangle$ and $|\lambda_3\rangle$ to stay in the subspace spanned by $\{|gg\rangle, |eg\rangle\}$.

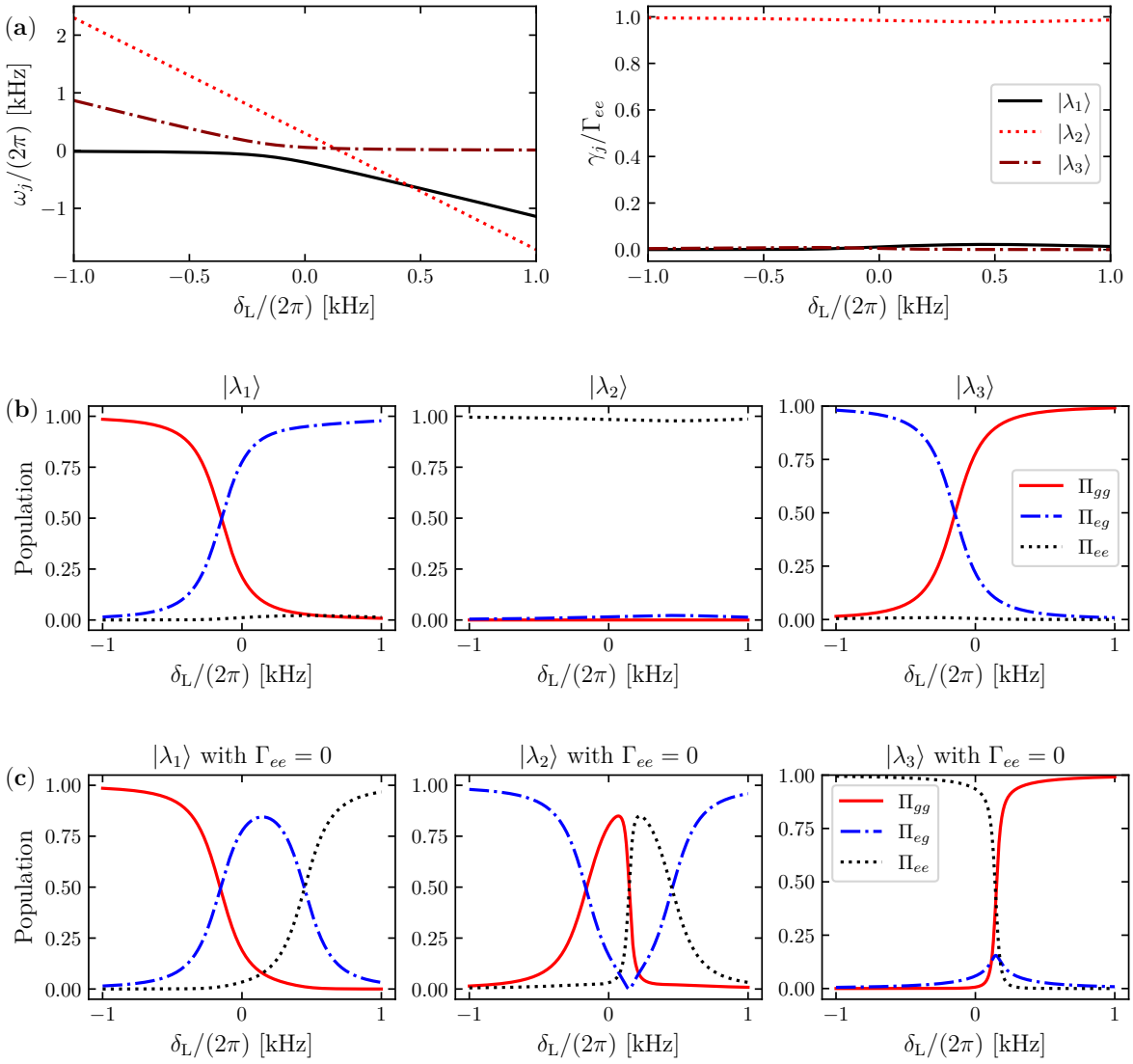

Figure 5.8 – Diagonalization of $\hat{H}^{(2)}$ in the weak coupling limit. **(a)** Real (**left**) and imaginary (**right**) parts of the eigenvalues. **(b)** Bare state composition of each dressed state. **(c)** Bare state composition of each dressed state in absence of dissipation.

Reduced loss subspace

The weak coupling regime can be reinterpreted with the quantum Zeno effect picture. In this regime the dissipation rate, *i.e.* the measurement rate of the state $|ee\rangle$ is much faster than the internal dynamics of the system, whose frequency is given by Ω_L. As a consequence a lattice site initially in the orthogonal subspace, spanned by $\{|gg\rangle, |eg\rangle\}$, will see its dynamics restricted to this subspace.

More formally this picture can be found back by deriving an effective Hamiltonian for the reduced-loss subspace: the Hamiltonian (5.29) can be split as $\hat{H}^{(2)} = \hat{H}_0 + \hat{V}$, with

$$\hat{H}_0 = \hbar \begin{pmatrix} 0 & 0 & 0 \\ 0 & \eta - \delta_{\mathrm{L}} & 0 \\ 0 & 0 & \chi - 2\delta_{\mathrm{L}} - \mathrm{i}\frac{\Gamma}{2} \end{pmatrix} \quad \text{and} \quad \hat{V} = \hbar \begin{pmatrix} 0 & \frac{\Omega_{\mathrm{L}}}{\sqrt{2}} & 0 \\ \frac{\Omega_{\mathrm{L}}}{\sqrt{2}} & 0 & \frac{\Omega_{\mathrm{L}}}{\sqrt{2}} \\ 0 & \frac{\Omega_{\mathrm{L}}}{\sqrt{2}} & 0 \end{pmatrix}. \tag{5.41}$$

We note E_X the matrix elements $\langle X|\hat{H}_0|X\rangle$ and introduce the projector on the hyperplane of the Hilbert space spanned by $\{|gg\rangle\}$, called $\mathcal{H}_P$ with its associated projector $\hat{P} = |gg\rangle\langle gg| + |eg\rangle\langle eg|$.

Since Ω_{L} is small compared to $|E_{ee} - E_{gg}|$ and $|E_{ee} - E_{eg}|$, second order perturbation theory allows us to derive an effective Hamiltonian that has the same eigenvalues in the subspace $\mathcal{H}_P$ as the full Hamiltonian $\hat{H}$. The matrix elements of the effective Hamiltonian are $\forall\, |i\rangle,\, |j\rangle \in \{|gg\rangle,\, |eg\rangle\}$:

$$\langle i|\hat{P}\hat{H}_{\mathrm{eff}}\hat{P}|j\rangle = \langle i|\hat{H}|j\rangle + \frac{1}{2}\left(\frac{1}{E_i - E_{ee}} + \frac{1}{E_j - E_{ee}}\right) \times \langle i|\hat{V}|ee\rangle\langle ee|\hat{V}|j\rangle. \tag{5.42}$$

In a more compact form, we have in the $\{|gg\rangle,\, |eg\rangle\}$ subspace:

$$\hat{P}\hat{H}_{\mathrm{eff}}\hat{P} = \hbar \begin{pmatrix} 0 & \frac{\Omega_{\mathrm{L}}}{\sqrt{2}} \\ \frac{\Omega_{\mathrm{L}}}{\sqrt{2}} & \delta_{\mathrm{eff}} - \mathrm{i}\frac{\gamma_{\mathrm{eff}}}{2} \end{pmatrix}. \tag{5.43}$$

with

$$\delta_{\mathrm{eff}} = \eta - \delta_{\mathrm{L}} - \frac{2\Omega_{\mathrm{L}}^2\left(\eta - \chi + \delta_{\mathrm{L}}\right)}{4\left(\eta - \chi + \delta_{\mathrm{L}}\right)^2 + \Gamma_{ee}^2} \quad \text{and} \quad \gamma_{\mathrm{eff}} = \frac{2\Omega_{\mathrm{L}}^2\Gamma_{ee}}{4\left(\eta - \chi + \delta_{\mathrm{L}}\right)^2 + \Gamma_{ee}^2}. \tag{5.44}$$

From this expression we find again that an increase of the loss rate Γ_{ee} would reduce γ_{eff}, *i.e.* the transfer to the dissipative state $|ee\rangle$, which plays here the role of the environment for the effective Hamiltonian acting on the reduced-loss subspace. We also recover the behavior $\gamma_{\mathrm{eff}} \propto \Omega_{\mathrm{L}}^2/\Gamma_{ee}$, given $\Gamma_{ee} \to \infty$, often typical of the quantum Zeno effect.

5.3 Adiabatic passages

5.3.1 Experimental protocol

The results of the experiments measuring the elastic and inelastic collision parameters for ^{174}Yb (see 5.2.2) have shown that the elastic collision constants g_{gg}, g_{eg} and g_{ee} are very close one to another. For optical lattices of depths on the order of $25\,E_{\mathrm{R}}$, the different resonance are only separated by a few hundred of Hertz, on the order of the standard deviation of the probe frequency. Consequently it may be difficult to driven separately the $|gg\rangle \to |eg\rangle$ and the $|gg\rangle \to |ee\rangle$ transitions. In the long term perspective for our experimental setup involving the creation of artificial gauge fields with ultracold ^{174}Yb atoms in an optical lattice, we need to be able to populate the $|eg\rangle$ state, while avoiding the lossy $|ee\rangle$ state. This issue can be circumvented by taking advantage of the existence of losses in the $|ee\rangle$ state and use the quantum Zeno

effect combined with adiabatic passages to populate significantly the state $|eg\rangle$ while preventing any transition toward the lossy $|ee\rangle$ state.

In this section we present the experimental results for the investigation of the properties of the non-Hermitian effective Hamiltonian $\hat{H}^{(2)}$ in the weak coupling regime, with $\Omega_{\mathrm{L}} = 2\pi \times 150\,\mathrm{Hz}$ fixed, at different detuning δ_{L}. The $N^{(2)}$ doubly occupied sites of the optical lattice, initially in $|gg\rangle$ in absence of coupling light are send to the states $|\lambda_1(\delta_{\mathrm{L}})\rangle$ and $|\lambda_3(\delta_{\mathrm{L}})\rangle$ for different values of δ_{L} thanks to an adiabatic following these states over the $(\Omega_{\mathrm{L}}, \delta_{\mathrm{L}})$ plane to the desired point. These adiabatic followings are performed according to the protocol presented below:

- Initial optical lattice: A BEC with $N_{\mathrm{atoms}} \approx 6 \times 10^4$ ^{174}Yb atoms is loaded in a deep [lattice depths $V_{x,y,z} = \{25, 25, 27\}E_{\mathrm{R}}$] optical lattice, and singly and doubly occupied sites are created in states $|g\rangle$ and $|gg\rangle$ respectively.
- Rabi frequency ramp: The Rabi frequency Ω_{L} is ramped from 0 Hz up to $2\pi \times 150$ Hz, at fixed detuning $\delta_{\mathrm{L,\,init.}} = -1.5\,\mathrm{kHz}$ (resp. $\delta_{\mathrm{L,\,init.}} = +1.5\,\mathrm{kHz}$) for a following along $|\lambda_1\rangle$ (resp. $|\lambda_3\rangle$) in a duration equal to one tenth of the total passage time, denoted T_{passage} (see Fig. 5.9).
- Detuning ramp: For a fixed Rabi frequency $\Omega_{\mathrm{L,\,fin.}} = 2\pi \times 150\,\mathrm{Hz}$, the detuning δ_{L} is ramped from $\delta_{\mathrm{L,\,init.}}$ to its final value $\delta_{\mathrm{L,\,fin.}}$ with a constant speed of 11.1 Hz/ms. This step takes the remaining nine tenths of the total passage duration T_{passage} (see Fig. 5.9).

At the end of these two ramps, we expect the remaining doubly occupied sites of the lattice to be in the dressed eigenstates $|\lambda_1\rangle$ (or $|\lambda_3\rangle$ depending on the sign of the initial detuning) of the Hamiltonian $\hat{H}^{(2)}$ for the parameters $(\Omega_{\mathrm{L,\,fin.}} = 2\pi \times 150\,\mathrm{Hz},\ \delta_{\mathrm{L,\,init}})$. From this we measure the internal states populations (see 5.3.3) or let the coupling light on to study their lifetimes (see 5.3.2).

According to our loading model, due to the auxillary confining potential, we cannot create doubly-occupied sites in the optical lattice without having a halo of singly-occupied sites around them , whose dynamics must also be taken into account in order to be able to interpret the experimental results. During the ramps, the $N^{(1)}$ singly-occupied sites, initially in $|g\rangle$ have evolved too, and follow the dressed states of a two-level atom in a near-resonant electric field (Haroche et al. 2013). Although their (unitary) dynamics is not the point of interest here, their evolution during the ramps has to be taken into account when it comes to interpret the relative and absolute populations of atoms in $|g\rangle$ and $|e\rangle$ at the end of the ramps.

The composition of the states of the lattice sites at the end of the ramp in term of bare state can be expressed from the wavefunctions $|\psi^{(1)}\rangle$ and $|\psi^{(2)}\rangle$ for singly and doubly occupied sites respectively, as:

$$\begin{aligned} &\text{For } \overline{n} = 1: \quad P_g = |\langle g|\psi^{(1)}\rangle|^2 \quad \text{and} \quad P_e = |\langle e|\psi^{(1)}\rangle|^2 \\ &\text{For } \overline{n} = 2: \quad P_{gg} = |\langle gg|\psi^{(2)}\rangle|^2, \quad P_{eg} = |\langle eg|\psi^{(2)}\rangle|^2 \quad \text{and} \quad P_{ee} = |\langle ee|\psi^{(2)}\rangle|^2 \end{aligned} \tag{5.45}$$

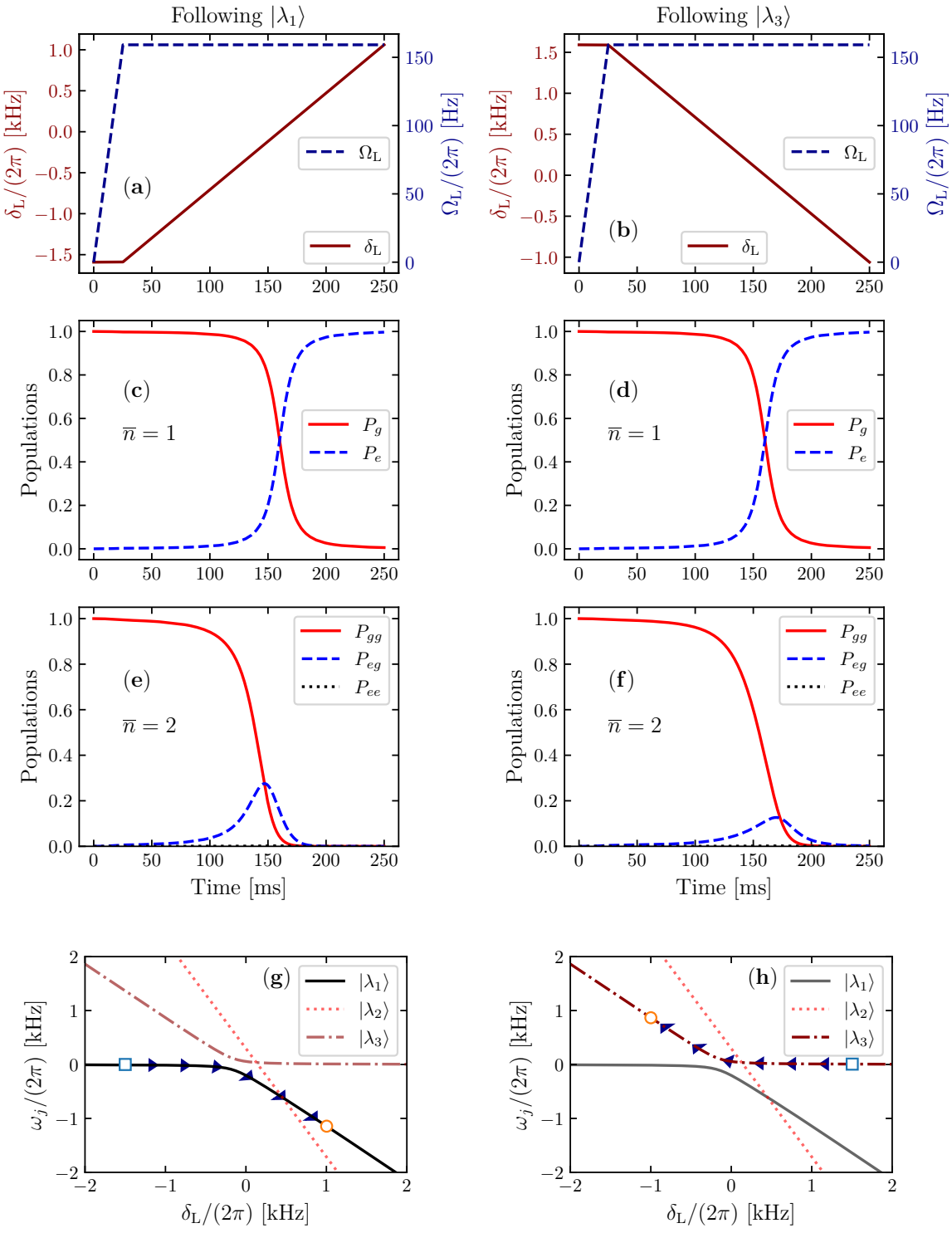

Figure 5.9 – Evolution of the sites populations during a passage performed in $|gg\rangle$ from $2\pi \times (0, -1.5)$ kHz to $2\pi \times (0.15, 1)$ kHz (**left**) and from $2\pi \times (0, 1.5)$ kHz to $2\pi \times (0.15, -1)$ kHz (**right**) on the parameter space (Ω_L, δ). The evolution of the population of the Fock states in singly **[(c)** and **(d)]** and doubly **[(e)** and **(f)]** occupied sites is computed by integrating the Schrödinger equation. The non-Hermitian nature of $\hat{H}^{(2)}$ is pointed out by the decay of the total population in the cases $\overline{n} = 2$. The passages (blue arrows) following $|\lambda_1\rangle$ **[(g)]** and $|\lambda_3\rangle$ **[(h)]** are schematized on the real part of the spectrum of $\hat{H}^{(2)}$. During a passage the, after the rise of the Rabi frequency, the detuning is ramped and the system follow the dressed state, starting form the blue square to the orange dot, on the $\{\delta_L\}$ line.

The evolution of these quantities during the two kind of passage are computed in Fig. 5.9.

Absorption imaging gives us access to the following quantities:

- The measured total population of atoms in $|g\rangle$, denoted $\mathcal{N}_g = \sum_{\mathbf{i}} \langle \hat{a}_g^\dagger \hat{a}_g \rangle_{\mathbf{i}}$ where the $\mathbf{i}$'s stand for the lattice sites indices, is measured by direct absorption imaging. This quantity is linked to the quantities defined in (5.45) by:

$$\mathcal{N}_g = N^{(2)} \left(2P_{gg} + P_{eg}\right) + N^{(1)} P_g \tag{5.46}$$

  .

- The measured total population of atoms in $|e\rangle$, denoted $\mathcal{N}_e = \Upsilon \sum_{\mathbf{i}} \langle \hat{a}_e^\dagger \hat{a}_e \rangle_{\mathbf{i}}$ is measured by absorption imaging after a "blast pulse" that removes the atoms in $|g\rangle$ from the lattices followed by a repumper pulse that send the atoms in $|e\rangle$ to $|g\rangle$ with an efficiency $\Upsilon_a pprox 0.86$, according to the process introduced in 3.1.2. Assuming Υ does not depend on the atomic density, the quantity $\mathcal{N}_e$ is linked to the quantities defined in (5.45) by:

$$\mathcal{N}_e = \Upsilon N^{(2)} \left(2P_{ee} + P_{eg}\right) + \Upsilon N^{(1)} P_e \tag{5.47}$$

- The measured total population of atoms in both ground and excited states, denoted $\mathcal{N}_{e+g} = \sum_{\mathbf{i}} \left[\langle \hat{a}_g^\dagger \hat{a}_g \rangle_{\mathbf{i}} + \Upsilon \langle \hat{a}_e^\dagger \hat{a}_e \rangle_{\mathbf{i}} \right]$ is measured by absorption imaging after a repumper pulse, without blasting away the atoms in $|g\rangle$. The quantity $\mathcal{N}_{e+g}$ is linked to the quantities defined in (5.45) by:

$$\mathcal{N}_{e+g} = N^{(2)} \left(2\Upsilon P_{ee} + (1+\Upsilon) P_{eg} + 2P_{gg}\right) + N^{(1)} (\Upsilon P_e + P_g). \tag{5.48}$$

5.3.2 Lifetime in the dressed states

In this section the decay of the eigenstates λ_1 and λ_3 of the Hamiltonian $\hat{H}^{(2)}$ for different values of δ_{L} is studied: after an adiabatic passage from $|gg\rangle$ to the eigenstate $|\lambda_j(\delta_{\mathrm{L}})\rangle$, with $j = 1$ or 3 depending on the initial detuning, the doubly occupied lattice are let evolve at fixed parameters $(\Omega_{\mathrm{L}}, \delta_{\mathrm{L}})$. As seen in Eqs. (5.35) to (5.37), the population of lattice sites in state $|\lambda_j\rangle$ will decay at rate $\gamma_j = \Gamma_{ee} \Pi_{ee}^{(j)} (\Omega_{\mathrm{L}}, \delta_{\mathrm{L}})$. We monitor the evolution of the total population of atoms in the lattice. Since there is no inelastic losses in the singly occupied sites, the decay of population is only accountable on the doubly occupied ones and the exponential decay can be fitted to measure γ_j, as it is done in Fig. 5.10.

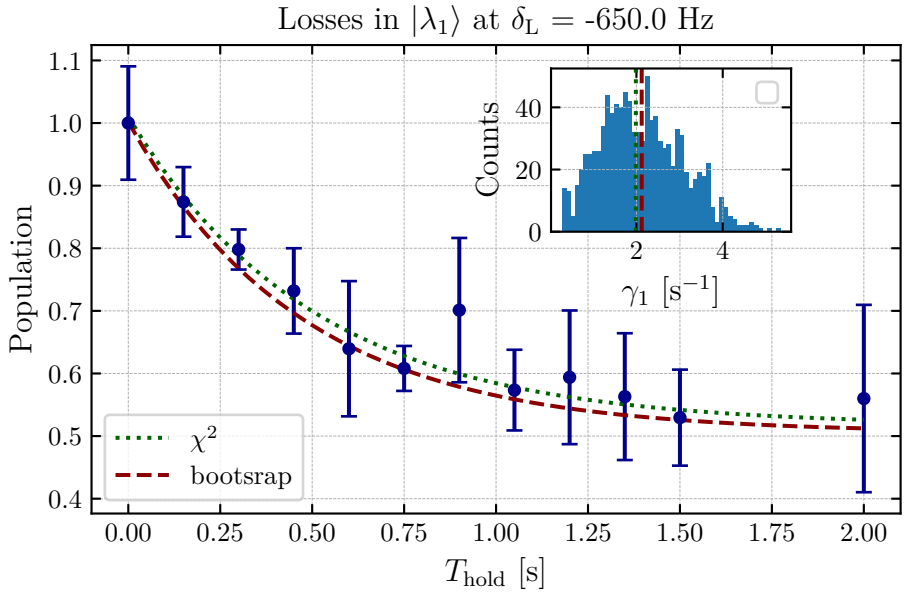

Figure 5.10 – Example of lifetime measurement. After the adiabatic passage that send the doubly occupied sites initially in the state $|gg\rangle$ to the eigenstate $|\lambda_j\rangle$ ($j \in \{1, 3\}$) at a given detuning δ_L, we fix the parameters (Ω_L, δ_L) at their final values and let the system evolve. The population of lattice sites in the eigenstate will decay exponentially because of the imaginary part of its corresponding eigenvalue. The fitted $N_{e+g}(t) = e^{-\gamma t}$ functions obtained by two different fit procedures (see B) are represented (dashed and dotted lines).

This experiment is repeated for different values for δ_L at the end of the passage. The fitted values for γ_j, with $j \in \{1, 3\}$ are presented in Fig. 5.11. Since γ_j is, up to a factor Γ_{ee} actually a measure of the contribution of the lossy bare state $|ee\rangle$ to the dressed state $|\lambda_j\rangle$, we compare $\gamma_j/\Gamma_{ee} = \Pi_{ee}^{(j)}(\Gamma_{ee})$ to what would have been the same quantity in absence of losses $\Pi_{ee}^{(j)}(\Gamma_{ee} = 0)$. The Fig. 5.11 shows that in presence of losses in the bare state $|ee\rangle$, contributes far less to the dressed states $|\lambda_1\rangle$ and $|\lambda_3\rangle$ compared to what it would have in absence of losses. These two eigenstates lie in a subspace almost decoupled from $|ee\rangle$: it is the manifestation of the quantum Zeno effect. The presence of two-body losses in the $|ee\rangle$ state allows us to produce state with a reduced component along $|ee\rangle$. This reduction, that corresponds to the difference between the dotted and solid lines in Fig. 5.11, is particularly important for the passages in $|\lambda_3\rangle$, reaching several order of magnitude. The main limitation of this procedure, preventing us to probe states to close to the resonance, is the loss of atoms due to the losses occurring during the ramp. Faster ramps, but still consistent with the adiabatic approximation for doubly occupied sites, could be an option to ramps more atoms in the dressed states of the reduced loss subspace close to the resonance. However faster ramps would not be adiabatic for singly occupied sites. To conclude adiabatic passages in $|\lambda_3\rangle$ up to detuning close to resonance are good candidates as procedures to selectively populate a significant fraction of lattice sites in the $|eg\rangle$.

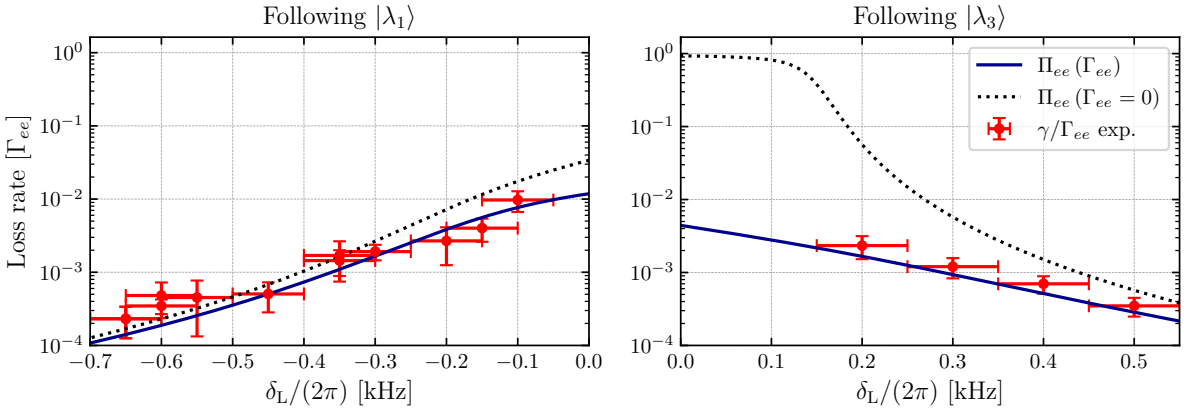

Figure 5.11 – Experimental decay rates $\gamma_{j=1,3}$ (red dots) extracted from lifetimes experiments performed on lattices sites at the end of adiabatic passages following $|\lambda_1\rangle$ (**left**) and $|\lambda_1\rangle$ (**right**) according to the protocol detailed in 5.3.1. The decay rates, rescaled by Γ_{ee} are compared to the the fractions $\Pi_{ee}^{(j)}$ of $|ee\rangle$ in the considered dressed state obtained by the diagonalization of the Hamiltonian $\hat{H}^{(2)}(\Gamma)$, in presence ($\Gamma = \Gamma_{ee}$; blue line) or absence ($\Gamma = 0$; dotted black line) of two-body inelastic losses in the state $|ee\rangle$. The losses reduce the coupling of the eigenstates $|\lambda_{j=1,3}\rangle$ with the lossy state $|ee\rangle$, confining them to the reduced-loss subspace spanned by $\{|gg\rangle, |eg\rangle\}$.

5.3.3 Composition of the dressed states

In order to monitor the following of the states $|\lambda_1\rangle$ and $|\lambda_3\rangle$ according to the protocol described in 5.3.1, we project the dressed lattice sites at different detuning and for $\Omega_L = 2\pi \times 150\,\text{Hz}$ fixed on the Fock basis, by switching off the coupling light and then measure the total population of atoms, and the total population of atoms in $|g\rangle$.

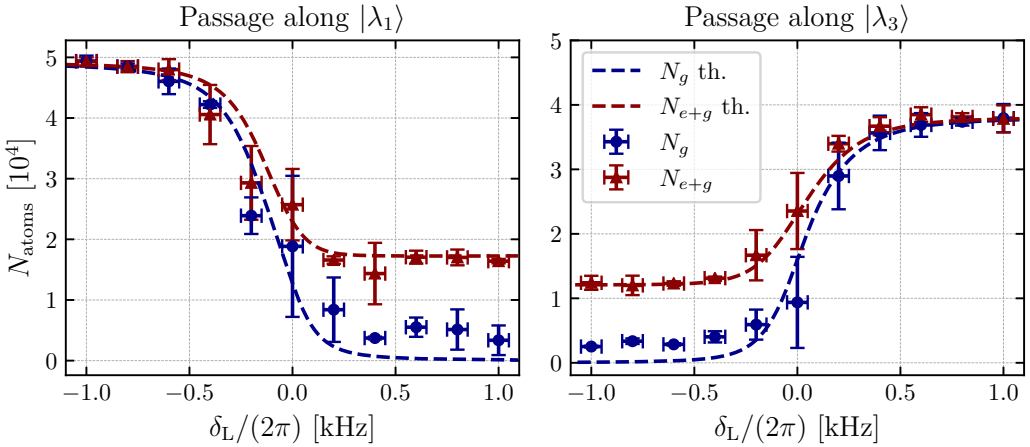

Figure 5.12 – Atomic populations evolution during the adiabatic following of the eigenstates of $\hat{H}^{(2)}$ $|\lambda_1\rangle$ (**left**) and $|\lambda_3\rangle$ (**right**). N_{e+g} is the measured total number of atoms after the repumper pulse. N_g is the measured total number of atoms in atomic state $|g\rangle$. The associated dashed lines are obtained by solving the Schrödinger equation during the passage.

The experimental evolution of the populations during the adiabatic passages, represented in Fig. 5.12 matches well with the predicted population, computed by integrating the Schrödinger equation for singly and doubly occupied sites, as long as the resonance $\delta_{\mathrm{L}} = 0$ is not crossed. After this detuning a small disagreement appears. However at these points of the passage, according to Fig. 5.9 the population of doubly occupied sites becomes negligible, and almost only singly occupied sites are responsible for the recorded signal.

The observed mismatch may be due to a failure of the adiabatic approximation which is less robust for singly occupied sites as shown in Figs. 5.14 and 5.15. A part of the discrepancy can be attributed to the clock laser frequency fluctuations characterized in 3.5.3. It can be studied by modelling the evolution by a *stochastic Schrödinger differential equation*:

$$\mathrm{i}\hbar\frac{\mathrm{d}|\psi_{\overline{n}=1}\rangle}{\mathrm{d}t} = \hat{H}^{(\overline{n}=1)}|\psi_{\overline{n}=1}\rangle - |e\rangle\langle e|\xi\,(t) \tag{5.49}$$

$$\mathrm{i}\hbar\frac{\mathrm{d}|\psi_{\overline{n}=2}\rangle}{\mathrm{d}t} = \hat{H}^{(\overline{n}=2)}|\psi_{\overline{n}=2}\rangle - (|eg\rangle\langle eg| + 2|ee\rangle\langle ee|)\,\xi\,(t) \tag{5.50}$$

and average it over several stochastic trajectories. Here $\xi\,(t)$ is a stochastic term, generated by a Ornstein-Uhlenbeck introduced in 3.5.3. ξ is obtained from a gaussian white noise term ξ' *via* the Langevin equation,

$$\frac{\mathrm{d}\xi}{\mathrm{d}t} = -\beta\xi\,(t) + \sigma\xi'\,(t)\,, \tag{5.51}$$

with β and σ the parameters measured in 3.5.3.

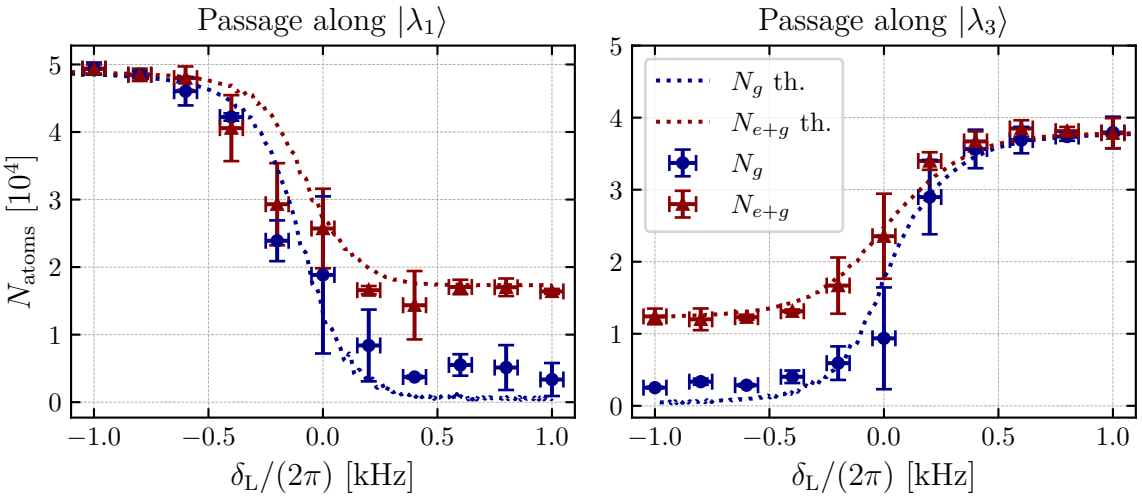

Figure 5.13 – Atomic populations evolution during the adiabatic following of the eigenstates of $\hat{H}^{(2)}$ $|\lambda_1\rangle$ (**left**) and $|\lambda_3\rangle$ (**right**). N_{e+g} is the measured total number of atoms after the repumper pulse. N_g is the measured total number of atoms in atomic state $|g\rangle$. The associated dotted lines are obtained by solving the stochastic Schrödinger differential equation (5.49).

The results of such simulations are represented in Fig. 5.13. If the introduction of the laser frequency noise allows to render the existence of a residual population of atoms

in $|g\rangle$ at the end of the passage, it is smaller than the measured one. This mismatch can be due to additional detrimental effect occurring during the ramp, which have not been identified so far. Moreover our (simple) characterization of the noise has been performed over timescales shorter than 50 ms, and may have failed to capture the effects of some component of the noise spectrum which are significant only at long times.

5.3.4 Adiabaticity of the passages

Now that the main the experimental results on the dressed states has been presented, we must address the question of the adiabaticity of the evolution of the states of the lattice sites according to the protocol proposed in 5.3.1. In the rest of this section, in order to ease the notations, we will denote the couple of time-dependent parameters $(\Omega_\mathrm{L},\, \delta_\mathrm{L})$ at time t as $\xi\,(t)$. Singly and doubly occupied sites are made continuously evolve from $\xi\,(t_0)$ to $\xi\,(t_1)$ on the parameter plane between the instants t_0 and t_1. The evolution operator for each system, denoted $\hat{U}^{(\overline{n})}\,(t_1,\, t_0)$ acts on the *right* eigenstates of the Hamiltonian $\hat{H}^{(\overline{n})}$ in the adiabatic limit (actually quasi-adiabatic limit for doubly occupied sites) $\hat{U}^{(\overline{n})}_{\text{adiab.}}$ as (see A):

$$\hat{U}^{(1)}_{\text{adiab.}}\,(t_1,\, t_0)\,|\pm\rangle_{\xi(t_0)} = \mathrm{e}^{-\mathrm{i}\int_{t_0}^{t_1}\omega_\pm(\xi(t))\,\mathrm{d}t}|\pm\rangle_{\xi(t_1)} \tag{5.52}$$

$$\hat{U}^{(2)}_{\text{adiab.}}\,(t_1,\, t_0)\,|\lambda_j\rangle_{\xi(t_0)} = \mathrm{e}^{-\frac{1}{2}\int_{t_0}^{t_1}\gamma_j(\xi(t))\,\mathrm{d}t}\mathrm{e}^{-\mathrm{i}\int_{t_0}^{t_1}\omega_j(\xi(t))\,\mathrm{d}t}|\lambda_j\rangle_{\xi(t_1)} \tag{5.53}$$

In order to quantify the adiabaticity of the experimental procedure used to study the eigenstates of $\hat{H}^{(2)}$ at different detuning δ_L, we compute the probability for a site, initially in a given eigenstate $|\lambda_k\,(\xi\,(t_0))\rangle$ of its Hamiltonian, to be send to another eigenstate $|\lambda_{j\neq k}\,(\xi\,(t))\rangle$ during the passage. These probabilities are given by:

$$p\,(|\pm\rangle \to |\mp\rangle) = \mathrm{e}^{\mathrm{i}\int_{t_0}^{t_1}\omega_\mp(\xi(t))\,\mathrm{d}t}{}_{\xi(t_1)}\langle\mp|\hat{U}^{(1)}\,(t_1,\, t_0)\,|\pm\rangle_{\xi(t_0)} \tag{5.54}$$

for singly occupied sites and

$$p\,(|\lambda_k\rangle \to |\lambda_j\rangle) = \mathrm{e}^{\frac{1}{2}\int_{t_0}^{t_1}\gamma_j(\xi(t))\,\mathrm{d}t}\mathrm{e}^{\mathrm{i}\int_{t_0}^{t_1}\omega_j(\xi(t))\,\mathrm{d}t}{}_{\xi(t_1)}\langle\tilde{\lambda}_j|\hat{U}^{(2)}\,(t_1,\, t_0)\,|\lambda_k\rangle_{\xi(t_0)} \tag{5.55}$$

for doubly occupied sites. Here $|\lambda\rangle_{\xi(t)} = |\lambda\,(\xi\,[t])\rangle$ is the eigenvector $|\lambda\rangle$ of the Hamiltonian in point ξ of the parameter plane, where stands the system at time t.

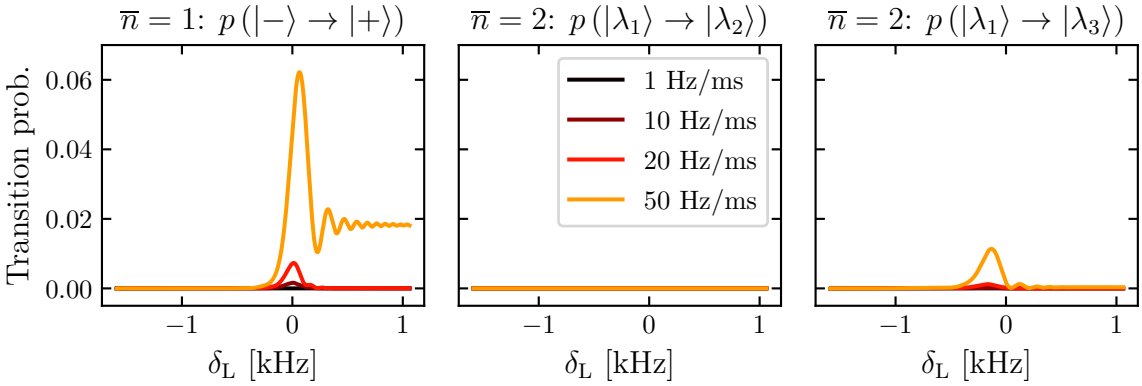

Figure 5.14 – **Adiabaticity following** $|-\rangle/|\lambda_1\rangle$: Probability for singly $\overline{n} = 1$ and doubly $\overline{n} = 2$ occupied sites, initially in state $|-\rangle$ for $\overline{n} = 1$ and $|\lambda_1\rangle$ for $\overline{n} = 2$, to populate other eigenspaces than the initial one (*i.e.* to populate $|+\rangle$ for $\overline{n} = 1$ and $\{|\lambda_2\rangle, |\lambda_3\rangle\}$ for $\overline{n} = 2$) during a ramp performed according to the protocol described in section 5.3.1, with $\delta_L : -1.5\,\text{kHz} \to +1\,\text{kHz}$. The extent of the passage is expressed in terms of detuning δ_L in order to compare the different speeds.

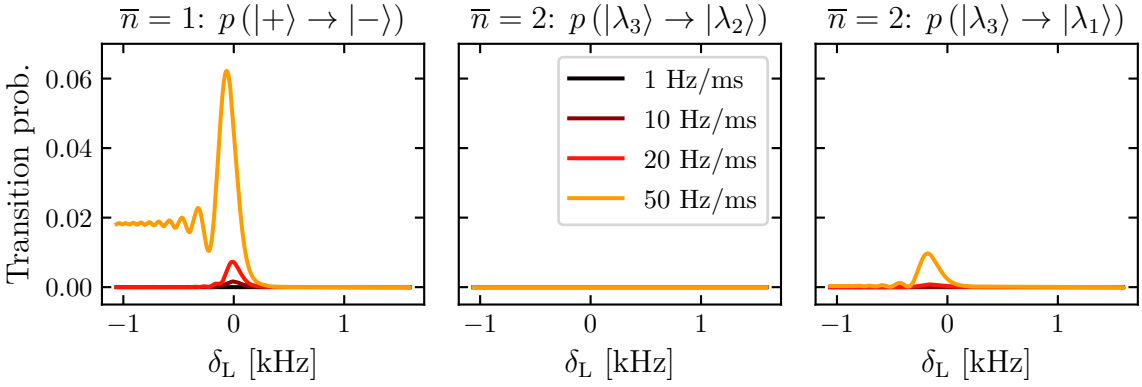

Figure 5.15 – **Adiabaticity following** $|+\rangle/|\lambda_3\rangle$: Probability for singly $\overline{n} = 1$ and doubly $\overline{n} = 2$ occupied sites, initially in state $|+\rangle$ for $\overline{n} = 1$ and $|\lambda_3\rangle$ for $\overline{n} = 2$, to populate other eigenspaces than the initial one (*i.e.* to populate $|-\rangle$ for $\overline{n} = 1$ and $\{|\lambda_1\rangle, |\lambda_2\rangle\}$ for $\overline{n} = 2$) during a ramp performed according to the protocol described in section 5.3.1, with $\delta_L : +1.5\,\text{kHz} \to -1\,\text{kHz}$. The extent of the passage is expressed in terms of detuning δ_L in order to compare the different speeds.

These quantities are numerically computed for ramps "following $|\lambda_1\rangle$" (Fig. 5.14) and ramps "following $|\lambda_3\rangle$" (Fig. 5.15) for singly and doubly occupied sites, and at different ramp speeds. From these figures, we can conclude that at the speeds considered, and more particularly for 10 Hz/ms used in most of our experiments, the probability for the lattice sites initially in $|gg\rangle$ to "smear" on other dressed states than their initial one during the passage is negligible. As a consequence we can assume that at the end of the passage, the lattice sites are actually in one of the eigenstate of their Hamiltonian, only depending on the sign of the initial detuning of the coupling field. It also ensures the identity $\Pi_{ij} \approx P_{ij}(t)$ between the quantities defined in (5.39) and (5.45) respectively.

5.3.5 Passages back and forth: an experimental verification of the adiabaticity

In order to test experimentally the adiabaticity of the passages performed in the experiment previously presented, back and forth passages have been performed. A forward passage according to the experimental protocol detailed in 5.3.1 two time faster (*i.e.* 22.2 Hz/ms for the detuning ramp). Then immediately after, the reverse ramp is performed at the same speed. Sending back all the lattice sites at their starting states, *i.e.* $|g\rangle$ and $|gg\rangle$ for singly and doubly occupied sites respectively at the end of this round trip on the parameter plane is a necessary (but not sufficient) condition for the passage to be adiabatic. From the Fig. 5.16 we can see that for ramps back and forth involving doubly occupied sites, all the atoms at the end of the ramp are in atomic state $|g\rangle$, which is consistent with an adiabatic passage. As for forward passage, the discrepancy occurs when the resonance δ_{L} is crossed, and concern mostly the dynamics of singly occupied sites.

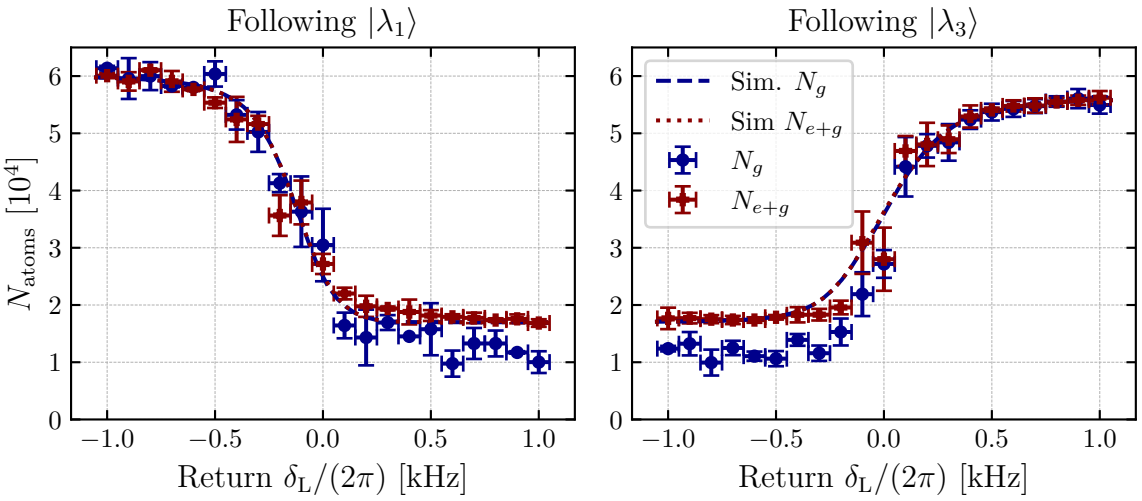

Figure 5.16 – Atomic populations evolution during the back and forth ramps of the eigenstates of $\hat{H}^{(2)}$ $|\lambda_1\rangle$ (**left**) and $|\lambda_3\rangle$ (**right**). N_{e+g} is the measured total number of atoms after the repumper pulse. N_g is the measured total number of atoms in atomic state $|g\rangle$. The associated dashed lines are the populations predicted by the integration of the Schrödinger equation.

5.4 Conclusion

In this section, we show that the dynamic of a collection of pairs of bosons in presence of inelastic-collision induced losses could be described by an effective non-Hermitian Hamiltonian. The diagonalization of the 3×3 non-Hermitian Hamiltonian describing our experimental situation show the existence of two regimes, depending on the strength of the coupling between internal states of the atoms, with different properties. The weak coupling regime in particular, comes with the emergence of a reduced-loss subspace, almost decoupled for the dissipative state, by a quantum Zeno effect mechanism.

This phenomenon has then been verified experimentally, by performing adiabatic passages, following the eigenstates of the Hamiltonian spanning the reduced-loss subspace. We have showed that the contribution of the dissipative bare state to these dressed states is, in presence of dissipation, several order smaller that it would have been in absence of dissipation. The adiabatic passages are also a way to populate coherently a significant number of lattice sites in the $|eg\rangle$ state, starting from $|gg\rangle$, without populating $|ee\rangle$ states, which could be of interest in the perspective of spin-orbit coupling experiments for quantum simulation.

In order to increase the loss suppression effect, the "slowing" factor $\Omega_{\mathrm{L}}^2/\Gamma_{ee}$, characteristic of the quantum Zeno effect, could be reduced by increasing Γ_{ee} *i.e.* by increasing the lattice depth or by reducing Ω_{L}. In practice the maximum lattice depth is limited by the amount of laser power available and the fact that Γ_{ee} increases slowly ($\propto V^{3/4}$) with the lattice depth V. On the other hand, reducing Ω_{L} imposes to perform slower passages in order stay in the adiabatic regime, which makes the experiment more sensitive to long-term dephasing mechanism and may ends in experiments longer than the tunneling time, invalidating the hypothesis of independent lattice sites.

CHAPTER 6

Dynamics in 1D lossy optical lattices

In the previous chapter, I have studied the influence of two-body inelastic collisions on atom pairs trapped in isolated sites of the optical lattice. I have shown the two-body losses decouples the dissipative state, with two ^{174}Yb atoms in the $^3P_0$ state, from the rest of the Hilbert space in which the pair of bosons evolves. We have also used this phenomenon, which is a manifestation of the *quantum Zeno effect* (QZE), to drive our system within the reduced loss subspace. Armed with this knowledge for the two particle case, I tackle in this chapter the many-body case by considering unidimensional optical lattices filled with ^{174}Yb atoms in the $^3P_0$ state.

Over the last decade, the use of dissipation or decoherence to control or protect quantum many-body system has arisen a growing interest (Syassen et al. 2008; Witthaut et al. 2008; Diehl et al. 2008; Kraus et al. 2008; Verstraete et al. 2009). This idea has been more particularly implemented with experiments involving ultracold atoms trapped in unidimensional optical lattices, using different kind of bosonic particles which are subject to inelastic losses, including pairs of ^{87}Rb atoms associated to molecules thanks to Feshbach resonances (Syassen et al. 2008) or ^{174}Yb atoms in the metastable $^3P_2$ state (Tomita et al. 2019). In these experiments the quantum Zeno effect generated by the two-body inelastic collisions between the atoms evolving in the optical lattices are used to protect the system from the dissipative subspace of their Hilbert space, slowing down the atomic losses.

Studying such system is also of interest for the further development of the setup because it will allow us to determine how much time it takes for the losses to affect the many body state created in the optical lattice. In the first part of this chapter, we introduce the first elements for the theoretical description of the system, showing how the quantum Zeno effect will slow down the loss dynamics. Then, the experimental protocol for the study of the loss dynamics is presented. Experimental results are then compared with two models describing the evolution of the average filling of the optical lattice. Finally, we will try to explain the observed difference between the experiments and the models for the lowest lattice depths probed by investigating the effects of some experimental aspects that are not taken into account in the models.

6.1 Theoretical description of the system

6.1.1 The dissipative Bose-Hubbard model

In this chapter we will study the loss dynamics in 1D optical lattices filled with ^{174}Yb atoms in the $^3P_0$ state, denoted $|e\rangle$ in the rest of this section, with an initial filling assumed to be equal or inferior to $\overline{n} = 1$. The presence of inelastic collisions-induced two-body losses for two atoms in this state lead us to describe its dynamics by a Lindblad master equation on the density of state $\hat{\rho}$, similarly to what has been done in 5.1.2:

$$\frac{\mathrm{d}\hat{\rho}}{\mathrm{d}t} = -\frac{\mathrm{i}}{\hbar}\left[\hat{H}_0,\, \hat{\rho}\right] + \frac{\Gamma_{ee}}{4}\sum_i \left(2\hat{a}_i\hat{a}_i\hat{\rho}\hat{a}_i^\dagger\hat{a}_i^\dagger - \hat{\rho}\hat{a}_i^\dagger\hat{a}_i^\dagger\hat{a}_i\hat{a}_i - \hat{a}_i^\dagger\hat{a}_i^\dagger\hat{a}_i\hat{a}_i\hat{\rho}\right), \tag{6.1}$$

with $\hat{H}_0$ the single-component 1D single-band Bose-Hubbard Hamiltonian:

$$\hat{H}_0 = \hat{H}_J + \hat{H}_{\mathrm{int}} \tag{6.2}$$

with

$$\hat{H}_J = -J\sum_{\langle i,j\rangle}\hat{a}_i^\dagger\hat{a}_j \quad \text{and} \quad \hat{H}_{\mathrm{int}} = \frac{U_{ee}}{2}\sum_i \hat{n}_i\left(\hat{n}_i - 1\right). \tag{6.3}$$

Here $\hat{a}_i$ is the annihilation operator for a boson in state $|e\rangle$ at site i of the 1D optical lattice and $\hat{n}_i = \hat{a}_i^\dagger\hat{a}_i$. The summation over $\langle i,\, j\rangle$ is made on the neighboring lattice sites.

In the rest of this chapter, we will consider the strong dissipation limit, where the two-body losses occurs at a rate much faster that the tunneling, *i.e.* $\Gamma_{ee} \gg J/\hbar$.

6.1.2 A simple model

In order to have some insight on the dynamics of interacting bosons trapped in a 1D optical lattice and subject to two-body losses, we present here the simplest case corresponding to this situation: a pair of bosons trapped in a double well. Using the non-Hermitian Hamiltonian framework introduced in the previous chapter in 5.2, the Hamiltonian describing the dynamics of the system writes:

$$\hat{H} = \begin{pmatrix} 0 & -\sqrt{2}J & -\sqrt{2}J \\ -\sqrt{2}J & U_{ee} - \mathrm{i}\frac{\hbar\Gamma_{ee}}{2} & 0 \\ -\sqrt{2}J & 0 & U_{ee} - \mathrm{i}\frac{\hbar\Gamma_{ee}}{2} \end{pmatrix}. \tag{6.4}$$

in the $\{|11\rangle, |20\rangle, |02\rangle\}$ basis, where $|n,\, m\rangle = |n\rangle_l \bigotimes |m\rangle_r$ is the Fock state with n bosons in the left well and m bosons in the right one.

In the strong dissipation limit ($\Gamma_{ee} \gg J/\hbar$), it is possible to proceed similarly to what has been done in 5.2.3 and adiabtically eliminate the rapidly decaying states with double occupancy. It results in an effective energy U_{eff} shift and loss rate Γ_{eff} for the "ground state" $|11\rangle$,

$$U_{\mathrm{eff}} = -\frac{4J^2}{U_{ee}^2 + \left(\frac{\hbar\Gamma_{ee}}{2}\right)^2}U_{ee} \quad \text{and} \quad \Gamma_{\mathrm{eff}} = \frac{4J^2}{U_{ee}^2 + \left(\frac{\hbar\Gamma_{ee}}{2}\right)^2}\Gamma_{ee}. \tag{6.5}$$

Here we observe that in presence of strong inelastic interactions ($\Gamma_{ee} \gg J, U_{ee}$) the dissipative part of the energy scales as $\Gamma_{\text{eff}} \propto J^2/\Gamma_{ee}$ and the two-body losses in the excited state actually enhance the lifetime of the ground state, by hindering the transitions toward the dissipative one *via* tunneling.

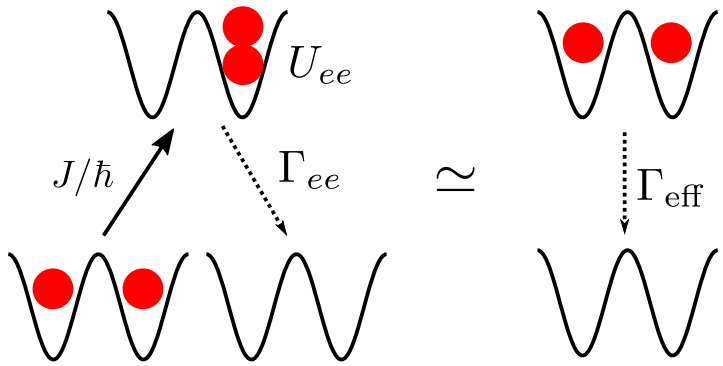

Figure 6.1 – Scheme of the perturbation treatment of the system composed of two bosons evolving in a double well with a tunnel energy J, subject to two-body interactions with the associated complex energy $\underline{U_{ee}} = U_{ee} - \mathrm{i}\hbar\Gamma_{ee}/2$. In the regime where the tunneling rate $J/\hbar$ is much smaller than the decay rate Γ_{ee} for the two-body losses the system can be approximated by two impenetrable bosons with an effective decay rate Γ_{eff} much smaller that Γ_{ee}.

In this chapter we show how the perturbative approach applied on this simple model to point out a quantum Zeno dynamics can be used on the more complex system of many bosons trapped in an optical lattice, strongly interacting via elastic and inelastic two-body collisions. It leads to the description of the dynamics of the system by an effective master equation, with an effective loss rate, analogous to the one found in (6.5).

6.1.3 The Tonks-Girardeau gas limit

This section summarizes the main steps of the theoretical work made in García-Ripoll et al. 2009 in order to establish the effective master equation used in this chapter to describe the dynamics of the system.

Since the Lindblad equation written in (6.1) is linear, it is possible to rewrite it in its linear form:

$$\frac{\mathrm{d}}{\mathrm{d}t}\hat{\rho} = \left(\mathcal{L}_{\text{kin}} + \mathcal{L}_{\text{int}}\right)\hat{\rho} \tag{6.6}$$

introducing the Liouvillian "superoperators" (linear operators acting on the density matrix ρ), defined by

$$\mathcal{L}_{\text{kin}}\hat{\rho} = -\frac{\mathrm{i}}{\hbar}\left[\hat{H}_J, \hat{\rho}\right] \tag{6.7}$$

$$\mathcal{L}_{\text{int}}\hat{\rho} = -\frac{\mathrm{i}}{\hbar}\left[\hat{H}_{\text{int}}, \hat{\rho}\right] + \frac{\Gamma_{ee}}{4}\sum_i \left(2\hat{a}_i\hat{a}_i\hat{\rho}\hat{a}_i^\dagger\hat{a}_i^\dagger - \hat{\rho}\hat{a}_i^\dagger\hat{a}_i^\dagger\hat{a}_i\hat{a}_i - \hat{a}_i^\dagger\hat{a}_i^\dagger\hat{a}_i\hat{a}_i\hat{\rho}\right). \tag{6.8}$$

Here the Liouvillian has been decomposed between $\mathcal{L}_{\text{kin}} \propto J$ rendering the tunneling dynamics and $\mathcal{L}_{\text{int}} \propto |U_{ee} - \mathrm{i}\frac{\Gamma_{ee}}{2}|$ enclosing the elastic (*via* $\hat{H}_{\text{int}}$) and inelastic (*via*

the Lindblad term) interactions. In the strong dissipation limit, $|U_{ee} - \mathrm{i}\frac{\Gamma_{ee}}{2}| \gg J$ the tunnel operator can be treated as a perturbation in order to derive an effective master-equation.

Similarly to the case of pair of atoms trapped in isolated lattice sites seen in the previous chapter (see 5.2.2), two-body losses act like continuous measurements, hindering the transition from the subspace of the Hilbert space without losses, spanned by the hard-core bosons states of the form:

$$|\psi\rangle = \bigotimes_j |p_j\rangle_j \quad \text{with} \quad p_j \in \{0,1\} \quad \forall j, \tag{6.9}$$

to the lossy states directly connected to them,

$$|\phi_{j_0}\rangle = |2\rangle_{j_0} \bigotimes_{j\neq j_0} |p_j\rangle_j \quad \text{with} \quad p_j \in \{0,1\} \quad \forall j \neq j_0. \tag{6.10}$$

Here $|p\rangle_j$ denotes the Fock state with p bosons at site j.

Consequently it is possible to restrict the description of the dynamics of the system to the loss-less subspace, corresponding to the Fock states with at most one atom per lattice site, by proceeding similarly to 6.1.2. After some algebra, one obtains the effective Lindblad master equation for the system (García-Ripoll et al. 2009):

$$\frac{\mathrm{d}\hat{\rho}}{\mathrm{d}t} = -\frac{\mathrm{i}}{\hbar}\left[\hat{H}_1 + \hat{H}_2,\, \hat{\rho}\right] + \frac{\Gamma_{\text{eff}}}{2}\sum_j \left(2\hat{L}_j\hat{\rho}\hat{L}_j^\dagger - \hat{L}_j^\dagger\hat{L}_j\hat{\rho} - \hat{\rho}\hat{L}_j^\dagger\hat{L}_j\right). \tag{6.11}$$

The unitary part of the master equation can be decomposed as the sum of the Hamiltonian

$$\hat{H}_1 = -J\sum_j \hat{a}_j^\dagger\hat{a}_{j+1} + \text{h.c.}, \tag{6.12}$$

with $\hat{a}_j$ *hard-core bosons* (HCB) annihilation operators, rendering the tunneling of the bosons in the optical lattice, and the Hamiltonian

$$\hat{H}_2 = -J'\sum_j \hat{L}_j^\dagger\hat{L}_j \tag{6.13}$$

that encloses both effective nearest-neighbor interactions and interaction-mediated tunneling *via* a virtual state out of the reduced-loss Hilbert subspace. To define these Hamiltonians we have introduced the operator

$$\hat{L}_j = \hat{a}_j\left(\hat{a}_{j+1} + \hat{a}_{j-1}\right), \tag{6.14}$$

that annihilates a pair of particles in neighboring sites, and the constants

$$\Gamma_{\text{eff}} = \frac{8J^2}{4U_{ee}^2 + \hbar^2\Gamma_{ee}^2}\Gamma_{ee} \quad \text{and} \quad J' = \frac{U_{ee}}{\Gamma_{ee}}\Gamma_{\text{eff}}. \tag{6.15}$$

The Hamiltonian $\hat{H}_1$ describes the hopping by tunnel effect of impenetrable hard-core bosons between the sites of a 1D lattice. This dynamics belongs to the family of the

Tonks-Girardeau gas (Tonks 1936; Girardeau 1960), which gathers the unidimensional gas of bosons whose dynamics is dominated by a repulsive interaction, enabling a mapping of the ensemble of bosons on a fermionic model (Girardeau 1960). The first experimental observation of a Tonks-Girardeau gas, implemented with ultrcaold atoms in an optical lattice, has been reported in Paredes et al. 2004. The quartic Hamiltonian $\hat{H}_2$ is coupling nearest neighbors on the lattice sites. Finally the last term in (6.11) enclose the dissipative component of the evolution, occurring at a rage Γ_{eff} with the jump operator $\hat{L}_j$.

One of the main feature of the effective Lindblad master equation (6.11) is the emergence of a new timescale Γ_{eff}^{-1} associated with the dissipative processes. In absence of elastic-interactions, the effective loss rate would scale as $\Gamma_{\text{eff}} \propto (J/\hbar)^2 \Gamma_{ee}^{-1}$, which is a signature of the quantum Zeno effect (see 5.1.2). When the perturbative approach is valid, we have the inequalities

$$\Gamma_{ee}^{-1} \ll \hbar/J \ll \Gamma_{\text{eff}}^{-1}. \tag{6.16}$$

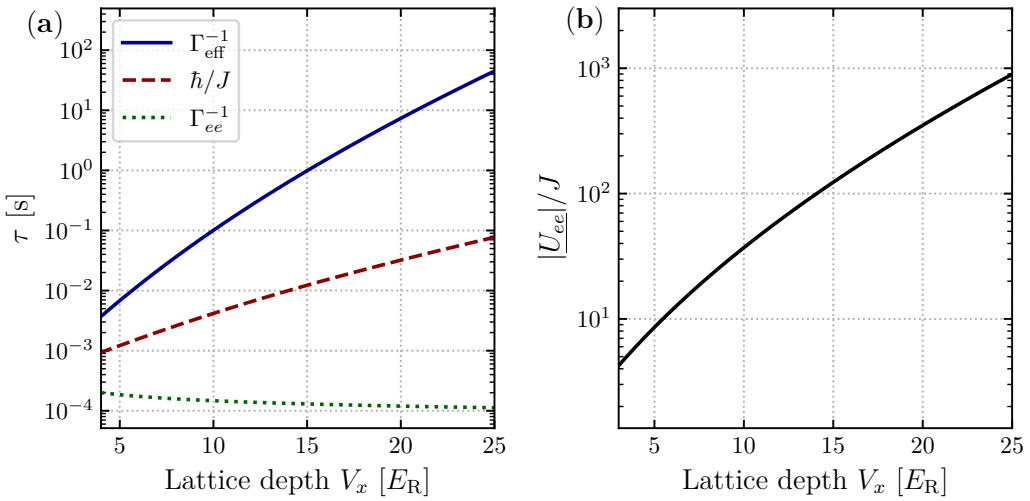

Figure 6.2 – Comparison between the timescales of the different dynamics at stake. (**a**) The different timescales τ associated with the different mechanisms involved in the description of the system made in (6.11) for 1D optical lattice of ^{174}Yb atoms with depth V_x in the shallow horizontal direction, and $V_{y,z} = \{25, 27\}\, E_{\text{R}}$ in the other directions. For the lattice depth studied in 6.2, the hypothesis used to derive (6.11) is satisfied. The quantity J' is not represented for it is equal to $\hbar\Gamma_{\text{eff}}$ up to a constant factor $U_{ee}/(\hbar\Gamma_{ee}) \approx 1.2$. (**b**) Evolution of the ratio between $|\underline{U_{ee}}| = |U_{ee} - \mathrm{i}\Gamma_{ee}/2|$ and J for different lattice depths. The increase of the lattice depth and consequently of the elastic and inelastic interactions made postpone the emergence of the non-unitary dynamics in the Tonks-Girardeau gas, by quantum Zeno effect.

This inequality can be interpreted in the quantum Zeno effect picture as follows: the two-body losses acts as a measurement for the sub-Hilbert space enclosing the states with at least one doubly occupied site. Since it occurs at a rate Γ_{eff}^{-1} much faster that the tunneling dynamics ($\Gamma_{ee} \ll \hbar/J$) that takes place in the sub-Hilbert space spanned by

the Fock states with at most one atom per site, transitions *via* tunneling are hindered and only occur at a rate Γ_{eff}^{-1}, much slower than the other timescales. Consequently, for timescales $\tau \ll \Gamma_{\text{eff}}^{-1}$, the system evolves according a Tonks-Girardeau unitary dynamics, while its long-time dynamics is characterized by losses at a rate proportional to Γ_{eff}. In the following we propose to probe this dynamics by studying the evolution of number of atoms. limit.

In our experiments, the system that emulates the unidimensional Bose-Hubbard model is realized with ultracold atoms trapped in a cubic optical lattice, where the depths of one of the horizontal axes, denoted y and the vertical axis are kept high, typically $V_{y,z} = \{25,\, 27\}\, E_{\text{R}}$. For these lattice depths the motion of the atoms along the y and z directions is inhibited at the timescales of our experiments. Consequently we end up with a quasi-unidimensional system, where the dynamics of the bosons takes place along the remaining horizontal direction x with a lower lattice depth compared to its transverse axis. The lattice depth of this shallow axis is varied across the experiments. The evolution of the timescales associated with the different mechanism involved in the effective master equation (6.11) with respect to the lattice depth V_x is represented Fig. 6.2 **(a)**. We observe that for the typical lattice depths used in our experiments ($V_x \in [8,\, 20]\, E_{\text{R}}$), the inequality (6.16) is satisfied. Moreover we observe that the decoupling between the mechanism timescales increases with the lattice depth V_x of the shallow axis.

6.1.4 A mean field approach for the losses in the lattice

A first description of the losses dynamics has been proposed in García-Ripoll et al. 2009 using a mean-field approach to compute the evolution of the total number of atoms in the lattice $N(t) = \langle \hat{N} \rangle_t = \sum_j \langle \hat{n}_j \rangle_t$. Here $\langle . \rangle_t$ denotes the average at time t. Under the effective master equation (6.11), the evolution of the quantity $\langle \hat{N} \rangle_t$ is given by the differential equation

$$\frac{\mathrm{d}N}{\mathrm{d}t} = -\frac{\Gamma_{\text{eff}}}{2} \sum_j \left\langle \left[\hat{L}_j^\dagger \hat{L}_j,\, \hat{N} \right] \right\rangle_t = -2\Gamma_{\text{eff}} \sum_j \langle \hat{L}_j^\dagger \hat{L}_j \rangle_t. \tag{6.17}$$

In order to simplify the solving of this differential equation, the authors of García-Ripoll et al. 2009 assume that the system is homogeneous and that the populations of different lattice sites are uncorrelated. It allows to rewrite the terms in the right-hand site of (6.17) as,

$$\langle \hat{L}_j^\dagger \hat{L}_j \rangle = \langle \hat{n}_j \hat{n}_{j+1} \rangle + \langle \hat{n}_j \hat{n}_{j-1} \rangle + \left\langle \hat{a}_{j+1}^\dagger \hat{n}_j \hat{a}_{j-1} \right\rangle + \left\langle \hat{a}_{j-1}^\dagger \hat{n}_j \hat{a}_{j+1} \right\rangle \tag{6.18}$$

$$\approx 2\overline{n}^2 \tag{6.19}$$

introducing $\overline{n}(t) = N(t)/N_{\text{sites}}$ the density of atoms in the lattice. The injection of (6.18) into (6.17) leads to a rate equation on $\overline{n}$,

$$\frac{\mathrm{d}\overline{n}}{\mathrm{d}t} = -4\Gamma_{\text{eff}} \overline{n}^2(t), \tag{6.20}$$

whose solution is

$$\overline{n}(t) = \frac{\overline{n}(0)}{1 + 4\overline{n}(0)\, \Gamma_{\text{eff}} t}. \tag{6.21}$$

The model of García-Ripoll et al. 2009 presented in this section provide a quantitative description of the system of a unidimensional optical lattice filled with bosons interacting *via* strong inelastic collisions. However the mean-field treatment the rate used to derive the rate equation (6.20) prevent the model to take into account the effect of the correlations between the sites that build up during the evolution of the system. More particularly the density correlation that appears in the expression (6.18) of $\langle \hat{L}_j^\dagger \hat{L}_j \rangle$ are neglected in the mean field treatment. In order to overcome this limitation, a beyond-mean field approach is introduced in Sec. 6.1.5

6.1.5 Beyond mean field: Rate equations

The hypothesis of uncorrelated populations between the lattice sites, used in Sec. 6.1.4 to derive the mean field model, fails to render the dynamics for low densities where the correlations can lo longer be neglected. We have an ongoing collaboration with Leonardo Mazza and Davide Rossini to overcome the limitations of the GR model and describe the correlated regime that emerges at long times. Starting from the HCB master equation, it is first convenient to perform a Jordan-Wigner transformation (Jordan et al. 1928) to "fermionize" the lattice gas, mapping the hard-core bosons field operators to fermionic ones. This is accomplished by the unitary transformation,

$$\hat{c}_j = \mathrm{e}^{\mathrm{i}\pi \sum_{m<j} \hat{n}_j} \hat{a}_j. \tag{6.22}$$

Here the phase factor counts how many particles are on the left (by convention) of the site j. This transformation maps the hard-core bosons operators $\hat{a}_j$ to canonical fermionic operators $\hat{c}_j$ that satisfy

$$\begin{aligned} \{\hat{c}_j,\, \hat{c}_m\} &= 0 \\ \{\hat{c}_j,\, \hat{c}_m^\dagger\} &= \delta_{j,\,m}. \end{aligned} \tag{6.23}$$

Here $\{\ ,\ \}$ stands for the anti-commutation brackets.

Then, the effective master equation (6.11) is rewritten using the momentum-space representation,

$$\hat{c}_j = \frac{1}{\sqrt{N_{\text{sites}}}} \sum_k \mathrm{e}^{\mathrm{i}kjd} \hat{c}_k \tag{6.24}$$

assuming periodic boundary conditions on the lattice, with N_{sites} and a period d.

In this representation the rate equations for the quantities $n_k(t) = \langle \hat{n}_k \rangle_t = \langle \hat{c}_k^\dagger \hat{c}_k \rangle_t$ can be extracted from the effective master equation:

$$\frac{\mathrm{d}n_k}{\mathrm{d}t} = \frac{\mathrm{i}}{\hbar} \Big\langle \left[\hat{H}_1 + \hat{H}_2, \hat{n}_k \right] \Big\rangle_t + \frac{\Gamma_{\text{eff}}}{2} \sum_j \left\langle 2\hat{L}_j^\dagger \hat{n}_k \hat{L}_j - \hat{L}_j^\dagger \hat{L}_j \hat{n}_k - \hat{n}_k \hat{L}_j^\dagger \hat{L}_j \right\rangle_t. \tag{6.25}$$

This master equation is directly derived from (6.11), using $n_k = \mathrm{Tr}\left[\hat{\rho}\hat{n}_k\right]$, without any further assumption. Here one can notice that the Hamiltonian $\hat{H}_1$ do not contribute to the evolution of $n_k(t)$, since $\left[\hat{H}_1,\, \hat{n}_k\right] = 0$. This term can consequently dropped in the rest of this section.

In order to simplify the master equation (6.25), a further assumption is made: the quantum state of the system is chosen so that it satisfies Wick's theorem,

$$\langle \hat{c}_i^\dagger \hat{c}_j^\dagger \hat{c}_k \hat{c}_l \rangle_t = \langle \hat{c}_i^\dagger \hat{c}_l \rangle_t \langle \hat{c}_j^\dagger \hat{c}_k \rangle_t - \langle \hat{c}_i^\dagger \hat{c}_k \rangle_t \langle \hat{c}_j^\dagger \hat{c}_l \rangle_t, \tag{6.26}$$

and factorization in the momentum space,

$$\langle \hat{c}_j^\dagger \hat{c}_k \rangle = \delta_{j,k} \hat{n}_k (t) . \tag{6.27}$$

Under these new assumptions it is possible to discard the contribution of $\hat{H}_2$, since $\langle \left[\hat{H}_2, \hat{n}_k \right] \rangle_t = 0$. Finally, the hypotheses on the nature of the quantum state allow to simplify the rate equation (6.25), which becomes

$$\frac{\mathrm{d}n_k}{\mathrm{d}t} = \frac{\Gamma_{\text{eff}}}{2} \Big\langle \sum_j \hat{L}_j^\dagger \left[\hat{n}_k, \hat{L}_j + \text{h.c.} \right] \Big\rangle_t . \tag{6.28}$$

It can be reformulated as a rate equation on the $n_k (t)$'s:

$$\frac{\mathrm{d}n_k}{\mathrm{d}t} = -\frac{4\Gamma_{\text{eff}}}{N_{\text{sites}}} \sum_q \left[\sin^2 (k) + \sin^2 (q) \right] n_k n_q . \tag{6.29}$$

We end up with a system of non-linear differential equations on the n_k's. The numerical resolution of this system shows that the decay of the population n_k in the momentum states corresponding to $k = 0$ and $k = \pi$ is slower than for the others states. From the numerical solutions n_k of (6.29), we compute the evolution of the average filling $\overline{n} (t)$, introduced in the previous section 6.1.4. This quantity is represented in Fig. 6.5 along with the same quantity computed with the mean field approach, for an initial average filling $\overline{n} (0) = 1$. We observe that for short times ($4\Gamma_{\text{eff}} \ll 1$) the two curves almost coincide, whereas for long times ($4\Gamma_{\text{eff}} \gg 1$) the decay of $\overline{n}$ computed with the rate equation is slower than for the mean-field approach. The divergence between the two models at long times is a manifestation of the correlations that build up in the system during its evolution. These correlations, not taken into account by the mean field model, slow down the dynamics of the atomic losses. From (6.20) on can show that at long times, the average filling for the mean field model behaves as $\overline{n} (t) \sim 1/ (4\Gamma_{\text{eff}} t)$, whereas it can be deduced from (6.29) that the asymptotic behavior of the rate equation model follows $\overline{n} (t) \sim 1/\sqrt{8\pi \overline{n} (0) \Gamma_{\text{eff}} t}$.

6.2 Experiences

6.2.1 Experimental protocol

To probe the quantum Zeno dynamics described above in 6.1, we study the evolution of the number of atoms in 1D optical lattices, in the regime of parameters where the inequality $J \ll \hbar \Gamma_{ee}$ is verified. The 1D optical lattices studied are obtained according the following common experimental protocol, starting from a Bose-Einstein Condensate (BEC) of ^{174}Yb atoms initially trapped in a crossed dipole trap :

- A BEC of N_{atoms} atoms is loaded in the optical lattice according to the procedure described in 2.3.1. The lattice depths are sets to $V_{x,y,z} = \{V_x, 25, 27\} E_{\text{R}}$. Here z denotes the vertical axis while x and y the horizontal ones. The lattice depth V_y is kept constant at $25\, E_{\text{R}}$, deep enough to prevent any tunneling in this direction at the timescales of the experiments (for this lattice depth, the tunneling time is equal to $\hbar/J = 77\,\text{ms}$). The lattice depth along x direction is varied over the experiments

- A π pulse of yellow light @ 578 nm, resonant with the $^1S_0 \rightarrow {}^3P_0$ transition of the ^{174}Yb atoms, is sent on the optical lattice. It transfers the atoms to the excited state. The pulse is sent along the "strong" horizontal axis y, to prevent any recoil effect and in order to be in the Lamb-Dicke regime.
- A a cleaning pulse of light resonant on the "blue" transition is sent on the atoms to remove any remaining atoms in the $^1S_0$ state.
- After the cleaning pulse we let the atoms evolve during a time T.
- Finally the lattice is switched off and the atoms are repumped to the $^1S_0$ state to be imaged after a short time of flight.

In the following we perform experiments using two different preparation protocols, depending on the number of atoms initially presents in the BEC that is loaded in the optical lattice:

- Protocol A: Initial atom number $N_{\text{atoms}} \approx 3 \times 10^4$. According to the model for the loading presented in 2.3.3 doubly occupied sites are formed in the center of the optical lattice, alongside with a shell of the singly occupied sites surrounding them. The doubly-occupied core quickly (within a millisecond) decays at the beginning of the evolution. The decay is much faster than any possible redistribution of populations by tunneling, so that we can assume that the inner core simply "disappears" before any dynamics takes place in the unit-filled outer shell. We simply wait and record the evolution of the total population after the core is emptied. We assume that the dynamics of these atoms can be described by the master equation (6.1) applied on 1D optical lattices with initial average filling $\overline{n} \leq 1$.
- Protocol B: Initial atom number $N_{\text{atoms}} \approx 8 \times 10^3$. According to the loading model presented in 2.3.3 only singly occupied sites are formed in the optical lattice. This preparation protocol is at first sight much simpler than the previous one. However, this simplicity comes at the cost of an deteriorated signal over noise ratio due to the smaller population recorded.

6.2.2 Experimental results

In Fig. 6.3 we present the evolution of the atomic populations in 1D e-lattice obtained for several lattice depths $V_x \in [8, 20]\ E_R$ ($V_x \in \{8, 12, 15, 18, 20\}\, E_R$ for protocol A and $V_x \in \{8, 11, 14, 17\}\, E_R$ for protocol B), using protocols A **(a)** and B **(b)**. The atomic population is normalized by the initial number of singly-occupied sites $N_{\text{init}}^{(1)}$. To determine this quantity for optical lattices prepared following the protocol A, we let the two-body losses deplete the atoms in doubly-occupied sites (see Sec. 6.2.1). As showed in Fig. 6.4, this process translates into a first decay of the atom number in the optical lattice that occurs at the scale of a millisecond. When all the atoms involved in doubly-occupied sites have been depleted, the atom number stabilizes at a value that we assume to correspond to $N_{\text{init}}^{(1)}$, before the emergence of the dynamics of interest in

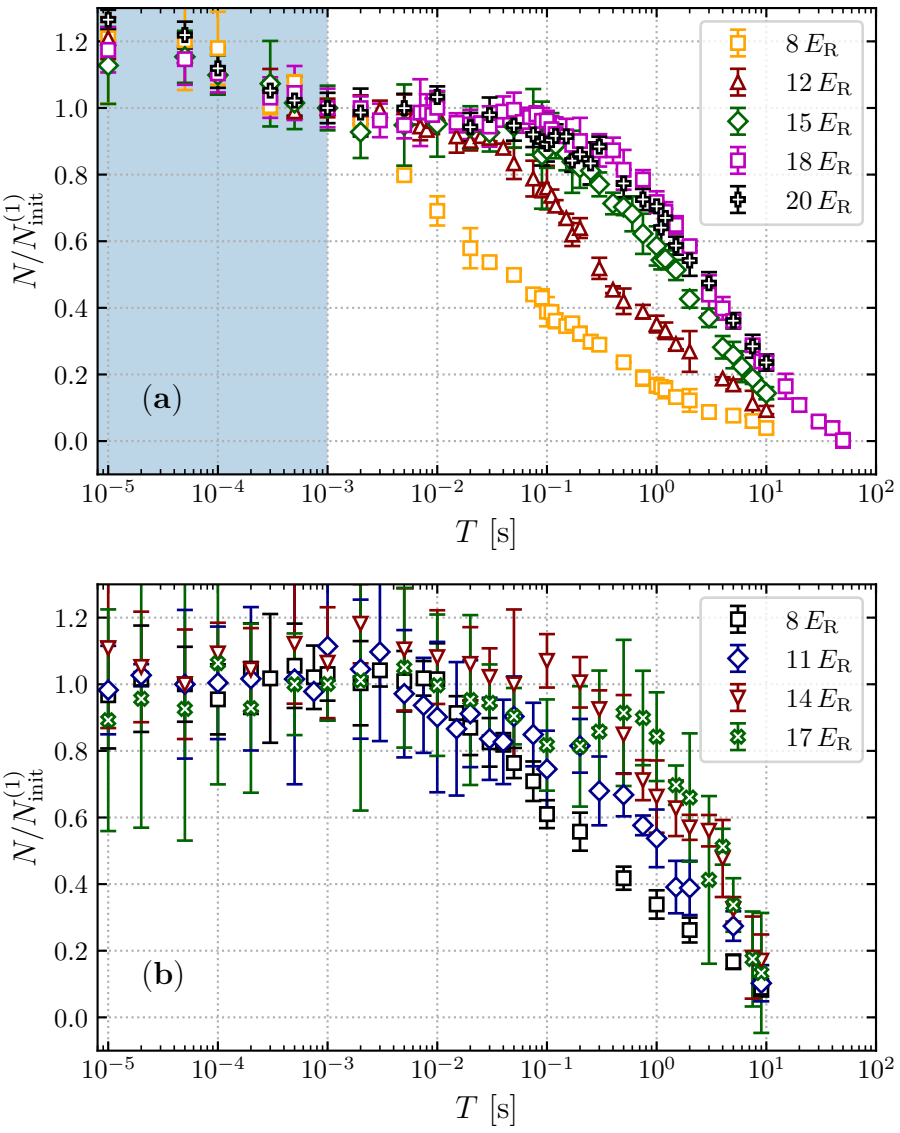

Figure 6.3 – Atom number decay in 1D optical lattices prepared according to the protocol A **(a)** for depths $V_x \in \{8, 10, 12, 15, 18, 20\}\, E_R$ and prepared according to protocol B **(b)** for depths $V_x \in \{8, 11, 14, 17\}\, E_R$. The atomic population for each lattice depths is normalized by the initial number of atoms in the singly occupied sites. For the protocol A, this quantity is determined by the plateau in the evolution of the number of atoms, that corresponds to the interval between the end of the two-body losses, here the blue shaded area, and the Zeno-dynamics related ones. For the protocol B, it simply correspond to the initial atom number.

this chapter, *i.e.* whose associated with bosons evolving in a unidimensional lattice, subject to strong elastic and inelastic collisions.

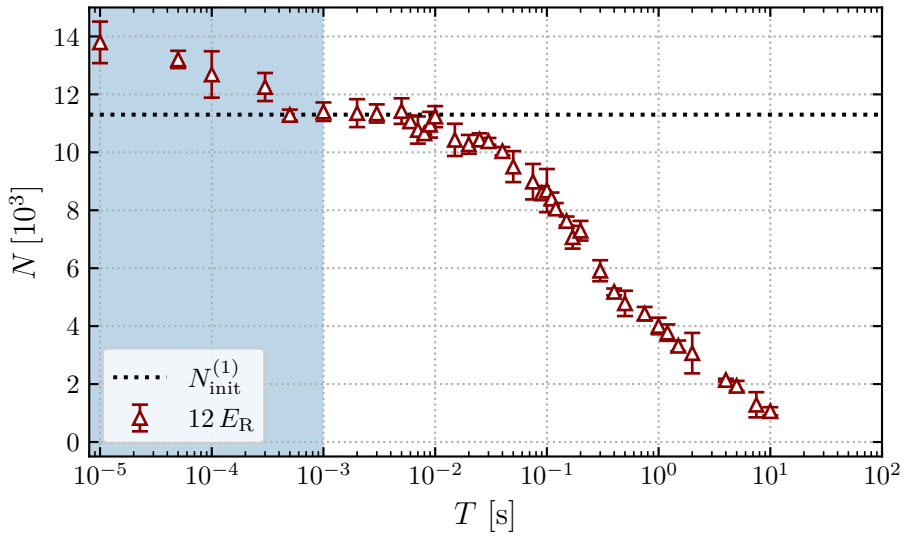

Figure 6.4 – Determination of the initial atom number for protocol A for the experiment performed at $V_x = 12\,E_{\mathrm{R}}$. In a first time, the atoms involved in doubly-occupied sites are depleted by the inelastic collision processes within a millisecond (blue shaded area). When all the bosons pair have been lost due to the two-body losses, the decay stops and the atom number stabilize around a value (dotted black line) that we assume to corresponds to $N^{(1)}_{\mathrm{init}}$. Then a second decay occurs, corresponding to the dynamics, studied in this chapter, of a bosons trapped in a unidimensional optical lattice, in presence of strong elastic and inelastic interactions.

6.2.3 Comparison of the models with the experimental data

In this section we compare the experimental data presented in Fig. 6.3 to the two model introduced above in 6.1.4 and 6.1.5. The experimental data points and both models are represented in Fig. 6.5, assuming an initial average filling in the optical lattices of $\overline{n} = 1$. We observe a discrepancy between the models at low lattice depths for both protocols. For the lowest lattice depths probed, the experimental data time-rescaled by $(4\Gamma_{\mathrm{eff}})^{-1}$ in Fig. 6.5 collapse on the same, curve. This point toward a good qualitative description of the mechanism, but the losses occurs at a slower rate than the ones expected from both models. In order to have more quantitative results to compare both dynamics, we fit the experimental decays by the function

$$n_{\mathrm{MF}}\left(T,\,\kappa\right) = \frac{1}{1+\kappa T}, \tag{6.30}$$

with κ left as a fit parameter. For $\kappa = \kappa_{\mathrm{th}} = 4\Gamma_{\mathrm{eff}}$, the function $n_{\mathrm{MF}}\left(T,\,\kappa\right)$ corresponds to the function introduced in 6.21, solution of the rate equation 6.20 given by the mean field model, assuming an initial average filling $\overline{n}\left(0\right) = 1$. The function $n_{\mathrm{Rate\,eq.}}\left(T,\,\kappa\right)$ is a heuristic function which, for $\kappa = 4\Gamma_{\mathrm{eff}}$ and $\overline{n}\left(0\right) = 1$ reproduces the numerically computed solution of the rate equation (6.29) with a good accuracy. The results of

the fits, for the data obtained with both protocol, are presented in Fig. 6.6 along with their comparison with their expected value κ_{th} from the models. This analytical formula, easier to handle, allows a simple comparison with the mean field formula, while rendering properly the behavior for the average filling at short and long times.

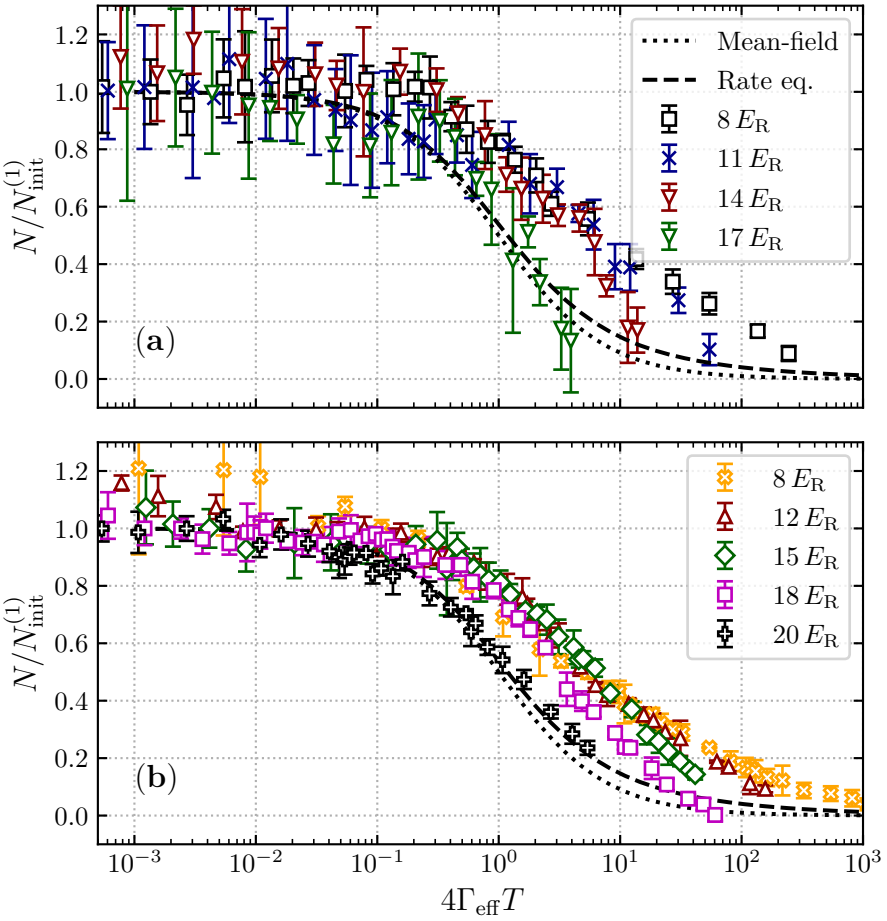

Figure 6.5 – Comparison between the time-rescaled population decay and the decay expected from the models presented in, for both protocols (A: (**a**); B: (**b**))

In Fig. 6.6 the discrepancy at low lattice depth is more straightforward: For the lowest lattice depths, the decay rate κ is smaller than the $\kappa_{\mathrm{th}} = 4\Gamma_{\mathrm{eff}}$ expected from the model introduced in Sec. 6.1.4, assuming $\overline{n}(0) = 1$, but vary similarly as the lattice depth increases. Then for intermediate lattice depths, the difference between the fitted κ and κ_{th} decreases to end up in an agreement between the experimental data and the models at $20\,E_{\mathrm{R}}$. Furthermore, for the lowest lattice depths, the dynamics for the optical lattices loaded according to protocol B is even slower than the one in lattices A. However for lattice depths $V_x < 15E_{\mathrm{R}}$, fitted parameters for both protocol seems to converge towards each other.

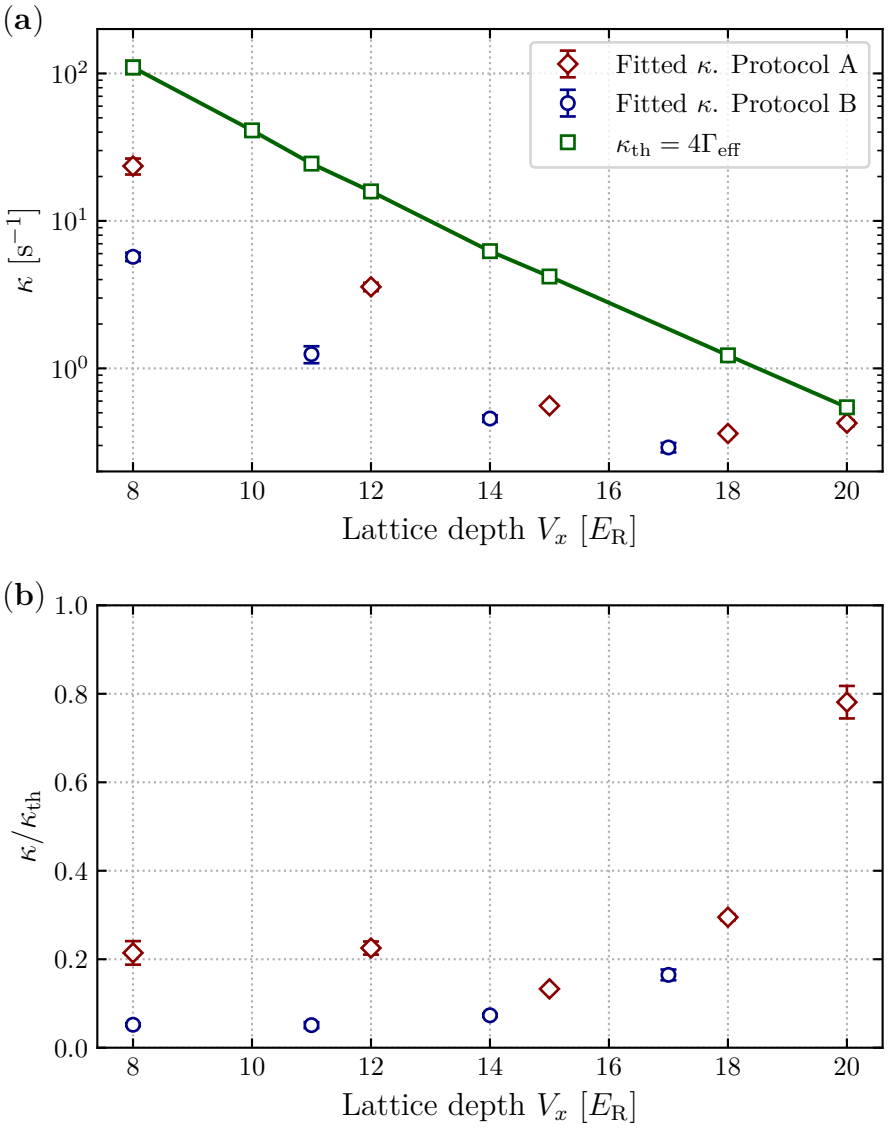

Figure 6.6 – Fitted effective decay rate κ from fit function introduced in (6.30), extracted from the experimental data obtained following protocol A (red diamonds) and protocol B (blue circles). In panel **(a)** the results of the fit procedure are compared to the expected value for κ from the models $\kappa_{\text{th}} = 4\Gamma_{\text{eff}}$ (green line and squares). In panel **(b)** the evolution of the ratio $\kappa/\kappa_{\text{th}}$ for the different lattice depths probed in our experiments.

6.2.4 Investigation on the possible causes for the slowing down of the losses dynamics

In order to explain the discrepancy between the experimentally observed decay of atomic populations in the optical lattice and the dynamics described by the models introduced earlier, we investigate several candidates for the slowing of the losses dynamics.

Evaluation of the physical quantities involved in the effective dynamics

In the discussion about the causes that could explain the observed discrepancy between the experimental data and the models observed in Fig. 6.6, we must firstly make sure that the uncertainties on the measures of the physical quantities involved in the expression of Γ_{eff} could not be sufficient. We remind from the expression (6.15) that the effective loss rate Γ_{eff} is function of the tunneling constant J and of the elastic and inelastic interaction energies, U_{ee} and $\hbar\Gamma_{ee}/2$ respectively.

The tunneling constants J and thus the lattice depths $V_{x,y,z}$ along each direction are estimated by the technique exposed in Sec. 2.3.2 relying on Kapitza-Dirac diffraction experiments, with an accuracy of $1\,E_{\text{R}}$ on the lattice depth. Given the lattice depth, the band theory introduced in Chap. 1 gives us the Wannier functions and their associated integrals for the lattice depths considered. Consequently, to determine the interaction energies, one has to estimate the values of the constants a_{ee} and β_{ee} characterizing respectively the elastic and inelastic collisions between two ^{174}Yb atoms in the excited state $|e\rangle$. The methods used to measure these quantities are presented in Sec. 5.2.2. We remind the estimates for the elastic collision parameter $a_{ee} = 126.7(2.3)$ found in Franchi et al. 2017 and for the inelastic collision parameter $\beta_{ee} = 2.5(1)\times10^{-11}\,\text{cm}^3.\text{s}^{-1}$.

The errorbars determined for all the quantities involved in the expression of Γ_{eff} are not sufficient to explain the ratio of 0.2 (see Fig. 6.6) between the experimentally recorded Γ_{eff} and the expected one from the estimated values of J, U_{ee} and $\hbar\Gamma_{ee}/2$ at low lattice depths. The uncertainty on the measures of the relevant physical quantities also fails to render the observed dependence with the lattice depth observed in Fig. 6.6. As a consequence we will consider other causes in order to explain the discrepancy between the experimental data and the models.

Initial average filling $\overline{n}$ in the 1D optical lattices

In the computations presented in Figs. 6.5 and 6.6 the inital average filling of the probed optical lattices $\overline{n}\,(0)$ has been assumed to be unity. However the experiments of time-domain Ramsey spectroscopy presented in chapter 4 have pointed out the fact that the initial average filling is inferior to unity. In order to test the hypothesis of lower filling, we compare in Fig. 6.6 **(b)** the fitted κ to the expected one $\kappa_{\text{th}} = 4\overline{n}\,(0)\,\gamma_{\text{eff}}$ for the different lattice depths and protocol probed.

Here we observe that a lattice depth-independent filling inferior to unity cannot explain the fact that the dynamics observed in our experiment is slower that the one described by the models. To ensure consistency between the experimental points and the models, an initial average filling around $\overline{n} = 0.2$ have to be considered at the lowest lattice depths for the protocol A ($\overline{n} = 0.05$ for the protocol B). However for higher lattice depths (above $15\,E_{\text{R}}$) the initial average filling has to be increased up to 1. There are numerous reasons that could make the average filling less than unity. Technical fluctuations of the optical lattice, the initial temperature of the cloud, imperfect adiabaticity during the transfer are only a few reasons that lead to an increase of entropy of the lattice gas (or even to a non-equilibrium situation). However such a wide variation of average fillings seems unreasonable, especially for the lowest lattice depths.

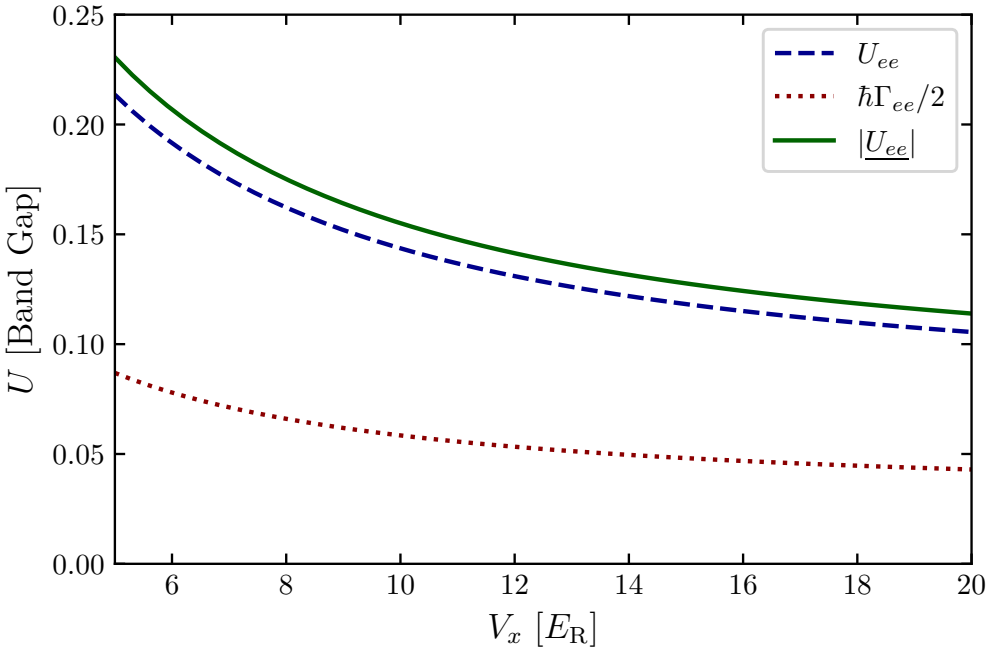

Figure 6.7 – Comparison between the energy scales at stake in the two-body elastic and inelastic collisions and the band gap for different lattice depths in the "shallow" V_x direction, assuming lattice depths of $V_{y,z} = \{25, 27\}\, E_R$ in the transverse directions. It appears that, for the lattice depths considered in our experiments these energy scales are small compared to the band gap.

Moreover, we expect that the initial average filling to be higher for the protocol B than for the protocol A. Indeed the presence of doubly occupied sites at the center of the optical lattice, which are depleted in the first millisecond of the experiment, should end up in a hole in the center of the optical lattice. At the timescales of the experiments, much longer than the tunneling time, one could expect than the empty sites in the middle of the optical lattice would lower the average filling. In addition, in order to match the models for the evolution of the atomic population in the optical lattice, we have to assume higher fillings for higher lattice depths. However, we expect adiabatic redistribution to be better fulfilled at low lattice depth. The average filling should be closer to unity in these cases.

Loss rates normalization by excited bands

Another way to explain the slowing down of the dynamics with respect to the models at low lattice depth could be to take into account the contribution of the excited bands in the dynamics. We expect them to increase the mobility of the atoms in the optical lattice. It has also been shown (Zhu et al. 2014) that in the regime where the energy scales associated to the two-body elastic and inelastic collisions are on the same order or larger than the band-gap, taking into account the excited bands could reduce the value of Γ_{eff}. However in our case, for the lattice depths probed, the energies U_{ee} and $\hbar\Gamma_{ee}/2$ are small compared to the band-gap (see Fig. 6.7), and the single-band approximation made in Chap. 1.2.1 when writing the Bose-Hubbard Hamiltonian is

relevant.

Effect of the auxiliary trapping potential

In the developments made all along this chapter, the auxiliary confining potential presented in has not be taken into account. We go back to the simple two-well model introduced in section 6.1.2 and modify it introducing an energy shift Δ between the two sites in order to have some insight on how the presence of an auxiliary confining harmonic potential will change the tunneling constant between neighboring sites in the 1D lattice. The Hamiltonian associated with this new system is:

$$\hat{H} = \begin{pmatrix} 0 & -\sqrt{2}J & -\sqrt{2}J \\ -\sqrt{2}J & U_{ee} - \Delta - \mathrm{i}\frac{\hbar\Gamma_{ee}}{2} & 0 \\ -\sqrt{2}J & 0 & U_{ee} + \Delta - \mathrm{i}\frac{\hbar\Gamma_{ee}}{2} \end{pmatrix} \tag{6.31}$$

in the $\{|1\rangle_l|1\rangle_r,\ |2\rangle_l|0\rangle_r,\ |0\rangle_l|2\rangle_r\}$ basis. If we consider the perturbation treatment of this Hamiltonian, restricted to the Hilbert space with at most one atom per site, we end up with a effective loss rate for the state $|1\rangle_l|1\rangle_r$ that can be expressed as:

$$\Gamma_{\mathrm{eff}}(\Delta) = \frac{2J^2\Gamma_{ee}}{U_{ee}^2}\left[\frac{1}{(1-\Delta/U_{ee})^2 + (\hbar\beta_{ee}/2g_{ee})^2} + \frac{1}{(1+\Delta/U_{ee})^2 + (\hbar\beta_{ee}/2g_{ee})^2}\right]. \tag{6.32}$$

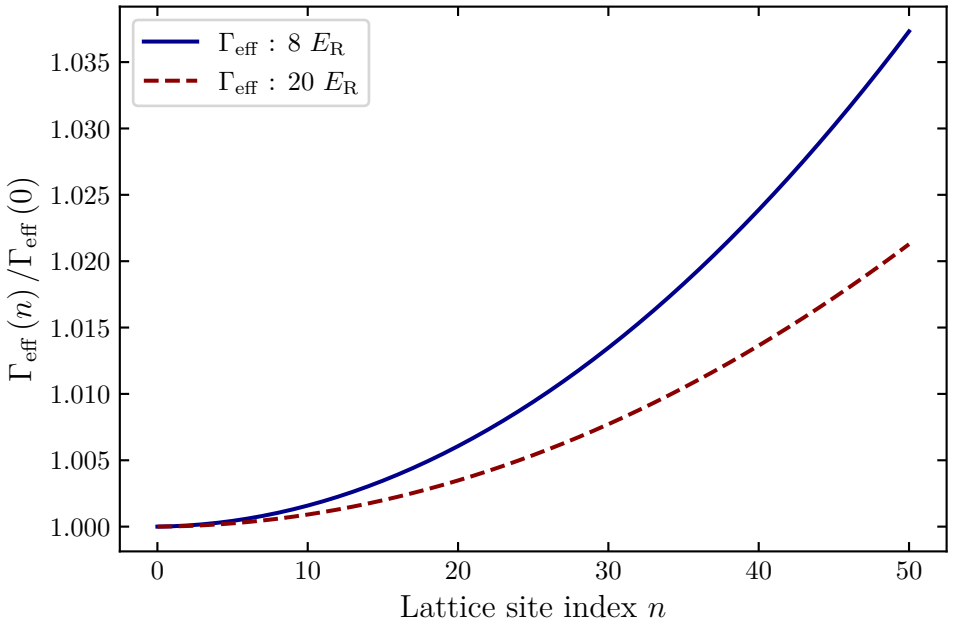

Figure 6.8 – Evolution of the correction on the effective loss rate Γ_{eff} for the two well system introduced in C.2, induced by the existence of a bias Δ between the two wells. For typical values of the ratio Δ/U_{ee} considered in the optical lattice, the additional bias reduce the gap between the ground state with one atom in each site $|1\rangle_l|1\rangle_r$ and the state with a double occupancy in the well of lower potential energy, increasing the effective loss rate.

In practice, for our experimental setup, we have shown in 2.3.1 that the harmonic auxiliary trapping potential, superposed on the optical lattice in the x "shallow" direction has a frequency $\Omega_x \approx 2\pi \times 40\,\mathrm{Hz}$. Moreover, according to the model for the loading of the optical lattice introduced in 2.3.3, the maximal radius of our optical lattice is inferior to $R_{\max} \approx 20\,\mu\mathrm{m}$. It allows us to give an upper bound for the maximal energy shift between two neighboring sites of the 1D optical lattices under study:

$$\Delta \approx m\Omega_x^2 d R_{\max} \approx 0.24\,E_{\mathrm{R}}, \tag{6.33}$$

where m is the mass of ^{174}Yb atoms, d the lattice period. When the lattice depth of the shallow axis vary from $V_x = 8\,E_{\mathrm{R}}$ to $V_x = 20\,E_{\mathrm{R}}$, the ratio Δ/U_{ee} vary from 0.4 to 0.3, which should translate into an increase of the effective loss rate Γ_{eff}, according to Fig. 6.8. This rough qualitative analysis points toward an acceleration of the losses dynamics due to the external confining potential, which do not explains the observed delay of our experimental points on the model curves. In Appendix C we perform similar analysis on slightly more complex systems of wells biased by an auxiliary potential, and end up to the same conclusion.

To conclude, the qualitative analysis performed from toy-models in this section tends to dismiss the harmonic auxiliary confining potential as the cause for the slowing down of the loss dynamics. On the contrary it could induce transport that would enhance the tunneling and consequently the formation of doubly occupied sites, where inelastic collisions will occur.

6.2.5 Relevance of the extended Bose-Hubbard model

The experiments performed to study the loss dynamics of the 1D Bose-Hubbard model in the strong dissipation regime required to consider timescales on the order of several Γ_{eff} that are very long compared to the one associated with the tunneling $\hbar/J$. Consequently the hypothesis used to write down the Bose-Hubbard Hamiltonian may be no longer valid, and some extra term, neglected so far, should be taken into account. More precisely the interaction term of the Hamiltonian:

$$\hat{H}_{\mathrm{int}} = \frac{1}{2}\sum_{i,j,k,l} U_{ijkl}\hat{a}_i^\dagger \hat{a}_j^\dagger \hat{a}_k \hat{a}_l \tag{6.34}$$

with the interaction matrix element given by:

$$U_{ijkl} = \left(g_{ee} - \frac{\mathrm{i}\hbar\beta_{ee}}{2}\right)\int \mathrm{d}\mathbf{r}\, w^*\left(\mathbf{r}-\mathbf{r}_i\right) w^*\left(\mathbf{r}-\mathbf{r}_j\right) w\left(\mathbf{r}-\mathbf{r}_k\right) w\left(\mathbf{r}-\mathbf{r}_l\right) \tag{6.35}$$

can be expanded as:

$$\hat{H}_{\text{int}} = \frac{1}{2}U_{0000}\sum_i \hat{a}_i^\dagger\hat{a}_i^\dagger\hat{a}_i\hat{a}_i \tag{6.36}$$

$$+ U_{0001}\sum_{\langle i,j\rangle}\left[\hat{a}_i^\dagger\hat{a}_i^\dagger\hat{a}_i\hat{a}_j + \text{h.c.}\right] \tag{6.37}$$

$$+ U_{0002}\sum_{\langle\langle i,j\rangle\rangle}\left[\hat{a}_i^\dagger\hat{a}_i^\dagger\hat{a}_i\hat{a}_j + \text{h.c.}\right] \tag{6.38}$$

$$+ \frac{1}{2}U_{0011}\sum_{\langle i,j\rangle}\left[\hat{a}_i^\dagger\hat{a}_i^\dagger\hat{a}_j\hat{a}_j + \hat{a}_i^\dagger\hat{a}_i\hat{a}_j^\dagger\hat{a}_j + \text{h.c.}\right] + ..., \tag{6.39}$$

where $\langle .,. \rangle$ stands for a sum on nearest-neighbors and $\langle\langle .,. \rangle\rangle$ stands for a sum on next-nearest neighbors (Dutta et al. 2015).

The first term of $\hat{H}_{\text{int}}$ with the matrix element U_{0000} is the usual interaction term of the Bose-Hubbard model. The second term (6.37) $\propto U_{0001}$ gives the first correction to the Bose-Hubbard model: it renders an *interaction induced tunneling* event from a site i to one of its nearest-neighbor j. The term (6.38) $\propto U_{0002}$ is associated to a similar event, occurring this between further lattice sites. Lastly the terms in (6.39) $\propto U_{0011}$ are associated with off-site interactions between neighboring sites, for the term $\propto \hat{a}_i^\dagger\hat{a}_i\hat{a}_j^\dagger\hat{a}_j$ and to correlated tunneling event where two particles tunnel simultaneously, called *co-tunneling*, for the term $\propto \hat{a}_i^\dagger\hat{a}_i^\dagger\hat{a}_j\hat{a}_j$. The real part of the matrix elements of the extended Bose-Hubbard model are compared to the tunneling constant and to $\hbar\Gamma_{\text{eff}}/2$ in Fig.6.9 for different lattice depths.

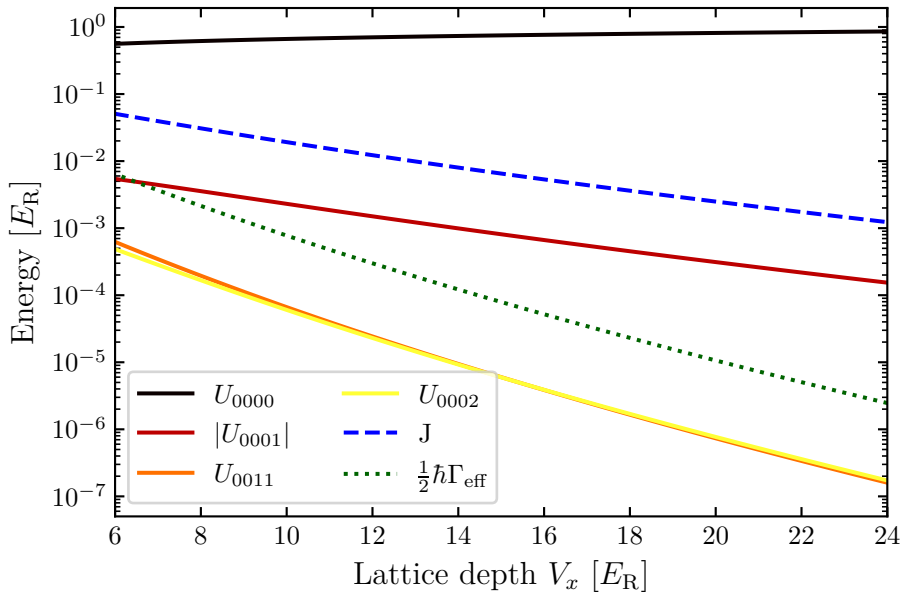

Figure 6.9 – Comparison between the first matrix elements of the extended Bose-Hubbard model, the tunneling energy and the effective loss rate for different depth of the 1D lattice, assuming $V_{y,z} = \{25, 27\}E_R$ in the strong directions of the optical lattice.

At the timescales of our experiments, we can neglect the terms $\propto U_{0011}$ and $\propto U_{0002}$. However, for lattice depths over $8\,E_{\mathrm{R}}$, the occurrence of interaction-induced tunneling cannot be neglected for timescales on the order of $\Gamma_{\mathrm{eff}}^{-1}$. This mechanism is not taken into account in the models presented earlier and cannot be easily integrated to it. Consequently, in order to have some qualitative insight on how the interaction-induced tunneling will alter the effective loss rate, we consider once again the simple model with two bosons evolving among two wells previously used in 6.1.2.

In the $\{|11\rangle, (|20\rangle + |02\rangle)/\sqrt{2}\}$ basis the Hamiltonian describing the dynamics of the system, including the interaction-induced tunneling gives:

$$\begin{pmatrix} 0 & -2J + 2\underline{V_{ee}} \\ -2J + 2\underline{V_{ee}} & \underline{U_{ee}} \end{pmatrix}. \tag{6.40}$$

Here $\underline{V_{ee}}$ denotes U_{0001} with $\underline{g} = g_{ee} - \mathrm{i}\hbar\beta_{ee}/2$. We extract from this Hamiltonian the effective loss rate for the state $|11\rangle$ using its second order perturbation expansion:

$$\Gamma_{\mathrm{eff}} = \frac{4|J - \underline{V_{ee}}|^2}{U_{ee}^2 + (\hbar\Gamma_{ee}/2)^2}\Gamma_{ee}. \tag{6.41}$$

The numerical computation of the Wannier integral associated with $\underline{V_{ee}} = U_{0001}$ gives negative values for $\mathrm{Re}\left(\underline{V_{ee}}\right)$. Consequently this correction will increase Γ_{eff} *i.e.* speed up the of the losses and therefore cannot explain the slower dynamics observed in our experiments.

6.2.6 Strength of the contact interaction

In the results of the experiments presented in 6.6, we observe that decay rates κ extracted from the experimental data are closer and closer to its expected value from the models κ_{th} as the lattice depth, and consequently the interactions strength, increases. Consequently the observed discrepancy between the models and the experiments could be due to the fact that at low lattice depths, the interactions between the bosons are not strong enough for the system to be described by the effective master equation (6.11). Under this hypothesis, the second order perturbation theory used on the Lindblad master equation (6.1) to derive (6.11) would start to be relevant only for lattice depths $V_x > 20\,E_{\mathrm{R}}$. In order to confirm or disprove this hypothesis, we plan to realize experiments in deeper lattices, in order to probe the loss dynamics in the regime where $V_x > 20\,E_{\mathrm{R}}$.

6.3 Conclusion

In this chapter we have studied experimentally the unidimensional optical lattice filled with interacting bosons subject to inelastic collision-induced two-body losses, in the strong dissipation regime. After a brief presentation of the theoretical framework used to describe the dynamics in the optical lattices, we have presented the results of our experiments on the evolution of the population of atoms in the optical lattice and compared them to two models derived from the theory of hard-core bosons in optical lattices. These results show up a behavior qualitatively consistent with the models, in a sense that $\Gamma_{\mathrm{eff}}^{-1}$ seems to be the relevant timescale associated with the losses, but not

quantitatively: for the lowest lattice depths the dynamics is slower than expected from the models. In the last part of this chapter we have tried to determine if some aspects of our experimental setup, neglected so far, could explain this slowdown of the dynamics. From our qualitative studies, it appears that initial average filling, the coupling with excited bands, the presence of a confining trapping potential and the effect of higher-order collisions terms in the expression of the Hamiltonian of the system are bad candidates to explain the observed slower dynamics of the atomic losses. Another approach to explain the slower dynamics would be to considers the assumptions made to derive the models. Indeed in order to derive the models briefly depicted in 6.1.4 and in 6.1.5, in addition to the conditions on the energy scales ($\hbar\Gamma_{ee} \gg J$), assumptions has been made in both case on the nature of the state of the system during its evolution. More particularly, in the mean-field model presented in García-Ripoll et al. 2009, the populations of the different sites of the lattice are assumed to be uncorrelated, while in the model developed in our ongoing collaboration, the derivation of the rate equation requires a state that satisfies Wick's theorem and factorization in momentum space. In both cases, simplifying assumptions on the correlations between the populations for different sites of the direct or the Fourier space have been made. Consequently, these models may fail to represent some highly correlated states.

Summary and outlook

Summary and conclusion

In the work presented in this thesis manuscript, I have studied several experiments involving ultracold ^{174}Yb atoms trapped in optical lattices, whose internal state is driven by laser light. I have shown how such experimental platforms can be used to probe the more general many-body physics of bosons evolving in a lattice, and its related effects. A particular emphasis is laid on the physics of bosons in unidimensional lattice and how the dissipative dynamics induced by inelastic collisions between ^{174}Yb atoms in their excited state can be used to control the driving of the bosons, *via* the quantum Zeno effect.

In Chapter 1, I have reminded some notions on the band theory and the Bose-Hubbard model. These notions have been used throughout this manuscript to describe and interpret the experiments performed. In this chapter they are more particularly used to discuss the effect of the auxiliary confining harmonic potential superimposed on the optical lattice and the adiabaticity of the protocol used to load the optical lattice.

The main experimental aspects of the realization of a Bose-Einstein Condensate of ^{174}Yb have been presented in Chapter 2, along with the electronic structure of ytterbium. Then the protocol to transfer the ^{174}Yb Bose-Einstein condensate into the optical lattice has been presented. Finally, from this protocol, a model describing the spatial distribution of the atoms in the optical lattice at the end of the loading has been proposed.

In Chapter 3, after introducing the experimental setup used to produce our narrow clock laser at $\lambda_{\text{clock}} = 759\,\text{nm}$, we have proposed a theoretical description of the coherent driving of ^{174}Yb on the ultranarrow $^1\text{S}_0 \longleftrightarrow {}^3\text{P}_0$ transition. This description has then been used to describe and analyze experiments, such as Rabi oscillations and Ramsey spectroscopy, preformed on single atoms trapped in isolated sites of deep optical lattices, so that the tunneling does not intervene. We have shown how these experiments could be used to study the temporal evolution of the coherence in the internal state of atoms driven on their clock transition. The results of the Ramsey experiments allowed us to point out the frequency fluctuations of our laser as the main cause of decoherence and to give an estimate of their power density spectrum, given some assumptions on its general form.

The framework and the results of the experiments detailed in Chapter 3 have then

been used in Chapter 4 to probe the dynamics taking place for two-component bosons evolving in an unidimensional lattice in the strong interaction regime, close to unit filling. A prior theoretical description of this system has pointed out two kind of mechanisms driving the system, tunneling and superexchange. Taking advantage of the site dependent phase imprinted on the atoms during their driving on the clock transition, we have seen that it is possible to relate the decay of the contrast observed for fringes obtained by time domain Ramsey spectroscopy to the dynamics of the system. The experimental data, which have pointed out the tunneling has the dominant effect, have finally been compared to numerical simulations, giving information on the initial filling of the system.

In Chapter 5 we have shown that the two-body losses induced by the inelastic collisions between a pair of ^{174}Yb atoms in the $^3P_0$ state enable a quantum Zeno effect that can be used to drive the system while hindering the transitions from the reduced-loss subspace of the Hilbert space to the lossy state. Then I have presented the implementation of this idea for isolated bosonic pairs of ^{174}Yb atoms trapped in the sites of a deep optical lattice, firstly theoretically, introducing the non-Hermitian Hamiltonian framework, in order to discuss in a second time the results of the passage experiments, to highlight the role of the quantum Zeno effect.

The physics of bosons evolving in an unidimensional lattice, interacting *via* both elastic and inelastic collisions studied in Chapter 6 combines some of the concepts introduced in Chapters 4 and 5. In this last chapter I have introduced the Lindblad master-equation describing bosons strongly interacting *via* strong elastic and inelastic interactions in an unidimensional lattice as an open quantum system. From this equation an effective master equation has been derived after perturbative expansion in the strong interaction limit, rendering the dynamics restricted to the reduced-loss subspace. This effective master equation is used as a starting point to present two theoretical models that allow to derive analytic expressions for the dynamics of the system. Then the results of experiments performed with ^{174}Yb atoms in the $^3P_0$ trapped in unidimensional optical lattices are compared with these models. We observe a qualitative agreement between the experiments and the models for the dynamics of the two-body losses in the optical lattice. However the decay of the atomic population in the optical lattices are slower than expected. This chapter ends with a discussion on the possible causes for this slow down.

Perspectives

Non-Hermitian linear response theory

Other transitions of ^{174}Yb besides the $^1S_0 \longleftrightarrow {}^3P_0$ clock one, can be used to study many-body physics. More particularly it is possible to take advantage of the finite width of the inter-combination transition $^1S_0 \longleftrightarrow {}^3P_1$ to enable spontaneous emission an optical lattice, to study the dynamics of bosons in a lattice in presence of dissipation. Such system, theoretically described in Poletti et al. 2013, have been experimentally studied in the work presented in Bouganne et al. 2019, that has not been discussed in this manuscript. The experiments performed in two dimensional optical lattices have pointed out the signature of dissipation-induced anomalous diffusion in the momentum

space.

In a subsequent theoretical work (Pan et al. 2020), it has been shown that the results of the experiments presented in Bouganne et al. 2019, realized on 2D optical lattices, were consistent with the *non-Hermitian linear response theory* developed in Pan et al. 2020. In order to confront this theory with experiment, we study in an ongoing project the evolution of the momentum distribution in a quasi-unidimensional optical lattice in presence of dissipation, enabled by driving the atoms on the inter-combination transition.

Artificial gauge field

As it has already be mentioned earlier in this manuscript, the long-term goal of our experimental setup is the implementation of the protocol presented in Gerbier et al. 2010 for the realization of artificial gauge field using the ultranarrow $^1S_0 \longleftrightarrow {}^3P_0$ transition of ytterbium. For that purpose, ultracold ^{174}Yb have to be loaded in an optical lattice with one horizontal arm at magic wavelength while the second arm will be at anti-magic wavelength (see Chap. 2). Along the first direction the atoms in states $^1S_0$ and $^3P_0$ will be indistinctly trapped. Along the second direction a state dependent lattice is formed, with the atoms in the $^1S_0$ state trapped at the nodes of the lattice potential while the atoms in the $^3P_0$ state are trapped at the anti-nodes. In the magic direction the atoms can tunnel *via* usual tunneling. In the anti-magic direction, the tunneling requires the atoms to change their internal state. The tunneling in that direction is enabled by *laser-assisted tunneling*, using a laser resonant with the clock $^1S_0 \longleftrightarrow {}^3P_0$ transition. The presence of the coupling light field results in the atoms acquiring when tunneling along the anti-magic direction.

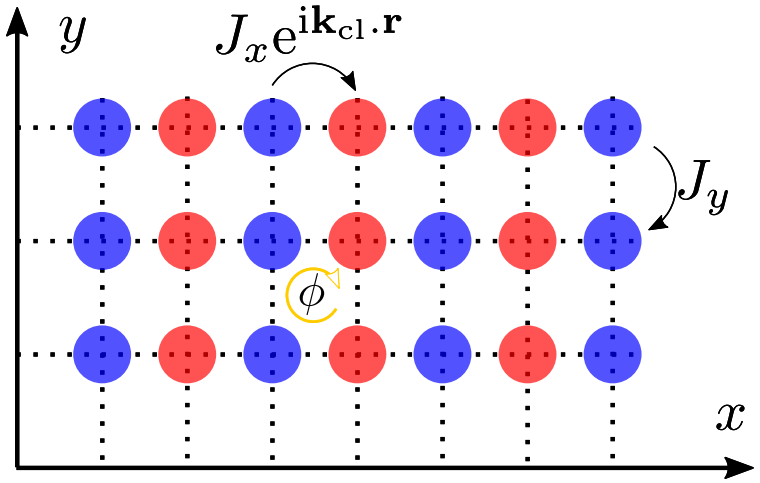

Figure O.1 – Scheme of the protocol proposed in Gerbier et al. 2010 for the implementation of artificial gauge fields. The lattice is at the magic wavelength in the y direction and at the anti-magic wavelength in the x direction. The laser-assisted tunneling in the state-dependent direction imprints a phase on the atomic state. When it circles over a closed loop in the lattice, the atom acquires a non-zero phase ϕ.

In this configuration, a particle that circles on a closed loop in the lattice acquires a non-zero phase, similarly to the case of a charged particle in presence of vector

potential described in the work of Aharonov et al. 1959, introducing the Aharonov-Bohm effect. However in this configuration, the lattice flux is staggered along the anti-magic wavelength. The protocol presented in Gerbier et al. 2010 suggests to use a *superlattice* in order to perform *flux-rectification* and create a uniform flux over the lattice.

We expect this experimental setup to allow us to realize artificial gauge field in a lattice, described by the Harper-Hofstadter Hamiltonian (Harper 1955; Hofstadter 1976). The single particle picture used in the previous paragraph is relevant in the weak interaction regime, where the number of lattice vortices is small compared to the number of atoms. Furthermore our experimental setup could be used to go beyond single-particle physics and study the new and richer phases that arise when the effect of interactions are combined to those of artificial magnetism in a lattice (Cooper 2008; Bloch et al. 2008). In particular we expect the emergence of incompressible quantum Hall phases in the phase diagram for the bare Bose-Hubdard model (Umucalılar et al. 2010).

Appendices

APPENDIX A

Adiabatic approximation

A.1 Adiabatic approximation for non-Hermitian Hamitonian

Let us consider a system whose dynamics is described by the time-dependent non-Hermitian Hamiltonian. If we assume that $\forall\, t$, $\hat{H}(t)$ is diagonalizable, it can be expressed as Ashida et al. 2020

$$\hat{H}(t) = \sum_j \lambda(t)\, |R_j(t)\rangle\langle L_j(t)| = \sum_j \lambda(t)\, \hat{P}_j(t)\,. \tag{A.1}$$

The $|R_j\rangle$ and $\langle L_j|$ are respectively the right and left eigenvectors of $\hat{H}$ defined by

$$\hat{H}|R_j\rangle = \lambda_j|R_j\rangle \tag{A.2}$$

$$\langle L_j|\hat{H} = \langle L_j|\lambda_j. \tag{A.3}$$

We also introduces $\hat{P}_j(t) = |R_j(t)\rangle\langle L_j(t)|$, the projector on the eigenspace associated with the complex eigenvalue $\lambda_j(t) = \hbar\omega_j(t) - \mathrm{i}\frac{\hbar\gamma_j(t)}{2}$. In the following for the sake of simplicity, we assume that the spectrum of $\hat{H}(t)$ is fully non-degenerate for all times t. This is the case for the system studied experimentally in Chap. 5. The system and the Hamiltonian evolve from an initial state, at the instant t_0 to a final state at time t_1. We introduce a rescaled time variable $s = \frac{t-t_0}{T}$, with $T = t_1 - t_0$ the total duration of the evolution. In the context of adiabatic passages, $1/T$ plays the role of the slowness parameter.

The evolution operator for Hermitian systems obeys

$$\mathrm{i}\hbar\frac{\mathrm{d}}{\mathrm{d}s}\hat{U} = T\hat{H}(s)\,\hat{U}(s) \quad \text{and} \quad \hat{U}(0) = \hat{\mathbb{1}}. \tag{A.4}$$

We search for the analog equation for the non-Hermitian case.

We introduce the similarity transformation $\hat{A}(s)$ (*a priori* non-unitary) transforming the basis of right eigenvectors of $\hat{H}(0)$ into the basis of eigenvectors of $\hat{H}(s)$, $|R_j(s)\rangle =$

$\hat{A}(s)|R_j(0)\rangle$. $\hat{A}^{-1}(s)$ acts similarly on left vectors, $\langle L_j(s)| = \hat{A}^{-1}(s)\langle L_j(0)|$. This implies

$$\hat{P}_j(s) = \hat{A}(s)\hat{P}_j(0)\hat{A}^{-1}(s) \quad \text{and} \quad \hat{A}(0) = \hat{\mathbb{1}}. \tag{A.5}$$

The derivative of this expression gives the condition

$$\left[\hat{K}(s), \hat{P}_j(s)\right] = \mathrm{i}\hbar\frac{\mathrm{d}\hat{P}_j}{\mathrm{d}s}, \tag{A.6}$$

where $\hat{K}$ is an invertible operator verifying (Messiah 1999)

$$\mathrm{i}\hbar\frac{\mathrm{d}\hat{A}}{\mathrm{d}s} = \hat{K}(s)\hat{A}(s) \quad \text{and} \quad -\mathrm{i}\hbar\frac{\mathrm{d}\hat{A}^{-1}}{\mathrm{d}s} = \hat{A}^{-1}(s)\hat{K}(s) \tag{A.7}$$

Reciprocally one can start from the condition (A.6) and inject the relations in (A.7) to recover (A.5).

In fact these relations only define $\hat{K}$ up to a $\sum_k \hat{P}_k(s)\hat{f}_k(s)\hat{P}_k(s)$ extra term, with $\hat{f}_k$ any operator. In order to dispel the mutiplicity of definition, we arbitrary impose that $\hat{K}$ must verify the relation:

$$\hat{P}_k(s)\hat{K}(s)\hat{P}_k(s) = 0. \tag{A.8}$$

which gives the expression for $\hat{K}(s)$:

$$\hat{K}(s) = \sum_j \frac{\mathrm{d}\hat{P}_j}{\mathrm{d}s}\hat{P}_j. \tag{A.9}$$

The operator $\hat{A}$ defined above can be use to perform the analogous of representation change for Hermitian dynamics in order to get rid of the evolution of the basis in the Schrödinger equation. Indeed, in this representation, the Schrödinger equation writes:

$$\mathrm{i}\hbar\frac{\mathrm{d}}{\mathrm{d}s}\hat{U}^{(A)} = \left[T\hat{H}^{(A)}(s) - \hat{K}^{(A)}(s)\right]\hat{U}^{(A)}(s), \tag{A.10}$$

introducing the transformed Hamiltonian:

$$\hat{H}^{(A)}(s) = \hat{A}^{-1}(s)\hat{H}(s)\hat{A}(s) = \sum_j \lambda_j(s)\hat{P}_j(0), \tag{A.11}$$

and the following operators in the new representation:

$$\hat{K}^{(A)}(s) = \hat{A}^{-1}(s)\hat{K}(s)\hat{A}(s) \tag{A.12}$$

$$\hat{U}^{(A)}(s) = \hat{A}^{-1}(s)\hat{U}(s). \tag{A.13}$$

In the Schrödinger equation (A.10), the footprint of the dynamics of the eigenvector basis is enclosed in the second term of the r.h.s. of the relation (this correspond to the Berry phase for Hermitian systems). If the evolution is slow enough, *i.e.*, we may hope that the first term of the r.h.s of the equation will dominate. We introduce $\hat{\Phi}_{\mathrm{R}}$ the solution of the Schödinger equation in absence of the $\hat{K}$ term:

$$\mathrm{i}\hbar\frac{\mathrm{d}}{\mathrm{d}t}\hat{\Phi} = \hat{H}^{(A)}(t)\,\hat{\Phi}(t)\,, \tag{A.14}$$

which corresponds to the situation where the eigenvectors basis are time independent. This operator takes charge of the phase acquired by the system during its evolution. The expressions for $\hat{\Phi}$ and its inverse are:

$$\hat{\Phi}(s) = \sum_j \mathrm{e}^{-\frac{\mathrm{i}}{\hbar}\int_0^s \lambda_j(\sigma)\,\mathrm{d}\sigma}\hat{P}_j(0) \quad \text{and} \quad \hat{\Phi}^{-1}(s) = \sum_j \mathrm{e}^{+\frac{\mathrm{i}}{\hbar}\int_0^s \lambda_j(\sigma)\,\mathrm{d}\sigma}\hat{P}_j(0)\,. \tag{A.15}$$

This operator can also be used as a similarity transformation to rewrite the Schrödinger equation (A.10) as:

$$\mathrm{i}\hbar\frac{\mathrm{d}}{\mathrm{d}s}\hat{U}^{(B)} = -\hat{K}^{(B)}(s)\,\hat{U}^{(B)}(s) \tag{A.16}$$

with

$$\hat{U}^{(B)} = \hat{\Phi}^{-1}\hat{U}^{(A)} = \hat{\Phi}^{-1}\hat{A}^{-1}\hat{U} \tag{A.17}$$

$$\hat{K}^{(B)} = \hat{\Phi}^{-1}\hat{K}^{(A)}\hat{\Phi} = \hat{\Phi}^{-1}\hat{A}^{-1}\hat{K}\hat{A}\hat{\Phi} \tag{A.18}$$

The evolution operator over the all transformation in this representation can be expressed as:

$$\hat{U}^{(B)}(1) = \hat{\mathbb{1}} + \frac{\mathrm{i}}{\hbar}\int_0^1 \hat{K}^{(B)}(s)\,\hat{U}^{B}(s)\;\mathrm{d}s \tag{A.19}$$

or

$$\hat{U}^{(B)}(1) = \hat{\mathbb{1}} - \int_0^1 \sum_{j,k} \alpha_{j,k}(s)\,\mathrm{e}^{\frac{\mathrm{i}}{\hbar}T\int_0^s \lambda_j(\sigma)-\lambda_k(\sigma)\,\mathrm{d}\sigma}|R_j(0)\rangle\langle L_k(0)|\hat{U}^{(B)}(s)\;\mathrm{d}s \tag{A.20}$$

with

$$\alpha_{jk}(s) = \langle L_j(s)|\frac{\mathrm{d}\hat{P}_k}{\mathrm{d}s}|R_k(s)\rangle \tag{A.21}$$

$$= -\frac{\mathrm{i}}{\hbar}\langle L_j(0)|\hat{A}^{-1}(s)\,\hat{P}_j(s)\,\hat{K}(s)\,\hat{P}_k(s)\,\hat{A}(s)\,|R_k(0)\rangle. \tag{A.22}$$

On may notice that $\forall j\,\alpha_{jj}(s) = 0$ since $\hat{K}$ verify the property.

Assuming that the system is initially in the eigenstate $|R_m\rangle$, its probability to have "followed" the evolution of the system is given by the modulus square of the matrix

element:

$$\langle L_m(0)|\hat{U}^{(B)}|R_m(0)\rangle = 1-\sum_{k\neq m}\int_0^1 \alpha_{m,k}(s)\,\mathrm{e}^{\frac{\mathrm{i}}{\hbar}T\int_0^s \lambda_m(\sigma)-\lambda_k(\sigma)\,\mathrm{d}\sigma}\langle L_k(0)|\hat{U}^{(B)}(s)\,|R_m(0)\rangle\,\mathrm{d}s \tag{A.23}$$

If we restrict ourselves to the a first order approximation, we conclude that the adiabatic approximation, starting in the eigenstate $|R_m(0)\rangle$ is valid only if the terms

$$\eta_{mk} = \int_0^1 \alpha_{j,k}(s)\,\mathrm{e}^{\frac{\mathrm{i}}{\hbar}T\int_0^s \lambda_m(\sigma)-\lambda_k(\sigma)\,\mathrm{d}\sigma}\,\mathrm{d}s \quad \text{for} \quad k\neq m \tag{A.24}$$

becomes negligible when $T\to+\infty$. From this expression, it is possible to show (Messiah 1999; Nenciu et al. 1992; Sun 1993; Ibáñez et al. 2014) that the adiabatic approximation is valid if the following condition is satisfied:

$$\Big|\frac{\hbar\alpha_{mk}(s)}{T|\lambda_m(s)-\lambda_j(s)|}\Big|\exp\left[\frac{T}{2}\int_0^s \gamma_m(\sigma)-\gamma_j(\sigma)\,\mathrm{d}\sigma\right]\ll 1 \quad \forall\, s \quad \forall\, j\neq m. \tag{A.25}$$

which can be rewritten for non rescaled times

$$\Big|\frac{\hbar\alpha_{mk}(t)}{|\lambda_m(t)-\lambda_j(t)|}\Big|\exp\left[\frac{1}{2}\int_{t_0}^t \gamma_m(\tau)-\gamma_j(\tau)\,\mathrm{d}\tau\right]\ll 1 \quad \forall\, t \quad \forall\, j\neq m. \tag{A.26}$$

From these expressions it comes that the adiabatic approximation can only be valid in the limit $T\to\infty$ for the least dissipative state, *i.e.* the one with the imaginary part with the smallest modulus, to ensure that exponential factor decays as $T\to\infty$. One may also remark that for finite T, if the quantity $\frac{T}{2}\int_0^s \gamma_m(\sigma)-\gamma_j(\sigma)\,\mathrm{d}\sigma$ remains close to $1\;\forall\, s$, *i.e.* if the values of γ_m and γ_j stay very close one to another during the evolution, the adiabatic approximation can be used, even if the initial state is not always the less dissipative state. This situation, which is observed in our experiment between the two states of the reduced-loss subspace, corresponds to the "weak non-Hermicity" case mentioned by Nenciu et al. 1992. Consequently, performing adiabatic passages that cross the detuning ($\delta_{\mathrm{L,\,cross.}}\approx -115\,\mathrm{Hz}$) where the ordering of the imaginary parts of the eigenvalues associated to the eigenstates $|\lambda_1\rangle$ and $\langle\lambda_3|$ is reversed is still relevant.

APPENDIX B

Fit procedures

Most of the fit functions used above are non linear and non linearisable, which made the fit procedure and the computation of confidence intervals a little more complicated. We present here the procedure used in the thesis to compute them in the non-linear case.

B.1 Weighted least squares ("χ^2 fit")

This method consists in minimizing the weighted residuals sum of squares RSS over the parameter $\mathbf{p} = [p_1, p_2, ..., p_k]$:

$$RSS = \sum_i^N \left(\frac{y_i - f(t_i; \mathbf{p})}{\sigma_i} \right)^2 \tag{B.1}$$

$$\mathbf{p}^* = \underset{\mathbf{p}}{\operatorname{argmin}} (RSS) \tag{B.2}$$

Then to estimate the confidence interval for a given parameter (e.g. p_k), we compute the quantity:

$$\tilde{F}(p_k) = (n-k) \frac{RSS(\tilde{\mathbf{p}}^*) - RSS(\mathbf{p}^*)}{RSS(\mathbf{p}^*)} \tag{B.3}$$

where $\tilde{\mathbf{p}}^* = \left[p_1^*, p_2^*, ..., p_{k-1}^*, p_k\right]$. Since $\tilde{F}$ has approximately a $F_{1,n-k}$ distribution, it is possible to compute confidence intervals. For more details see Chap. 8 of (2002)

B.2 Boostrap

The bootstrap is a Monte Carlo like approach to determine the statistical distribution of the regression parameters Bohm et al. 2010. Our experimental curves are made of 5 measurements of atom numbers $N_{t,i=1,2,3,4,5}$ after different wait times t. To perform the bootstrap we proceed as follow: for each wait time T we pick randomly a value for N_T among the 5 available. Then we perform a regression by minimizing the residual least squares RSS. This step is repeated several times (e.g. 1000 times) and each set

of fitted parameters obtained are stored. In the end we compute the mean and the standard deviation for each parameter.

APPENDIX C

Effect of the auxiliary trapping potential

In Sec. 6.2.4, we adapt the simple two-well model introduced in Sec. 6.1.2 to have some insight on the effect of the presence of the auxiliary trap on the quantum Zeno dynamics under study in Chap. 6. From the pertubative treatment performed on this simple model we conclude that the presence of an auxiliary confining potential should accelerate the loss dynamics, whereas we experimentally observe a slowdown.

However one may object that the difference between the models and the experimental points occurs at long timescales, when the losses has already taken place, reducing the average filling of the optical lattice. In order to take the presence of empty sites in the optical lattice in our qualitative analysis of the effect of the auxiliary confining potential, we perform perturbation expansion on the system made of two bosons interacting *via* elastic and inelastic collisions, evolving in a triple well, with an energy shift Δ between the central well, indexed by 0 and the lateral ones, indexed by -1 and 1. In the basis $\{[|110\rangle + |011\rangle]/\sqrt{2}, |101\rangle, [|200\rangle + |002\rangle]/\sqrt{2}, |020\rangle\}$, the Hamiltonian of the system writes:

$$\begin{pmatrix} 0 & -\sqrt{2}J & -\sqrt{2}J & -2J \\ -\sqrt{2}J & \Delta & 0 & 0 \\ -\sqrt{2}J & 0 & U_{ee} + \Delta - \mathrm{i}\hbar\Gamma_{ee}/2 & 0 \\ -2J & 0 & 0 & U_{ee} - \Delta - \mathrm{i}\hbar\Gamma_{ee}/2 \end{pmatrix}. \tag{C.1}$$

Assuming that $\Delta > 0$, $\Delta \gg J$ and that $\Delta \ll U_{ee}$, the perturbation expansion of this Hamiltonian gives:

$$\Gamma_{\text{eff}} = \frac{2J^2\Gamma_{ee}}{U_{ee}^2}\left[\frac{2}{\left(1-\Delta/U_{ee}\right)^2 + \left(\hbar\beta_{ee}/2g_{ee}\right)^2} + \frac{1}{\left(1+\Delta/U_{ee}\right)^2 + \left(\hbar\beta_{ee}/2g_{ee}\right)^2}\right] \tag{C.2}$$

as effective loss rate for the ground state $[|110\rangle + |011\rangle]/\sqrt{2}$.

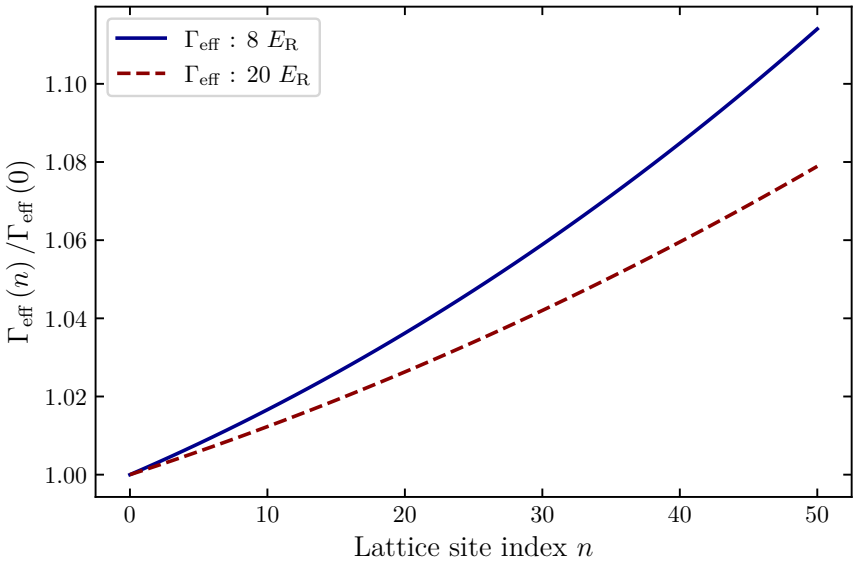

Figure C.1 – Evolution of the correction on the effective loss rate Γ_{eff} for the two well system introduced in C.2, induced by the existence of a bias Δ between the two wells. For the typical values of the ratio Δ/U_{ee} considered in the optical lattice, the additional bias reduce the gap between the ground state with one atom in each site $|1\rangle_l|1\rangle_r$ and the state with a double occupancy in the well of lower potential energy, increasing the effective loss rate.

Similarly we consider an ensemble of two bosons interacting *via* elastic and inelastic interactions, evolving in three wells, indexed by the integers {0, 1, 2} connected by a tunneling constant J, and with energy shifts Δ_1 and Δ_2 on the wells 1 and 2 respectively. In the $\{|110\rangle, |101\rangle, |011\rangle, |200\rangle, |020\rangle, |002\rangle\}$ basis, the Hamiltonian describing the dynamics of the system writes as:

$$\begin{pmatrix} \Delta_1 & -J & 0 & -\sqrt{2}J & -\sqrt{2}J & 0 \\ -J & \Delta_2 & -J & 0 & 0 & 0 \\ 0 & -J & \Delta_1+\Delta_2 & 0 & -\sqrt{2}J & -\sqrt{2}J \\ -\sqrt{2}J & 0 & 0 & \underline{U_{ee}} & 0 & 0 \\ -\sqrt{2}J & 0 & -\sqrt{2}J & 0 & \underline{U_{ee}}+2\Delta_1 & 0 \\ 0 & 0 & -\sqrt{2}J & 0 & 0 & \underline{U_{ee}}+2\Delta_2 \end{pmatrix}, \tag{C.3}$$

with $\underline{U_{ee}} = U_{ee} - \mathrm{i}\Gamma_{ee}/2$. Similarly to what has been done for the previous studied systems, a perturbation expansion is performed in order to derive an effective Hamiltonian acting in the loss-reduced subspace of the Hilbert space, spanned by the Fock states with at most one boson per well. We end up writing the effective loss rates for these states :

$$\begin{aligned} \Gamma_{\text{eff},|110\rangle} &= \frac{2J^2\Gamma_{ee}}{U_{ee}^2}\left[\frac{1}{(1-2\Delta_1/U_{ee})^2+(\hbar\beta_{ee}/2g_{ee})^2}+\frac{1}{(1+2\Delta_1/U_{ee})^2+(\hbar\beta_{ee}/2g_{ee})^2}\right] \\ \Gamma_{\text{eff},|101\rangle} &= 0 \\ \Gamma_{\text{eff},|011\rangle} &= \frac{2J^2\Gamma_{ee}}{U_{ee}^2}\left[\frac{1}{(1-\delta_{21}/U_{ee})^2+(\hbar\beta_{ee}/2g_{ee})^2}+\frac{1}{(1+\delta_{21}/U_{ee})^2+(\hbar\beta_{ee}/2g_{ee})^2}\right] \end{aligned} \tag{C.4}$$

with $\delta_{21} = \Delta_2 - \Delta_1$. More particularly, if we map the three wells on three adjacent sites of the lattice of index $\{n,\, n+1,\, n+2\}$ with n an integer equal to 0 at the center of the lattice, shifted by the auxiliary confining harmonic potential, the detuning Δ_1 and Δ_2 introduced in C.4 becomes:

$$\begin{aligned} \Delta_1(n) &= \frac{1}{2} m\Omega_x^2 d^2 (2n+1) \\ \Delta_2(n) &= 2m\Omega_x^2 d^2 (n+1)\,. \end{aligned} \tag{C.5}$$

We use these expression to represent the evolution of the effective loss rates introduced in C.4 in Fig. C.2. We observe that for our experimental parameters, the correction induced by the confining potential on the effective loss rate is very small, and tends to increase the effective loss rate.

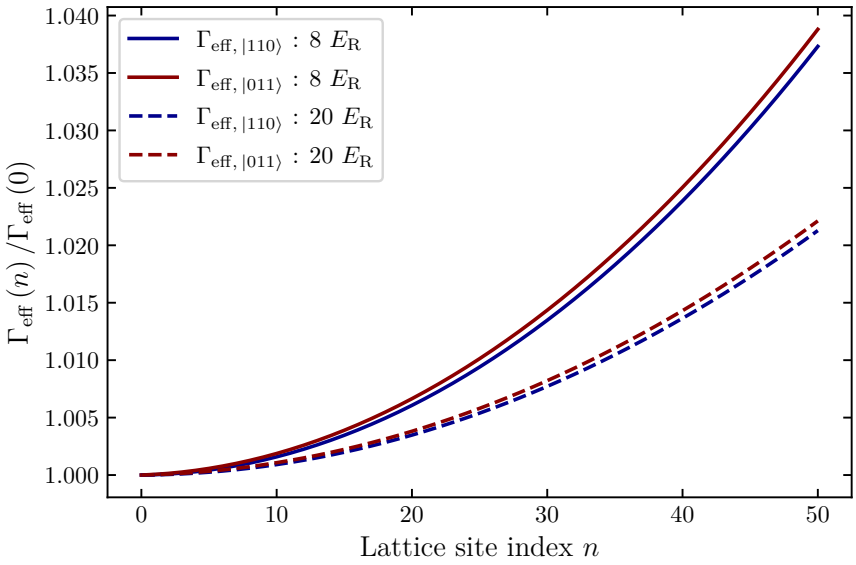

Figure C.2 – Evolution of the correction on the effective loss rate Γ_{eff} for the three well system introduced in C.2, induced by the existence of a bias Δ between the two wells. For the typical values of the ratio Δ/U_{ee} considered in the optical lattice, the additional bias reduce the gap between the ground state with one atom in each site $|1\rangle_l|1\rangle_r$ and the state with a double occupancy in the well of lower potential energy, increasing the effective loss rate.

Bibliography

Aharonov, Y. and D. Bohm (1959). *Significance of electromagnetic potentials in the quantum theory*. Physical Review **115.3**, 485–491 (cited on page 152).

Aidelsburger, M., M. Atala, M. Lohse, J. T. Barreiro, B. Paredes, and I. Bloch (2013). *Realization of the Hofstadter Hamiltonian with Ultracold Atoms in Optical Lattices*. Phys. Rev. Lett. **111** (18), 185301 (cited on page 79).

Aikawa, K, A Frisch, M Mark, S Baier, A Rietzler, R Grimm, and F Ferlaino (2012). *Bose-Einstein condensation of erbium*. Physical review letters **108.21**, 210401 (cited on page 2).

Altman, E., W. Hofstetter, E. Demler, and M. D. Lukin (2003). *Phase diagram of two-component bosons on an optical lattice*. New Journal of Physics **5**, 113–113 (cited on page 81).

Anderson, B. M., I. B. Spielman, and G. Juzeliunas (2013). *Magnetically Generated Spin-Orbit Coupling for Ultracold Atoms*. Phys. Rev. Lett. **111** (12), 125301 (cited on page 79).

Anderson, M. H., J. R. Ensher, M. R. Matthews, C. E. Wieman, and E. A. Cornell (1995). *Observation of Bose-Einstein condensation in a dilute atomic vapor*. Science **269.5221**, 198–201 (cited on page 1).

Andrews, M. R., C. G. Townsend, H.-J. Miesner, D. S. Durfee, D. M. Kurn, and W. Ketterle (1997). *Observation of interference between two Bose condensates*. Science **275.5300**, 637–641 (cited on page 1).

Ashcroft, N. and N. Mermin (1976). *Solid state physics*. HRW international editions. Holt, Rinehart and Winston (cited on pages 8, 13, 59, 60).

Ashida, Y., Z. Gong, and M. Ueda (2020). *Non-Hermitian Physics*. arXiv: 2006.01837 [cond-mat.mes-hall] (cited on pages 3, 111, 155).

Barber, Z. W., C. W. Hoyt, C. W. Oates, L. Hollberg, A. V. Taichenachev, and V. I. Yudin (2006). *Direct excitation of the forbidden clock transition in neutral 174-Yb atoms confined to an optical lattice*. Physical Review Letters **96.8**, 083002 (cited on page 31).

Barber, Z. W., J. E. Stalnaker, N. D. Lemke, N. Poli, C. W. Oates, T. M. Fortier, S. A. Diddams, L. Hollberg, C. W. Hoyt, A. V. Taichenachev, and V. I. Yudin (2008). *Optical lattice induced light shifts in an Yb atomic clock*. Physical Review Letters **100.10**, 103002 (cited on pages 31, 32).

Bardon, A. B., S. Beattie, C. Luciuk, W. Cairncross, D. Fine, N. S. Cheng, G. J. A. Edge, E. Taylor, S. Zhang, S. Trotzky, and et al. (2014). *Transverse Demagnetization Dynamics of a Unitary Fermi Gas*. Science **344.6185**, 722–724 (cited on page 84).

Ben Dahan, M., E. Peik, J. Reichel, Y. Castin, and C. Salomon (1996). *Bloch Oscillations of Atoms in an Optical Potential*. Phys. Rev. Lett. **76** (24), 4508–4511 (cited on page 23).

Berry, M. V. (1984). *Quantal phase factors accompanying adiabatic changes*. Proceedings of the Royal Society of London. A. Mathematical and Physical Sciences (cited on page 114).

Bertet, P., S Osnaghi, A Rauschenbeutel, G Nogues, A Auffeves, M Brune, J. Raimond, and S Haroche (2001). *A complementarity experiment with an interferometer at the quantum–classical boundary*. Nature **411.6834**, 166–170 (cited on page 3).

Bethe, H. A. and E. E. Salpeter (1957). *Quantum mechanics of one- and two-electron atoms*. Berlin Heidelberg: Springer-Verlag (cited on page 28).

Blakie, P. B. and J. V. Porto (2004). *Adiabatic loading of bosons into optical lattices*. Physical Review A **69.1**, 013603 (cited on page 22).

Bloch, I., T. W. Hänsch, and T. Esslinger (2000). *Measurement of the spatial coherence of a trapped Bose gas at the phase transition*. Nature **403.6766**, 166 (cited on page 1).

Bloch, I., J. Dalibard, and W. Zwerger (2008). *Many-body physics with ultracold gases*. Reviews of Modern Physics **80.3**, 885–964 (cited on pages 1, 11, 15, 27, 152).

Bloch, I., J. Dalibard, and S. Nascimbene (2012). *Quantum simulations with ultracold quantum gases*. Nature Physics **8.4**, 267–276 (cited on page 2).

Bohm, G. and G. Zech (2010). *Introduction to Statistics and Data Analysis for Physicists* (cited on page 159).

Borkowski, M., A. A. Buchachenko, R. Ciuryło, P. S. Julienne, H. Yamada, Y. Kikuchi, K. Takahashi, Y. Takasu, and Y. Takahashi (2017). *Beyond-Born-Oppenheimer effects in sub-kHz-precision photoassociation spectroscopy of ytterbium atoms*. Physical Review A **96.6**, 063405 (cited on page 40).

Bosch Aguilera, M. (2019). *Coherence and relaxation of an optically-driven bosonic quantum gas*. PhD Thesis. Sorbonne Université, Université Pierre et Marie Curie, Paris 6 (cited on pages 27, 37, 41, 54–57, 60).

Bose, S. N. (1924). *Plancks gesetz und lichtquantenhypothese* (cited on page 1).

Bouganne, R., M. Bosch Aguilera, A. Dareau, E. Soave, J. Beugnon, and F. Gerbier (2017). *Clock spectroscopy of interacting bosons in deep optical lattices*. New Journal of Physics **19.11**, 113006 (cited on pages 105, 107–110).

Bouganne, R. (2018). *Probing ultracold ytterbium in optical lattices with resonant light: from coherent control to dissipative dynamics*. PhD Thesis. Sorbonne Université, Université Pierre et Marie Curie, Paris 6 (cited on pages 27, 36, 37, 54).

Bouganne, R., M. Bosch Aguilera, A. Ghermaoui, J. Beugnon, and F. Gerbier (2019). *Anomalous decay of coherence in a dissipative many-body system*. Nature Physics, 1–5 (cited on pages 150, 151).

Bowers, C. J., D. Budker, E. D. Commins, D. DeMille, S. J. Freedman, A.-T. Nguyen, S.-Q. Shang, and M. Zolotorev (1996). *Experimental investigation of excited-state lifetimes in atomic ytterbium.* Physical Review A **53.5**, 3103–3109 (cited on page 57).

Bradley, C. C., C. A. Sackett, J. J. Tollett, and R. G. Hulet (1995). *Evidence of Bose-Einstein condensation in an atomic gas with attractive interactions.* Physical Review Letters **75.9**, 1687–1690 (cited on page 1).

Breuer, H. P. and F. Petruccione (2007). *The theory of open quantum systems.* Oxford University Press (cited on pages 102, 103).

Bromley, S. L., S. Kolkowitz, T. Bothwell, D. Kedar, A. Safavi-Naini, M. L. Wall, C. Salomon, A. M. Rey, and J. Ye (2018). *Dynamics of interacting fermions under spin–orbit coupling in an optical lattice clock.* Nature Physics **14.4**, 399 (cited on pages 3, 84).

Bylander, J., S. Gustavsson, F. Yan, F. Yoshihara, K. Harrabi, G. Fitch, D. G. Cory, Y. Nakamura, J.-S. Tsai, and W. D. Oliver (2011). *Noise spectroscopy through dynamical decoupling with a superconducting flux qubit.* Nature Physics **7.7**, 565–570 (cited on page 66).

Cazalilla, M. A., A. F. Ho, and M. Ueda (2009). *Ultracold gases of ytterbium: ferromagnetism and Mott states in an SU(6) Fermi system.* New Journal of Physics **11.10**, 103033 (cited on page 2).

Chen, W., Ş. Kaya Özdemir, G. Zhao, J. Wiersig, and L. Yang (2017). *Exceptional points enhance sensing in an optical microcavity.* Nature **548.7666**, 192–196 (cited on page 114).

Cheuk, L. W., A. T. Sommer, Z. Hadzibabic, T. Yefsah, W. S. Bakr, and M. W. Zwierlein (2012). *Spin-Injection Spectroscopy of a Spin-Orbit Coupled Fermi Gas.* Phys. Rev. Lett. **109** (9), 095302 (cited on page 79).

Chin, C., R. Grimm, P. Julienne, and E. Tiesinga (2010). *Feshbach resonances in ultracold gases.* Rev. Mod. Phys. **82** (2), 1225–1286 (cited on page 1).

Chu, S. (1998). *Nobel lecture: The manipulation of neutral particles.* Reviews of Modern Physics **70.3**, 685–706 (cited on page 1).

Cloizeaux, J. D. (1964). *Energy Bands and Projection Operators in a Crystal: Analytic and Asymptotic Properties.* Phys. Rev. **135** (3A), A685–A697 (cited on page 10).

Cohen-Tannoudji, C. N. (1998). *Nobel lecture: Manipulating atoms with photons.* Reviews of Modern Physics **70.3**, 707–719 (cited on page 1).

Cook, R. J. (1988). *What are Quantum Jumps?* Physica Scripta **T21**, 49–51 (cited on pages 3, 100, 101).

Cooper, N. R. (2011). *Optical Flux Lattices for Ultracold Atomic Gases.* Phys. Rev. Lett. **106** (17), 175301 (cited on page 33).

Cooper, N. (2008). *Rapidly rotating atomic gases.* Advances in Physics **57.6**, 539–616 (cited on page 152).

Cornish, S. L., N. R. Claussen, J. L. Roberts, E. A. Cornell, and C. E. Wieman (2000). *Stable 85 Rb Bose-Einstein condensates with widely tunable interactions.* Physical Review Letters **85.9**, 1795 (cited on page 1).

Cywiński, u., R. M. Lutchyn, C. P. Nave, and S. Das Sarma (2008). *How to enhance dephasing time in superconducting qubits*. Physical Review B **77**.**17** (cited on page 66).

Dalfovo, F., S. Giorgini, L. P. Pitaevskii, and S. Stringari (1999). *Theory of Bose-Einstein condensation in trapped gases*. Reviews of Modern Physics **71**.**3**, 463–512 (cited on page 40).

Dalibard, J., Y. Castin, and K. Mølmer (1992). *Wave-function approach to dissipative processes in quantum optics*. Physical Review Letters **68**.**5**, 580–583 (cited on page 104).

Dalibard, J., F. Gerbier, G. Juzeliūnas, and P. Öhberg (2011). *Colloquium: Artificial gauge potentials for neutral atoms*. Reviews of Modern Physics **83**.**4**, 1523–1543 (cited on pages 62, 79).

Dareau, A. (2015). *Manipulation cohérente d'un condensat de Bose-Einstein d'ytterbium sur la transition "d'horloge" : de la spectroscopie au magnétisme artificiel*. PhD Thesis. École Normale Superieure (cited on pages 27, 36–38, 53, 54).

Davis, K. B., M. O. Mewes, M. R. Andrews, N. J. van Druten, D. S. Durfee, D. M. Kurn, and W. Ketterle (1995). *Bose-Einstein Condensation in a Gas of Sodium Atoms*. Physical Review Letters **75**.**22**, 3969–3973 (cited on page 1).

DeMarco, B. and D. S. Jin (1999). *Onset of Fermi degeneracy in a trapped atomic gas*. Science **285**.**5434**, 1703–1706 (cited on page 1).

Dembowski, C., H.-D. Gräf, H. L. Harney, A. Heine, W. D. Heiss, H. Rehfeld, and A. Richter (2001). *Experimental Observation of the Topological Structure of Exceptional Points*. Phys. Rev. Lett. **86** (5), 787–790 (cited on page 114).

Dembowski, C., B. Dietz, H.-D. Gräf, H. L. Harney, A. Heine, W. D. Heiss, and A. Richter (2004). *Encircling an exceptional point*. Phys. Rev. E **69** (5), 056216 (cited on page 114).

Denschlag, J. H., J. E. Simsarian, H. Häffner, C. McKenzie, A. Browaeys, D. Cho, K. Helmerson, S. L. Rolston, and W. D. Phillips (2002). *A Bose-Einstein condensate in an optical lattice*. Journal of Physics B: Atomic, Molecular and Optical Physics **35**.**14**, 3095 (cited on page 45).

Dicke, R. H. (1953). *The Effect of Collisions upon the Doppler Width of Spectral Lines*. Phys. Rev. **89** (2), 472–473 (cited on page 62).

Diehl, S., A. Micheli, A. Kantian, B. Kraus, H. P. Büchler, and P. Zoller (2008). *Quantum states and phases in driven open quantum systems with cold atoms*. Nature Physics **4**.**11**, 878–883 (cited on page 129).

Doppler, J., A. A. Mailybaev, J. Böhm, U. Kuhl, A. Girschik, F. Libisch, T. J. Milburn, P. Rabl, N. Moiseyev, and S. Rotter (2016). *Dynamically encircling an exceptional point for asymmetric mode switching*. Nature **537**.**7618**, 76–79 (cited on page 114).

Drever, R. W. P., J. L. Hall, F. V. Kowalski, J. Hough, G. M. Ford, A. J. Munley, and H. Ward (1983). *Laser phase and frequency stabilization using an optical resonator*. Applied Physics B **31**.**2**, 97–105 (cited on page 55).

Duan, L.-M., E. Demler, and M. D. Lukin (2003). *Controlling Spin Exchange Interactions of Ultracold Atoms in Optical Lattices*. Phys. Rev. Lett. **91** (9), 090402 (cited on page 80).

Dum, R., P. Zoller, and H. Ritsch (1992). *Monte Carlo simulation of the atomic master equation for spontaneous emission*. Physical Review A **45.7**, 4879–4887 (cited on page 104).

Dutta, O., M. Gajda, P. Hauke, M. Lewenstein, D.-S. Lühmann, B. A. Malomed, T. Sowiński, and J. Zakrzewski (2015). *Non-standard Hubbard models in optical lattices: a review*. Reports on Progress in Physics **78.6**, 066001 (cited on page 146).

Dzuba, V. A. and A. Derevianko (2010). *Dynamic polarizabilities and related properties of clock states of the ytterbium atom*. Journal of Physics B: Atomic, Molecular and Optical Physics **43.7**, 074011 (cited on page 32).

Efetov, K. and A. Larkin (1976). *Correlation functions in one-dimensional systems with a strong interaction*. Sov. Phys. JETP **42.390**, 11 (cited on page 3).

Einstein, A. (1925). *Quantentheorie des einatomigen idealen Gases: Abhandlung 2* (cited on page 1).

Essler, F. H. L., H. Frahm, F. Göhmann, A. Klümper, and V. E. Korepin (2005). *The One-Dimensional Hubbard Model*. Cambridge University Press (cited on page 81).

Feng, L., Z. J. Wong, R.-M. Ma, Y. Wang, and X. Zhang (2014). *Single-mode laser by parity-time symmetry breaking*. Science **346.6212**, 972–975. eprint: https://science.sciencemag.org/content/346/6212/972.full.pdf (cited on page 114).

Feynman, R. P. (1982). *Simulating physics with computers*. International Journal of Theoretical Physics **21.6**, 467–488 (cited on page 2).

Fisher, M. P. A., P. B. Weichman, G. Grinstein, and D. S. Fisher (1989). *Boson localization and the superfluid-insulator transition*. Physical Review B **40.1**, 546–570 (cited on pages 2, 14).

Foss-Feig, M., M. Hermele, and A. M. Rey (2010). *Probing the Kondo lattice model with alkaline-earth-metal atoms*. Physical Review A **81.5**, 051603 (cited on page 2).

Franchi, L., L. F. Livi, G. Cappellini, G. Binella, M. Inguscio, J. Catani, and L. Fallani (2017). *State-dependent interactions in ultracold 174Yb probed by optical clock spectroscopy*. New Journal of Physics **19.10**, 103037 (cited on pages 107, 108, 110, 142).

García-Ripoll, J. J., S. Dürr, N. Syassen, D. M. Bauer, M. Lettner, G. Rempe, and J. I. Cirac (2009). *Dissipation-induced hard-core boson gas in an optical lattice*. New Journal of Physics **11.1**, 013053 (cited on pages 4, 131, 132, 134, 135, 148).

Georgescu, I., S. Ashhab, and F. Nori (2014). *Quantum simulation*. Reviews of Modern Physics **86.1**, 153–185 (cited on page 2).

Gerbier, F., S. Trotzky, S. Fölling, U. Schnorrberger, J. D. Thompson, A. Widera, I. Bloch, L. Pollet, M. Troyer, B. Capogrosso-Sansone, N. V. Prokof'ev, and B. V. Svistunov (2008). *Expansion of a quantum gas released from an optical lattice*. Physical Review Letters **101.15**, 155303 (cited on page 49).

Gerbier, F., A. Widera, S. Fölling, O. Mandel, T. Gericke, and I. Bloch (2005). *Phase coherence of an atomic Mott insulator*. Physical Review Letters **95.5**, 050404 (cited on page 50).

Gerbier, F. and J. Dalibard (2010a). *Gauge fields for ultracold atoms in optical superlattices*. New Journal of Physics **12.3**, 033007 (cited on pages 2, 62, 151, 152).

Gerbier, F. and Y. Castin (2010b). *Heating rates for an atom in a far-detuned optical lattice*. Physical Review A **82.1**, 013615 (cited on pages 33, 99).

Gericke, T., F. Gerbier, A. Widera, S. Fölling, O. Mandel, and I. Bloch (2007). *Adiabatic loading of a Bose–Einstein condensate in a 3D optical lattice*. Journal of Modern Optics **54.5**, 735–743 (cited on page 25).

Girardeau, M. (1960). *Relationship between systems of impenetrable bosons and fermions in one dimension*. Journal of Mathematical Physics **1.6**, 516–523 (cited on pages 3, 133).

Goldman, N., G. Juzeliūnas, P. Öhberg, and I. B. Spielman (2014). *Light-induced gauge fields for ultracold atoms*. Reports on Progress in Physics **77.12**, 126401 (cited on page 62).

Gorini, V., A. Kossakowski, and E. C. G. Sudarshan (1976). *Completely positive dynamical semigroups of N-level systems*. Journal of Mathematical Physics **17.5**, 821–825. eprint: https://aip.scitation.org/doi/pdf/10.1063/1.522979 (cited on page 102).

Gorshkov, A. V., M. Hermele, V. Gurarie, C. Xu, P. S. Julienne, J. Ye, P. Zoller, E. Demler, M. D. Lukin, and A. M. Rey (2010). *Two-orbital SU(N) magnetism with ultracold alkaline-earth atoms*. Nature Physics **6.4**, 289–295 (cited on pages 2, 33).

Greiner, M. (2003). *Ultracold quantum gases in three-dimensional optical lattice potentials*. PhD Thesis. Ludwig-Maximilians-Universität München (cited on page 23).

Greiner, M., O. Mandel, T. Esslinger, T. W. Hänsch, and I. Bloch (2002). *Quantum phase transition from a superfluid to a Mott insulator in a gas of ultracold atoms*. Nature **415.6867**, 39–44 (cited on pages 1, 18, 49).

Griesmaier, A., J. Werner, S. Hensler, J. Stuhler, and T. Pfau (2005). *Bose-Einstein condensation of chromium*. Physical Review Letters **94.16**, 160401 (cited on page 2).

Grimm, R., M. Weidemüller, and Y. B. Ovchinnikov (2000). *Optical dipole traps for neutral atoms*. Advances In Atomic, Molecular, and Optical Physics **42**, 95 –170 (cited on pages 32, 42).

Hahn, E. L. (1950). *Spin Echoes*. Physical Review **80.4**, 580–594 (cited on pages 3, 66).

Haroche, S. and J.-M. Raimond (2013). *Exploring the quantum: atoms, cavities, and photons*. OCLC: 894721442. Oxford: Oxford University Press (cited on pages 63, 102, 103, 111, 118).

Harper, P. G. (1955). *Single band motion of conduction electrons in a uniform magnetic field*. Proceedings of the Physical Society. Section A **68.10**, 874–878 (cited on page 152).

Hartmann, M. J., F. G. Brandao, and M. B. Plenio (2008). *A polaritonic two-component Bose–Hubbard model*. New Journal of Physics **10.3**, 033011 (cited on page 2).

Heiss, W. D. (2012). *The physics of exceptional points*. Journal of Physics A: Mathematical and Theoretical **45.44**, 444016 (cited on pages 3, 112).

Hess, H. F. (1986). *Evaporative cooling of magnetically trapped and compressed spin-polarized hydrogen*. Physical Review B **34.5**, 3476–3479 (cited on page 1).

Hild, S., T. Fukuhara, P. Schauß, J. Zeiher, M. Knap, E. Demler, I. Bloch, and C. Gross (2014). *Far-from-equilibrium spin transport in Heisenberg quantum magnets*. Physical Review Letters **113.14**, 147205 (cited on pages 81, 84, 86).

Hinkley, N., J. A. Sherman, N. B. Phillips, M. Schioppo, N. D. Lemke, K. Beloy, M. Pizzocaro, C. W. Oates, and A. D. Ludlow (2013). *An atomic clock with 10–18 instability*. Science **341.6151**, 1215–1218 (cited on page 2).

Hänsch, T. W. and A. L. Schawlow (1975). *Cooling of gases by laser radiation*. Optics Communications **13.1**, 68–69 (cited on page 1).

Ho, T.-L. and Q. Zhou (2009). *Squeezing out the entropy of fermions in optical lattices*. Proceedings of the National Academy of Sciences **106.17**, 6916–6920 (cited on page 22).

Hofstadter, D. R. (1976). *Energy levels and wave functions of Bloch electrons in rational and irrational magnetic fields*. Physical Review B **14.6**, 2239–2249 (cited on page 152).

Honda, K., Y. Takahashi, T. Kuwamoto, M. Fujimoto, K. Toyoda, K. Ishikawa, and T. Yabuzaki (1999). *Magneto-optical trapping of Yb atoms and a limit on the branching ratio of the 1P1 state*. Physical Review A **59.2**, R934–R937 (cited on page 29).

Ibáñez, S. and J. G. Muga (2014). *Adiabaticity condition for non-Hermitian Hamiltonians*. Physical Review A **89.3**, 033403 (cited on page 158).

Itano, W. M., D. J. Heinzen, J. J. Bollinger, and D. J. Wineland (1990). *Quantum Zeno effect*. Physical Review A **41.5**, 2295–2300 (cited on pages 3, 101).

Jaksch, D., C. Bruder, J. I. Cirac, C. W. Gardiner, and P. Zoller (1998). *Cold bosonic atoms in optical lattices*. Physical Review Letters **81.15**, 3108–3111 (cited on pages 2, 14, 49, 80).

Jaksch, D. and P. Zoller (2005). *The cold atom Hubbard toolbox*. Annals of physics **315.1**, 52–79 (cited on page 2).

Jepsen, N., J. Amato-Grill, I. Dimitrova, W. W. Ho, E. Demler, and W. Ketterle (2020). *Spin transport in a tunable Heisenberg model realized with ultracold atoms*. arXiv: 2005.09549 [cond-mat.quant-gas] (cited on page 84).

Jordan, P. and E. Wigner (1928). *Über das Paulische Äquivalenzverbot*. Zeitschrift fur Physik **47.9-10**, 631–651 (cited on page 135).

Jotzu, G., M. Messer, R. Desbuquois, M. Lebrat, T. Uehlinger, D. Greif, and T. Esslinger (2014). *Experimental realization of the topological Haldane model with ultracold fermions*. Nature **515.7526**, 237–240 (cited on page 79).

Kajtoch, D., E. Witkowska, and A. Sinatra (2018). *Adiabaticity when raising a uniform three-dimensional optical lattice in a bimodal Bose-Einstein condensate*. Physical Review A **98.2**, 023621 (cited on page 24).

Kapitza, P. L. and P. a. M. Dirac (1933). *The reflection of electrons from standing light waves*. Mathematical Proceedings of the Cambridge Philosophical Society **29.2**, 297–300 (cited on page 45).

Kato, T. (1966). *Perturbation Theory for Linear Operators*. Vol. 132. Grundlehren der mathematischen Wissenschaften. Springer-Verlag Berlin Heidelberg (cited on pages 3, 112).

Ketterle, W, D. Durfee, and S. Kurn (1999b). "Making, probing and understanding Bose-Einstein condensates". *Bose-Einstein Condensation in Atomic Gases (Proceedings of the International School of Physics "Enrico Fermi," Course CXL)*. IOS Press (cited on page 38).

Ketterle, W, D. Durfee, and D M. Stamper-Kurn (1999a). *Making, probing and understanding Bose-Einstein condensates*. Vol. 140. Proceedings of the International School of Physics "Enrico Fermi" (cited on pages 27, 39).

Kitagawa, M., K. Enomoto, K. Kasa, Y. Takahashi, R. Ciuryło, P. Naidon, and P. S. Julienne (2008). *Two-color photoassociation spectroscopy of ytterbium atoms and the precise determinations of s-wave scattering lengths*. Physical Review A **77.1**, 012719 (cited on pages 14, 40, 107).

Kohn, W. (1959). *Analytic properties of Bloch waves and Wannier functions*. Physical Review **115.4**, 809–821 (cited on page 10).

Kolkowitz, S., S. L. Bromley, T. Bothwell, M. L. Wall, G. E. Marti, A. P. Koller, X. Zhang, A. M. Rey, and J. Ye (2017). *Spin–orbit-coupled fermions in an optical lattice clock*. Nature **542.7639**, 66–70 (cited on page 79).

Korepin, V. E., N. M. Bogoliubov, and A. G. Izergin (1997). *Quantum inverse scattering method and correlation functions*. Vol. 3. Cambridge university press (cited on page 3).

Kraus, B., H. P. Büchler, S. Diehl, A. Kantian, A. Micheli, and P. Zoller (2008). *Preparation of entangled states by quantum Markov processes*. Physical Review A **78.4** (cited on page 129).

Kraus, K., A. Böhm, J. D. Dollard, and W. H. Wootters (1983). *States, Effects, and Operations Fundamental Notions of Quantum Theory*. Vol. 190 (cited on page 103).

Krauth, W., M. Caffarel, and J.-P. Bouchaud (1992). *Gutzwiller wave function for a model of strongly interacting bosons*. Physical Review B **45.6**, 3137–3140 (cited on page 15).

Kuklov, A. B. and B. V. Svistunov (2003). *Counterflow Superfluidity of Two-Species Ultracold Atoms in a Commensurate Optical Lattice*. Phys. Rev. Lett. **90** (10), 100401 (cited on page 81).

Lahaye, T., C Menotti, L Santos, M Lewenstein, and T Pfau (2009). *The physics of dipolar bosonic quantum gases*. Reports on Progress in Physics **72.12**, 126401 (cited on page 2).

Langen, T., S. Erne, R. Geiger, B. Rauer, T. Schweigler, M. Kuhnert, W. Rohringer, I. E. Mazets, T. Gasenzer, and J. Schmiedmayer (2015). *Experimental observation of a generalized Gibbs ensemble*. Science **348.6231**, 207–211 (cited on page 2).

Leek, P. J., J. M. Fink, A. Blais, R. Bianchetti, M. Goppl, J. M. Gambetta, D. I. Schuster, L. Frunzio, R. J. Schoelkopf, and A. Wallraff (2007). *Observation of Berry's Phase in a Solid-State Qubit*. Science **318.5858**, 1889–1892 (cited on page 3).

Leib, M. and M. J. Hartmann (2010). *Bose–Hubbard dynamics of polaritons in a chain of circuit quantum electrodynamics cavities*. New Journal of Physics **12.9**, 093031 (cited on page 2).

Lewenstein, M., A. Sanpera, and V. Ahufinger (2012). *Ultracold atoms in optical lattices: simulating quantum many-body systems*. Oxford University Press (cited on page 2).

Lin, Y.-J., K. Jiménez-García, and I. B. Spielman (2011a). *Spin–orbit-coupled Bose Einstein condensates*. Nature **471.7336**, 83–86 (cited on page 79).

Lin, Z., H. Ramezani, T. Eichelkraut, T. Kottos, H. Cao, and D. N. Christodoulides (2011b). *Unidirectional invisibility induced by PT-symmetric periodic structures*. Physical Review Letters **106.21**, 213901 (cited on page 114).

Lindblad, G. (1976). *On the generators of quantum dynamical semigroups*. Comm. Math. Phys. **48.2**, 119–130 (cited on page 102).

Livi, L., G. Cappellini, M. Diem, L. Franchi, C. Clivati, M. Frittelli, F. Levi, D. Calonico, J. Catani, M. Inguscio, and L. Fallani (2016). *Synthetic dimensions and spin-orbit coupling with an optical clock transition*. Physical Review Letters **117.22**, 220401 (cited on page 79).

London, F. (1938). *On the bose-einstein condensation*. Physical Review **54.11**, 947 (cited on page 1).

Lu, M., N. Q. Burdick, S. H. Youn, and B. L. Lev (2011). *Strongly dipolar Bose-Einstein condensate of dysprosium*. Physical review letters **107.19**, 190401 (cited on page 2).

Ludlow, A. D., M. M. Boyd, J. Ye, E. Peik, and P. Schmidt (2015). *Optical atomic clocks*. Reviews of Modern Physics **87.2**, 637–701 (cited on pages 2, 29, 33, 79).

Madison, K., F Chevy, W Wohlleben, and J. Dalibard (2000). *Vortex formation in a stirred Bose-Einstein condensate*. Physical review letters **84.5**, 806 (cited on page 1).

Maiman, T. H. (1960). *Stimulated optical radiation in ruby*. nature **187.4736**, 493–494 (cited on page 1).

Masuhara, N., J. M. Doyle, J. C. Sandberg, D. Kleppner, T. J. Greytak, H. F. Hess, and G. P. Kochanski (1988). *Evaporative cooling of spin-polarized atomic hydrogen*. Physical Review Letters **61.8**, 935 (cited on page 1).

Matthews, M. R., B. P. Anderson, P. C. Haljan, D. S. Hall, C. E. Wieman, and E. A. Cornell (1999). *Vortices in a Bose-Einstein condensate*. Physical Review Letters **83.13**, 2498–2501 (cited on page 1).

Messiah, A. (1999). *Quantum mechanics*. Dover books on physics. Dover Publications (cited on pages 22, 156, 158).

Metcalf, H. J., P. v. d. Straten, and P. v. d. Straten (1999). *Laser cooling and trapping*. Graduate Texts in Contemporary Physics. New York: Springer-Verlag (cited on pages 27, 35).

Milburn, T. J., J. Doppler, C. A. Holmes, S. Portolan, S. Rotter, and P. Rabl (2015). *General description of quasi-adiabatic dynamical phenomena near exceptional points*. Physical Review A **92.5**, 052124 (cited on page 114).

Misra, B. and E. C. G. Sudarshan (1977). *The Zeno's paradox in quantum theory*. Journal of Mathematical Physics **18.4**, 756–763 (cited on pages 3, 100).

Miyake, H., G. A. Siviloglou, C. J. Kennedy, W. C. Burton, and W. Ketterle (2013). *Realizing the Harper Hamiltonian with Laser-Assisted Tunneling in Optical Lattices*. Phys. Rev. Lett. **111** (18), 185302 (cited on page 79).

Modern Applied Statistics with S (2002). Springer (cited on page 159).

Morsch, O. and M. Oberthaler (2006). *Dynamics of Bose-Einstein condensates in optical lattices*. Reviews of Modern Physics **78.1**, 179–215 (cited on page 24).

Nenciu, G. (1983). *Existence of the exponentially localised Wannier functions*. Communications in Mathematical Physics **91.1**, 81–85 (cited on page 10).

Nenciu, G. and G. Rasche (1992). *On the adiabatic theorem for nonself-adjoint Hamiltonians*. Journal of Physics A: Mathematical and General **25.21**, 5741–5751 (cited on page 158).

Ovchinnikov, Y. B., J. H. Müller, M. R. Doery, E. J. D. Vredenbregt, K. Helmerson, S. L. Rolston, and W. D. Phillips (1999). *Diffraction of a released Bose-Einstein condensate by a pulsed standing light wave*. Physical Review Letters **83.2**, 284–287 (cited on page 45).

Pan, L., X. Chen, Y. Chen, and H. Zhai (2020). *Non-Hermitian linear response theory*. Nature Physics **16.7**, 767–771 (cited on page 151).

Paredes, B., A. Widera, V. Murg, O. Mandel, S. Fölling, I. Cirac, G. V. Shlyapnikov, T. W. Hänsch, and I. Bloch (2004). *Tonks–Girardeau gas of ultracold atoms in an optical lattice*. Nature **429.6989**, 277 (cited on pages 3, 133).

Peng, B., K. Ozdemir, S. Rotter, H. Yilmaz, M. Liertzer, F. Monifi, C. M. Bender, F. Nori, and L. Yang (2014a). *Loss-induced suppression and revival of lasing*. Science **346.6207**, 328–332 (cited on page 114).

Peng, B., a. K. Özdemir, F. Lei, F. Monifi, M. Gianfreda, G. L. Long, S. Fan, F. Nori, C. M. Bender, and L. Yang (2014b). *Parity–time-symmetric whispering-gallery microcavities*. Nature Physics **10.5**, 394–398 (cited on page 114).

Phillips, W. D. (1998). *Nobel lecture: Laser cooling and trapping of neutral atoms*. Reviews of Modern Physics **70.3**, 721–741 (cited on page 1).

Plenio, M. B. and P. L. Knight (1998). *The quantum-jump approach to dissipative dynamics in quantum optics*. Reviews of Modern Physics **70.1**, 101–144 (cited on page 104).

Poletti, D., P. Barmettler, A. Georges, and C. Kollath (2013). *Emergence of glasslike dynamics for dissipative and strongly interacting bosons*. Physical Review Letters **111.19**, 195301 (cited on page 150).

Pollet, L. (2012). *Recent developments in quantum Monte Carlo simulations with applications for cold gases*. Reports on Progress in Physics **75.9**, 094501 (cited on page 15).

Porsev, S. G., A. Derevianko, and E. N. Fortson (2004). *Possibility of an optical clock using the* $6^1S_0 \rightarrow 6^3P_0^o$ *transition in* ^{171,173}Yb *atoms held in an optical lattice*. Phys. Rev. A **69** (2), 021403 (cited on page 29).

Ramsey, N. (1986). *Molecular beams*. Oxford Classic Texts in the Physical Sciences. Oxford, New York: Oxford University Press (cited on page 64).

Ramsey, N. F. (1950). *A molecular beam resonance method with separated oscillating fields*. Physical Review **78.6**, 695 (cited on page 3).

Rokhsar, D. S. and B. G. Kotliar (1991). *Gutzwiller projection for bosons*. Physical Review B **44.18**, 10328–10332 (cited on page 15).

Savard, T. A., K. M. O'Hara, and J. E. Thomas (1997). *Laser-noise-induced heating in far-off resonance optical traps*. Physical Review A **56.2**, R1095–R1098 (cited on page 37).

Scholl, M. (2014). *Probing an ytterbium Bose-Einstein condensate using an ultranarrow optical line : towards artificial gauge fields in optical lattices*. PhD Thesis. Université Pierre et Marie Curie - Paris 6 (cited on pages 27, 36, 38, 39).

Sheshadri, K., H. R. Krishnamurthy, R. Pandit, and T. V. Ramakrishnan (1993). *Superfluid and insulating phases in an interacting-boson model: mean-field theory and the RPA*. EPL (Europhysics Letters) **22.4**, 257 (cited on page 15).

Struck, J., C. Ölschläger, M. Weinberg, P. Hauke, J. Simonet, A. Eckardt, M. Lewenstein, K. Sengstock, and P. Windpassinger (2012). *Tunable Gauge Potential for Neutral and Spinless Particles in Driven Optical Lattices*. Phys. Rev. Lett. **108** (22), 225304 (cited on page 79).

Sun, C.-P. (1993). *High-order adiabatic approximation for non-Hermitian quantum system and complexification of Berry's phase*. Physica Scripta **48.4**, 393–398 (cited on page 158).

Syassen, N., D. M. Bauer, M. Lettner, T. Volz, D. Dietze, J. J. García-Ripoll, J. I. Cirac, G. Rempe, and S. Dürr (2008). *Strong dissipation inhibits losses and induces correlations in cold molecular gases*. Science **320.5881**, 1329–1331 (cited on pages 4, 129).

Taichenachev, A. V., V. I. Yudin, C. W. Oates, C. W. Hoyt, Z. W. Barber, and L. Hollberg (2006). *Magnetic field-induced spectroscopy of forbidden optical transitions with application to lattice-based optical atomic clocks*. Physical Review Letters **96.8**, 083001 (cited on pages 29, 30).

Takamoto, M., F.-L. Hong, R. Higashi, and H. Katori (2005). *An optical lattice clock*. Nature **435.7040**, 321–324 (cited on page 2).

Takasu, Y., K. Maki, K. Komori, T. Takano, K. Honda, M. Kumakura, T. Yabuzaki, and Y. Takahashi (2003). *Spin-singlet Bose-Einstein condensation of two-electron atoms*. Physical Review Letters **91.4**, 040404 (cited on page 2).

Tomadin, A., S. Diehl, M. D. Lukin, P. Rabl, and P. Zoller (2012). *Reservoir engineering and dynamical phase transitions in optomechanical arrays*. Physical Review A **86.3** (cited on page 2).

Tomita, T., S. Nakajima, Y. Takasu, and Y. Takahashi (2019). *Dissipative Bose-Hubbard system with intrinsic two-body loss*. Physical Review A **99.3**, 031601 (cited on page 129).

Tonks, L. (1936). *The complete equation of state of one, two and three-dimensional gases of hard elastic spheres*. Physical Review **50.10**, 955–963 (cited on pages 3, 133).

Tsui, D. C., H. L. Stormer, and A. C. Gossard (1982). *Two-dimensional magneto-transport in the extreme quantum limit.* Physical Review Letters **48.22**, 1559–1562 (cited on page 2).

Umucalılar, R. O. and E. J. Mueller (2010). *Fractional quantum Hall states in the vicinity of Mott plateaus.* Physical Review A **81.5**, 053628 (cited on page 152).

Venables, W. N. and B. D. Ripley (2002). *Modern Applied Statistics with S.* Springer New York (cited on page 109).

Verstraete, F., M. M. Wolf, and J. I. Cirac (2009). *Quantum computation and quantum-state engineering driven by dissipation.* Nature physics **5.9**, 633–636 (cited on pages 3, 129).

Von Neumann, J. (1932). *Mathematische Grundlagen der Quantenmechanik.* Berlin [u.a.]: Springer (cited on page 101).

Wall, M. L., A. P. Koller, S. Li, X. Zhang, N. R. Cooper, J. Ye, and A. M. Rey (2016). *Synthetic Spin-Orbit Coupling in an Optical Lattice Clock.* Physical Review Letters **116.3**, 035301 (cited on page 79).

Wallraff, A., D. I. Schuster, A. Blais, L. Frunzio, J. Majer, M. H. Devoret, S. M. Girvin, and R. J. Schoelkopf (2005). *Approaching Unit Visibility for Control of a Superconducting Qubit with Dispersive Readout.* Physical Review Letters **95.6** (cited on page 3).

Wang, P., Z.-Q. Yu, Z. Fu, J. Miao, L. Huang, S. Chai, H. Zhai, and J. Zhang (2012). *Spin-Orbit Coupled Degenerate Fermi Gases.* Phys. Rev. Lett. **109** (9), 095301 (cited on page 79).

Wannier, G. H. (1937). *The structure of electronic excitation levels in insulating crystals.* Physical Review **52.3**, 191–197 (cited on page 9).

Westergaard, P. (2010). *Strontium Optical Lattice Clock: In Quest of the Ultimate Performance.* PhD Thesis. Télécom ParisTech (cited on page 76).

Wiersig, J. (2014). *Enhancing the Sensitivity of Frequency and Energy Splitting Detection by Using Exceptional Points: Application to Microcavity Sensors for Single-Particle Detection.* Phys. Rev. Lett. **112** (20), 203901 (cited on page 114).

Witthaut, D., F Trimborn, and S Wimberger (2008). *Dissipation induced coherence of a two-mode Bose-Einstein condensate.* Physical review letters **101.20**, 200402 (cited on page 129).

Xu, H., D. Mason, L. Jiang, and J. G. E. Harris (2016). *Topological energy transfer in an optomechanical system with exceptional points.* Nature **537.7618**, 80–83 (cited on page 114).

Xu, Z.-F., L. You, and M. Ueda (2013). *Atomic spin-orbit coupling synthesized with magnetic-field-gradient pulses.* Phys. Rev. A **87** (6), 063634 (cited on page 79).

Zhang, X., M. Bishof, S. L. Bromley, C. V. Kraus, M. S. Safronova, P. Zoller, A. M. Rey, and J. Ye (2014). *Spectroscopic observation of SU(N)-symmetric interactions in Sr orbital magnetism.* Science **345.6203**, 1467–1473 (cited on page 3).

Zhu, B., B. Gadway, M. Foss-Feig, J. Schachenmayer, M. Wall, K. Hazzard, B. Yan, S. Moses, J. Covey, D. Jin, J. Ye, M. Holland, and A. Rey (2014). *Suppressing the loss of ultracold molecules via the continuous quantum Zeno effect.* Physical Review Letters **112.7**, 070404 (cited on page 143).

Zwerger, W. (2003). *Mott–Hubbard transition of cold atoms in optical lattices*. Journal of Optics B: Quantum and Semiclassical Optics **5**.**2**, S9 (cited on page 16).